A PHYSICS-BASED DEGRADATION MODELING FRAMEWORK FOR DIAGNOSTIC AND PROGNOSTIC STUDIES IN ELECTROLYTIC CAPACITORS

By

CHETAN S. KULKARNI

Dissertation

Submitted to the Faculty of the

Graduate School of Vanderbilt University

in partial fulfillment of the requirements

for the degree of

DOCTOR OF PHILOSOPHY

in

Electrical Engineering

May, 2013

Nashville, Tennessee

Approved:

Dr. Gautam Biswas

Dr. Xenofon Koutsoukos

Dr. Gabor Karsai

Dr. Sankaran Mahadevan

Dr. Mitchell Wilkes

Dr. Kai Goebel

Dr. José R. Celaya

Copyright © 2013 CHETAN S. KULKARNI
All Rights Reserved

In loving memory of my grandmother
Late Smt. Kamalabai Laxman Kulkarni (Tai Aji)
and
To Baba, Aai, Aditi
for their unconditional love, guidance and sacrifice to live my dreams

PREFACE

Avionics systems play a critical role in many aspects of aircraft flight control. As the complexity of these systems increase, the chances of in-flight malfunctions are also likely to increase. This drives the need for Integrated Vehicle Health Management (IVHM) technologies for flight-critical avionics. Studying and analyzing the performance degradation of embedded electronics in the aircraft domain will help to increase aircraft reliability, assure in-flight performance, and reduce maintenance costs. Further, an understanding of how components degrade as well as the capability to anticipate failures and predict the remaining useful life (RUL) can provide a framework for condition-based maintenance. To support a condition-based maintenance and a safety-critical analysis framework, this thesis conducts a detailed study of the degradation mechanisms of electrolytic capacitors, an important component of most electronic systems.

Electrolytic capacitors are known to have lower reliability than other electronic components that are used in power supplies of avionics equipment and electrical drivers of electro-mechanical actuators of control surfaces. Therefore, condition-based health assessment that leverages the knowledge of the device physics to model the degradation process can provide a generalized approach to predict remaining useful life as a function of current state of health and anticipated future operational and environmental conditions.

We adopt a combined model and data-driven (experimental studies) approach to develop physics-based degradation modeling schemes for electrolytic capacitors. This approach provides a framework for tracking degradation and developing dynamic models to estimate the RUL of capacitors. The prognostics and RUL methodologies are based on a Bayesian tracking framework using the Kalman filter and Unscented Kalman filter approaches.

The thesis makes contributions to physics-based modeling and a model-based prognostics methodology for electrolytic capacitors. Results discuss prognostics performance metrics like the median relative accuracy and the α-λ (alpha-lambda) accuracy. We have also demonstrated the derived physics-based degradation model is general, and applied to both accelerated and nominal degradation phenomena. Our overall results are accurate

and robust, and, therefore, they can form the basis for condition-based maintenance and performance-based evaluation of complex systems.

ACKNOWLEDGEMENTS

I would firstly like to express my deepest gratitude and appreciation towards my advisor, Prof. Gautam Biswas for the continuous support and invaluable guidance he has provided me during the course of my Ph.D. work. Our paths crossed way back in early 2007, which was the genesis of a long journey, at the culmination of which I feel extremely honored and fortunate to have completed my Ph.D. dissertation under his supervision. He has, in many ways, led by example on how to approach and solve problems encountered in research and his strong understanding and proficiency in science and technical concepts has helped me resolve many issues related to my research work. Over these past five years, he has been an excellent mentor to me and I owe him a lot for all the knowledge and encouragement he has showered on me at an important stage of my career.

My earnest thanks to Dr. Kai Goebel and Dr. José Celaya from the NASA Ames Research Center for agreeing to be on my dissertation committee and for all the technical discussions and valuable inputs they have provided me over the years. Their in-depth knowledge in the area of prognostics, physics modeling and ability to resolve fundamental research related problems from a practical standpoint has immensely helped me throughout my Ph.D. work. The experimental work on electrolytic capacitors at the research center forms the core part of this dissertation and required funding and my access to all the laboratory facilities within the research center. This would not have been possible without their continuous support.

I would also like to mention my utmost thanks to Prof. Xenofon Koutsoukos, Prof. Gabor Karsai, Prof. Mitchell Wilkes and Prof. Sankaran Mahadevan for serving on my committee and for their constructive inputs during the preliminary stages of my research. I am greatly honored to have them on my committee.

My sincere thanks to the graduate secretary of the Electrical Engineering program, Linda Koger, along with Kristy Fisher, Tonya Coleman and rest of the staff at the Institute of Software Integrated Systems for all the assistance they provided right from my very first day at Vanderbilt.

This work was supported in part by NASA NRA# NNA08BA45C, ISIS IDC funds, Aviation Safety Program, SSAT Project at NASA Ames and Vanderbilt University under a University Graduate Fellowship.

This work started with the Honeywell - NASA NRA collaborative project and I would like to take this opportunity to thank Raj Bhardwaj, Kyusung Kim and Robert McCroskey of Honeywell Aerospace, who during the time of the project, gave useful insights to improve and develop the work. Countless number of hours were spent in Building 269 during my stay at the research center and this would not have been possible without the dedicated support of the people at NASA Ames. I owe thanks to members of the Prognostics Center of Excellence team, Ann Patterson-Hine, Scott Poll, Adam Sweet, Edward Balaban, Abinav Saxena, Indranil Roychoudhury, Sriram Narasimhan, Phil Wysocki and all the interns along with Bhaskar Saha and Sankalita Saha, who helped in the basic experimental testbed development, model-building, algorithm development and participated in research discussions. A special thanks to Matthew Daigle for his help in understanding the prognostic methodologies, algorithm implementation and feedbacks on the dissertation chapters.

I have been fortunate enough to have some very motivated and talented colleagues during the length of my Ph.D., which made this journey even more enjoyable - Ashraf Tantawy, Anibal Bregon, Abhishek Dubey, Nagabhushan Mahadevan, Akshay Dabholkar, Noemi Alonso, Heath LeBlanc and Emeka Eyisi. All my Water polo and Triathalon club friends for the intense practice sessions, competitions, and races. Moreover, the journey would not have been gratifying without the company of Daniel Mack and Joshua Carl who were an integral part of our intellectual and philosophical sessions at and outside of ISIS.

I will forever be grateful to my friends - Saumitra Vajandar, Ranjit Pawar, Rohit Afzalpurkar, Mandar Jadhav, Amit Gulavani, Srikesh Menon, Sagar Gadkari, Rajan Arora, Jaideep Prabhu, Nikkon Ghosh, Neha Takawale, Bhumi & Shruti Singh, Saikat Sengupta, Gourija Menon, Ameet Dravid and others, who have contributed in their own unique ways during this period and always.

Last but not least, I would like to express my heartfelt gratitude to my parents, Dr. Shrikant Kulkarni and Mrs. Uma Kulkarni for instilling the importance of education in me. They have forever encouraged me positively during the highs and lows of my educational

career. My brother, Kapil Kulkarni, sister-in-law, Priya Kulkarni, brother-in-law, Dr. Kunal Joshi, and rest of my family members have also shown their unconditional love and support over these years. A very special thanks to my in-laws, Dr. Sadanand Joshi and Dr. Asha Joshi for their trust in me. Also to our notorious cat, Kumar with all his pranks and tricks which were part of everyday conversations back home. To my wife, Aditi, thanks for suspending your dream, leaving your family and friends and joining me, so that I could pursue my dream. Your moral and emotional support has helped me go through my (our) difficult times without any problems, this uphill journey has been a much smoother ride than I had initially anticipated.

This acknowledgment would be incomplete without offering my sincere appreciation to Vanderbilt University and the Institute of Software Integrated Systems for giving me this opportunity to complete my graduate studies.

CONTENTS

Page

PREFACE iv

ACKNOWLEDGEMENTS vi

LIST OF TABLES xiii

LIST OF FIGURES xiv

Chapter

I. INTRODUCTION 1

Motivation 1
Problem Statement 5
Goals 7
Research Challenges 8
Organization 9

II. LITERATURE SURVEY 12

Introduction to Prognostics 12
Prognostics Methods 14
Model Based Prognostic Approach 14
Data Driven Approach 16
Electronics Prognostics Methods 17
Physics-Based Reliability Modeling 18
Physics-based Reliability Modeling under Accelerated Testing 20
Summary 23

III. CASE STUDY: AVIONICS SYSTEM 25

GPS Model 26
INAV Model 30
Power Supply Model 33
Background 33
DC-DC Converter Fault/Degradation List 36
Fault Simulation and FDI Results 38
Fault Detection and Isolation: GPS 38
Fault Detection and Isolation: INAV 40
DC-DC Converter System 40
Results 47
Summary 54

IV. RESEARCH APPROACH 56

Approach Steps 56

Electrolytic Capacitors . . . 56
Accelerated Aging Experiments . . . 57
System Identification . . . 59
Degradation Modeling . . . 61
Parameter Estimation for Degradation Models . . . 61
Prognostics . . . 61
Summary . . . 62

V. CAPACITOR DEGRADATION MODELS . . . 63

Electrolytic Capacitors . . . 63
Degradation Mechanisms . . . 65
Equivalent Internal Circuit Model . . . 68
Degradation Phenomenons Under Study . . . 71
Electrolyte Evaporation . . . 72
Computing Initial Electrolyte Volume . . . 78
Oxide Layer Breakdown . . . 81
Physics-Based Degradation Models . . . 84
Capacitance Degradation Model . . . 85
ESR Degradation Model . . . 86
Time Dependent Degradation Models . . . 87
Increase in Capsule Internal Pressure . . . 87
Summary . . . 89

VI. ELECTRICAL OVERSTRESS . . . 91

Electrical Stress Degradation . . . 92
Equivalent Electrical Circuits . . . 92
Electrical Overstress Experiments . . . 93
Power Supply . . . 94
Function Generator . . . 94
Amplification Stage . . . 94
Load Resistor . . . 94
Measurements . . . 95
Impedance measurement . . . 95
Experiment I - 12V EOS . . . 97
Prognostics Problem Formulation . . . 99
Empirical Model for Capacitance Degradation . . . 101
Degradation Model . . . 101
State-Space Model for Degradation Estimation . . . 103
Prediction of Remaining Useful Life Results . . . 103
Validation Tests . . . 104
Physics Based Modeling Framework using Unscented Kalman Filter . . . 107
Unscented Kalman Filter . . . 107
Capacitance Degradation Dynamic Model . . . 112
UKF for Capacitance State Estimation . . . 116
ESR Degradation Dynamic Model . . . 117
UKF for ESR State Estimation . . . 118
Experiment II - 10V EOS Experiment . . . 119

Prediction of Remaining Useful Life Results and Validation Tests 121
Results for Capacitor Degradation Model ($\mathcal{D}_4$) for Experiment I 122
Results for Capacitor Degradation Model ($\mathcal{D}_4$) for Experiment II 126
Results for ESR Degradation Model ($\mathcal{D}_5$) for Experiment I 130
Results for ESR Degradation Model ($\mathcal{D}_5$) for Experiment II 133
Discussion and Summary 135

VII. THERMAL OVERSTRESS 138

Introduction 138
Physics Based Modeling of Capacitor Degradation 139
Equivalent Electrical Circuits 139
Capacitance Degradation Model 140
Experimental Setup 141
Experimental Data Analysis 142
Electrolyte Volume Degradation Model 143
Parameter Estimation Approach 145
Parameter Estimation Results 146
Physics-Based Degradation Models using Kalman Filter 149
Dynamic Models 150
Kalman Filter for Sate Estimation 152
RUL and Validation Results 154
Physics-Based Modeling Framework using Unscented Kalman Filter 157
Prediction of RUL and Validation Tests 159
Physics Based Modeling Framework using UKF for 2200 μF capacitors 164
Prediction of RUL and Validation Tests 165
Physics Based Modeling Framework using UKF for 10000 μF capacitors . . . 169
Prediction of RUL and Validation Tests 170
Discussion and Summary 175

VIII. NOMINAL DEGRADATION 177

Introduction 177
Equivalent Electrical Circuits 178
Nominal Degradation Experiment 178
Empirical Model 181
Degradation Dynamic Models 184
Prediction of RUL and Validation Tests for Capacitance Degradation Model, $\mathcal{D}_4$ 186
Prediction of RUL and Validation Tests for ESR Degradation Model, $\mathcal{D}_5$ 191
Discussion and Summary 197

IX. CONCLUSIONS 199

Summary of Contributions 199
Future Directions 204
System Level Prognostics 204
Granularity of the Models 205
Handling Uncertainty 206

Appendix

A. PUBLICATIONS 209

B. ELECTRICAL OVERSTRESS - PRINTED CIRCUIT BOARD 213

BIBLIOGRAPHY 216

LIST OF TABLES

Table Page

1 GPS Receiver Faults . . . 28
2 INAV Faults . . . 32
3 Basic Bond graph elements . . . 35
4 DC-DC Converter Fault Signatures . . . 47
5 Approximate lumped parameter values associated with Capacitor . . . 70
6 Electrical Overstress Degradation Experiments . . . 92
7 Degradation model parameter estimation results. . . . 102
8 Summary of validation results based on RA for model $\mathcal{E}_2$ . . . 107
9 Parameter values used for degradation models capacitance($\mathcal{D}_4$) and ESR($\mathcal{D}_5$) at 12V EOS . . . 119
10 Parameter values used for degradation models capacitance($\mathcal{D}_4$) and ESR($\mathcal{D}_5$) at 10V EOS . . . 122
11 Summary of validation results based on RA for Capacitance degradation model $\mathcal{D}_4$ - 12V EOS Experiment . . . 125
12 Summary of validation results based on RA for Capacitance degradation model $\mathcal{D}_4$ - 10V EOS Experiment . . . 129
13 Summary of validation results based on RA for ESR degradation model $\mathcal{D}_5$ - 12V EOS Experiment . . . 132
14 Summary of validation results based on RA for ESR degradation model $\mathcal{D}_5$ - 10V EOS Experiment . . . 135
15 Thermal Overstress Degradation Experiments . . . 139
16 Parameter Estimation for Degradation Model, $\mathcal{D}_3$ . . . 148
17 Error Summary for Degradation Model, $\mathcal{D}_3$ . . . 149
18 Parameter values used for model $\mathcal{D}_4$ - 2200 μF at 105°C . . . 158
19 Summary of RUL forecasting results with j_{eo} estimation - 2200μF . . . 163
20 Parameter values used for models $\mathcal{D}_4$ - 2200 μF at 105°C . . . 165
21 Summary of RUL forecasting results with j_{eo} and c_b estimation - 2200μF . . . 168
22 Parameter values used for models $\mathcal{D}_4$ - 10000 μF at 105°C . . . 170
23 Summary of RUL forecasting results with j_{eo} and c_b estimation - 10000μF . . . 174
24 Parameter values used for degradation models $\mathcal{D}_4$ and $\mathcal{D}_5$ - Nominal . . . 186
25 Summary of validation results based on RA for Capacitance degradation model $\mathcal{D}_4$ - Nominal . . . 191
26 Summary of validation results based on RA for Capacitance degradation model $\mathcal{D}_5$ - Nominal . . . 196

LIST OF FIGURES

Figure Page

1 Approaches to Implement Prognostic Methodologies 15
2 Avionics Simulated System 26
3 Loss of satellite lock simulation 29
4 Satellite Drift 30
5 Feedback implementation of the complementary extended Kalman filter 31
6 Gyro bias, injected faulty signal 33
7 Buck Boost Converter Circuit 34
8 Buck Boost Converter Bond Graph Model 36
9 Buck Boost Converter Simulink Model 36
10 Loss of lock to satellites Input data frame for GPS receiver showing satellites variable from 149th - 160th secs. 39
11 GPS receiver BIT indicating the loss of satellite making the GPS solution unusable from 152nd to 155th secs. 39
12 IMU accelerometer bias detection in the z-axis 40
13 Gyro bias drift detection 41
14 TCG of the Power Supply Model from BG 45
15 Residual Plot for the DC-DC converter 46
16 Fault Injection in the PSM model 48
17 GUI for injecting fault 48
18 Fault Injection GUI for injecting Capacitor faults in PSM 49
19 Capacitor Fault Injection and Output Voltage plots 50
20 MOSFET Fault Injection and Output Current plots 50
21 Algorithm output results for the injected capacitor fault 51
22 Fault Injection GUI for injecting MOSFET faults in PSM 51
23 Capacitor Fault Injection and Output Voltage plots 52
24 MOSFET Fault Injection and Output Current plots 52
25 Algorithm output results for the injected MOSFET fault 53
26 Incipient Fault Injection 53
27 Fault Isolation Results 54
28 Research Approach Methodology 57
29 Lumped parameter model ($\mathcal{M}_1$) for a real capacitor. 60
30 Low pass filter model 60
31 Capacitor Physical Structure[1] 64
32 Physical Model of Electrolytic Capacitor 64
33 Capacitor Open Structure 65
34 Cross sectional Details of Internal Capacitor Structure 65
35 Ishikawa Diagram of Failure Mechanisms in Aluminum Electrolytic Capacitor . 66
36 Equivalent Electrical Model of Electrolytic Capacitor ($\mathcal{M}_1$) 69
37 Simplified lumped parameter electrical Model ($\mathcal{M}_2$) 71
38 Lumped parameter electrical Model ($\mathcal{M}_3$) 71
39 Comparative Radial Heat Flow in Electrolytic Capacitor 73
40 Heat flow Model of Electrolytic Capacitor under electrical Stress 73
41 Heat flow Model of Electrolytic Capacitor under thermal Stress 77

42 Equivalent circuit for the interpretation of a breakdown event 82
43 Electrical Overtress Degradation Electrical Equivalent Model($\mathcal{M}_4$) 93
44 Lumped Parameter Model ($\mathcal{M}_1$) 93
45 Block diagram of the experimental setup. 93
46 Custom Module PCB developed for EOS Experiment 95
47 EOS experimental setup. 96
48 Electro-impedance measurements at different aging times. 98
49 Degradation of capacitor performance, ESR increase as a function of aging time. 99
50 Degradation of capacitor performance, capacitance loss as a function of aging time. 100
51 Estimation results for the empirical degradation model. 102
52 Tracking results for the Kalman filter implementation applied to test capacitor (capacitor #6). 104
53 T_6: Health state estimation and forecasting of capacitance loss (%) at different times t_p during the aging time; $t_p = [0, 24, 47, 71, 94, 116, 139, 149, 161, 171]$. . . 105
54 Performance based on Alpha-Lambda performance metric. 106
55 Degradation of capacitor performance, ESR increase as a function of aging time. 120
56 Degradation of capacitor performance, capacitance loss as a function of aging time. 121
57 Tracking filter output against measurement data for Cap # 2 123
58 Estimation of capacitance dependance oxide layer breakdown factor (c_b) 123
59 Capacitance decrease prediction at different Aging Time for Cap # 2 124
60 Performance based on Alpha-Lambda metric for Cap#2 125
61 Tracking filter output against measurement data for Cap # 5 127
62 Capacitance decrease prediction at different Aging Time for Cap # 5 128
63 Performance based on Alpha-Lambda metric for Cap#5 129
64 Tracking filter output against measurement data for Cap # 2 130
65 ESR prediction at different Aging Time for Cap # 2 by Model $\mathcal{D}_5$ 131
66 Performance based on Alpha-Lambda metric for Cap#2 132
67 Tracking filter output against measurement data for Cap # 5 133
68 ESR prediction at different Aging Time for Cap # 5 by Model $\mathcal{D}_5$ 134
69 Performance based on Alpha-Lambda metric for Cap#5 134
70 Lumped Parameter Model ($\mathcal{M}_1$) 139
71 Lumped Parameter Model ($\mathcal{M}_2$) 140
72 Capacitors in Thermal Chamber 141
73 Nyquist Plot of a typical capacitor under Thermal Stress 143
74 Bode Plot of a typical capacitor under Thermal Stress 144
75 Thermal Overstress at 105° C - 2200uF 144
76 Volume and Capacitance Estimation (Cap # 4) 146
77 Volume and Capacitance Estimation (Cap # 5) 147
78 Estimation results for the degradation model 147
79 Electrolyte volume (V_e) estimation residuals 148
80 Capacitance (C) measured and estimation residuals 149
81 Tracking filter outuput against measurement data for Cap # 5 155
82 Capacitance decrease prediction at different Aging Time for Cap # 5 156
83 Performance based on Alpha-Lambda metric for Cap#5 156
84 Tracking filter output against measurement data for Cap # 5 159
85 Capacitance decrease prediction at different Aging Time for Cap # 5 160

86 Performance based on Alpha-Lambda metric for Cap#5 161
87 Tracking filter output against measurement data for Cap # 8 165
88 Capacitance decrease prediction at different Aging Time for Cap # 8 166
89 Performance based on Alpha-Lambda metric for Cap#8 167
90 Thermal Overstress at 105° C - 10000uF 169
91 Tracking filter output against measurement data for Cap # 7 171
92 Capacitance decrease prediction at different Aging Time for Cap # 7 172
93 Performance based on Alpha-Lambda metric for Cap#7 173
94 Lumped Parameter Model ($\mathcal{M}_1$) 178
95 DC-DC converter Hardware 179
96 Experimental Setup for 3 DC-DC converter Units 180
97 ESR degradation under Nominal Operating Conditions 181
98 Capacitance Degradation under Nominal Operating Conditions 181
99 Arrhenius model data against measurement data for Cap# 1 183
100 Arrhenius model data against measurement data for Cap# 2 183
101 Arrhenius model data against measurement data for Cap# 3 184
102 Tracking filter output against measurement data for Cap # 1 187
103 Tracking filter output against measurement data for Cap # 2 187
104 Tracking filter output against measurement data for Cap # 3 187
105 Capacitance decrease prediction at different Aging Time for Cap # 1 188
106 Capacitance decrease prediction at different Aging Time for Cap # 2 189
107 Capacitance decrease prediction at different Aging Time for Cap # 3 189
108 Performance based on Alpha-Lambda metric for Cap#1 190
109 Performance based on Alpha-Lambda metric for Cap#2 190
110 Performance based on Alpha-Lambda metric for Cap#3 190
111 Tracking filter output against measurement data for Cap # 1 192
112 Tracking filter output against measurement data for Cap # 2 192
113 Tracking filter output against measurement data for Cap # 3 192
114 ESR prediction at different Aging Time for Cap # 1 by Model $\mathcal{D}_5$ 193
115 ESR prediction at different Aging Time for Cap # 2 by Model $\mathcal{D}_5$ 194
116 ESR prediction at different Aging Time for Cap # 3 by Model $\mathcal{D}_5$ 194
117 Performance based on Alpha-Lambda metric for Cap#1 195
118 Performance based on Alpha-Lambda metric for Cap#2 195
119 Performance based on Alpha-Lambda metric for Cap#3 196
120 Top Layout of the EOS Board 213
121 Bottom Layout of the EOS Board 214
122 Component Layout of the EOS Board 215

CHAPTER I

INTRODUCTION

Most devices and systems today contain embedded electronic modules for monitoring, control and enhanced functionality. However, these modules may contain components that have higher failure rates than the other electronic components [1,2] thus affecting the overall operational functionality and reliability of the system. These component failures can be attributed to adverse operating conditions, such as high temperatures, voltage surges and current spikes [3,4]. Studying and analyzing the degradation of these systems (i.e.,degradation in performance) will help us meet a number of safety critical goals that include :

1. advance failure warnings;
2. better detection of degradation, therefore, the ability to minimize unscheduled maintenance, and
3. extend regular maintenance cycles through tolerance and repair action;
4. better understanding of component behaviors under different operating conditions, thus decreasing inspection costs, downtime, and inventory for replacement parts resulting in reduced life cycle costs; and
5. improved incident and system qualification, leading to better logistical support of fielded systems and better design of future systems.

In the rest of the chapter, we first describe the motivation for our work, followed by the specific research objectives. We then describe the specific contributions of the dissertation, and conclude with the organization of the thesis work.

Motivation

In safety critical domains, such as aircraft operations, flight and ground staff need to acquire information regarding the current health state for all subsystems, such as the structures,

propulsion, control, guidance and navigation systems of the aircraft on a regular basis to maintain safe operation. This has given rise to research projects that focus on accurate diagnosis of faults, developing precursors to failure, and predicting remaining component life [5, 6]. Most avionics systems and subsystems in modern aircraft contain significant electronic components, which perform a critical role in on-board, autonomous operations for vehicle controls, communications, navigation and radar systems. Future aircraft systems in an attempt to reduce weight and fly in a more autonomous manner, will rely on a great number of electric and electronic components. This may also increase the likelihood of electronics related faults in these systems, with perhaps higher unanticipated fault modes that will be hard to detect and isolate. It is very important to develop methodologies for system health awareness in aircraft systems, to improve aircraft reliability, assure in-flight performance, and reduce maintenance costs. To achieve this, we need to develop an understanding of how components degrade and use these methods to anticipate failures and predict the remaining useful life of electronic components [5, 6].

In the past, reliability based methodologies have been implemented for making health assessment of the systems. Reliability is the ability of a system to operate within specified performance limits without failing for a pre-specified period of time. Traditional reliability prediction methods have been applied to electronic systems [7–10]. These data driven methods rely on a collection of failure data, and the general assumption is that the components in a system have specified failure rates (assumed to be constant) that can be modified to take into account varying quality, operating, and environmental conditions. There are well-documented concerns of this type of analysis [11–14]. The general consensus is that data reported in handbooks should not be used for prognostics, because they represent average conditions and it is not conditions based, hence are inaccurate when predicting actual field failures [12, 15]. Therefore, alternate methods should be developed for making prognostics predictions for electronics systems.

Some of earlier efforts in diagnostic health monitoring of electronic systems and subsystems involved the use of a built-in test (BIT), defined as an on-board hardware-software diagnostic tests to identify and locate faults. In addition to a test, a BIT can consist of correction circuits, self-checking circuits, and self-verification circuits [15]. Two types of BIT

concepts are employed in electronic systems: interruptive BIT (I-BIT) and continuous BIT (C-BIT). The concept behind I-BIT is that normal equipment operation is suspended during BIT operation. The concept behind C-BIT is that equipment is monitored continuously and automatically without affecting normal operation. But the use of this method also has several limitations. Studies [16, 17] conducted on the use of BIT methodology for fault identification and diagnostics showed that they can be prone to false alarms and can result in unnecessary costly replacement, re-qualification, delayed shipping, and loss of system availability. BIT concepts are still being developed to reduce the occurrence of spurious failure indications [18]. The persistence of such issues over the years is perhaps because the use of BIT has been restricted to low-volume systems. In general, BIT methodologies have not been designed to provide prognostics or remaining useful life due to accumulated damage or progression of faults. Rather, it has served primarily as a diagnostic tool.

The term "diagnostics" relates to the ability to detect and isolate faults or failures in a system. "Prognostics" on the other hand is the process of predicting health condition and remaining useful life based on current state, previous conditions and future operating conditions. Prognostics and health management (PHM) is a method that permits the assessment of the health of a system under its actual application conditions. PHM methods combine sensing, data collection, interpretation of environmental, operational, and performance related parameters to indicate systems health. PHM methodologies can be implemented through the use of various techniques that study parameter value changes, which can be considered to be indicators for:

- Performance degradation, such as the deviation of operating parameters from their expected nominal values, causing the performance of the system to deteriorate gradually.

- Changes operation profile, such as usage duration and frequency, ambient temperature and humidity, vibration, and shock. In other words, the components or systems may be operated beyond their specified operating regions, causing faster than expected degradation.

Prognostics and Health Management methodologies have emerged as one of the key enablers for achieving efficient system level maintenance as part of a busy operations schedule, and lowering overall life cycle costs in military systems [5, 18]. PHM is also emerging as a high-priority issue in space applications, where the focus is on conducting fundamental research in the field of integrated systems health management (ISHM). This includes design of health management systems, selection and optimization of sensors, *in-situ* monitoring, data analysis, prognostics, and diagnostics to ensure safety and reliability of missions. Presently, innovative work is carried out in the area of power semiconductor devices (investigation of the effects of aging on power semiconductor components, identification of failure precursors to build a physics based model [5, 19], and development of algorithms for end-of-life prediction), batteries (algorithms for batteries prognosis) [20], flight actuators (modeling and development of algorithms for estimation of remaining life) [6], solid rocket motor failure prediction, rocket fueling pumps [21] and aircraft wiring health management [5, 22].

Prognostics and health management for electronic systems aims to detect, isolate, and predict the onset and source of system degradation as well as the time to system failure. The goal is to make intelligent decisions about the system health and to arrive at strategic and business case decisions. As electronics become increasingly complex, performing PHM efficiently and cost-effectively is becoming more demanding [18].

The development of prognostics methodologies for the electronics field has become more important as more electrical systems are being used to replace traditional systems in several applications in the aeronautics, maritime, and automotive fields. The development of prognostics methods for electronics presents several challenges due to the great variety of components used in a system, a continuous development of new electronics technologies, and a general lack of understanding of how electronics fail. Traditional reliability techniques in electronics tend to focus on understanding the time to failure for a batch of components of the same type by running multiple experiments and making probabilistic estimates from the accumulated data. Recently there has been a push to understand, in more depth, how faults progress as a function of loading and environmental conditions. Furthermore, just until recently, it was believed that there were no precursor to failure indications for electronics components and systems. That is now understood to be incorrect, since electronics

systems, much like mechanical systems, undergo a measurable wear process from which one can derive features that can be used to provide early warnings of failure. The indications of degradation caused by the wear can be detected fairly early, and by modeling the process, one can potentially predict the remaining useful life as a function of future use and environmental conditions.

Avionics systems perform critical functions on aircraft greatly escalating the ramification of an in-flight malfunction [23, 24]. These systems combine physical processes, computational hardware and software; and present unique challenges for fault detection and isolation. A systematic analysis of these conditions is very important for analysis of aircraft safety and also to avoid catastrophic failures during flight. Power supplies are critical components of modern avionics systems. Degradations and faults in the DC-DC converter unit propagate to the GPS (global positioning system) and navigation subsystems affecting the overall operations of the aircraft. Some of the more prevalent fault effects, such as a ripple voltage surge at the power supply output can cause glitches in the GPS position and velocity output, and this in turn, if not corrected can propagate and distort the navigation solution.

Problem Statement

Prognosis methods have been widely used in medical practice to discover the probable cause of a disease and predict its eventual consequences [25]. In engineering domains, a lot of work in PHM has also been done in the area of mechanical and structural systems [18]. PHM algorithms have also been implemented in economic markets and weather forecasting [22]. Safety critical mechanical systems and structures such as propulsion engines, aircraft structures, bridges, buildings, roads, pressure vessels, rotary equipment, and gears have benefited from advanced sensor systems developed specifically for *in-situ* fault diagnosis (condition monitoring), and health and usage monitoring [26–30]. As a result, a considerable body of knowledge exists on prognostics and health management of mechanical and structural systems, with research conducted in establishing failure precursors (such as changes in vi-

bration signatures of roller bearings and variations in acoustic levels due to wear) and developing reasoning algorithms to detect and compute the extent of degradations [1, 27].

Prognostics failure predictions have to be accurate, if they are to be used in taking decisions in repair, replacement or some adaptive control scheme of components and subsystems. Detailed examinations of actual parameter variations and degradation process should be understood and interpreted using physics-based degradation models so that the results can be generalized and applied across systems. Pure data driven approaches have the disadvantage of not generalizing to similar components made by different manufacturers, or analyzing component degradation under different operating conditions. It is difficult to quantify product degradation and the progression from degradation to complete failure by pure data-driven methods [31].

The inability to accurately identify failure mechanisms in prediction models often results in inaccurate remaining useful life estimates, unnecessary complexity and lowered cost effectiveness. Consequently, it can be difficult to implement diagnostic and prognostic methodologies that can directly monitor the faults or conditions, which occur in electronic systems, particularly at the component level. The major elements of the prognostic prediction process involve envournmental conditions, various stressors, device manufacturing standard, and similar considerations.

The problem addressed in this research applies effective PHM methodologies to electronic devices and systems, an area that has not been studied in as much detail as mechanical systems and structures. Degradation in electronic components is difficult to detect and characterize because of the complexities in developing degradation models of electrical and electronic phenomena, and the complex interactions electronic components have with the rest of the system. In many cases, degradation of a single component in a electronic system may lead to failure or loss of designated electrical performance, and it may be difficult to quantify product degradation based on the precursors to isolate the degrading component and the progression from degradation to complete failure. Lack of accurate identification of failure mechanisms in the prediction models often results in making inaccurate remaining useful life predictions [31].

Goals

The research work focuses on developing and implementing effective diagnostic and prognostic methodologies, that includes the ability to detect degradation in electrical and electronic components through failure precursors in the system. The main goals and problems that we address in this thesis research include -

1. Developing models for fault detection and isolation methods;
2. Detailed physics-based component degradation dynamic models to track changes in behavior and performance of the components projected at the system level;
3. Methodology to make accurate predictions of remaining useful life based on the derived degradation models or time to failure of components to impact maintenance and cost decisions.

This research work is directed towards studying and implementing PHM methodologies to electronic components. Specifically as a case study we use DC-DC converters in avionics systems of aircrafts as an motivating examples and case study. Capacitors and metaloxidesemiconductor field-effect transistor(MOSFETs) are the two major components, which cause degradation and failures in DC-DC converters [32]. Capacitors are used as filtering elements on power electronics systems.

Low reliability and their criticality in avionics systems makes electrolytic capacitors important candidates for a health management solution. In addition to this, degradation at component level could lead to cascading faults at sub-system and system level. In order to mitigate the effects of capacitor failures in critical to safety systems, we introduce here, a condition-based prognostics methodology. This methodology provides the ability to identify degradation effects and to estimate the remaining useful life of the components periodically. This method will further allow for prognostics-based decision making for optimal maintenance scheduling of the system or for implementation of mitigation strategies in case of contingencies during operation.

Research Challenges

The modeling methodology in our work is based on the premise that degradation leading to failures in components is a result of fundamental mechanical, chemical, electrical, and thermal phenomena that can be represented by physics-based degradation models evolved from the first principles of the component. The objective of physics-based degradation modeling methodology in implementing a PHM process is to calculate the cumulative damage due to various failure mechanisms for a system operating in typical environments, and be able to make accurate predictions based on current state and previous operating conditions. This approach to implementing the degradation models for PHM can be derived based on different failure modes. A failure mode is defined as the effect by which a failure is observed to occur [33]. It can also be defined as the way in which a component, subsystem, or system could degrade over time and eventually fail to deliver the intended operational functionality. All possible failure modes of interest for each identified element should be listed and modeled independently [34]. Generally, potential failure modes can be identified using available underlying structure, material physics, material properties, first principles of operation, operational data, monitoring degradation in devices, running accelerated life testing and collecting degradation data, and Failure mode and effect analysis (FEMA) methods [33].

Design capture is the process of collecting structural (dimensional) and material information about a product to generate a model. This step involves characterizing the product at all levels, that is, parts, systems, and physical interfaces [34]. The potential failure identification step involves using the geometry and material properties of the product, together with the measured life-cycle loads acting on the system based on the experimental data, to methodically identify the potential failure modes, mechanisms, and failure sites in the system or a particular component [35]. A load-stress analysis is conducted using material properties, operating conditions and the operating life-cycle loads. With the computed stresses and the failure models, an analysis is conducted to determine the cycles to failure and then the accumulated damage is estimated using a damage model. Studying the dynamics of the device is the key in developing the degradation models from first principles of operation. Developing degradation models from the underlying first principles gives the

most accurate behavior of the device under varying operating conditions and a good prediction estimate of degradation parameters in the device. The physics-based degradation modeling methodology could provide a systematic approach to reliability assessment early in the design process [34].

Even though there are advances in certain areas related to prognostics, many challenges still remain. The key issues with regard to implementing PHM methodologies for a component/system includes decisions related to, system parameters to monitor, selection of sensors to monitor parameters, power supply for sensors, on-board memory for storage of sensed data, *in-situ* data acquisition, and feature extraction from the collected data. One of the critical task of implementing PHM methodology is tracking the degradation based on the developed models. Getting information and developing models from one component /system and implementing it onto other could be hard, especially when the systems are made by different vendors [18, 36] and hence condition based monitoring becomes very essential for implementing PHM methods. It is further a challenging task of projecting the developed physics-based degradation models to predict the RUL of a device and the overall system performance. Accurate prognostics predictions are very important to demonstrate economic effectiveness of PHM methods through condition based maintenance, losses due to down time.

Organization

Chapter II presents a literature review and overview of the concept of prognostics and health management. First, we introduce Prognostics and Health Management methodologies and their general application in prognostics. Then, we discuss the model based, data driven and probabilistic methodologies to PHM. Since our work is more focused on electrical and electronic systems we further discuss in detail the application of PHM methodologies to electronics. We implement a physics-based degradation approach to prognostics and the rest of the chapter discusses the background, conceptual models implemented and the failure mechanisms observed in electronics prognostics.

Chapter III presents the case study for avionics systems. This research is conducted at the system level, which includes avionics systems components like Global Positioning System (GPS), Inertial Navigation (INAV) System and power supply. Models were developed for each of the system and we implemented a fault detection and isolation methodology for the overall system. The chapter discusses each of the model in detail with the fault simulation and diagnosis work. Some interacting faults were studied between the DC-DC converters, GPS and INAV the results of which are discussed in the chapter. Since our work was more focused on DC-DC power converters we discuss the modeling of DC-DC converters using bond-graph models and fault detection and isolation using model based methods.

Chapter IV presents the approach for building physics-based degradation models for electrolytic capacitors. The models were verified using accelerated aging data as well as nominal degradation data for capacitor components in the DC-DC converters. In particular we conducted three sets of experiments i.e., nominal, thermal and electrical overstress experiments. These are introduced in this chapter while the details of the experiments and results are discussed in the respective chapter later in the work. This chapter summarizes the overview of the research work.

Chapter V discusses the detailed study for deriving the physics based degradation models of electrolytic capacitors. We first, discuss the basic structure of an electrolytic capacitor and the different degradation mechanisms. Each of the underlying phenomenon leading to degradation is explained and its link to the degradation process. Based on the degradation mechanisms the physics-based models are developed. A step by step method implemented for deriving the degradation models for the failure precursors capacitance (C) and equivalent series resistance (ESR) is explained. The chapter ends with deriving the time dependent degradation models to be implemented in a Bayesian framework.

Chapter VI presents the work on electrical overstress experiments. We discuss the degradation phenomenon under electrical overstress and link them to the precursors to failure. An electrical experimental setup was developed for this experiment and we describe this complete setup along with details of boards designed and instruments used. Based on the degradation data our first approach was to implement an physics inspired empirical model based on the experimental data. We present the derived model and the prognostic

and validation results for the model. We further discuss the physics-based degradation model derived and implemented in a Bayesian framework. The prognostics and validation results are presented for the derived degradation model.

Chapter VII presents the work on thermal overstress experiments. First, we discuss the degradation phenomenon under thermal overstress conditions. We then present the methodology for deriving the physics-based degradation models based on the discussion in Chapter V along with the thermal overstress experiment setup. As initial part of the research work, we derived a electrolyte degradation model which is discussed along with the development of the model and results. The next step was to derive a physics-based degradation model and since this was the first data set use for the model we first implemented a Kalman Filter approach keeping most of the parameters constant. We discuss the approach taken, steps involved in deriving the model and the results. The model was updated to estimate some the critical degradation parameters to be estimated online based on the state. An Unscented Kalman Filter was used for the updated model which gave better results. The prognostics results and the validation tests are discussed in the concluding sections.

Chapter VIII presents the work related to nominal degradation experiments. Under different conditions the underlying degradation phenomenon changes leading to different parameters being degraded. First, we discuss the underlying degradation phenomenon for nominal degradation. The later part of the chapter discusses the experimental setup, data and the derived models. We also present our results for the work done based on the nominal degradation data.

Chapter IX summarizes the contributions of this dissertation. We then point out the current limitations of the approach, and describe directions in which this work may be improved in the future.

CHAPTER II

LITERATURE SURVEY

The term prognosis has been used widely in medical practice to imply the foretelling of the probable course of a disease [25]. In the industrial and manufacturing areas, prognosis is interpreted as the methodology to predict the remaining useful lifetime of a machine or a component once an impending failure condition is detected, isolated, and identified [36]. If a fault can be detected early, before its effects propagate and affect other components, then only the degraded components (e.g., a capacitor, or a transistor) needs to be replaced. Higher severity levels of faults in components may require the entire subsystem(e.g., a Power Supply to be replaced. Often, severe and complete failures in components may also cause damage to adjoining components and subsystems(e.g., a capacitor failure may cause high ripple currents that causes downstream subsystems, such as the GPS and INAV of the avionics system to fail). It is clear that predictions about fault severity and impending failures are essential to maintaining reliability of system operations and the overall safety of the system. Prognostics methods have been applied for forecasting the future states of a system in a large number of disciplines from business and finance to weather predictions, among many others. It has also attracted a lot of interest among researchers and practitioners recently [18, 36].

Introduction to Prognostics

Prognostics and health management methodologies evaluate remaining useful life of a system under actual usage conditions [37]. In particular, 'prognostics' covers the process of predicting future system states based on the past operations, current conditions and anticipated future operation. Overall PHM is directed towards achieving multiple practical goals, such as systems safety, reductions in operational and support costs, maintenance costs, and the life cycle total ownership costs [18, 27]. For safety critical systems, which require constant monitoring of the systems and its components, prognosis methods plays

a very important role in early detection of component degradation, which in turn plays a key role in predicting the evolving conditions of the components. This in turn helps make important performance related decisions about the subsystem or system which can then influence maintenance decisions by tracking components as they reach limits of their useful life cycle. Diagnostic systems assist the predictive process by providing the initial detection and isolation capabilities [27, 37].

Prognostics is broadly defined as the detection of a failure precursor followed by the prediction of remaining useful life (RUL). For end-of-life predictions of critical systems, it becomes imperative to establish high confidence in the prognostic conclusions before incorporating their predictions into the decision-making process [18]. The aerospace industry, one of the major users of PHM technologies, is leading significant research and development activity in prognostics related to aircraft systems [6, 22]. Health inspections and monitoring spacecraft and aircraft systems are often difficult and costly, often because relevant sensors cannot be installed at the right places [37–39]. However, in aircraft systems consequences of a premature failure can be catastrophic. Therefore prognostics methods have been developed for monitoring the condition of aircraft structures, avionics systems, wiring, control actuators, power supplies, and propulsion systems. Prognostic functionality is also being incorporated into the health management systems of the latest military aircraft [40] and civilian aircraft, in order to reduce the overall life-cycle cost and improve flight readiness. However as discussed earlier, prognostics studies and applications to electronics components and subsystems are currently less advanced than the work being done in prognostics of mechanical systems [22, 37, 39].

Electronic components such as power amplifiers, power converters, electronic control units, and avionics present substantial challenge to applying PHM methodologies [36, 39, 41, 42]. Normally system engineers use the failure rates of electronic systems from laboratory test data, which is used to define mean time between failures (MTBF) [36]. Empirical analysis of electronic components has shown to exhibit typical failure behaviors that can be represented as a bathtub curve [42, 43] which show a the apriori statistics over a large population of components(and should not be confused with prognostics). The conventional assumption is that the overall manufactured batch of the electronics components manufac-

tured, have constant (and low) failure rates for most of their installed life, after they have gone past the initial period of possible infant mortality.

Electronic systems are continually evolving, and the life cycle of some computer chips and other components typically is only 3 to 5 years [1, 18, 36, 43]. It is possible that some failure modes may occur only as a small fraction of the entire system and subsystem component failures, making it very difficult to apply the typical data driven methodologies of diagnostic and prognostic processes [1, 18, 31]. Therefore, design analysis at the beginning of system design should examine these factors to ensure that the optimal balance of technology upgrades and prognosis is achieved [1, 18]. Next we discuss some of the prognostic methods used for studying and analysis of system and subsystem degradation.

Prognostics Methods

A number of different methods have been applied to study prognosis of degraded components. In general, prognostics approaches can be classified into three primary categories: (1) model based techniques, (2) data driven and (3) Hybrid approaches, which combine both data-driven approaches as well as model-based approaches. Fig. 1 summarizes the range of prognosis approaches applied to different systems and their relative cost for implementation and operation.

Model Based Prognostic Approach

Model based prognostic techniques use analytic and/or physics-based models of the degradation phenomenon to predict the dynamics and degradation in system behavior. These approaches apply to situations where accurate mathematical models of system behavior can be constructed from first principles [45, 46]. Model-based methods assume that the system is represented as a model. Adams [49] proposed to model damage accumulation in a structural dynamic system as first/second order nonlinear differential equations. Chelidze [50] modeled degradation as a slow-time process, which is coupled with a fast-time, observable subsystem. The model was used to track battery degradation (voltage) of a vibrating beam system. The main advantage of model-based approach is the ability to incorporate physical

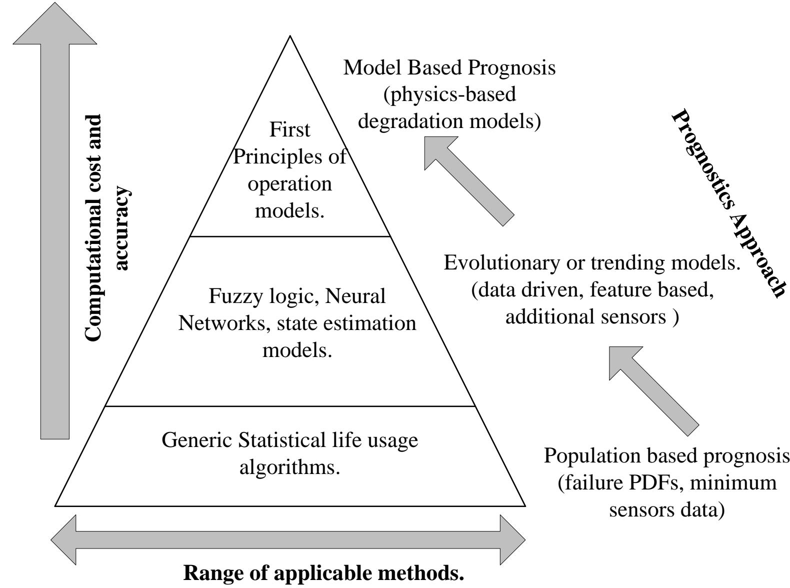

Figure 1: Approaches to Implement Prognostic Methodologies

understanding of the system to monitoring. Another advantage is that, in many situations, the changes in feature vector are closely related to model parameters [51]. Therefore, it can also establish a functional mapping between the drifting parameters and the selected prognostic features. Moreover, if understanding of the system degradation improves, the model can be adapted to increase its accuracy and to address subtle performance problems. Consequently, it can significantly outperform data-driven approaches. Work by [21,138] discusses prognostics methodologies implemented in valves, [20] discusses the implementation of prognostics methodologies to lithium-ion batteries.

However, developing complete and accurate state space models of the degradation process in a complex system may be practically infeasible. Statistical models of historical operational profiles, represented as standard probability density functions (pdf), can compliment physics based models for calculating future damage accumulation. The results from such models can be used for real-time failure prognostic predictions with confidence bounds [36]. Physics-based modeling methodologies provide mechanisms for calculating the rate of degradation and resultant damage in critical components of the system as a function of the operating conditions and the present state [45, 52].

Data Driven Approach

Data-driven techniques primarily rely on process health data to model a relationship between the data features and different fault and degradation phenomenon. Typically such techniques drive probability distributions of the degradation process from available data [47]. The data is gathered using specific sensors that are tailored to capture faulty behavior in the system requirements. In many applications, measured input/output data are often the only source for studying and understanding system degradation behavior [53, 54]. Data-driven approaches rely on the assumption that the statistical characteristics of data change from nominal to degrading and this can be reliably detected by statistical hypothesis testing [47, 55].

Many data-driven approaches use statistical learning techniques derived from patten recognition and machine learning methodologies. These include probabilistic neural networks [56], dynamic wavelet neural networks [57], graphical Bayesian network models [58, 59], hidden Markov models [60], self-organizing feature maps, signal analysis filters, autoregressive models, and fuzzy rule-based systems [47, 53]. Typically data driven approaches have higher accuracy and computational cost as compared to the reliability based techniques, but they may be more cost effective and less accurate as compared to model driven approaches [61]. When additional sensors need to be added to gather more data, data driven techniques can be become expensive, especially for legacy systems [28, 36].

In the electronics industry, Health Monitoring (HM) and Electronics Prognostics (EP) methods have been implemented to allow the identification of faults and failures in systems during normal operating conditions [62]. HM and EP methods consist of the continuous monitoring of a systems operating environment and performance to determine deviations from expected normal operating conditions. The data collected through this monitoring makes it possible to obtain estimates of the product reliability, execute proactive maintenance activities, increase product availability and prognostics. Some of the methods of electronic prognostics were developed by Sun Microsystems for their enterprise servers [63]. These methods included Principles of Continuous System Telemetry Harness, Sequential

Probability Ratio Test, and Multivariate State Estimation Technique as pertaining to EP applications [64, 65].

The practice of monitoring the health of a system entails understanding or learning about health-versus-unhealthy system behavior. Predicting future behavior is tied to the ability to learn from the past. In this regard, the field of machine learning is appropriate for data driven approaches to PHM. Learning algorithms can be combined to increase the efficiency and effectiveness of the estimated distributions. In combination with numerical optimization, statistics and probability are used to make decisions about current and future system health based on the data. Machine learning methods extract relevant data to explain the trends and characteristics of system health in such a way as to make statistical and probabilistic estimates more accurate. The major focus of machine learning research is to extract information from data automatically by computational and statistical methods, then apply supervised and unsupervised learning methodologies [18].

Combined statistical and data driven methods that rely on historical data of previous failures in the given system is another approach that is often applied for prognostic analysis [36]. Starting with the assumption that the statistical distribution is known, the data may be used to derive the parameters of the known pdf function. If no assumptions are made about the degradation distribution, the data may be employed to derive an empirical distribution. These combined methods are often more effective because they require less detailed information than the differential equation models used in model-based techniques [36]. The pdfs of the captured data typically are sufficient to predict required parameters of interest for prognosis. Statistical methods also provide confidence limits, which are important for confirming the accuracy and precision of the predictions.

Electronics Prognostics Methods

A method for Electronic Prognostics (EP) in computer systems was introduced in 2001 by Gross [71] and his team of researchers at Sun Microsystems . This approach circumvents many of the deficiencies of traditional HM and EP methods that were previously discussed, providing the tools needed to capture relevant system data and identifying signal patterns,

correlations between signals, and root causes of failures, effectively reducing no-trouble found instances and increasing Reliability, Availability and Serviceability (RAS). The EP approach consists of a Continuous System Telemetry Harness(CSTH) coupled with real-time pattern recognition algorithms [71, 72].

The CSTH enables the capture, conditioning, synchronizing, and storage of computer system telemetry signals, which allows the subsequent statistical analysis of data [73]. The CSTH categorizes the information provided by the server into three different kinds: soft variables, canary variables, and physical variables. Soft variables (internal variables) are values generated by the operating system which provide information on the performance of the hardware [73]. Canary variables are values generated by software programs (other than the operating system) which provide information on the quality of the service, such as number of transactions per minute, service availability, user wait times, etc. Physical variables are direct measurements made in the system by means of sensors, such as temperature, voltage, current, vibration, fan speed, and relative humidity. All of these variables originate from multiple locations, formats, time stamps, sampling frequencies, and signal resolutions [72, 73].

The analysis of signals obtained by the CSTH is done by means of pattern recognition algorithms. The first of these is the Sequential Probability Ratio Test, and the second is the Multivariate State Estimation Technique [72, 73]. Statistical analysis methods were implemented with the CSTH for the monitoring of signals in computer systems. The work by Gross [72, 73] discusses the the application of these algorithms to enable Electronic Prognostics in enterprise servers.

Physics-Based Reliability Modeling

Physics-based modeling (PBM) approach to prognosis, attempts to model failure mechanisms based on the first principles of operation,using principles of physics, as opposed to a traditional approach of using models based on empirical data. Physics-based modeling techniques can be very effective for estimating lifetimes due to specific failure mechanisms [74]. The fact that a degradation/failure rate can be predicted for a given part under a specific

set of conditions does not imply that a failure rate is an inherent quality of a part [75, 76]. The failure rate depends of the present health of the device/system and the conditions under which it will be operated and suppose to operate for which the prognostics predictions are done [18]. Therefore to apply PBM techniques accurately, one must take into account environmental variables and operating conditions.

In critical systems such as aircraft, manufacturing processes or any other complex system, defect initiation and propagation must be estimated for effective fault prognosis. Dynamic models of fault propagation and failure can be derived by using principles of physics. Recent studies in materials research have focused on microstructural characterization materials and modeling frameworks that describe robustly and reliably the anomaly initiation and propagation as a function of time [77]. Such models addressing the constitutive material properties down to the single particle level generally are not suitable for realtime treatment owing to their immense computational complexity. Combined models, called lumped models, usually are derived from the microstructural characterizations so that they may be used to estimate in almost real-time the failures in a system or subsystem. For example, crack initiation and propagation models must account for variations in temperature, cycle frequency, stress ratio, sustained load hold time, and interactions of damage mechanisms such as fatigue, environment, and creep [66, 78].

On the other hand PBM methodology is incorporated into the design process by establishing a scientific basis for evaluation new materials, structures, and electronics technologies. Information to plan tests, maintenance screening and to determine electrical and thermal-mechanical stress margins are identified by the approach [74]. The PBM approach encourages innovative, cost-effective design through the use of realistic reliability assessment. It is equally important to understand how equipment works and fails in the environment for which it is expected to operate. Factors, such as temperature cycling, vibration, humidity, and radiation cause stress, which leads to failure of the component in the system [74]. PBM tools model the stress-failure relationship for the dominant environmentally-induced failure mechanisms. Once these relationships are developed, the expected remaining useful life of the system/subsystem can be computed. The prime focus with development

in these types of models is to quantify the unknown and uncertain events and operating conditions [79, 80].

Physics-based Reliability Modeling under Accelerated Testing

Rapid advances in technology, coupled with the relentless drive to remain competitive in world markets, are motivating the electronics industry to focus on effective reliability verification and enhancement techniques [76, 79]. The process begins with a thorough understanding of the failure mechanisms that can occur in electronic systems and sub-systems. Effective measures can then be taken not only to prevent their manifestation under life-cycle stresses, but also precipitate them in a controlled manner during accelerated stress testing (AST) [80]. Accelerated stress testing has been recognized to be a valuable activity to assess the reliability and quality of electronics in a timely manner. Accelerated stress tests are often carried out under increased or exaggerated environmental conditions to enhance the damage accumulation rate due to any physical or environmental phenomena in the product [81].

In traditional accelerated testing techniques , root-cause identification and analysis is not adequately emphasized. In the physics-based modeling approach understanding of the underlying failure mechanisms is essential for designing and conducting successful accelerated tests [74, 81]. The amount of test-time compression achieved in an accelerated test must be determined quantitatively. This can be achieved only through understanding the underlying physics of the relevant failure mechanisms, and can lead to break-through in the following:

- Reducing the product development cycle time
- Increasing confidence in products life-time reliability
- Controlling manufacturing variabilities

The electronics industry has not yet achieved the required maturity in adopting a physics-based modeling methodologies using AST standards [76, 79]. Research is focused more on conducting accelerated testing under combinations of multiple stresses, to enhance

test time compression [80]. This has only served to increase the confusion in the literature, in standards, and in industry, regarding the most cost-effective and scientific way to conduct accelerated stress testing for electronic assemblies. Researchers agree that PBM principles hold the greatest promise of providing a systematic approach to plan, conduct, implement and evaluate accelerated life tests, especially under combined environments where synergistic effects of different environmental loads could be of high significance [74, 76, 80].

The first step is to determine the sources of reliability risks under life-cycle loads by identifying the potential weak-links and dominant failure mechanisms associated with the application. While general-purpose software, such as Ansys, Abaqus, FloTherm and IcePack, are used to evaluate stress within electronic assemblies, time constraints tend to prevent analysis of individual parts and components [76,79]. Further, stress simulations alone do not reveal product reliability. Significant time savings can be realized when engineers develop a flow-through process of life-cycle characterization, product modeling, load transformation, and failure assessment to qualify electronic systems. This process is termed virtual qualification. The three main activities for deriving physics-based models include:

- Understanding the hardware configuration,
- Determining the product life-cycle loads for each potential failure site,
- Performing an initial assessment of the potential failure modes of the device. The output of this step is ranking of the potential weak-links expected under life-cycle load.

The key activity in implementing PBM methodology involves stress analysis tests to determine how the applied life-cycle loads (electrical, thermal, mechanical and chemical) are transmitted and distributed throughout the electronic assembly [80, 82]. In the next step, the stress fields are used to identify where the failure might occur (failure site), the failure mode, and what the underlying root cause might be (failure mechanism). After the failure mechanisms have been identified, the relevant failure mechanism models are employed to predict the remaining useful life of the system. If no theoretical models are available, semi-empirical models are developed using statistically designed experiments [74].

The designed experiments are used to identify critical design factors and stresses governing failure, and to identify mathematical relationships relating the dominant factors to reliability measures. Variability in the factors is specified using statistical distribution functions. Variations in material properties and geometry due to manufacturing variability and defects are addressed at this juncture. The PBM approach can be used to qualify nominal design and manufacturing processes and to conduct design trade-offs to ensure that the product has adequate stress margins and meets or exceeds reliability targets. During the products development cycle, PBM is often employed to establish robust controls as a means of continuously monitoring and improving quality from early prototype fabrication through final manufacture.

Conceptual Models of Failure

Hansen in his work on PBM [74, 80, 83] defines conceptual models for degradation and failures. Failures are due to a complex set of interactions between stressors that act on and within the system; and the materials that the system is comprised of. Three simple conceptual models of failure are defined. The first two are due to irreversible material damage while the third is caused by reversible changes in material properties.

1. Stress-Strength: A material fails when the stress exceeds the strength. Strength is treated as a stochastic (random) variable and failure depends on the occurrence of critical events rather than mere repetition of cycles, i.e., electrical overstress of a transistor with a voltage applied across the emitter-collector; and thermal overstress in a polymer beyond glass transition temperature.

2. Damage-endurance: Stress events cause damage that accumulates irreversibly and failure results when and only when damage exceeds the endurance limit of the material. Accumulated damage does not appear when the stresses are removed, although sometimes annealing and healing of materials can occur i.e. electromigration.

3. Performance-tolerance: A system performance characteristic is satisfactory if it remains within the specified tolerances i.e. excessive propagation delay in integrated

circuits at high temperature, excessive thermal transients due to inadequate diffusivity.

Failure Mechanisms

Failure mechanisms are the fundamental thermodynamic processes by which stresses cause damage to elements comprising the system, ultimately leading to failure that can be explained by by one or more of the conceptual models [80, 83]. PBM design guidelines, which emphasize the understanding of potential failure mechanisms, are more effective if quantitative models can be developed to describe the relevant failure mechanisms. It is necessary therefore to identify the failure mechanisms that could be activated by the applied stresses during the life-cycle of the system [74, 82]. Failure mechanisms are mainly divided into two major groups overstress mechanisms and wearout mechanisms. Overstress failure are catastrophic sudden failures due to a single occurrence of a stress event that exceeds the intrinsic strength of a material. Examples of overstress failures include buckling of materials, electrical failures resulting in electrical discharge.

Accumulation of incremental damage leads to failure when the accumulated damage exceeds the material endurance limit, and is termed wearout failure. By definition, only wearout failure can be accelerated during an AST. Verification of overstress failures, on the other hand, is performed through proof-tests. Therefore, failure acceleration models used in accelerated stress tests must focus on the relevant wearout failure mechanisms [80, 83].

Summary

In this chapter we did a literature review of the current state of art techniques that have been developed and implemented for prognostics in electronics components and systems. We studied and discussed the model based approach, data driven methods that rely on historical data of previous failures in the given system is another approach that is often applied for prognostic analysis while the third approach discussed was the combined model and data driven methods, where each of the methods discussed have their own advantages and disadvantages. We further reviewed some of the accelerated aging methods used for

implementing prognostics methodologies. The accelerated aging of components and systems lead to earlier failure and by systematically capturing the failure mechanisms and degradation phenomenon, they can be used effectively for implementing prognostics methodologies using either of the three approaches discussed. Most of the earlier work related to electronics has been done by implementing reliability based prognostics methodologies at the sub-system and system level [84, 85].

Our research work focuses on developing and implementing effective diagnostic and prognostic technologies with the ability to detect degradation/failure in electronics at the component level. Early detection and analysis may lead to better prediction and end of life estimates by tracking and modeling the degradation process. The idea is to use these estimates to make accurate and precise prediction of the remaining useful life (RUL) of the components. Early detection also helps in avoiding catastrophic failures. We adopt a physics-based degradation modeling approach at the component level to predict the dynamic behavior of the component under nominal and degraded conditions. Faults and degradations appear as parameter value changes in the model, and this provides the mechanisms for tracking the component behavior under different operating conditions.

CHAPTER III

CASE STUDY: AVIONICS SYSTEM

Avionics systems play a critical role in many aspects of aircraft flight. As the system complexity and the flight criticality of functions performed by these systems increases, the ramifications of in-flight malfunctions will increase. This drives the need for IVHM technologies for flight-critical avionics. Flight and ground crews require accurate health state estimates of these critical avionics components, including accurate detection of faults and prediction of time to the functional failure of the avionics system. The main focus/objectives of this research work can be summarized as:

1. Increase the aircraft safety and reduce the aircraft maintenance by improving the accuracy of the fault determination in critical avionics systems.

2. Develop technologies which will detect, model, and predict degradations, malfunctions and failures in avionics.

3. Developed technologies are intended to be adaptable to running onboard an aircraft.

We propose a model based approach to study fault diagnosis for avionics systems. This chapter discusses the hybrid model developed for the power supply system and the Matlab/Simulink® models that have been developed for the GPS and integrated navigation system (INAV) subsystems [87–90]. Additional modeling constructs to capture the combined discrete-continuous interactions between the systems are also modeled.

The avionics system modeled contains both hardware (power supply, GPS receiver, IMU) and software (GPS software, INAV - integrated navigation solution) components. A topological energy based modeling scheme based on the bond graph (BG) modeling language for building parametric models of multi-domain physical systems forms the core of the Fault Adaptive Control technology (FACT) component-based visual modeling system that has been used for developing the power supply system model. We have developed automated methods for generating Simulink block diagram models from bond graph representations

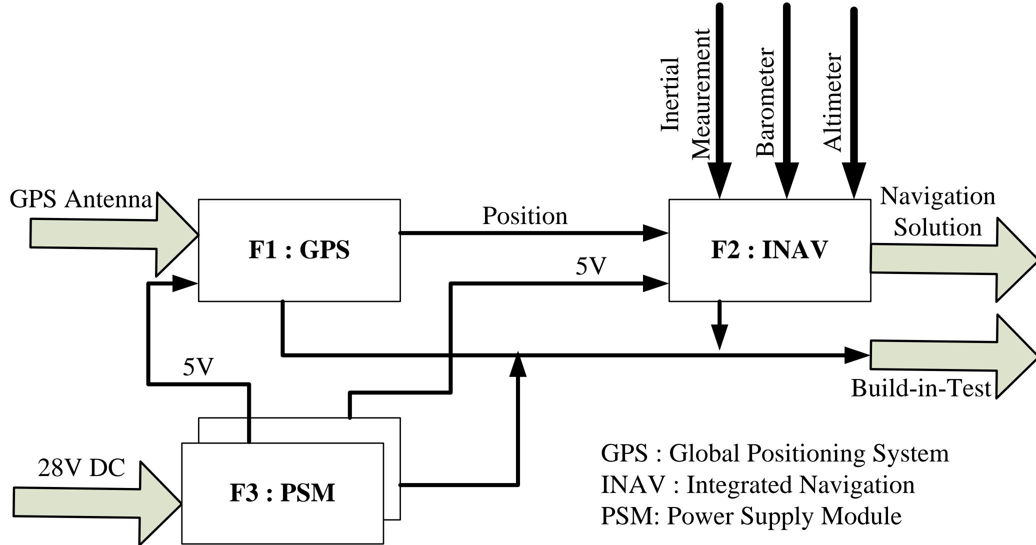

Figure 2: Avionics Simulated System

of physical models [41, 89]. The GPS and INAV modules are modeled directly as block diagram models in Simulink. The three subsystem models form the testbed for running our monitoring and diagnosis studies of the combined hardware/software avionics system. Figure 2 shows the block diagram of the simulated system along with the sample fault insertion subsystems. This section contains fault mode descriptions for potential system faults identified for the Honeywell - NASA NRA NNA08BA45C project. The project was done in collaboration with Honeywell Aerospace-Advance Technology and NASA Ames. The details of the work are discussed in [41,91]. We summarize the leading fault conditions from the literature and from select recent accident reports which have been reviewed in [92, 93].

GPS Model

An abstract GPS model is developed to compute the position of a GPS receiver's Earth-Centered, Earth-Fixed (ECEF) reference frame [94, 95] . The receiver has three main subsystems, namely the high frequency hardware, low frequency hardware, and the software systems. The high frequency and medium frequency hardware together make up the systems that receive the GPS satellite signals decode the information and compute the pseudo ranges. Our GPS model essentially includes the software part of the GPS receiver which

takes the pseudo ranges and the satellite decoded information as input and computes the receiver position. The module is implemented in SIMULINK and is based on the GPS Easy Suite [94,95]. The main inputs of the model are the pseudo-range and the ephemerids data. The output is the receiver position. The input data of the model is obtained from Receiver Independent Exchange Format (RINEX) O and N files.

The purpose of the RINEX file format is to enable easy exchange of the GPS data among different GPS receivers. The format consists of six ASCII file types and we use two of them to extract data as the input to our GPS abstract model; 1) O file - Observation Data File, and 2) N file - Navigation Message File [91]. The observation data file contains the GPS measurements data and the navigation message file contains the ephemeris - the orbit information. The RINEX files are parsed by a MATLAB script to extract the model inputs, thus using a different input format that corresponds to modifying the initialization script to fill the model inputs. This way we can avoid making modifications to the model itself.

The RINEX O and N files to compute the receiver position using an iterative least squares procedure. The detailed description on computing the receiver position is widely known and available in the literature [96]. It should be noted that in the current form the GPS model essentially simulates the GPS receiver low frequency hardware and software functions. The high frequency portions of the GPS receiver such as the antenna are not directly simulated. However, the faults in the high frequency components are modeled by simulating the effect on the respective pseudo-ranges. Table 1 shows the different faults which were selected for this study.

According to the satellite operators, the satellite vehicle data transmission failure is a generic spacecraft problem. Command uplinks to Block II satellites occasionally cause a conflict in the spacecraft computer. A conflict causes the spacecraft to emit a non-standard PRN code during one navigation data sub-frame (six seconds). The receiver sees this event as a loss of signal from that satellite and this causes temporal loss of receiver lock leading to reduced number of satellites available for computing the receiver position. This can result in degradation and loss of GPS solution, if less than 4 satellites are initially visible. If only 4 satellites were visible at the time of the error. This error will cause a temporary drift in

Table 1: GPS Receiver Faults

Fault	Type	Reason Selected	Description
Satellite vehicle data transmission	Discrete, soft, intermittent.	Cause of loss of lock in all GPS receivers, caused an approach abort during FMS testing [97].	Generic spacecraft problem. Command uplinks to block II satellites occasionally cause a conflict in the spacecraft computer. A conflict causes the spacecraft to emit a non-standard PRN code during one navigation data sub-frame (6 secs).The receiver sees this event as a loss of signal from that satellite.
Satellite vehicle clock drift	Continuous, soft, persistent.	PRN 23 on 1 January 2004 experienced a clock drift error that grew gradually to a few kilometers.	The errors and drifts of the satellites' clock are calculated and included in the messages that are transmitted by the satellites. In computing distance to the satellites, GPS receivers subtract the satellite clock errors from the reported transmit time to come up with the true signal time. This type of clock misbehavior introduces a slow ramp type error in transmitted signal.
GPS receiver RF filter failures	Discrete, hard, intermittent.	This failure makes it difficult for typical antennae to lock on to signals.	The RF front-end of a GPS receiver first filters the unwanted signals and then amplifies the filtered RF signal. If the RF filter failure occurs, side lobes in the antenna radiation patter may be corrupted. There can be sudden jumps or slow fluctuation in signal frequencies [23]
GPS receiver delay shift	Continuous, soft, intermittent.	Signal delays in the receiver are accounted for in the receiver hardware and/or software.	Receiver noise can introduce 2-3 ns of zero bias noise in the timing measurements of a GPS receiver. Delays within a receiver can be calibrated by the manufacturer, but if receiver delays change with temperature or change differently between channels of a multi-channel receiver, timing bias errors can result. Antenna cable delays must be recomputed or calibrated for change in length, material. They also vary with temperature and signal strength [98].

the INAV (navigation) solution as GPS updates are no longer usable. The modeled GPS receiver checks the input data and computes the rank of the pseudo range observations. If the computed rank is less than 4 it sets the flag to indicate the receiver position calculation to be invalid. Figure 3 shows the simulation setup for simulating the satellite loss of lock [96].

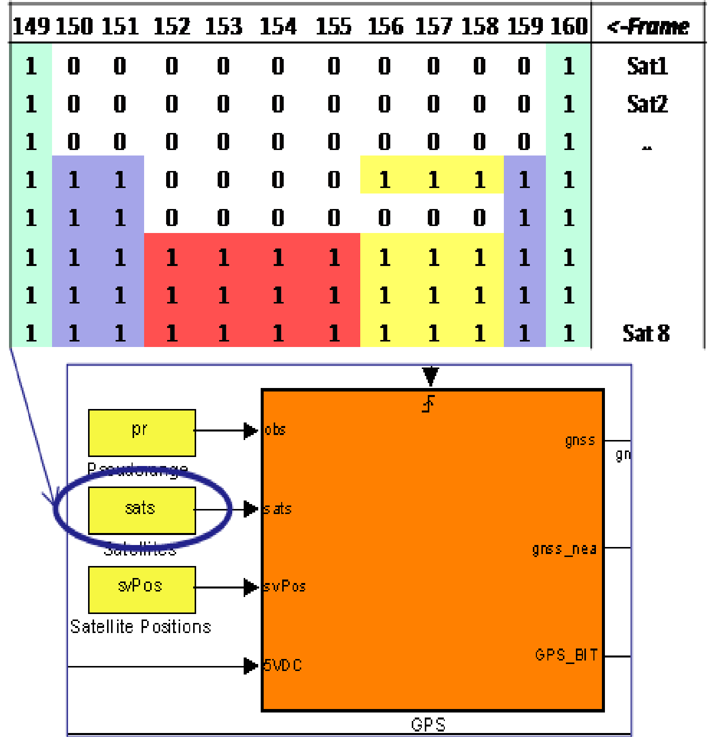

Figure 3: Loss of satellite lock simulation

The satellite clock drift is simulated by changing the pseudorange (PR) to GPS block (Figure 4), such that

$$PR_{measured} = PR_{actual} + clock_drift * speed_of_light \quad (1)$$

where:

- $PR_{measured}$ is the PR computed by the GPS receiver,
- PR_{actual} is true PR in absence of satellite clock drift $clock_drift$ is the cumulative clock drift

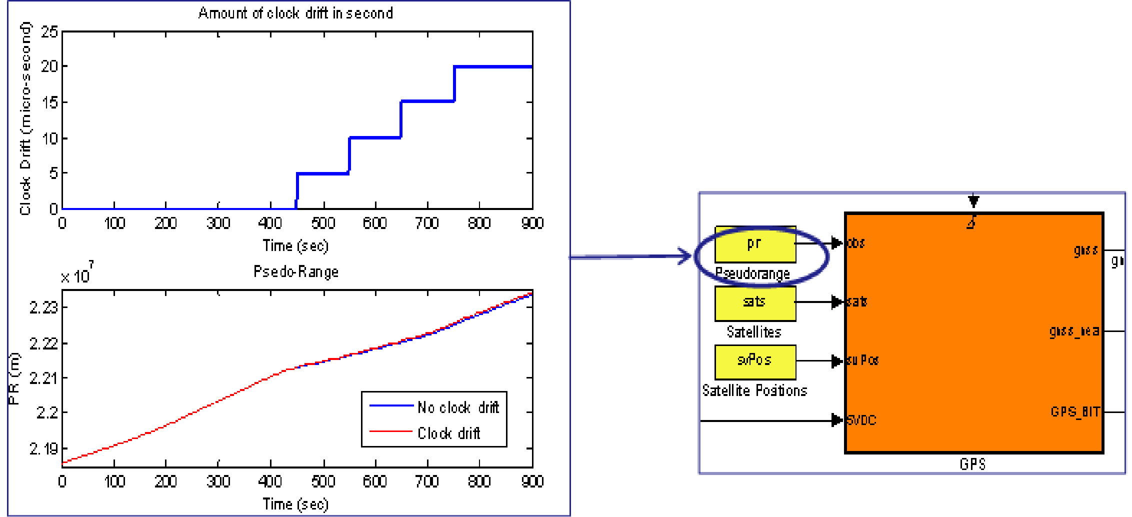

Figure 4: Satellite Drift

INAV Model

In the avionics system that we have modeled, the Inertial Navigation System (INS) is the primary navigation system that calculates the navigation states at high rate and uses the measurements from Inertial Measurement Unit (IMU) [99]. The IMU, which serves as the INS input, is a set of three accelerometers and three gyroscopes that together measure acceleration in 6-DOF. The basic function of an INS is to integrate accelerations to determinate velocity and position of the vehicle in a desired coordinate frame. Considering the possibility of relative angular motion between frames, gyroscopes are required to maintain the sensor-to-navigation frame transformation.

In the INAV system, a loosely coupled integration was used for the INS/GPS integration, expanded with additional sensors like the barometer, magnetometer and odometer. This approach combines the strengths of both INS and GPS based NAV system by bounding the drift of the INS using GPS position. The combined solution is robust to the temporary loss of GPS signal. The INS operates at a higher frequency than the GPS (typically 100 Hz and 1 Hz), therefore, at each GPS update step the navigation filter estimates bias for all IMU sensors by giving more weight to the GPS observations.

In an INS implemented in the complementary filter structure, the output of the INS provides the navigation solution and an Extended Kalman Filter (EKF) estimates the INS

errors [99]. The INS error vector is fed back to correct the INS internal states [100]. This is illustrated in Figure 5. When the GPS measurements are within expected solution bound the INAV treats the GPS measurements as the true values (with added measurement noise), i.e. it believes GPS over other sensor measurements. INAV assigns (stochastically) the navigation innovations to bias estimates of other aiding sensors (such as the altimeter, accelerometers, and the gyro).

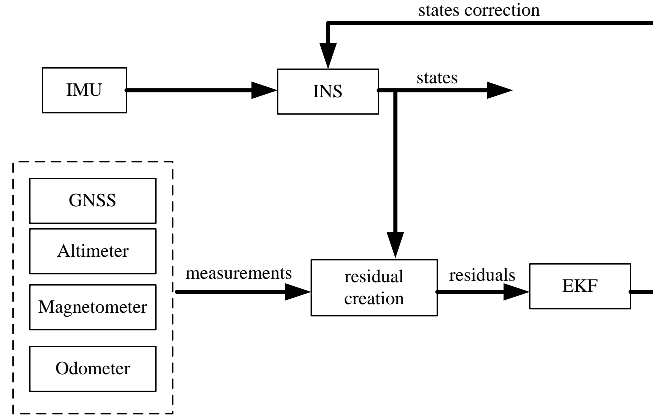

Figure 5: Feedback implementation of the complementary extended Kalman filter

Table 2 shows the list of faults selected for this work. Accelerometer failed high is a special case of the stuck accelerator. The failure of an accelerometer in an unexpected high state corrupts the input to the INAV and eventually leads to a failure in the flight control system. If the problem is not detected and corrected in a timely fashion it will lead to divergence of the navigation solution. In a system fed by single set of accelerometers the divergence in the solution is very rapid. To simulate this failure we inject the failure accelerometer as a fault with a fixed bias in the failed axis of measurement. One source of error in the measurement of the angular velocity from a gyroscope is an offset in the measurement called bias. The bias is not necessarily constant but will typically cause the calculation of the attitude to drift away from the actual heading. Because an error in the heading is extrapolated over the linear distance traveled, a small error in the calculated attitude leads to a large position error. A drift of 0.01 degree/hr can lead to a position error of 1 nmi/hr [99].

Table 2: INAV Faults

Fault	Type	Reason Selected
Accelerometer Fault /IMU measurement fault	Discrete	Caused emergency situation on MAS 777 in 2005 when the flight control system simultaneously thought the aircraft was approaching stall and overspeed due to the failure.
Gyroscope bias/drift	Continuous	Most common gyroscope error and leading cause of position error.

Inclusion of a wrong measurement in the EKF can cause a severe degradation of the navigation solution; the residuals test is performed prior to inclusion of measurement data into the filter. Data from the aiding sensors are compared against the INS predicted values using the a-priori sensor statistics. From the residuals and their statistical properties a scalar test statistic chi-square distributed with n degrees of freedom is created, where n is the number of measurements used for creating the test statistic. This statistic is later compared with a predefined threshold to evaluate if a failure has occurred. Using the chi-square distribution allows INAV to test together a group of measurements that are correlated to each other improving the chances to successfully detect a failure. INAV also estimates the bias for accelerometer and gyro measurements on-line. The Gauss-Markov (GM) process is used to model a time varying bias.

Accelerometer bias estimation model is simplified by estimating the constant bias at initialization. Then varying bias and the white noise are the remaining error sources of the sensor. The accelerometer bias fault detection uses the bias estimate as computed by the EKF along with the multiple of 1-σ confidence level generated using the a-priori sensor noise variance. The fault detection routine alarms when the bias estimate exceeds multiple of 1-σ bias estimate bound. Isolation is performed by attributing the persistent alarm on the accelerometer bias estimates to the faulty accelerometer.

The gyro bias drift fault indicator is based on the gyro bias estimates calculated by the EKF navigation filter. The fault detection routine the sets up alarms when the bias

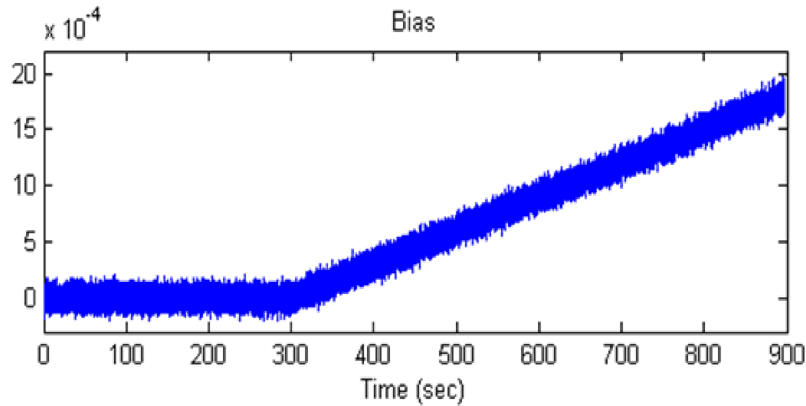

Figure 6: Gyro bias, injected faulty signal

estimate exceeds a chosen multiple of the 1-σ bias estimate bound. Isolation is performed by confirming persistent alarm on the gyro bias estimates.

Power Supply Model

Switched-mode power supplies are widely used in DC-DC converters because of their high efficiency and compact size. The buck-boost DC-DC converter converts from one voltage level to another, by storing the input energy temporarily in inductors and then releasing that energy to the output at a different voltage value through the fast switching sequence. The efficiency of conversion ranges from 75% to 98%. This high efficiency is typically achieved by using power MOSFET's (metal oxide semiconductor field-effect transistor). MOSFET can provide high frequency switching more efficiently than power bipolar transistors, which, in addition to greater switching losses require more complex drive circuits. A buck boost approach is used for conversion to the required DC voltage output. Our particular application has an input of 28V DC from a battery source, and the required output voltage is 5V. The schematic of the circuit used in this work is shown in Figure 7.

Background

Model-based identification methodologies require system models that accurately represent system dynamics and are also capable of linking system measurements to damage in the

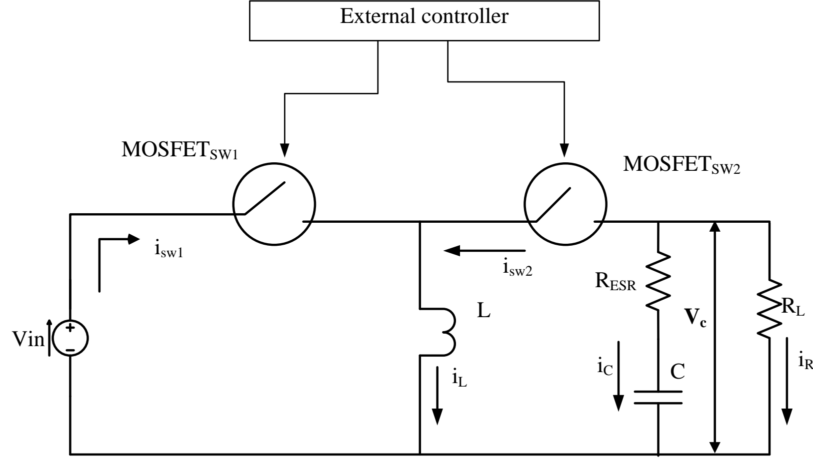

Figure 7: Buck Boost Converter Circuit

components of the model. The bond graph (BG) modeling framework provides both these features [101]. BGs provide a systematic framework for lumped parameter modeling across multiple domains that include the electrical, mechanical, hydraulic, and thermal domains [84, 89]. They are an explicit topological modeling language for capturing the dynamic energy transfer among components of a systems based on the principles of continuity of power and conservation of energy.

This energy distribution reflects the history of the system and, therefore, defines its state at a point in time. Behavior of the system at future time points is determined by the current state description and subsequent input to the system [89]. Changes in the state of the physical system are related to energy exchange among its components, which can be expressed in terms of power. The basic working principle of bond graphs is that power transmitted between connected components can be expressed as a product of 'effort' and 'flow', irrespective of the application domain [84].

Bond graph elements are classified into one of five basic elements, (1) energy storage elements, Capacitance (C), the Inertia (I), (2) the dissipative element, Resistor (R), (3) two idealized energy transformation elements, the transformer (TF) and the Gyrator (GY), (4) two source elements, Se, source of effort and Sf , source of flow, and (5) two junction elements, 0 (for parallel connections) and 1 (for series connections). All these elements

Table 3: Basic Bond graph elements

Symbol	Type of element	Name of element	Electric Domain
C	storage	capacitance	capacitor
L	storage	inductance	inductor
R	dissipator	resistance	resistor
TF	transducer	transformer	transformer
GY	transducer	gyrator	transformer
Se	source	effort source	voltage source
Sf	source	flow source	current source
1	junction	1-junction	series connection
0	junction	0-junction	parallel connection

exchange energy with other elements through ports or bonds. Bonds are energy transfer pathways that connect elements and junctions and are represented as half arrows. Effort and flow signals are the information transferred through these pathways. The two ideal source elements model energy flow in and out of a system, and are active elements since they introduce energy into the system. All the other elements are passive.

A passivity based approach discussed in [102] is used for deriving the BG model of the buck boost converter and is shown in Figure 8. The representation of the switching devices as MTFs is derived directly from the algebraic relations of the effort and flow variables. In an average model of the buck-boost converter, the switching bond is replaced by a 'duty-ratio-modulated bond'. This 'average' bond can be effectively interpreted as an ideal lossless transformer with turns ratio specified by the complementary duty ratio function associated with the controlling scheme. The switching frequency of the MTFs depends upon the value α. The value of α is calculated from the values of R2, C, L and the input/output voltage requirements. Reference [94] provides the detailed equations used for deriving the value of α. The regulation of the converter output at a desired output voltage v_{Cd} depends on the steady state value of the average inductor current i_L. This is determined by replacing dynamic element L (inductor) of the average bond graph by a SS-element (source-sensor element), represented as flow source Sf in the BG. The desired steady state value for the current can then be obtained as $i_L = (1 + v_{Cd}/\mathrm{vs})v_{Cd}$ /R2. An input injection from the external passivity controller to the modulated effort source is added to the bond graph model of DC-DC converter in the form of a Se element [94].

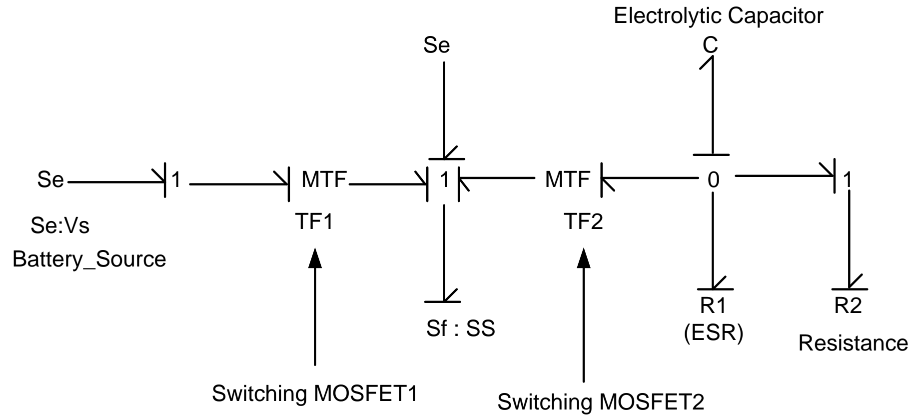

Figure 8: Buck Boost Converter Bond Graph Model

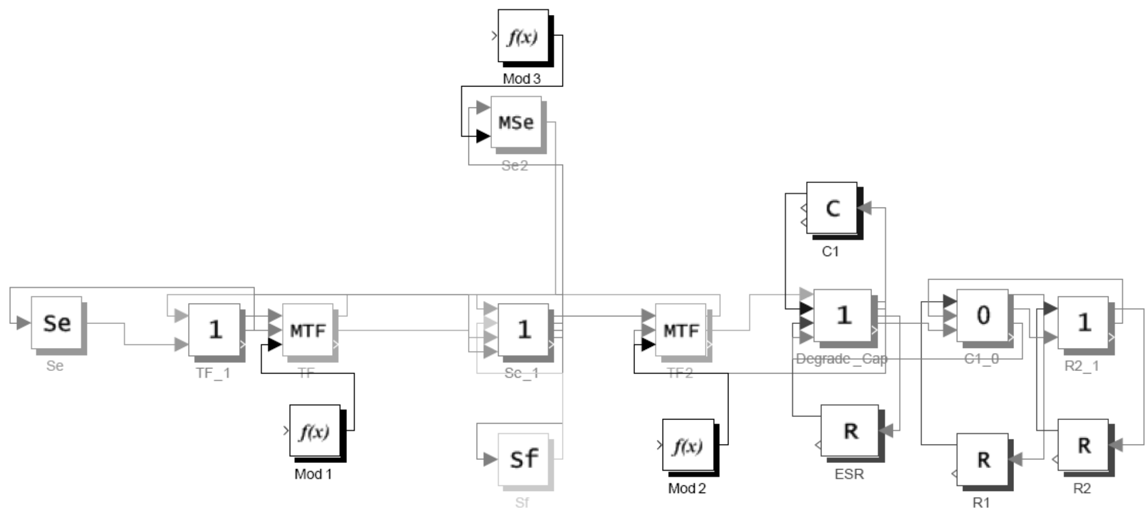

Figure 9: Buck Boost Converter Simulink Model

For conversion of the topological bond graph model to its equivalent SIMULINK model we use the approach presented in [103]. An interpreter is used for converting the BG model into an intermittent block diagram model from which the simulation model is derived [104]. A simulink model generated from the bond graph using the approach is shown in Figure 9

DC-DC Converter Fault/Degradation List

Fault 1: Electrolytic capacitor degradation in DC/DC converter

Type: Continuous, Degradation.

Reason Selected: Of all components in DC-DC converters, capacitors have the highest failure rates and the leading cause for breakdowns in these systems. Degradation in the capacitors can be monitored over the period of time, and with this available data trending and fault prediction for prognosis can be done.

Description: The performance of the electrolytic capacitor is significantly affected by its operating conditions such as voltage, current, frequency, and working temperature. If the electrolytic capacitor is used as a part of the power stage components of switching-mode power converters, they are most affected by degradation and aging effects. The electrolytic capacitor plays a very important role for the switching-mode converters quality and reliability hence it is very important to diagnose the degradation and failures predict the expected lifetime of the electrolytic capacitor.

The main factors that influence the reliability in electrolytic capacitors are oxide layers, impregnation layer, foil porosity, and paper. The wear out of aluminum electrolytic capacitors is due to vaporization of electrolyte that leads to a drift of the main electrical parameters of the capacitor. It can be indirectly measured by the equivalent series resistance (ESR), which is the sum of the resistance due to aluminum oxide, electrolyte, spacer, and electrodes (foil, tabbing, leads, and ohmic contacts). The increase of ESR is interesting, since at the switching frequency of the converters, the impedance of the electrolytic capacitors is approximately equal to ESR. In addition, this latter evolution is important since it determines the self-heating and, therefore, indirectly, the capacitor lifetime.

Fault 2: Power transistor failure in DC/DC converter

Type: Typically discrete, Degradation, Continuous.

Reason Selected: Power transistor faults are the second most leading cause of DC/DC converter failures. Previously fault detection and isolation work has been done on power transistor failures, but less on failures related to transistor in DC-DC converters.

Description: In the past years, power MOSFET's have become established in a wide variety of control and conversion applications. Most of applications require that the MOSFET be switched a high frequency. The thermal and electrical changes the device undergoes during switching can be particularly high during turn-off with an inductive load at the drain terminal.

It is commonly assumed that any mechanism that permits the “parasitic” bipolar transistor to become active will usually lead to failure of the power MOSFET, particularly if the drain voltage is greater than the collector-emitter sustaining voltage of the bipolar transistor. It has also been that avalanche injection in the drain region of the MOSFET may lead to failure without the parasitic bipolar transistor becoming active.

One of the known reasons of power MOSFET failing is when they are subjected to very rapid turn off, i.e., very high dV_{DS}/dt (rapid change in the drain to source voltage.). In the early days of power MOSFET development, the turn-on of the parasitic bipolar transistors (BJT) was the major cause of MOSFET failures. The new generation of MOSFETs is almost immune to this problem, but still the parasitic turn-on of BJT still remains the major root cause of power MOSFET failures. The other cause of failure in MOSFETS is the Body Diode Reverse Recovery failure. When a MOSFET , that has some residual charge stored in it body-diode, is turned off, this leads to the forward biasing of the parasitic BJT emitter base junction turning on the BJT leading to the eventual destruction of the MOSFET. Of all the faults the most frequent faults occuring in MOSFETs are due to the package related failures and are very important [5]

Fault Simulation and FDI Results

In this section we will discuss one case study for fault injection in GPS and INAV systems. We will discuss in more details fault injected in the power supply system and discuss the results.

Fault Detection and Isolation: GPS

Figure 10 shows the data input frame and the output of the GPS receiver, rank < 4. built-in test. An eleven channel GPS receiver was simulated. Figure 10 shows the satellites to which the receiver has lock from 149th to 160th sec in the trajectory. At 150th sec the receiver losses lock to 3 satellites and at 152nd sec it loses lock to 2 more satellites thereby resulting in only 3 satellites being locked from 152nd to 155th sec. This fault event is detected by the GPS Bit at 152nd sec as shown in Figure 11.

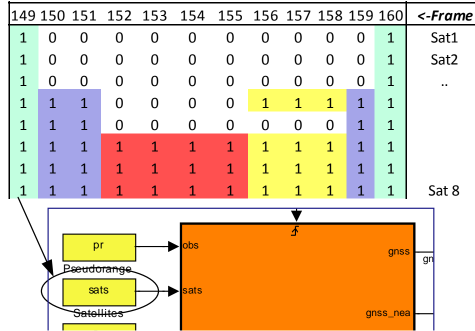

149	150	151	152	153	154	155	156	157	158	159	160	<-Frame
1	0	0	0	0	0	0	0	0	0	0	1	Sat1
1	0	0	0	0	0	0	0	0	0	0	1	Sat2
1	0	0	0	0	0	0	0	0	0	0	1	..
1	1	1	0	0	0	0	1	1	1	1	1	
1	1	1	0	0	0	0	0	0	0	1	1	
1	1	1	1	1	1	1	1	1	1	1	1	
1	1	1	1	1	1	1	1	1	1	1	1	
1	1	1	1	1	1	1	1	1	1	1	1	Sat 8

Figure 10: Loss of lock to satellites Input data frame for GPS receiver showing satellites variable from 149th - 160th secs.

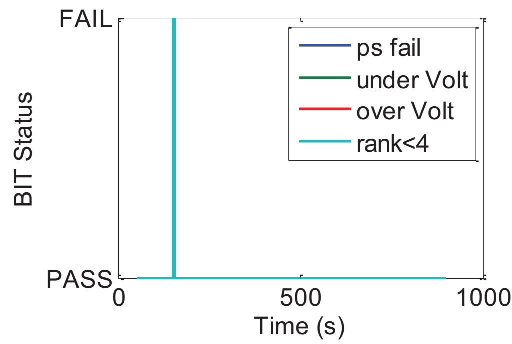

Figure 11: GPS receiver BIT indicating the loss of satellite making the GPS solution unusable from 152nd to 155th secs.

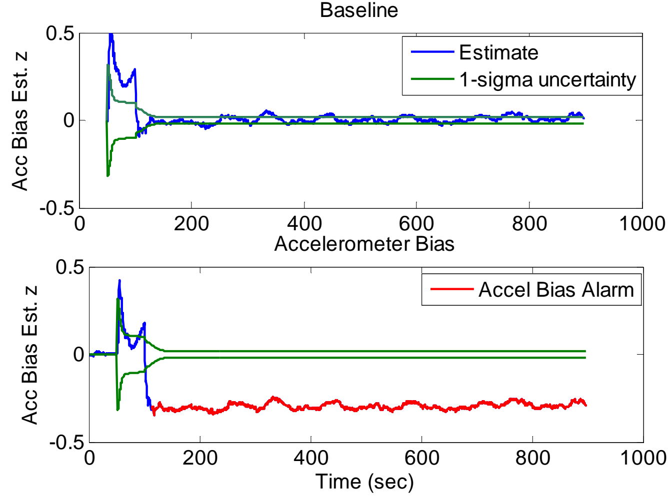

Figure 12: IMU accelerometer bias detection in the z-axis

Fault Detection and Isolation: INAV

The IMU fault results for accelerometer bias change and gyro bias drift cases are shown in Figure 12 and Figure 13, respectively, using the methodology explained earlier in the section. Figure 12 shows the simulation results for z-axis accelerometer fault. The fault adds a bias of 0.3 m/sec^2 at the beginning of the run. The bias estimate shows a clear shift when compared to the baseline no fault case. Figure 13 shows the results for the gyro bias case with injected bias of 1.7×10^{-5} rad/sec/sec. The red portion of the curves indicates the fault has been detected and the faulty accelerometer/gyro alarm is on.

DC-DC Converter System

The power supplies are a critical component of modern avionics systems. Degradations and faults of the DC-DC converter unit propagate to the GPS and navigation subsystems and affect the overall solution. Capacitors and MOSFETs are the two major components, which cause degradations and failures in DC-DC converters [32]. Some of the more prevalent fault effects, such as a ripple voltage surge at the power supply output can cause glitches in the GPS position and velocity output, and this, in turn, if not corrected will propagate and distort the navigation solution. Further, our models for the GPS and INAV units have allowed us to study INAV input faults, such as faults in the GPS receiver and inertial measurement (IMU) units. In this work [41,91] we have included case studies that consider

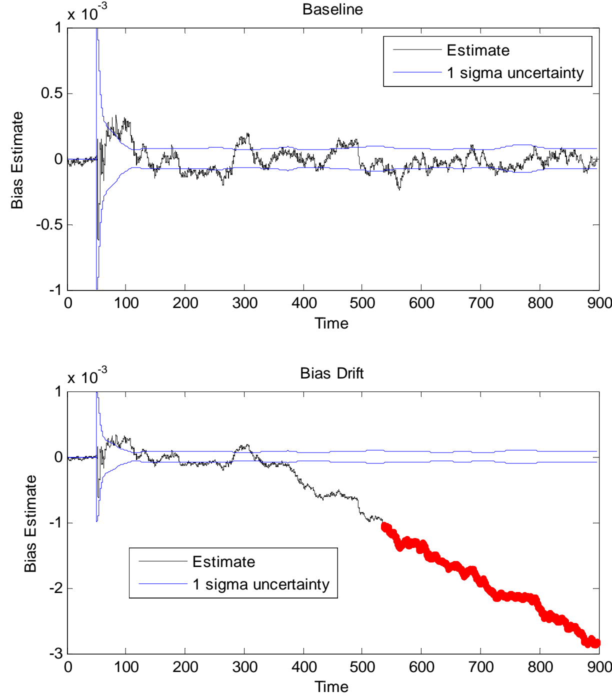

Figure 13: Gyro bias drift detection

(1) faults in the DC-DC converter capacitor, (2) loss of receiver lock in the GPS satellites, and (3) two IMU fault modes, namely increase in accelerometer bias and gyro bias drift.

To conduct our case studies, we have developed an integrated simulation model in Matlab/Simulink® for the navigation system, with the power supplies, the GPS, and the INAV units. Our qualitative fault signature methods for detecting and isolating faults in all three subsystems (modules) of the avionics system. Fault signature generation is based on establishing causal relations between system parameters and measurements, and estimating the effect of a parameter value change (representing a fault) on the measured values [94, 95, 105]. This is followed by a characterization of the continuous and discrete faults in the system as fault signatures. The fault signatures form the basis for design and development of the model-based FDI algorithms for the combined system [95, 101].

All performance degradation and fault diagnosis methods can be broadly classified into two types, quantitative and qualitative [87,88]. The quantitative approach relies on advance information processing techniques such as state and parameter estimation and adaptive filtering. The qualitative approach makes use of causal analysis which links individual component malfunctions expressed in qualitative form with deviations in measured values.

This approach is usually employed when a precise numerical model for the system is not available. For our work we will be implementing the qualitative approach for fault detection and isolation.

Fault Detection

The fundamentals of fault diagnosis presented here are based on the work reported in [87, 88, 90, 104]. We focus on small abrupt changes and degradation in components of the system. A component fault manifests as a change in the value of a bond-graph element parameter. These faults affect the coefficients of the system matrix in the state-space or transfer function representation of the system, that is, they have multiplicative effects on the system dynamics. The bond graph representation preserves a one-to-one correspondence between the component parameters and the physical components of the system. As a contrast, in state-space or transfer function representations the model coefficients are typically functions of more than one physical component parameter. For fault isolation this implies that the bond graph representation creates a direct link between the changes in a parameter value with a fault in a specific system component. We present a brief overview of the methodology in this section.

The work describes an approach for model-based FDI of abrupt faults in component parameters of a continuous dynamic system [87, 88]. Abrupt faults correspond to changes that occur at time scales much faster than the nominal dynamics of the system. We model abrupt faults as discrete and persistent changes in the value of component parameters [87]. An abrupt fault in a component parameter results in transients in the system variables. Typically, the transient behavior vanishes after an interval, and for certain faults no evidence of the fault is observable in the measurements after some time. Our approach, named TRANSCEND, is based on the analysis of the fault transient. A model-based fault isolation scheme for qualitative analysis of the fault transients developed by [88] has been implemented.

Fault Isolation

Qualitative reasoning using bond graphs is based on an analysis of the Temporal Causal Graph (TCG) structure. TCGs capture causal and temporal relations among the system variables that characterize dynamic system behavior. They are an extended form of Signal Flow Graphs [88], with vertices representing the system variables (e.g., pressures, temperatures, and flow rates) and labeled directed edges capturing the relations between the variables. Labels on the edges further qualify the relations between the vertices. A label of $\pm$ 1 on an edge implies a direct (inverse) directional proportionality between the associated variables, and '=' implies an equality relation between the associated variables. Component parameters, R's, TF's, GY's, C's and I's appear on links, and play a role in establishing the relations between the associated variables. R, TF, and GY impose algebraic relations, whereas the energy-storage elements, C and I, impose integral, i.e., temporal delay relations between the associated variables.

The algorithm to derive the TCG from a BG model utilizes the Sequential Causality Assignment Procedure (SCAP). The SCAP algorithm, outlined in [106], sequentially assigns causality to all of the bonds in the BG model. This causal structure is then unfolded into a directed graph. We start from the source effort and flow values, and sequentially following the algebraic (direct, inverse, and equality) as well as the temporal relations imposed by the constituent elements till all of the bonds and nodes have been traversed.

The fault isolation engine follows the generate-and-test approach to residual evaluation using the TCG structure. Qualitative transient behavior is expressed as a fault signature that describes the expected fault transient immediately after fault occurrence. The signature corresponds to a qualitative interpretation of the Taylor series expansion of the residual around the time point of fault occurrence [87, 90, 104]. The order of the signature is defined by the highest derivative computed (a design parameter). Symbolic values for the elements of a signature are: '+' for a positive or increasing value, '0' for a zero or unchanged value, and ' - ' for a negative or decreasing value. An unknown value is represented by '$*$'. The description of a fault signature in terms of the behavior around the point of fault occurrence is unique to the TRANSCEND [90, 106] approach.

Fault isolation is triggered by the first non-zero magnitude symbol that is output by the signal-to-symbol generation module. This initial symbol reflects the magnitude deviation in the residual at the onset of the fault transient. The hypotheses generation step produces a set of fault hypotheses that can explain the observed deviation. A fault hypothesis consists of a candidate parameter with a direction of change for the parameter value and a fault signature for each of the measured variables. During hypothesis refinement, the signatures are compared with symbolic values computed from the measurements using a scheme called progressive monitoring. When a match fails, the candidate is dropped. Further details of the qualitative fault isolation scheme are presented in [106].

Fault Simulation

It has been reported in the literature that electrolytic capacitors are the leading cause for breakdowns in power supply system's [99, 107]. The performance of the electrolytic capacitor is strongly affected by its operating conditions, which includes voltage, current, frequency, and working temperature. A degraded electrolytic capacitor cannot provide a low impedance path for the AC current in the output filter of these converters, thus introducing a ripple voltage on top of the desired DC voltage. Continued degradation of the capacitor leads the converter output voltage to drop below specifications, and in some cases it may even damage the converter itself.

Literature indicates that the fluctuation in power supply voltage and excessive ripple currents could lead to various failures in the GPS receiver module. In this work we have simulated the GPS reset events due to voltage fluctuations. The detailed analysis for fault diagnosis and isolation is carried out in several steps. These are outlined in the next section.

Experiments

As discussed earlier we employ the method to derive fault signatures on measured variables using our Temporal Causal Graph (TCG) scheme [88]. The TCG is automatically derived from a bond graph model of a system [89]. Figure 14 shows the TCG for the DC-DC converter which is derived from the Bond Graph(BG) model discussed in the earlier chapter.

To diagnose and isolate the faults their fault signatures should be unique, i.e. no two faults should have the same fault signatures for all measured values. At present, we are focusing on capacitor faults in the DC-DC converters. We derive the fault signatures for the two capacitor-related faults that can occur: (1) decrease in capacitance, and (2) increase in equivalent series resistance (ESR).

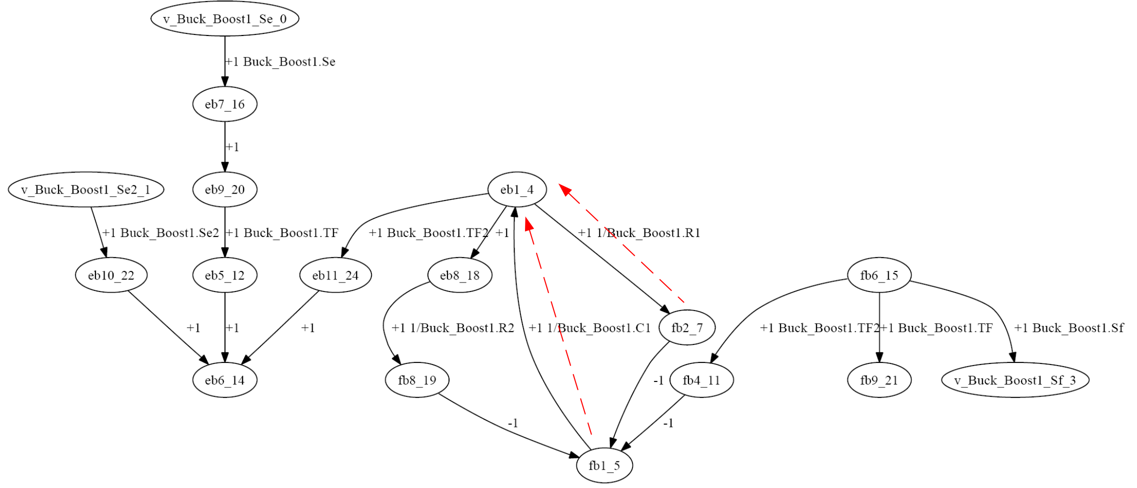

Figure 14: TCG of the Power Supply Model from BG

The Fault Detection and Identification (FDI) method [88, 90] in this paper is implemented using bond graphs as the underlying modeling language. Dynamic characteristics of system behavior derived from the bond graph are represented as a temporal causal graph. The algorithms [90] for monitoring, fault isolation, and prediction are based on this representation. The fault analysis and refinement process continues till fault transients are masked by interactions or the system reaches a steady state. The goal is to uniquely identify the true fault using a combination of transient and steady state analysis.

The fault detection mechanism was tested for an abrupt fault in the DC-DC converter model. The steps below show the procedure for fault injection in the converter system and implementation of the fault detection algorithm.

- Run the nominal DC-DC converter MATLAB/SIMULINK® model and record the sensor readings.

- Run the model with an abrupt fault case.

- A fault was introduced in the system at 250th time step.
- In this case a fault is introduced in the capacitor which is shown in the the residual plot of Figure 15. A glitch is observed in the output voltage of the DC-DC converter.
- The residuals are generated from the nominal and faulty data.
- This residual data is passed through the Fault detector algorithm.
- The fault detector detects the fault from the residual at 252nd time step.

The plot in Figure 15 shows the nominal behavior of the DC-DC converter where the residuals are around zero. At the 250th time step there is an abrupt change in the residual as seen in the plot where the fault is injected.

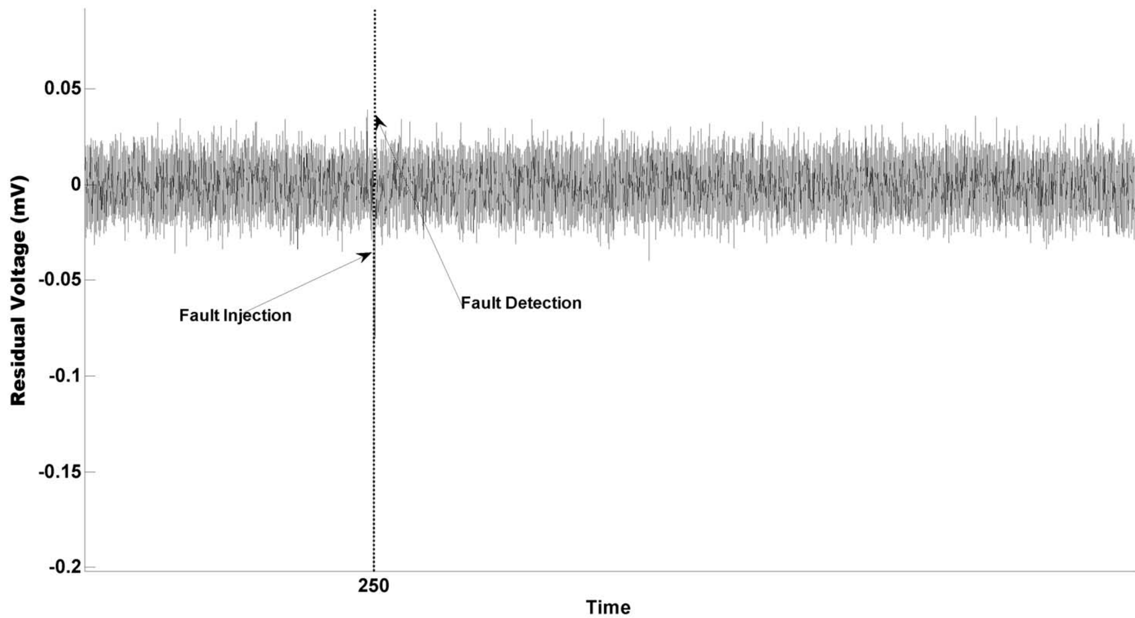

Figure 15: Residual Plot for the DC-DC converter

We implement the fault isolation algorithm discussed earlier for isolating the fault component in the system. In this case this component is the capacitor in the DC-DC converter. Fault signatures for isolation on measured variables are derived using our Temporal Causal Graph (TCG) scheme [88]. To isolate the faults their fault signatures should be unique i.e. each fault should have a unique signature. As can be seen from the TCG in Figure 14 any degradation in the capacitor component is related either to the change in the capacitance

Table 4: DC-DC Converter Fault Signatures

Components	Fault Hypothesis	Indicating Sensors	Fault Signature	Signal Deviation from Nominal
Electrolytic Capacitor	ESR increase (ESR+): abrupt or incipient	Voltage Sensor@ converter output	(0,-)	A gradual increase in ESR will cause a gradual decrease in output voltage of the converter.
	Capacitance decrease (C): abrupt	Voltage Sensor@ converter output	(+,-)	Abrupt decrease in capacitance will cause a high voltage spike and then a decrease in the output voltage of the converter.
	Capacitance decrease (C): incipient	Voltage Sensor@ converter output	(0,+)	A gradual (incipient) decrease in the capacitance will cause a gradual increase in output voltage of the converter
MOSFET's	Internal Voltage drop	Current Sensor in series with MOSFET	(+,-)	Voltage drop internally in the MOSFET.
	Internal Currents of MOSFET	Current sensor in series with MOSFET	(-,∗)	Increase/ Decrease in the current. Leakage currents in MOSFET

(-,∗) : the dot indicates either +/- change.

or change in the R i.e. the ESR value. The graph shows the node eb1_4 is affected by the two node fb2_7 and fb1_5 which are the ESR and capacitance nodes respectively. These two faults are marked in the TCG and the red arrows indicate how the faults affect the measured output voltage at the converter. Each of the faults generates a different signature which isolates the faults from each other. Table 4 lists the derived fault signatures for the capacitor faults.

Results

Figure 16 below shows the PSM model. The two components marked are Capacitor and MOSFET respectively in which the fault is introduced. The degradation equations derived and discussed later in the chapter were implemented in the model to simulate the degradation process.

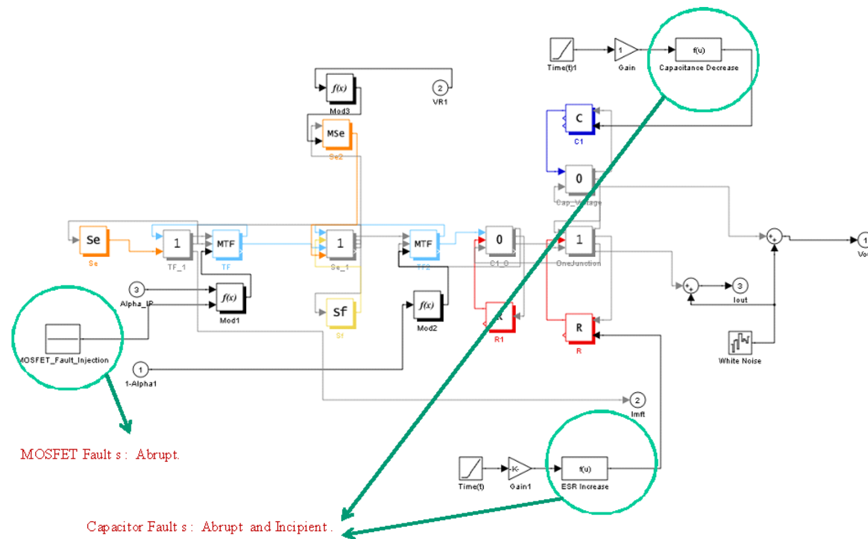

Figure 16: Fault Injection in the PSM model

The faults are introduced in the model through a GUI which allows the user to simulate different faults. Figure 17 shows the GUI where the user can simulate a situation to introduce faults in the PSM. This fault can either be introduced in the capacitor or MOSFET devices. The faults can either be abrupt or incipient faults.

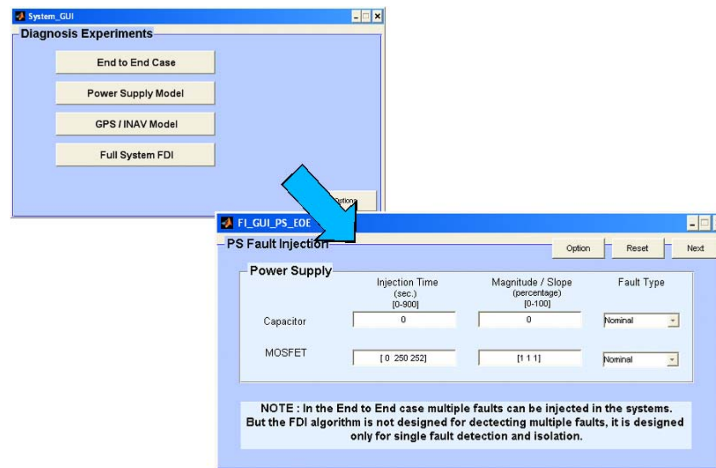

Figure 17: GUI for injecting fault

Abrupt Faults

Abrupt faults correspond to changes that occur at time scales much faster than the nominal dynamics of the system. We model abrupt faults as discrete and persistent changes in

the value of component parameters. An abrupt fault in a component parameter results in transients in the system variables. Typically, the transient behavior vanishes after an interval, and for certain faults no evidence of the fault is observable in the measurements after some time. Next we demonstrate two examples of an abrupt capacitor and MOSFET fault simulation.

Capacitor Fault Injection

Fault is injected in the capacitor of the PSM through the GUI as shown in Figure 18. The injection time, fault magnitude and the type of fault to be injected is selected.

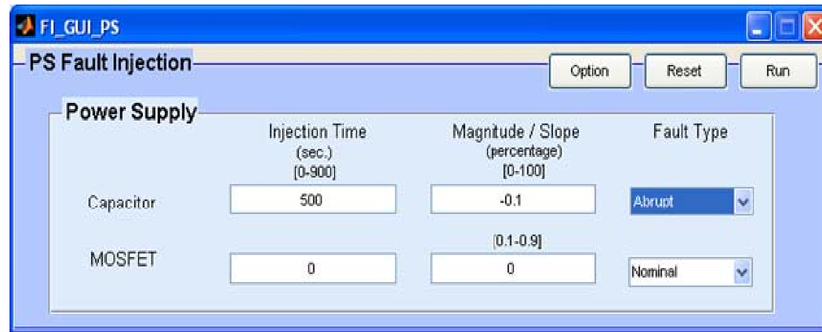

Figure 18: Fault Injection GUI for injecting Capacitor faults in PSM

Figure 19 shows an abrupt fault injected in the power supply. The first plot shows the output voltage for both nominal mode operation and fault injected operation of the Power Supply Module.

The second plot Figure 20 shows the fault detection for a fault injected in the capacitor. Similarly when we study the plots for the MOSFET as seen below, we observe that the MOSFET is healthy as no residue in the output current.

The fault detection uses the algorithm discussed earlier in the work. The output of the algorithm is displayed in the command window. The fault simulation result for a capacitor abrupt fault is shown below in the Figure 21.

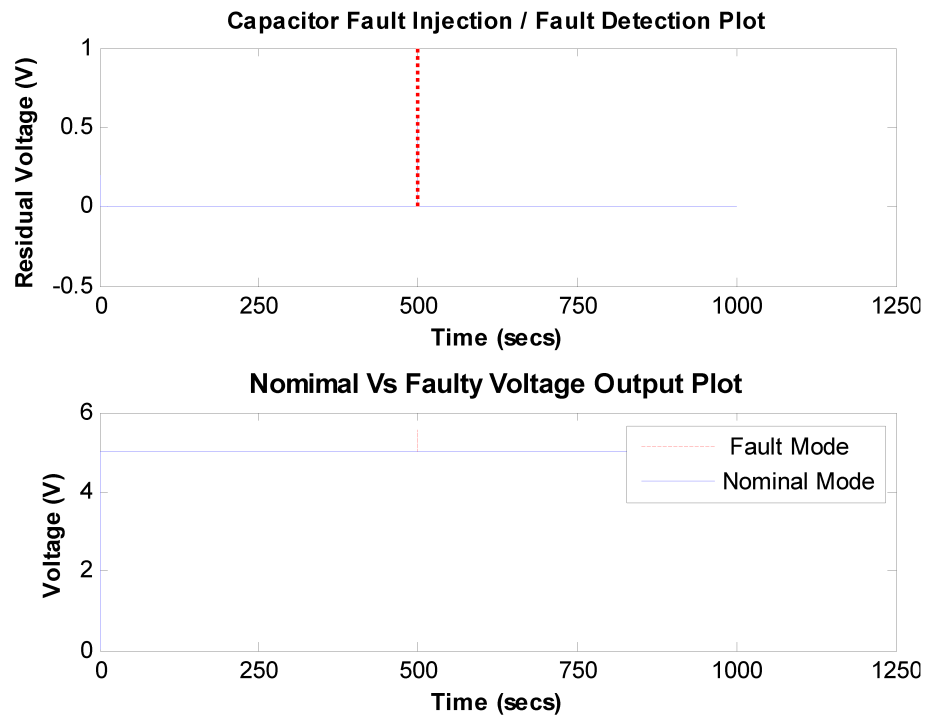

Figure 19: Capacitor Fault Injection and Output Voltage plots

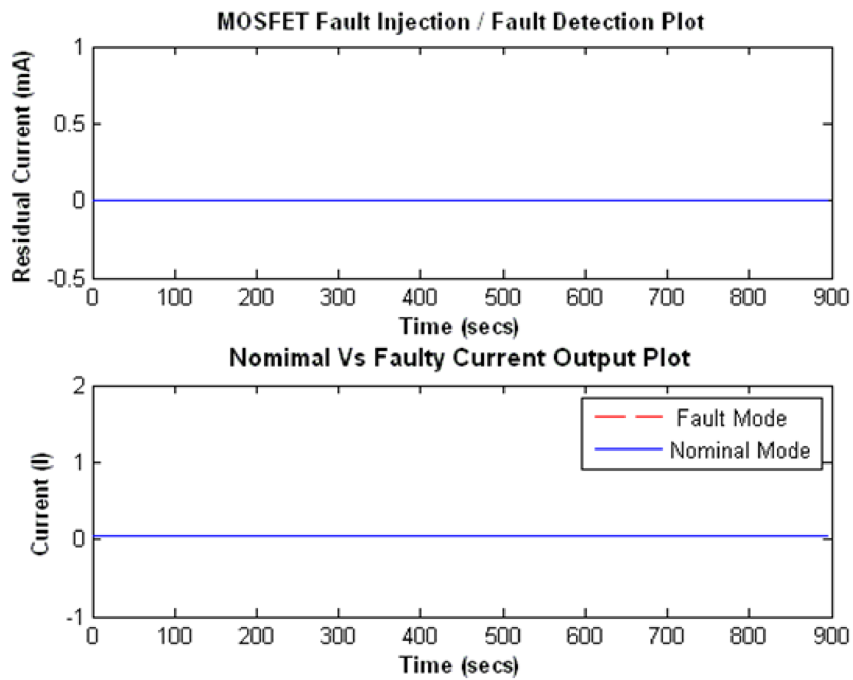

Figure 20: MOSFET Fault Injection and Output Current plots

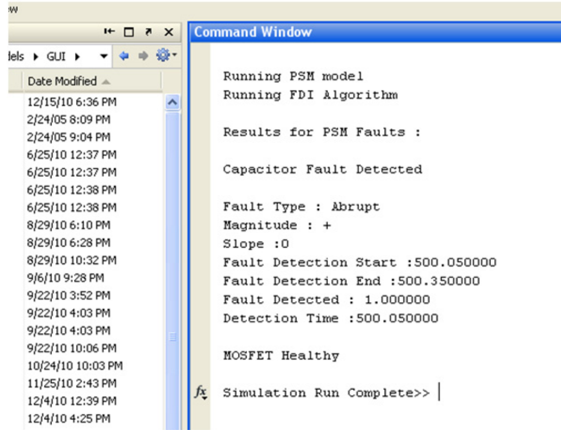

Figure 21: Algorithm output results for the injected capacitor fault

MOSFET Fault Injection

Similar to the capacitor fault injection, the injection time, magnitude and fault type for the MOSFET is selected for running the simulation. This is shown in the snapshot of the GUI in Figure 22. The model was run for 900 steps and the data was collected.

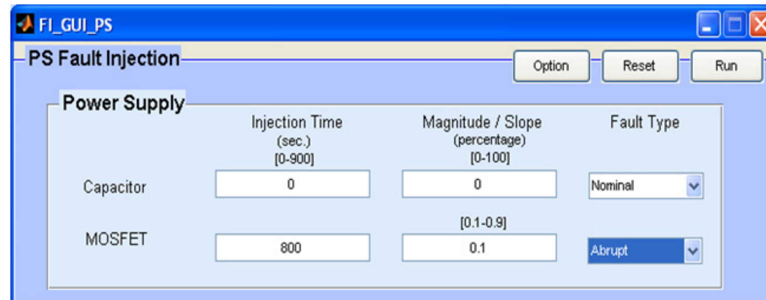

Figure 22: Fault Injection GUI for injecting MOSFET faults in PSM

From the plots it is observed that the output voltage does not change due to a fault injected in the MOSFET as seen in Figure 23.

An abrupt fault injected changes the current abruptly in the system which is detected shown in plot of Figure 24 by the current sensor.

The results of the simulation run are displayed in the command line window as shown in Figure 25.

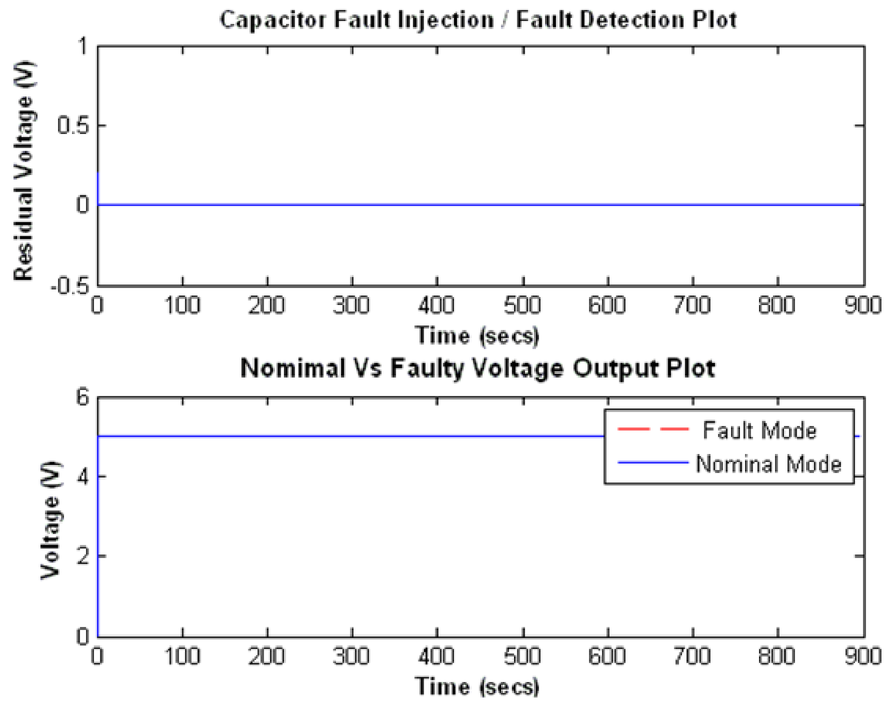

Figure 23: Capacitor Fault Injection and Output Voltage plots

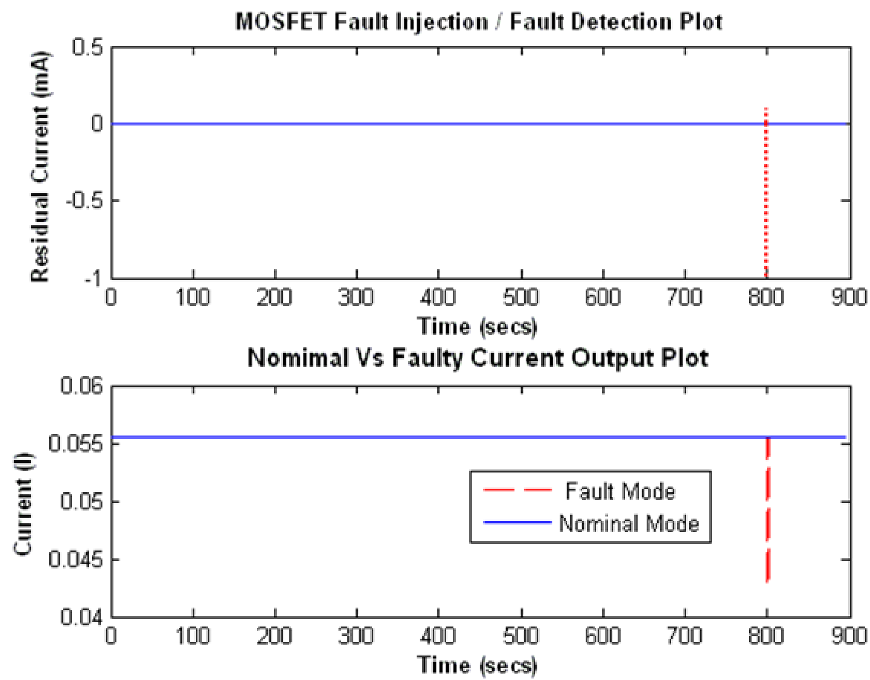

Figure 24: MOSFET Fault Injection and Output Current plots

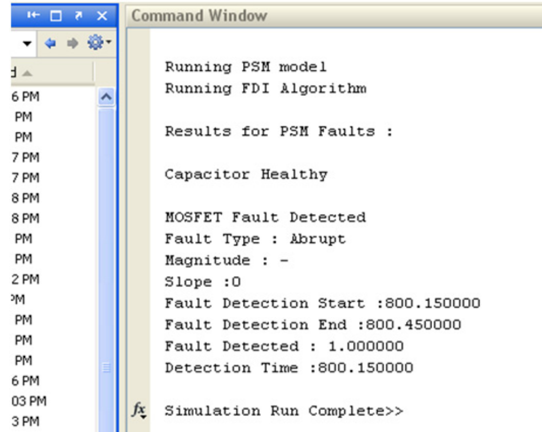

Figure 25: Algorithm output results for the injected MOSFET fault

Incipient Faults

Incipient faults occur slowly over time, and are linked to the wear and tear of components and drift parameter values. These faults are usually related to aging of the component due to long period of operation due to which the component degrades. In our work the capacitor degradation process is linked to increase in the ESR and decrease in the capacitance under normal operating conditions. The plots in Figure 26 below shows decrease in the output voltage over the period of time when an incipient fault is injected in the capacitor of PSM system.

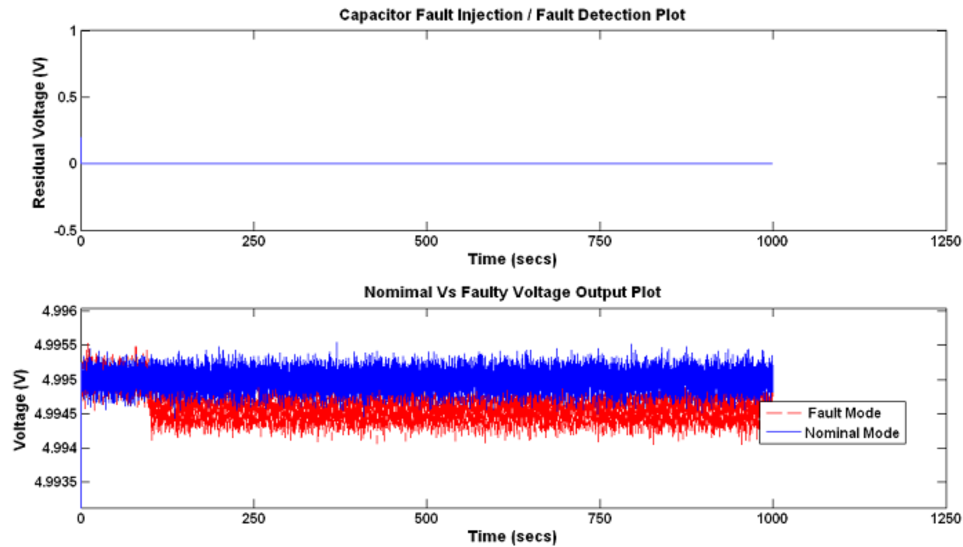

Figure 26: Incipient Fault Injection

Experiment Results

Component	Fault Type	Fault Magnitude/Slope	Fault Injection Time (secs)	Dectection Time (secs)	Fault Isolation Result
Capacitor	Abrupt	-0.01	500	Not Detected	**Not Faulty**
	Abrupt	-0.1	500	500.05	**Faulty**
	Abrupt	-0.3	500	500.05	**Faulty**
	Incipient	-1.00E-06	100	Not Detected	**Not Faulty**
	Incipient	-3.00E-06	500	957.5	**Faulty**
	Incipient	-4.00E-06	650	994	**Faulty**
MOSFET	Abrupt	1.00E-03	800	Not Detected	**Not Faulty**
	Abrupt	5.00E-02	800	800.1	**Faulty**
	Abrupt	1.00E-01	800	800.1	**Faulty**

Figure 27: Fault Isolation Results

The table in Figure 27 below shows the different faults injected in PSM system. These include faults injected in the capacitor and MOSFET components respectively. The table gives details relating to the type of fault injected, fault magnitude, the time when fault was injected in the component and detection time for the algorithm to detect the fault. The final column gives the fault isolation result if the algorithm detected the fault.

Summary

Our methodology provides a framework for developing efficient qualitative fault signature methods for fault detection and fault isolation. The future work include conducting more detailed analysis of degradation effects, discussed later in the chapters and their propagation to the different components of the system. We will also develop methods to quantify the effects of degradation on overall system performance. This is step towards one of the goals stated earlier to study system performance.

Overall, this research work demonstrated the use of fault signature techniques that can be applied to online diagnosis of faults in important components of aircraft systems. In this case, the task was especially challenging because the system was embedded in that it contained a significant number of software (computational) as well as hardware components. Therefore, our fault modeling, detection, and isolation schemes had to apply to very different kinds of subsystems, and also to handle interactions between these subsystems.

We developed a fault signature framework, where the fault signatures were derived by systematic analysis of either a physical system model (e.g., bond graph models for the power supply systems) or computational models (e.g., the Simulink models used for the GPS and INAV systems). In all of these cases, the challenge was to build these models at the right level of abstraction, so as not to be overwhelmed by computational complexity, at the same time, include sufficient detail to model capture the fault effects. The accomplishments of this work can be summarized as below.

1. Integrated Avionics Simulator : Simulink-based simulator includes: model for the GPS receiver, model for integrated navigation solution software, and Hybrid Bond Graph-based model for DC-DC power converter

2. Fault Injection: Identified ten critical HW and SW faults. Developed mechanism for simulating these faults within the avionics simulator.

3. Fault Indicators and Reasoner: Developed fault indicators for detecting all ten faults. Developed a reasoner to demonstrate the disambiguation and failure isolation

4. Degradation Data and Model: Ran experiments to generate the capacitor aging data under electrical and thermal stresses. Incorporated experimental data on capacitor aging under electrical within the avionics simulator.

CHAPTER IV

RESEARCH APPROACH

As mentioned earlier, prognostics approaches play an important role in improving system safety, reliability, and availability. Prognostics deals with determining the health state of components, and projecting this state into the future to make end of life (EOL) and RUL estimations. Our approach performs these tasks employing dynamic physics-based degradation models that capture knowledge about the system, its components, and their degradation mechanisms [21,108]. Faults and degradations appear as parameter value changes in the model, and this provides the mechanism for tracking system behavior under degraded conditions [109,110].

Approach Steps

We implement the prognostics modeling process illustrated in Figure 28. The main activity in implementing PHM methodology involves: a) identify the basic working principle and deriving the operating model of the device/system; b) identifying the degradation mechanisms (electrical, thermal, mechanical and chemical), and that govern the aging of components under various environmental conditions [80, 82]; c) derive relevant degradation models to predict the remaining useful life of the system and d) run experimental studies to compare the accuracy and validity of empirical models and models derived using physics-based principles [74]. We discuss each step involved in the approach in details.

Electrolytic Capacitors

Since we are implementing a physics-based modeling methodology for our approach, understanding the structure and behavior of the device under test is essential. Depending upon the granularity of the model implemented the necessary device parameters need to be known. In this case

1. the structural geometry i.e., details of the capacitors;

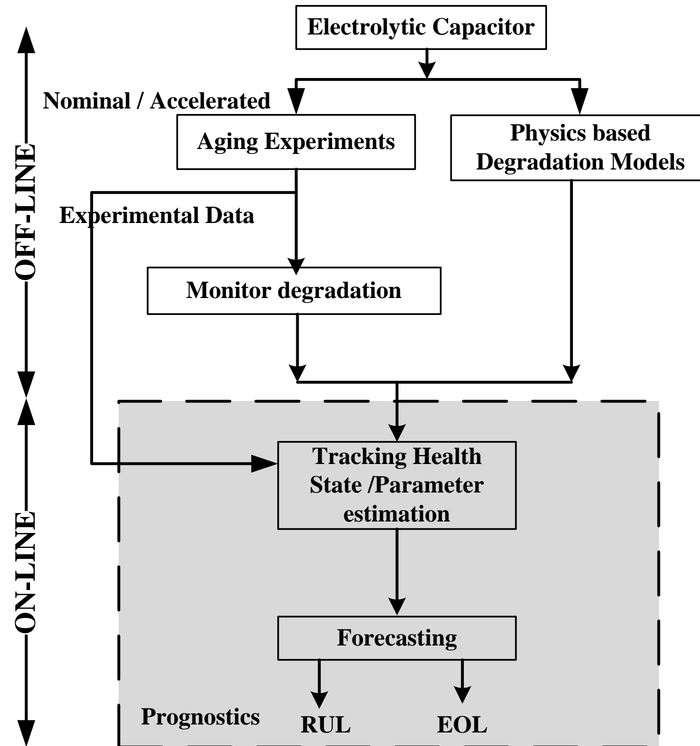

Figure 28: Research Approach Methodology

2. materials used;

3. thermal and electrical properties of the material;

4. manufacturer details.

These details are used for deriving the physics-based degradation models of the capacitor. First principles physics-based models are derived to study and analyze degradation through the aging cycle, rather then just observing abrupt failures. These models give a more better understanding of how the devices operate under different conditions.

Accelerated Aging Experiments

This research work focuses on developing physics-based degradation models of components that include descriptions of how fault parameters evolve in time, governed by their operating conditions. Under normal operating conditions the device operates for several years and systematic studies of condition based monitoring of these components and systems becomes difficult. So to study the systematic degradation of the component in shorter period of time,

we apply increased stress levels on the component to accelerate lifetime. The advantage of accelerated stressors is that we can run the component to failure. The disadvantages of accelerated experiments is that the process of testing and test control are tedious and complex in nature. Specific testbeds need to be developed depending upon the nature of the stress applied and monitoring degradation in the device/system frequently. In this work, we are particularly interested in studying electrical and thermal stressors. The challenge then is to consider intervals of accelerated degradation and extrapolate those to nominal degradation conditions.

Under normal operating conditions usually a device/subsystem does not degrade rapidly, since all the operating parameters are within threshold limits. In such cases it takes a longer time to study and observe the underlying failure modes. Accelerated stress tests (AST) have been recognized to be a valuable activity to assess the reliability and quality of electronics in a timely manner [80]. Accelerated stress tests are often carried out under extreme environmental conditions to enhance the damage accumulation rate due to any physical or environmental phenomena in the component [81]. In the PBM approach it is necessary to understand the underlying failure mechanisms essential for designing and conducting successful accelerated aging tests [74, 81].

The electronics industry is yet to adopt PBM methodologies based on AST standards [76, 79]. Research is focused more on conducting accelerated testing under combinations of multiple stresses, to enhance test time compression [80]. This has only served to increase the confusion in literature, in standards, and in industry, regarding the most cost-effective and scientific way to conduct accelerated stress testing for electronic assemblies. Researchers [74,76,80] agree that implementing PBM methodologies hold a greater promise of providing a systematic approach plan, conduct, implement and evaluate accelerated life tests, under combined environmental loads.

Thermodynamic processes can produce stresses that cause damage to basic elements of the system, ultimately leading to system failure that can be explained by a corresponding physics based model [80, 83]. PBM design guidelines, which emphasize the understanding of potential failure mechanisms, are more effective if first principles based models can be derived to describe the relevant failure mechanisms. Therefore it is very important to

identify the different failure mechanism modes, which occur due to the applied stresses during the life-cycle of the system [74, 82].

These mechanisms are mainly divided into two major groups overstress mechanisms and wearout mechanisms. Overstress failures are catastrophic failures observed due to a single occurrence of a stress event that exceeds the intrinsic strength of the material, i.e. failure due to high voltage or current pulses. Under normal operating conditions the device is constantly degrading, damages are also observed under overstress operating conditions. Accumulation of incremental damage leads to failure when the accumulated damage exceeds the material endurance threshold, and is termed wearout failure. By definition, only wearout failure can be accelerated during an AST. Verification of overstress failures, on the other hand, is performed through laboratory experimental tests. Therefore, failure acceleration models used in accelerated stress tests must focus on the relevant wearout failure mechanisms [80, 83].

As summarized in the flow diagram of Figure 28, we combine experimental studies on the device and combines the electrical and mechanical configuration information with physics based modeling of behavior phenomena.

System Identification

Under normal operations an ideal capacitor model is assumed. A lumped-parameter model of the non-ideal capacitor impedance is assumed in this work. This model is then further expressed at higher granularity depending upon the type of operational stress conditions. This impedance model includes a capacitance element and an equivalent series resistance (ESR) parasitic element. The Electrochemical-impedance spectroscopy (EIS) measurements along with the impedance model structure are used in a systems identification setting to estimate the model parameters available throughout the aging test. This results in time-dependent capacitance and ESR measurements trajectories reflecting capacitor degradation.

ESR and capacitance values are estimated by using a system identification using a lumped parameter model consistent of the capacitance and the ESR in series as shown in Figure 29. The frequency response of the capacitor impedance (measured with electro-impedance spectroscopy) is used for the parameter estimation. It should be noted that the

lumped-parameter model used to estimate ESR and capacitance, is not the model to be used in the prognostics algorithm; it only allows us to estimate parameters which provide indications of the degradation process through time.

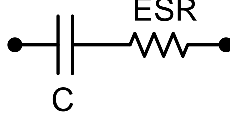

Figure 29: Lumped parameter model ($\mathcal{M}_1$) for a real capacitor.

The non-ideal capacitor model $\mathcal{M}_1$ can be used as part of electronics circuits that make use of capacitors. An example is the low-pass filter implementation in Figure 30. In this circuit, input voltage V_i is considered as the voltage to be filtered and the voltage across the capacitor (this includes ESR as well) is the output voltage V_o which is filtered. Let $v(t) = V_o(t)$ and $u(t) = V_i(t)$ in the low-pass system circuit with non-ideal capacitor shown in Figure 30. A state-space realization of the dynamic system is given by

$$\begin{aligned} \dot{z}(t) &= \frac{-1}{C(R+ESR)} z + \frac{1}{C(R+ESR)} u(t), \\ v(t) &= \left[1 - \frac{ESR}{R+ESR}\right] z + \frac{ESR}{R+ESR} u(t), \end{aligned} \tag{2}$$

where $z(t) = V_C(t)$ is the state variable representing the capacitor voltage, C, ESR and R are system parameters. Furthermore, C and ESR are parameters that will change through time as the capacitor degrades.

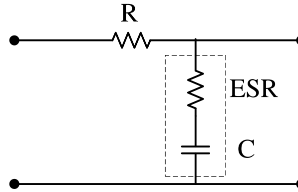

Figure 30: Low pass filter model

Model $\mathcal{M}_1$ describes the nominal dynamics of a low-pass filter with a non-ideal capacitor. While this model may be useful for fault detection and isolation, it does not provide the information we need to perform model-based prognostics. We extend this model to describe the degradation process as time-varying functions of the changes in the model parameters.

This model by itself is not sufficient to implement a model-based prognostics algorithm since the degradation process as reflected on model parameters is not modeled. Degradation models describing the time evolution of ESR or C are needed in order to enhance $\mathcal{M}_1$ for model-based prognostics.

Degradation Modeling

Identifying the failure precursors and developing accurate models of degradation/failure from an understanding of the physics-based model is an important challenge that we address in this research work. Early detection and analysis may lead to more accurate estimation of parameter changes, and therefore, better prediction and end of life estimates of the capacitor.

Our primary focus is to derive and validate physics-based degradation models for both capacitance and ESR values of degraded capacitors. Our hypothesis is that the physics-based models will be more accurate and more general, and we demonstrate this by comparing the accuracy of these models against the date-driven models.

Parameter Estimation for Degradation Models

For the empirical derived model parameters are estimated using nonlinear least-squares regression. Unknown and time varying parameters in the degradation model are estimated online. The derived state space models are then implemented in a Bayesian framework for prognostics.

Prognostics

A Bayesian framework is employed to estimate (track) the state of health of the capacitor based on measurement updates of key capacitor parameters. The Kalman filter and Unscented Kalman Filter algorithms are implemented to track the state of health and the degradation model is used to make predictions of remaining useful life once no further measurements are available.

Summary

This chapter gives an overview of the research methodology we have implemented in our work. Figure 28 summarizes the steps and approach of the research work. We discussed each step in brief and will be studying them in detail for each of the implemented stress conditions in the respective chapters.

CHAPTER V

CAPACITOR DEGRADATION MODELS

In this chapter we develop physics-based models of capacitor degradation phenomena that can be attributed to adverse operating conditions. Operating conditions and environmental effects that differ from the rated nominal conditions specified by the manufacturer are labeled as stressors. In this research, we study the effects of two primary stressors on capacitor performance: electrical and thermal. The study of stressor effects are derived by analyzing the internal physical structure and material properties of the electrolytic capacitors. The models of the degradation process, derived from the structure and material properties, define how the capacitance and internal series resistance of the capacitor change over aging time.

Electrolytic Capacitors

The configuration of an aluminum electrolytic capacitor, exposing its internal structure is shown in Figure 31. Figure 32 provides an illustration of the internal components of the capacitor wrapped in the shape of a layered cylinder. The primary components of an electrolytic capacitor are: (1) cathode aluminum foil, (2) electrolytic paper, (3) electrolyte, and (4) an aluminum oxide layer on the anode foil surface. The paper strip is impregnated with liquid electrolyte. When in contact with the electrolyte, the oxide layer provides an excellent forward direction insulation property [111]. A magnified effective surface area is attained by etching the foil, provides for high capacitance values in a small volume [112]. Since the oxide layer has rectifying properties, a capacitor has polarity. If both the anode and cathode foils are coated with an oxide layer, the capacitors are bipolar [113].

Figure 33 illustrates the unfolded separator paper into which the electrolyte is embedded by soaking. The paper height, h_c is the height of the capacitor capsule and l_c indicates the length of the combined roll of paper separator, anode, and cathode. The paper separator

[1] http://en.wikipedia.org/wiki/file:Electrolyticcapacitordisassembled.jpg

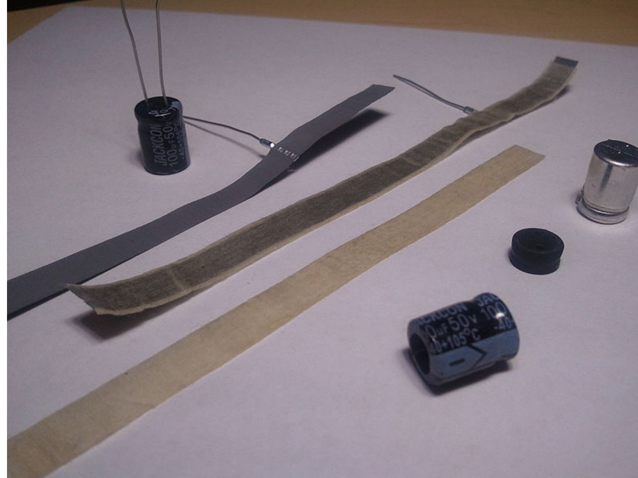

Figure 31: Capacitor Physical Structure[1]

is sandwiched between the anode and the cathode. Each has a thickness d_S, d_A and d_C, respectively, and in general $d_S \approx d_A \approx d_C$.

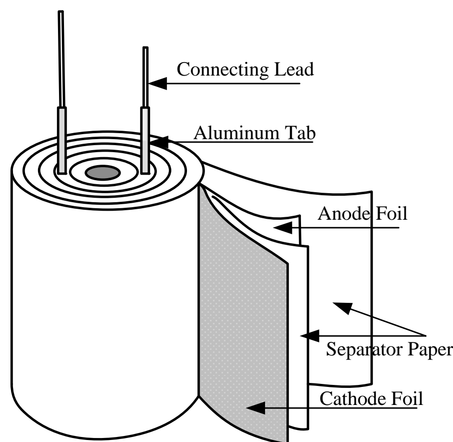

Figure 32: Physical Model of Electrolytic Capacitor

Figure 34 presents a detailed view of the cross section of the electrolytic capacitor structure. The anode and cathode foils are are anodized by coating them with a thin aluminum oxide layer on the surface of the foil. This layer of aluminum oxide acts as the dielectric (insulator) and serves to block the flow of direct current between the anode and cathode foil surfaces [112]. When a DC voltage is applied to a discharged capacitor there is an initial surge of current observed because of charge accumulation on the anode and cathode foils. This causes a corresponding voltage increase across the terminals of the

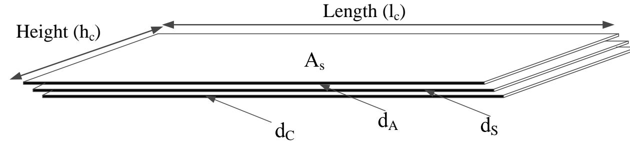

Figure 33: Capacitor Open Structure

capacitors, and correspondingly, the current flow drops exponentially towards zero as the capacitor terminal voltage increases to equal the applied voltage [114].

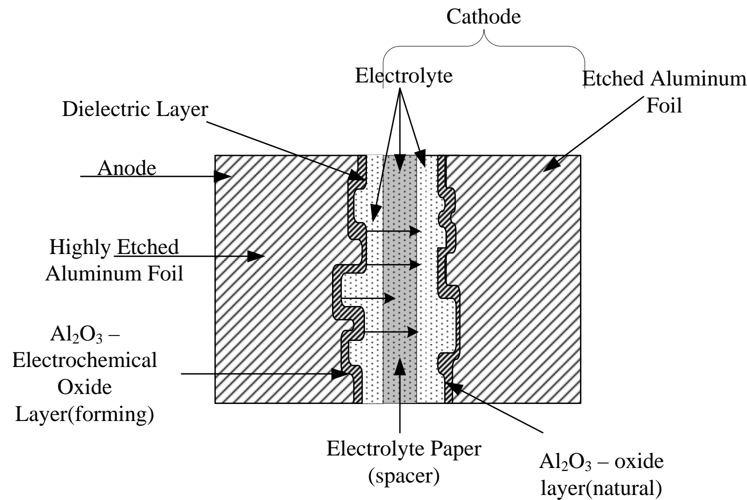

Figure 34: Cross sectional Details of Internal Capacitor Structure

Degradation Mechanisms

There are several factors that cause degradation in electrolytic capacitors. Failures in a capacitor can be one of two types: (1) catastrophic failures, where there is complete loss of functionality due to an internal short between the anode and cathode or an open circuit caused by a break in the leads, and (2) degradation failures, where there is gradual deterioration of the capacitor due to accumulated damage to its internal structures. From an electrical circuit viewpoint, degradation in the capacitor manifests an increase in the equivalent series resistance (ESR) and decrease in capacitance (C). The degradation in these health parameters can be attributed primarily to decreases in electrolyte volume caused by evaporation, weakening of the oxide insulation layer leading to oxide layer breakdown [47, 115] along with deterioration in electrolyte quality, and increase in internal pressure.

The primary causes of degradation during nominal operation of a capacitor can be linked to thermal and electrical processes. The flow of current during the charge/ discharge cycle of the capacitor causes the internal temperature to rise. The heat generated is transmitted from the core to the surface of the capacitor body, but not all of the heat generated can escape. The excess heat causes an increase in the internal temperature of the capacitor, which in turn increases the electrolyte evaporation rate. Similarly, in situations where the capacitor operates or is stored under high temperature conditions, the capacitor body is at a higher temperature than its core, and heat travels from the body surface to the core of the capacitor thus increasing the internal temperature and causing the electrolyte evaporation rate to increase [116]. The phenomenon of increase in internal temperature is modeled using a physics-based thermal model of heat conduction that we discuss later in this chapter.

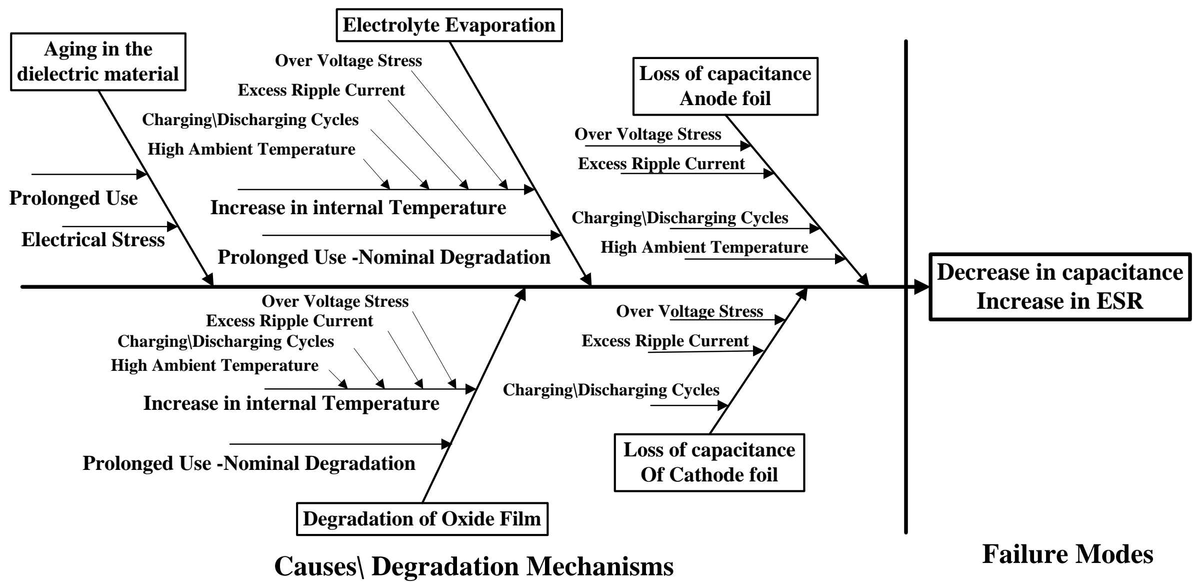

Figure 35: Ishikawa Diagram of Failure Mechanisms in Aluminum Electrolytic Capacitor

We first study the degradation phenomena qualitatively, and then discuss the steps to derive the physics-based analytic degradation models for different operating conditions. The fishbone diagram (also called the Ishikawa diagram shown in Figure 35) summarizes the comprehensive list of failure modes that occur in electrolytic capacitors [114, 117–121] along with their primary causes. The major degradation phenomena shown in the figure are:

1. Aging of the dielectric material,
2. Electrolyte Evaporation,
3. Degradation of Anode Foil,
4. Degradation of Cathode Foil, and
5. Degradation of oxide film.

Elaboration of the main causes, represented as minor bones linking to the degradation and failure phenomena are:

1. Prolonged Use,
2. Increase in internal temperature,
3. Over voltage stress, and
4. Charging/discharging cycles.

These are then linked to the finer bones, which explain the root causes for the different failure mechanisms in the capacitor. These root causes can occur individually or in groups depending upon the operating conditions for the capacitor. In this thesis research, we primarily focus on the electrical and thermal stressors that govern capacitor degradation. Specifically, we study conditions where the capacitors are subjected to high voltage and high temperature conditions. For example, over voltage stress, which results in an increase in the capacitor internal temperature can cause loss of electrolyte and also degradation in the oxide film leading to increased leakage currents along with increase in internal pressure. Electrolyte evaporation can be attributed to internal heat generation or high ambient external temperature both which cause increased internal core temperatures. In all of these situations, the capacitor degradation results in simultaneous changes in its capacitance and internal resistance values.

Defined industry standards [122,123] specify a capacitor to be degraded (i.e., unhealthy), if under thermal stress the capacitance value decreases by 10% and the ESR value increases

by 250% or more from its pristene rated value. Similary, a capacitor is considered unhealthy if, under electrical stress operations, its ESR increases by 280%-300% over and capacitance decreases by 20% below its pristine condition values. The ratings are different for electrical and thermal stress conditions, because thermal stress conditions are considered for situations when the capacitor is in storage, and not in operation. Hence the threshold standards are defined seperately for different conditions. Phenomena associated with the root causes include:

1. Studying the increase in internal temperature due to excessive ripple current and frequent charging/discharging cycles, or high ambient temperatures which lead to decrease in the electrolyte volume.

2. Estimating the decrease in capacitance (C) due to electrolyte evaporation and degradation in contact with the oxide layer.

3. Estimating the increase in ESR due to electrolyte evaporation and oxide layer degradation.

4. Determining how short circuits occur due to insulation breakdown of the electrolytic film and insufficient electrolyte volume.

We first discuss the equivalent internal electric circuit model of the capacitor and then discuss each of the underlying degradation phenomenon in the sections that follows.

Equivalent Internal Circuit Model

In this section, we first discuss the derived equivalent electrical circuit model of an electrolytic capacitor. We then discuss the link between the equivalent circuit parameters to the the physical variables of the capacitor, especially those that are impacted by the degradation process.

A detailed lumped parameter equivalent circuit model of electrolytic capacitors presented in [124] is shown in Figure 36. Inductive parameters are not considered in the model since the capacitors under study are operated in the DC mode. The mapping between the electrical circuit components and internal capacitor components are listed below:

1. The resistances R_{al} and R_{cl} are attributed to the lugs connecting the terminals to the anode and cathode foils, respectively.

2. The elements associated with the anode foil are the resistance of the foil, R_{af}, the capacitance of oxide layer deposit on the foil, C_{af}, and parallel resistance, R_{afp} representing the resistive losses caused by the oxide layer.

3. The circuit elements introduced by the electrolyte include the resistance due to the electrolyte in the etched tunnels in the anode and cathode foils, R_{aot} and R_{cot}, respectively. An additional resistance is due to the electrolyte in the paper separator, R_E. A parallel capacitance C_E represents the electrolyte dispersion of the paper, which is impregnated with the electrolyte.

4. Similar to the components present in the anode foil, circuit elements associated with the cathode include oxide capacitance on the cathode foil, C_{cf}, the parallel resistance, R_{cfp}, representing the losses due to the dielectric on the cathode, and finally resistance of the cathode foil, R_{co}.

The cathode capacitance, C_{cf}, is typically at least ten times larger in value than the anode capacitance, C_{af}. This is because the dielectric of the capacitor is present on the anode foil, which is a thin layer of aluminum oxide, Al_2O_3 chemically grown on the anode foil using a process know as "formation". During the process of formation the effective anode foil surface area is reduced since the microscopic tunnels are partially obstructed by the Al_2O_3 deposits, thus reducing the number of tunnels and hence anode capacitance, C_{af}, whereas the formation has no effect on the cathode foil and hence C_{cf} is comparatively very much higher than C_{af}.

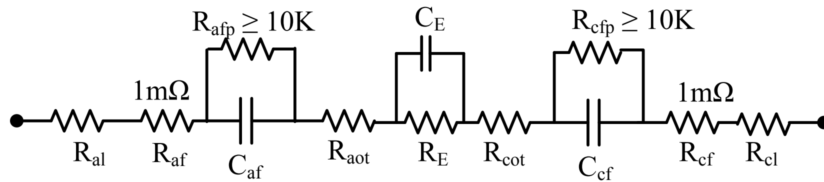

Figure 36: Equivalent Electrical Model of Electrolytic Capacitor ($\mathcal{M}_1$)

This anodization also determines the anode and cathode parallel resistances, R_{afp} and R_{cfp}, respectively. The electrolyte impregnation affects the resistance due to the electrolyte on the separator paper, R_E and the parallel capacitance, C_E due to dispersion. The set of parameters and their expected nominal values for a typical 2200 μF capacitor are listed in Table 5.

Table 5: Approximate lumped parameter values associated with Capacitor

Parameter	**Approximate Value** (Ω)
Anode oxide resistance (R_{afp})	$\geq 1 \times 10^4$
Cathode oxide resistance (R_{cfp})	$\geq 1 \times 10^4$
Series cathode foil capacitance (C_{af})	2400μF
Parallel electrolyte Capacitance (C_E)	$\ll C_{af}$
Series anode foil capacitance (C_{cf})	$\gg C_{af}$
Resistance of electrolyte in paper (R_E)	5×10^{-2}
Resistance of electrolyte in etched tunnels of anode foil (R_{aot})	6×10^{-3}
Resistance of electrolyte in etched tunnels of cathode foil (R_{cot})	13×10^{-3}
Resistance of anode foil (R_{af})	1×10^{-3}
Resistance of cathode foil (R_{cf})	1×10^{-3}
Lug resistance on anode (R_{al})	1×10^{-4}
Lug resistance on cathode (R_{cl})	1×10^{-4}

In this work, our goal is to derive an analytic degradation model of the capacitor, based on the internal capacitor structure and the associated physical processes. The parameter values of the model will be derived from experimental data. Our current experimental setup is better suited to directly derive the parameters corresponding to the internal circuit, with a simpler, abstract form of the model, $\mathcal{M}_2$ as shown in Figure 37. As an approximation, series resistance components R_{al}, R_{cl}, R_{af}, R_{cf}, R_{aot} and R_{cot} are combined into an equivalent single resistance R_c. The parallel resistance, R_{afp} and R_{cfp}, each $\geq 1 \times 10^4 \Omega$ in magnitude can be ignored compared to the series resistances that are of the order of $1 \times 10^{-3}\Omega$. The cathode foil capacitance C_{cf} is usually very much greater than the anode foil capacitance, C_{af},($C_{cf} \gg C_{af}$) hence C_{cf} can be ignored. The parallel capacitance C_E and anode foil capacitance can be combined to form a series capacitance, C_c.

As explained from equivalent circuit lumped parameter model ($\mathcal{M}_2$) ESR is approximated as the sum of two component resistances :

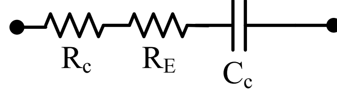

Figure 37: Simplified lumped parameter electrical Model ($\mathcal{M}_2$)

$$ESR = R_c + R_E. \tag{3}$$

R_c, as discussed is the combined series resistance of the lugs, cathode and anode foils respectively, which remains almost constant since its a combination of the resistances attributed to mechanical aspects of the capacitor that do not change much over the life of the capacitor. However, as discussed earlier (also, see Table 5) R_E is orders of magnitude higher than R_s, therefore, changes in ESR are primarily influenced by changes in R_E. In [125] it is discussed that R_c remain relatively constant and electrolyte resistance, R_E increases as the capacitor degrades, which can be attributed to the evaporation (i.e.,decrease) and degradation (chemical breakdown caused by ion exchange) of the electrolyte during operation. R_c and R_E are combined to define the overall degradation resistance combined together to form the equivalent internal series resistance (ESR) as summarized in model $\mathcal{M}_3$, Figure 38.

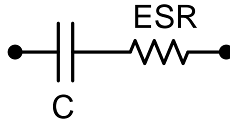

Figure 38: Lumped parameter electrical Model ($\mathcal{M}_3$)

Degradation Phenomenons Under Study

In earlier sections, we discussed the internal structure of the capacitor, the associated degradation mechanisms, and an equivalent lumped parameter electrical circuit that captures the internal structure and degradation mechanisms of the capacitor. Before we take the next step to derive the physics-based degradation models we recap the three major phenomenons leading to degradation in electrolytic capacitors:

1. Electrolyte Evaporation that can be attributed to electrical and thermal stress conditions. This is the dominant degradation phenomenon,

2. Oxide Breakdown, which is mainly observed under electrical overstress conditions; under thermal overstress condition the phenomenon is less dominant.

Secondary causes of degradation are linked to:

1. Increase in internal Pressure that is mainly observed only under electrical overstress conditions,
2. Electrolyte degradation, due to chemical reactions between the electrolyte and the anode & cathode foils.

We first discuss the primary degradation phenomenon in detail and then derive physics-based degradation models linking the phenomena to the operation conditions. We do not build explicit degradation models for the secondary degradation phenomena in this thesis.

Electrolyte Evaporation

In this section, we derive the degradation model for changes in electrolyte volume over time caused by evaporation due to stress effects. This is one of the primary contributors to the degradation of electrolytic capacitors.

Heat Transfer in Capacitor Capsule

It has been observed that the temperature of the cartridge remains almost constant across the diameter and along the length of the capacitor [116]. This is also true for the casing. Therefore, it is reasonable to assume that cartridge and casing are isothermal bodies. As as result, the capacitor can be treated as two concentric isothermal cylinders as shown in Figure 39, which are at temperature values T1 and T2, respectively. Further heat flow can be considered to be radial. These assumptions hold for capacitors having cylindrical surface area much greater than the end areas i.e., top and bottom surface areas of the rolled unit [111].

Electrical Stress

Heat generation in the capacitor takes place at the core, from where it travels radially outwards towards the surface as explained earlier. The heat generation can be attributed

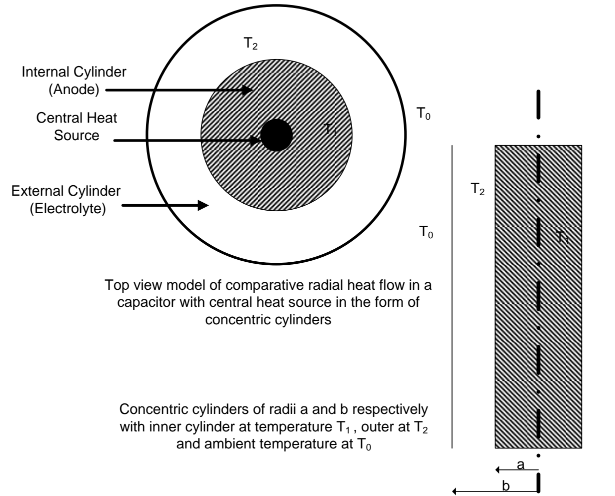

Figure 39: Comparative Radial Heat Flow in Electrolytic Capacitor

to the ripple current passing through the ESR of the capacitor. Figure 40 describes the heat flow when the capacitor is charged, the flow direction is considered to be unidirectional from the core to the outer surface. The capacitor structure is made up of different layers as discussed earlier in the section, through which the heat flow occurs before it is radiated out to the surrounding atmosphere. In the thermal model these layers represent successive thermal capacitances and thermal resistances. In the capacitor, the anode and electrolyte layers along with the ambient surroundings are represented as the thermal capacitances, labeled as C1, C2 and C3, respectively. Similarly the dielectric and body (cathode) layers are modeled as thermal resistances R1 and R2, respectively.

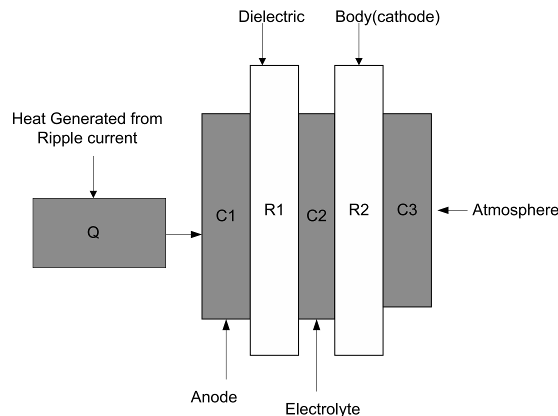

Figure 40: Heat flow Model of Electrolytic Capacitor under electrical Stress

Operation of the capacitors under $V_{applied} > V_{rated}$ results in rise of the internal core temperature of the capacitor. The current flow through the capacitor during the charge/discharge cycle has an exponential temporal relation with the applied voltage [114]. When the applied voltage is within the range of V_{rated} the amount of heat generated because of the current and internal resistance of the capacitor is relatively low. For $V_{applied} > V_{rated}$

$$I \propto \exp(V_{applied}) \tag{4}$$

The current flow is due to the transport of ions under the action of applied voltage. Some of the heat generated is conducted or radiated out through the capacitor body and leads, and the rest leads to the increase in the internal temperature. When the applied voltage, $V_{applied}$ is above V_{rated} the rate of current flow increases at a much faster rate, thus increasing the amount of heat generated. Lesser amounts of this heat gets dissipated to the outside, since most of the heat gets trapped in the multiple layers of the rolled unit of capacitor capsule, which leads to a rise in the core temperature. The increase in temperature accelerates the electrolyte evaporation, thus increasing the ESR of the capacitor [32].

Heat Generation

Referring to discussion regarding heat transfer in section V the amount of heat generated is calculated as :

$$P = V \times I \tag{5}$$

where:

V: $V_{applied}$, applied voltage in Volts.

I: current through the capacitor which is calculated from the current density in Amperes.

When the applied voltage is within the range of V_{rated} the amount of heat generated because of the current and internal resistance of the capacitor is relatively low. Under normal operating conditions i.e $V_{applied} \leq V_{rated}$ the conduction through the anodic oxide obeys the Poole - Frenkel mechanism [114] which is given by:

$$j = QE^{3/2}\exp(\beta E^{1/2})$$

with (6)

$$\beta = 2e^{3/2}/\epsilon_i^{1/2}KT$$

where:

j: current density.

Q: space charge $\rightarrow$ charge on the capacitor.

E: electric field intensity in dielectric.

ϵ_i: dielectric constant.

e: electron charge.

K: Boltzmann constant.

T: absolute temperature.

From Eqn. 6 we can calculate the total current flowing in the capacitor.

This generated heat increases the internal core temperature of the device. Under normal operating conditions the amount generated is low hence the internal temperature does not rise much above the nominal value (i.e., room temperature). Under high electrical stress operating conditions the amount is generated is high as compared to normal operation and this will increase the internal core temperature considerably.

Thermal Stress

Similar to accelerated degradation under electrical stress we study capacitor degradation for the thermal overstress condition. Under this operating condition when the surrounding temperature gets high, the temperature of the can body of the capacitor also increases. Heat travels from the surface of the body to the core of the temperature, this phenomenon is described through the thermal model as shown in Figure 41. In the thermal over stress (TOS) condition we study the effect of high temperatures on capacitors i.e., $T_{applied} > T_{rated}$, where $T_{applied}$ is the applied overstress temperature in storage (i.e., not during actual operation when the capacitor may charge and discharge) and T_{rated} is the rated temperature

at which the capacitor can be stored. A study of the literature [126] indicated that the degradation could be primarily attributed to evaporation of the electrolyte due to high temperatures.

When the ambient temperature (controlled chamber temperature) is increased, the core temperature of the capacitor also increases. The raised temperature in the capacitor core causes the electrolyte to start evaporating at faster than normal rates [122]. It has been observed that the temperature of the cartridge and casing remain almost constant across the diameter and along the length of the capacitor. Therefore, it is reasonable to assume that cartridge and casing are isothermal bodies. As a result, the capacitor can be treated as two concentric isothermal cylinders as shown in Figure 41(a) with temperature values T1 and T2 respectively. Further heat flow can be considered to be radial. These assumptions hold for capacitors having cylindrical surface area much greater than the end areas [116].

High temperature on the surface causes heat flow radially towards the core of the capacitor (Fig. 41(b)) [111, 122]. The heat flow is considered only in one direction from the outer surface to the core. The capacitor structure is made up of different layers through which the heat flows as shown in the Fig. 41. In the thermal model these layers represent successive thermal capacitances and thermal resistances. In the capacitor, the anode and electrolyte layers are represented as the thermal capacitances, labeled as C1, C2 respectively (Figure 41(b)). Similarly the dielectric and cathode layers are modeled as thermal resistances R1 and R2, respectively.

The models for heat transfer under electrical and thermal stress that lead to increase in the temperature are the cause of electrolyte evaporation which is discussed next.

Electrolyte Evaporation Model

The evaporation rate, j_{eo} is directly linked with change in the core temperature. The relationship between electrolyte evaporation rate and temperature for a particular electrolyte can be found in [125]. In this work the electrolyte under study is ethylene glycol. When the surrounding temperature of the capacitor capsule is high, heat transfer from the capsule to the capacitor core causes the internal temperature of the capacitor to increase, and as a result the electrolyte evaporates at a faster rate. Under prolonged high temperate exposure

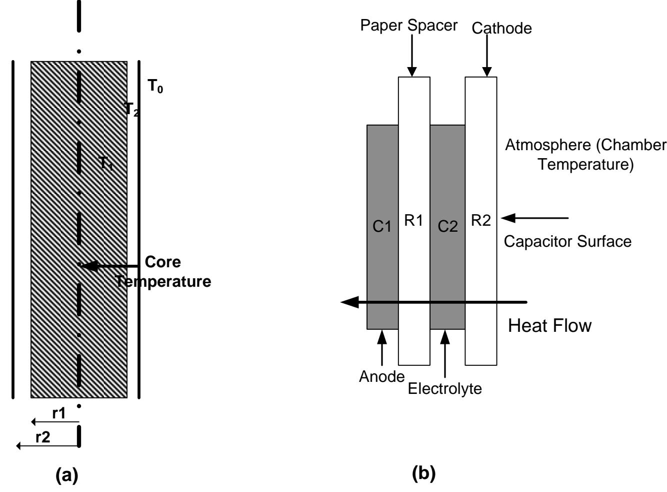

Figure 41: Heat flow Model of Electrolytic Capacitor under thermal Stress

the electrolyte evaporation accelerates, which in turn decreases effective oxide surface area A_s, leading to decreases in capacitance, (C) [125,127,128]. The change in electrolyte volume as a function of the evaporation rate and time elapsed is given by:

$$V_e(t) = V_{e0} - (A_s j_{eo} w_e \times t), \tag{7}$$

where:

$V_{e(t)}$: dispersion volume at time t

V_{e0}: initial electrolyte volume

A_s: effective oxide surface area

w_e: volume of ethyl glycol molecules

j_{eo}: evaporation rate (mg min^{-1} $area^{-1}$)

t: aging time in hours.

From Eqn.(7) we derive the effective oxide surface areas A_s in terms of the decrease in electrolyte volume over time:

$$A_s = \frac{V_{e0} - V_e(t)}{j_{eo}\ t\ e} \tag{8}$$

In the next section we derive the equations for computing the initial electrolyte volume in a capacitor, V_{e0}, based on its structure and internal manufacturing geometry and standards.

Computing Initial Electrolyte Volume

Earlier we discussed that under high stress conditions, the electrolyte evaporates at faster rates due to the increase in internal core temperature. The exact amount of electrolyte in the capacitor is unknown, but we can compute the initial volume of the electrolyte from the dimensions and type of the capacitor. The equation for computing the approximate electrolyte volume is derived from total capacitor capsule volume,V_c given by:

$$V_c = \pi r_c^2 h_c \tag{9}$$

where:

r_c: radius of capacitor

h_c: height of capacitor

From the structural geometry and data in Figure 33, the total internal volume (V_i) can be computed as:

$$V_i = A_s(d_A + d_S + d_C) \tag{10}$$

where:

d_A: anode oxide layer thickness,

d_C: cathode oxide layer thickness

d_S: spacer paper thickness

The total volume:

$$V_c = V_i + V_{can} \tag{11}$$

where:

V_c: total capacitor volume

V_{can}: volume of can material

V_i: internal volume of can

Referring to the open structure diagram of capacitor shown in Figure 33 we can assume that the can thickness is very small, so $V_{can} \approx 0$, and d_A, d_S and d_C are known from

capacitor geometry. Therefore,

$$\pi r_c^2 h_c = A_s(d_A + d_S + d_C) \tag{12}$$

Correspondingly, the paper spacer volume is given by:

$$V_s = A_s d_S,$$

The electrolyte is completely soaked in the paper spacer. Hence the total spacer volume can be expressed as combination of actual paper volume, V_{paper} and the electrolyte volume, V_{e0},

$$V_s = V_{paper} + V_{e0}$$

Since the capacitor paper is completely soaked under pristine conditions, the initial electrolyte volume, V_e is given by:

$$V_{e0} = V_s - V_{paper}$$

The amount of electrolyte present depends on the type of paper used and number of pores present in the paper. Typically, a highly porous paper type is used in the construction of the capacitor so that the maximum amount of electrolyte can be soaked in the paper. Hence the electrolyte volume can be approximated as:

$$V_{e0} \approx V_{paper} \tag{13}$$

from Eq. (11) and Eq. (12), Eq. (10) can be expressed as:

$$V_i = A_s(d_A + d_C) + A_s d_S$$

$$A_s d_S = V_s$$

$$V_i = A_s(d_A + d_C) + V_s$$

From Eq. (13) we have:

$$V_s \approx V_{e0}$$

hence we get:

$$V_i = A_s(d_A + d_C) + V_{e0}$$

Based on the geometric structure the approximate volume of electrolyte, (V_{e0}) in a capacitor can be expressed as follows:

$$V_{e0} = V_i - A_s(d_A + d_C) \tag{14}$$

Referring to Eq. (11) and assumption $V_{can} \approx 0$ we have,

$$V_i = V_c$$

hence:

$$V_{e0} = V_c - A_s(d_A + d_C)$$

From Eq. (12) and Eq. (14) the approximate pristine condition volume of electrolyte, V_{e0} based on geometry of the capacitor is expressed in terms of following equation:

$$V_{e0} = \pi r_c^2 h_c - A_s(d_A + d_C) \tag{15}$$

Note that Eq.(15) gives us the initial electrolyte volume, V_{e0}, for a particular type of capacitor based on its geometry and manufacturing parameters. In the later section of this chapter we will discuss how the effective oxide surface area is linked with degradation in the capacitance and ESR values.

Oxide Layer Breakdown

Degradation in the oxide layer can be attributed to defects that appear on the oxide surface. High electrical stress is known to accentuate the degradation of the oxide layer due to localized dielectric breakdowns on the oxide layer [118, 119]. Changes in the electrical parameters due to degradation in the oxide layer causes changes in the leakage current of the capacitor leading to high voltage charges that travel over the surface of the oxide and lead to increased crystallization and deposits on the surface [130]. When this crystalline oxide layer breaks away, some of the insulating oxide layer also peels off, causing formation of pits and loss of insulation on the oxide surface [129], the electrical conductivity between the anode and cathode surfaces increases, thus decreasing the ability of the capacitor etched surface to hold charge because of the impregnation of these defects by electrolytes. As the peeling off continues and the leakage current continues to increase, the resulting impact ionization eventually leads to an avalanche of electron flow [129, 130]. Therefore, the high electrical current due to applied voltage leads to irreversible changes in the oxide layer structure and correspondingly the electrical properties of the capacitor. This degradation in the insulation resistance, R_i and capacitance, C_i, further accelerates the degradation process toward the end of capacitor life, i.e., a complete breakdown of the capacitance function [119].

Similarly, during thermal cycling the phenomenon of electrolyte evaporation leads to cracks, fissures, chemical segregation, and lamellar tearing of oxide layer in addition to increase in the insulation resistance and decrease in insulation capacitance caused by degradation and breakdown in the oxide layer. The eventual breakdown phenomenon is similar to an avalanche breakdown explained theoretically by a equivalent circuit shown in Figure 42.

In Figure 42, C_i and R_i are insulator capacitance and resistance, respectively and R_E is the electrolyte series resistance (major element of ESR and explained in detail in the later part of the chapter). R_f is the resistance of breakdown filament, R_{ef} is the electrolyte resistance in series with the filament, and R_c is the resistance of the of the ionic charge layer at the oxide interface for cylindrical current flow into the filament. R_c is calculated as:

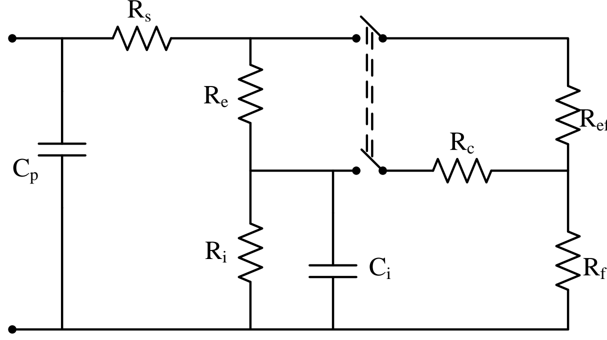

Figure 42: Equivalent circuit for the interpretation of a breakdown event

$$R_c = \frac{d_c}{2\pi\epsilon_R\epsilon_0\mu V_{applied}} ln \frac{V_e}{V_{e0}} \tag{16}$$

where:

$V_{applied}$: applied voltage,

V_e: Current electrolyte volume,

V_{e0}: initial electrolyte volume under pristine conditions.

The resistance R_{ef} is calculated as:

$$R_{ef} = \frac{\rho_e}{2\pi\ V_e} \tag{17}$$

where:

ρ_e: resistivity of electrolyte.

In the conventional technology, an insulator capacitance component, C_i is generated at the portion where void is created in-between the oxide layers of the anode and cathode as the electrolyte evaporates. The insulator resistance, R_i is also directly related to the void formation phenomenon. In addition, under electrical stress when a high voltage is applied to the oxide layer, a partial discharge (corona discharge) occurs in the vacant layer where the insulator capacitance component forms. Since the partial discharge during operation of

the module causes deterioration in the oxide layer, this has a corresponding effect on the insulation between the foils, leading to degradation [129,131]. Hence the capacitor degrades faster under electrical overstress conditions than if subjected to just thermal overstress(no charge). Oxide breakdown is a similar phenomenon to an avalanche breakdown, and, therefore, deterioration of the insulation is also an avalanche effect and hence both the insulation resistance, R_i and insulation capacitance, C_i degrade exponentially.

Under charged operation, a local breakdown is represented by closing of the switch as shown in Figure 42. On closing, the capacitors C_p and C_i discharge through the the filament resistance R_f. When the switch closes at breakdown an additional resistance network is added to the initial circuit hence the overall equivalent series resistance (ESR) which is combination of all the series and parallel resistive components, does not increase exponentially since a parallel network of resistance dampens the exponential rise and instead causes more of a linear change in the slope of ESR. While the total capacitance, computed from the parallel capacitance network of C_p and C_i, decreases exponentially since C_p decreases linearly due to electrolyte evaporation which is dominant in the early aging life cycle and C_i decreases exponentially due to the avalanche breakdown phenomenon which becomes dominant in the later stages of aging cycle as the avalanche effect kicks in.

As discussed earlier evaporation of the electrolyte creates voids in the oxide layers, which over the period of thermal cycling due to high temperature fissures and crack develop on the oxide surface which leads to degradation. The insulation capacitance, C_i is indirectly related to the electrolyte evaporation and more directly to the oxide layer breakdown, which results in the avalanche effect phenomenon, causing C_i to decrease exponentially. And since C_p and C_i are in parallel the overall capacitance starts to decreases in an exponential way, once the degradation in C_i starts dominating in the later stages of the aging cycle. Under thermal stress conditions since no charge is applied to the device, the R_c value is remains constant, while resistance values of R_{ef}, R_f and R_i increase. At breakdown when the switch is closed due to the parallel and series combination of the resistances the degradation observed due to change in overall resistance is relatively less dominant as compared to degradation observed in the capacitance value.

The breakdown phenomenon is represented by a capacitance dependence factor, c_b and resistance breakdown dependence factor, e_b which are directly proportional to the electrolyte evaporation and operating conditions, hence any changes in these factors have a direct impact on the capacitance and ESR parameters respectively. Under normal operating conditions, degradation due to breakdown is minimal since the devices operate well within the bounds of operational limits, and hence these factors are not seen as a contributing elements to the overall degradation phenomenon. But during the aging cycle under overstress conditions breakdown phenomenon is more prominent and observed in the measurement data hence these dependence factors are included as a parameter of the underlying first principle equation. As explained c_b has an exponential effect while e_b has a linear effect, as the breakdown phenomenon starts dominating in the aging cycle. The relationship between capacitance dependent breakdown factor and electrolyte volume decrease is given as:

$$c_{b(t)} = exp(f(V_{e0} - V_{e(t)}) \tag{18}$$

Similarly the relationship between ESR dependent breakdown factor and electrolyte volume decrease is given as:

$$e_{b(t)} = f(V_{e0} - V_{e(t)}) \tag{19}$$

Physics-Based Degradation Models

The fishbone diagram in Figure 35 discussed a fairly complete set of underlying phenomena that cause capacitor degradation and eventual breakdown. Given our approximate internal lumped parameter electrical circuit model of the capacitor, we have determined that the capacitance value, C and the resistance value, ESR are the primary determinants of capacitor health. We will use a physics-based modeling approach that links degradation of C and ESR parameters of the capacitor to physical phenomena associated with electrolyte evaporation and oxide layer deterioration.

Capacitance Degradation Model

The input impedance of the capacitor network is defined in terms of the total lumped series and parallel impedance of the simplified circuit model [133] shown in Figure 38. Capacitance represents the ability of a body to store electrical charge. It can be calculated from knowledge of the configuration and the geometry of the conductors and dielectric properties of the insulator between the conductors. Based on the cylindrical geometry the total lumped capacitance for a foil type electrolytic capacitor [133] is given by:

$$C = \frac{2\epsilon_R \epsilon_0 A_s}{d_C} \tag{20}$$

where:

ϵ_R: relative dielectric constant,

ϵ_O: permitivity of free space,

d_C: oxide layer thickness,

A_s: effective oxide surface area,

c_b: capacitance dependence breakdown factor.

Under overstress conditions, as discussed earlier, capacitance dependence factor c_b, also affects the capacitance value, and Eqn (20) can be re-written as:

$$C = \frac{2\epsilon_R \epsilon_0 A_s c_b}{d_C} \tag{21}$$

where:

c_b: capacitance dependence breakdown factor.

Studies reported in the literature [129, 131] and our own experiments show that this parameter in the initial life aging cycle of the device remains less dominant based on the operating conditions and is directly proportional to decrease in electrolyte as discussed earlier. In Eq. (20) and Eq. (21) the parameters ϵ_R, ϵ_0, and d_C remain more or less constant through the capacitance aging time.

ESR Degradation Model

The ESR dissipates some of the stored energy in the capacitor. An ideal capacitor would offer no resistance to the flow of current at its leads. Based on the first principles parameters the series electrolyte resistance, R_E is computed as a function of the effective oxide surface area, A_s [133] as:

$$R_E = \frac{1}{2}\left(\frac{\rho_E d_C P_E}{A_s}\right) \tag{22}$$

where:

ρ_E: electrolyte resistivity

P_E: correlation factor related to electrolyte spacer porosity and average liquid pathway.

These two parameters are also relatively constant through the aging life of the capacitor. Since $R_E \approx ESR$, increase in R_E due to evaporation of electrolyte, which decreases A_s, will lead to increase in ESR, given by:

$$ESR = \frac{1}{2}\left(\frac{\rho_E d_C P_E}{A_s}\right) \tag{23}$$

Under overstress conditions, as discussed earlier the resistance dependence factor e_b is factored into Eqn (23), to define the updated model as:

$$ESR = \frac{1}{2}\left(\frac{\rho_E d_C P_E e_b}{A_s}\right) \tag{24}$$

Under normal circumstances when the capacitors are stored at room temperature or below rated temperatures, no singnificant damage or decrease in the life expectancy is observed for long periods of time. But in cases where the capacitors are stored under temperature conditions higher than their rated value, the capacitors show irreversible degradation over time. For both the capacitance and degradation models, we employ derived relation between, oxide surface area, A_s and elctrolyte volume, $V_{e(t)}$ to define temporal degradation in the C and ESR values when stress is applied. Under thermal overstress conditions no charge is applied to the device, therefore no exchange of ions in the electrolyte takes place

hence one observes a very minor degradation in in the e_k factor. The change in ESR is mainly affected by the change in electrolyte volume.

Time Dependent Degradation Models

Using the physics-based model of electrolyte evaporation, we derive the time dependent degradation models for capacitance (C) and ESR. Using Eq. (20) and Eq. (8) we derive the *capacitance degradation model* as:

$$\mathcal{D}_1 : C(t) = \left(\frac{2\epsilon_R \epsilon_0 c_b}{d_C}\right)\left(\frac{V_{e0} - V_e(t)}{j_{eo}\ t\ w_e}\right). \tag{25}$$

V_{e0} Eq. 8 in is computed from the capacitor geometery in Eq. (15), and the other parameters are specific to capacitor depending upon its structure and manufacturing specifications. Evaporation rate, j_{eo} is a temperature dependent parameter, electrolyte volume changes with time and evaporation rate and c_b is the breakdown capacitance dependence factor directly dependent on the change in electrolyte volume. Similarly increase in ESR, is computed from Eq. (15) as:

$$\mathcal{D}_2 : ESR(t) = \frac{1}{2}\left(\rho_E\ d_C\ P_E\right)\left(\frac{j_{eo}\ t\ w_e e_b}{V_{e0} - V_e(t)}\right) \tag{26}$$

In model, $\mathcal{D}_2$ the parameters which are temperature dependent are the rate of evaporation j_{eo} and the correlation factor, P_E related to electrolyte spacer porosity and average liquid pathway and e_b, breakdown resistance dependence factor directly dependent on the change in electrolyte volume, operating conditions.

Increase in Capsule Internal Pressure

Internal pressure increases due to increase in the core temperature and chemical reactions taking place during the charge/ discharge cycle. Gas generation in capacitors [132] is principally controlled by two processes outlined below:

The first process is based on Faraday's first law of electrolysis. The law states that *''Mass of any substance deposited or liberated at any electrode is directly proportional to the quantity of electricity (charge) passed"*. The quantity of charge passed is the product of

current (A) and time (sec) which is the polarization time. The mass (W) of ions liberated, is directly proportional to the amount of charge passed through the electrolyte (Q) [120].

During the charging cycle, a charge q, equal to $C_A \times V_{applied}$ is built up on the anode, where C_A is the anode capacitance and $V_{applied}$ the applied voltage. This applied charge leads to oxidation at the anode and will cause a reduction reaction at the cathode resulting in the generation of hydrogen. As studied from the first law the number of moles of gas generated is linearly dependent on the polarization time. Similarly during the discharge cycle, on discharge of the anode, electron transfer from the solution to the aluminum cathode takes place which causes discharge of hydrogen to produce either molecular oxygen or anodic aluminum oxide. These observations suggest that, under any condition, we would observe gas evolution and damage on the oxide layer due to oxidation [120].

The simultaneous aging process during the operation is the absorption of the generated gas. The continuous evolution of the gas during the operation is diminished by the absorption of hydrogen by the depolarizer. Hydrogen absorption takes place at a constant rate through the reduction reaction of the quinone and picric acid (components in the electrolyte) [120, 132]. The reduction reaction follows the first order of kinetics where, the rule states that in a chemical reaction in which the rate of decrease in the number of molecules of a substrate is proportional to the concentration of substrate molecules remaining. The reduction reaction is given by:

$$n(t) = n_d \left[1 - \exp(-kt)\right] \tag{27}$$

where:

n: number of reacting moles with hydrogen.

n_d: total number of depolarizer moles.

k: absorption constant.

t: time

The anodic reaction during this phenomenon is given by:

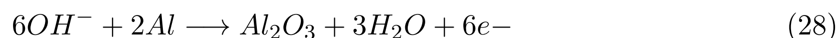

$$6OH^{-} + 2Al \longrightarrow Al_2O_3 + 3H_2O + 6e- \tag{28}$$

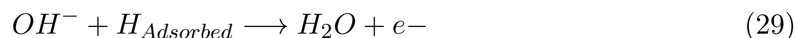

$$OH^{-} + H_{Adsorbed} \longrightarrow H_2O + e- \tag{29}$$

The phenomenon described in Eqn. (29) is more likely than the phenomenon attributed to Eqn. (28) since Eqn. 28 requires that aluminum (Al) atoms overcome the barrier effects at the interface in order to react where as in Eqn. 29 the H^{+} atoms are already on the surface of the metal and available for combination with OH^{-} [32, 120, 125].

Under normal operating conditions, $V_{applied} \leq V_{rated}$ the amount of gas generated is small and all of it is absorbed by the depolarizer. At high temperatures caused by the over stress voltage, $V_{applied} > V_{rated}$, rate of reaction accelerates leading to increase in the generation of hydrogen gas. With increase in internal temperature the electrolyte depletes and thus the amount of depolarizer present reduces. This leads to decrease in the rate at which hydrogen gas is absorbed causing some of the hydrogen to be left unused and results increase in the internal pressure. Though this is a slow process and is secondary to the previous two phenomena described, the end result causes the capacitor cap to "pop" and complete failure of the device. Evaporation also leads to increase in the internal pressure of the capacitor but this has a smaller effect than the increase in the pressure due to generation of gases, which also decreases electrolyte evaporation rate .

Summary

In this chapter, we first discussed discussed the structure of an electrolyte capacitor and its equivalent electrical models. Literature survey revealed a variety of underlying degradation mechanisms that change with operating conditions. For example the phenomenon of electrolyte evaporation occurs for nominal, electrical overstress, and thermal overstress conditions, but the mechanisms which lead to these failure vary as the operating conditions change. Nominal operation provides a baseline on how the capacitor degrades under normal

operating conditions. We then derived from the structure and manufacturing details, the initial electrolyte amount in each capacitor.

The most common stressors leading to degradation in capacitors are electrical and thermal overstress conditions, respectively. We further studied these operating conditions and their effects leading to degradation phenomenon on the internal parameters. We studied each of the degradation mechanism in detail and derived formulae for how the capacitance and ESR of a degraded capacitor changed with time.

We then derived the physics-based degradation models for the capacitor. For our further research work we conducted laboratory experiments where we developed specific hardware and setups for simulating the operating conditions for the capacitors to degrade. Under these conditions the capacitors were regularly monitored and characterized to study the degradation phenomenon. Data from these experiments is then used to test and validate each of the derived models. The experiments, derived degradation models, implementation and results are discussed in the next chapters.

CHAPTER VI

ELECTRICAL OVERSTRESS

In this chapter, we study capacitor degradation under electrical over stress (EOS) conditions. In these situations, the applied voltage on the capacitor exceeds its rated voltage, i.e., $V_{applied} > V_{rated}$. A study of the literature [122, 126] indicates that the degradation in electrolytic capacitors under EOS can be primarily attributed to three related phenomena:

1. Electrolyte evaporation,
2. Oxide Breakdown and leakage current, and
3. Increase in internal Pressure.

The heat generated internally when current passes through the capacitor during its charge and discharge cycle, leads to evaporation of the electrolyte [116]. In addition to this, as the capacitor continues to degrade overtime, other phenomena, such as oxide layer breakdown, leads to further deterioration causing the capacitance to decrease significantly. The physics-based degradation models associated with electrolyte evaporation and oxide layer breakdown were discussed in Chapter V.

In this chapter we first we discuss the electrical equivalent model and setup for the electrical overstress experiments. Our first approach uses the experimental degradation data to implement an empirical model for capacitance degradation. We derive the empirical capacitance degradation model , validate it using a leave-one-out methodology, and then use the model to make RUL calculations. Next we present the methodology for deriving generalized physics-based degradation models for capacitance and ESR, respectively. We validate the dynamic physics-based model by comparing its predictions against additional data generated from the experimental study.

Table 6 describes the datasets for the experiments that have been conducted to study capacitor degradation under different operating conditions. The first column describes the type of experiment conducted, the second column in the table gives details of the capacitors

used for the experiment while the third column gives the details of the experimental setup for stressing the capacitors. The last column indicates the number of capacitor devices used in each experiment.

Table 6: Electrical Overstress Degradation Experiments

Experiment	**Capacitors**	**Setup**	**Units**
Electrical Overstress	2200μF, 10V, 85°C	10V, 25°C	8
Electrical Overstress	2200μF, 10V, 85°C	12V, 25°C	6

Electrical Stress Degradation

In this section we present an approach for deriving physics-based degradation models for capacitors under electrical overstress conditions. To derive the degradation model we first discuss the equivalent electrical circuit model to link the degradation phenomenons summarized in the fishbone diagram in Figure 35.

Equivalent Electrical Circuits

A simplified electrical circuit equivalent lumped parameter model of impedance, $\mathcal{M}_1$, defined for an electrolytic capacitor is shown in Figure 44. An ideal capacitor offers no resistance to the flow of current at its leads. However, the electrolyte, aluminum oxide, space between the plates and the electrodes combined produces a small equivalent internal series resistance (ESR), which dissipates some of the stored energy in the capacitor. Under the overstress conditions, electrolyte evaporates at a faster rate causing the ESR to increase, and the overall ability to store charge, i.e., the capacitance to decrease. The degradation models derived in Chapter V indicate that these changes in the two parameter values are mostly linear.

However, as the amount of electrolyte decreases significantly, the increased temperatures and the charging and discharging cycles of the capacitor lead to additional degradation in the oxide insulation layer of the capacitor. The degradation due to the crystallization deposits on the oxide layer caused by voltage sparking on the surface of the oxide [129]. In an equivalent circuit damage model, this behavior can be reproduced as a small capacitance

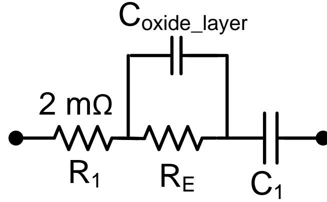

Figure 43: Electrical Overtress Degradation Electrical Equivalent Model($\mathcal{M}_4$)

with resistance in parallel along with the existing ESR and capacitance parameters linked to electrolyte evaporation as shown in Figure 43. The equivalent electrical model,$\mathcal{M}_4$ in Figure 43 shows the simplified electrical equivalent of the breakdown model. This degradation model is generated into a simpler approximation, shown as a capacitance, C and dissipation resistance, ESR in series. This equivalent circuit is illustrated in Figure 44. We derive the parameter values for this simplified model from our experimental data.

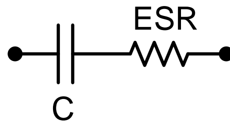

Figure 44: Lumped Parameter Model ($\mathcal{M}_1$)

Electrical Overstress Experiments

In this setup, the capacitors are subjected to high voltage stress through an external supply source using a specifically developed hardware described by the block diagram in Figure 45.

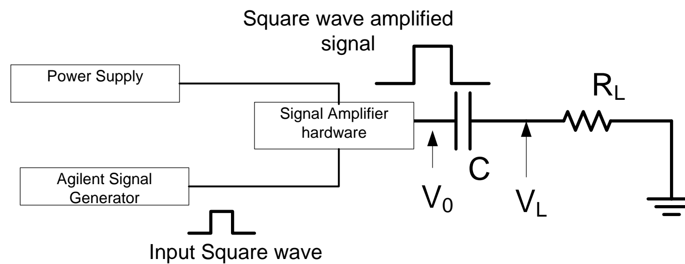

Figure 45: Block diagram of the experimental setup.

Power Supply

The power supply used for the experiment is a BK Precession 1761 triple output DC power supply. A constant DC voltage of ±15V is required by the amplification hardware, which is provided by this power supply.

Function Generator

In this experiment, we charged/discharged the capacitors at a fixed frequency using a square wave input. This input square wave was generated using a Agilent 33220A 20 MHz Function/Arbitrary Waveform Generator. This is a 14-bit, 50 MSa/s, 64 k-point arbitrary waveforms generator and can be controlled over USB, GPIB and LAN ports.

The function generator is programmed for a 1V square wave output at 100mHz. This frequency is calculated from the RC time constant, where R is the load connected for the capacitor to discharge and C the capacitance values of the capacitor. At this frequency the capacitors are charged completely, stabilized at the charged value for a few seconds and then discharged completely.

Amplification Stage

The manufacturer rates the capacitor at maximum 10V operating voltage. To observe the degradation due to electrical charge/discharge stress on the capacitor we stress the capacitors are different voltage levels specifically 12V and 10V.

To generate these different voltage levels from the function generator for a same square wave input we have developed a specific hardware as shown in Figure 46. Opamp 714 IC's are used in the inverting amplification mode with varying gains to obtain the required square wave voltages.

Load Resistor

To discharge the capacitor completely before the next charging cycle, a resistive load was connected. The load selected is calculated such that the capacitor is completely discharged before the next charge cycle at 100 mHz and the load should be able to sink sufficient

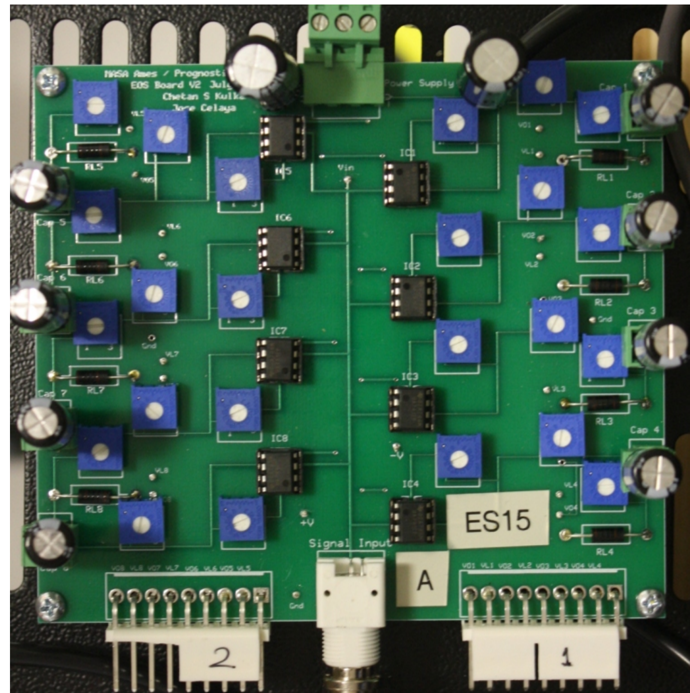

Figure 46: Custom Module PCB developed for EOS Experiment

amount of current to dissipate enough power. From these calculation a 1W 100Ω resistor was selected as a load.

Measurements

Due to the charging/ discharging cycle the internal temperature of the capacitor increases. To monitor the rise in the temperature, a temperature sensor was connected to the bare aluminum part on the top of the can. Along with this measurement we also monitored the ambient room temperature in which the experiment was conducted. The schematic shown in Figure 45 shows the measurements made on each capacitor. Figure 47 shows the current EOS experimental setup.

Impedance measurement

The SP-150 Biologic SAS impedance measuring instrument uses Electrochemical Impedance spectroscopy (EIS), and finds applications in corrosion, battery, fuel cell development, sensors, and physical electrochemistry. Impedance measurements can be made in a poten-

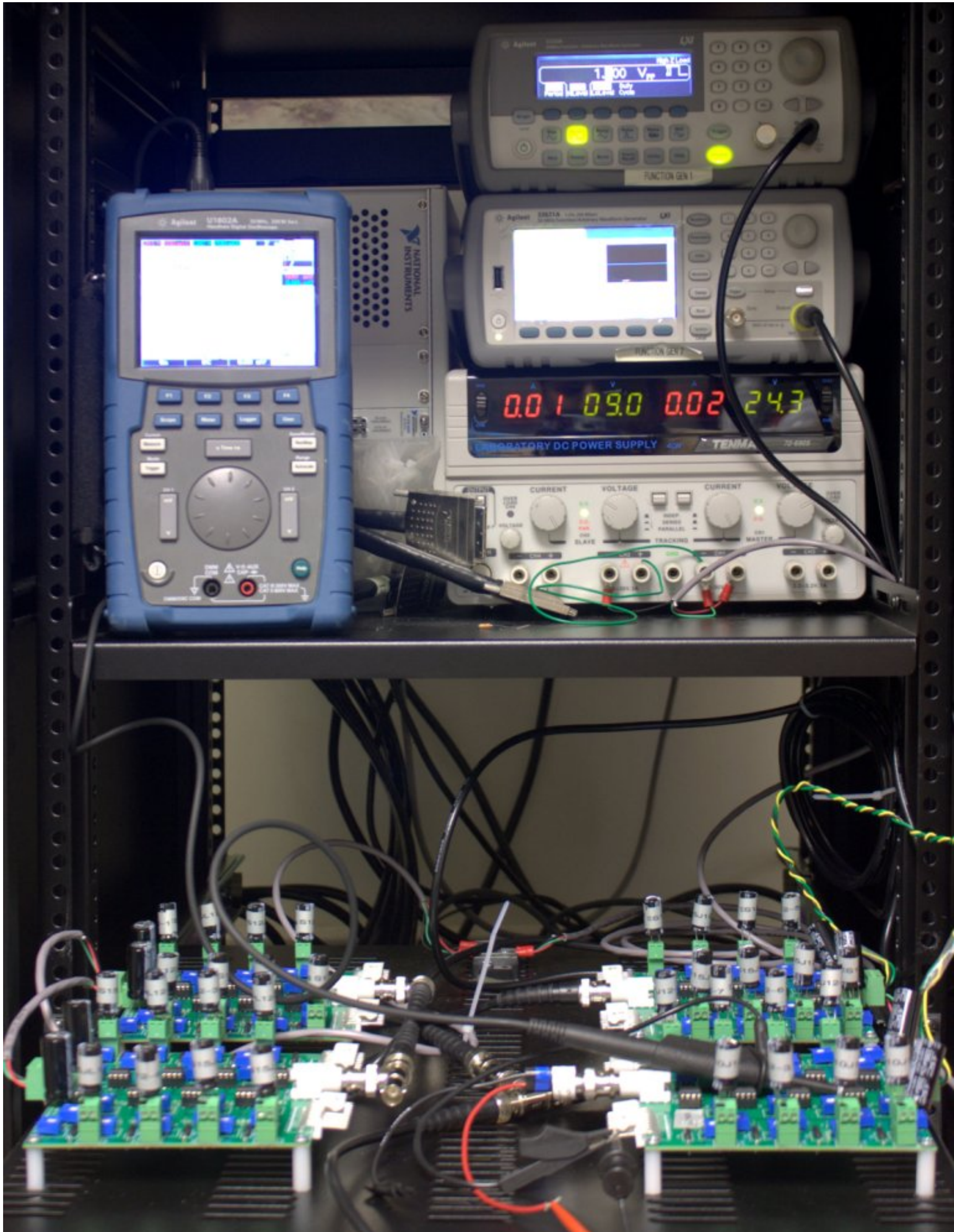

Figure 47: EOS experimental setup.

tiostatic mode (PEIS) or in a galvanostatic mode (GEIS). The PEIS mode is used for characterizing all the capacitors under test.

An ideal capacitor has complex impedance $Z_I = 1/sC_I$ where C_I is the ideal capacitance value. The complex impedance of model $\mathcal{M}_1$ is given by

$$Z = R_E + \frac{1}{sC_R} \tag{30}$$

where

R_E : the equivalent series resistance (ESR),

C_R : real capacitance (C).

It should be noted that the lumped-parameter model used to estimate ESR and capacitance, is not the model to be used in the prognostics algorithm; it only allows us to estimate parameters which provide indications of the degradation process through time. PEIS mode experiments perform impedance measurements by adding a small sinusoidal voltage to a DC potential that can be set to a fixed value, or relative to the cell equilibrium potential. The equation of the working electrode versus time is:

$$E_{WE}(t) = E_{WE} + V_a sin(2\pi f t), \tag{31}$$

where V_a is the applied potential amplitude and f the frequency.

Experiment I - 12V EOS

For this experiment six capacitors of 2200μF capacitance, with a maximum rated voltage of $10V$, maximum current rating of $1A$ and maximum operating temperature of $85°C$ were used for the study. The ESR and capacitance values were estimated from the capacitor impedance frequency response measured using the EIS instrument. Using the lumped parameter model, $\mathcal{M}_1$ the ESR and capacitance (C) values given by Eqns. (25) and (26) in Chapter V, were estimated at each measurement. The average pristine condition ESR value was measured to be 0.121 Ω and average capacitance of 2029 μF for the set of capacitors under test. The

ambient temperature for the experiment was controlled and kept at $25°C$. During each measurement the voltage source was shut down, the capacitors were discharged completely, and then the characterization procedure was carried out. Figure 47 shows the experimental setup for the 12V EOS experiment.

Electrochemical impedance spectroscopy measurements are available to observe electrical performance of the capacitor. Figure 48 shows Nyquist plots of the impedance measurements for capacitor #1 at pristine condition, and after accelerated electrical overstress aging at intervals of 71, 161 and 194 hours. The degradation can be observed as the Nyquist plot shifts to the right as a function of aging time due to increase in R_E. These measurements are then used to estimate the parameters of the impedance model $\mathcal{M}_1$ from Eqn. (30). The parameter estimation for computing the values of capacitance and ESR are performed using the EIS instrument software (EC lab). This is basically and optimization problem using an aggregate of mean squared error as an objective function. The error is aggregated at different frequencies for which measurements are available. The optimization is set up to minimize the objective function by finding optimal values for ${C_R}^*$ and ${R_E}^*$. This parameter estimation is performed every time an EIS measurement is taken resulting on values of C_R and R_E at different points in time through the aging of the components.

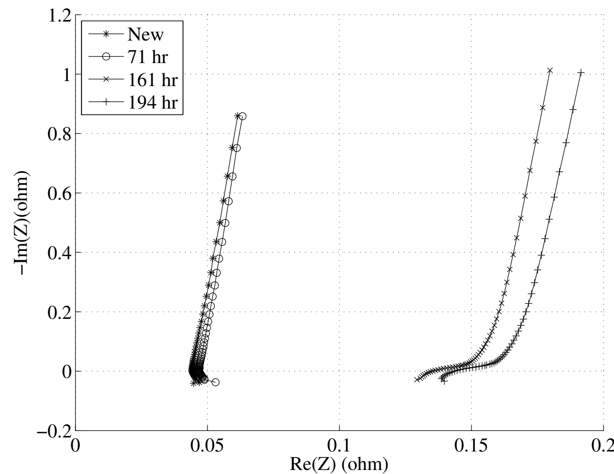

Figure 48: Electro-impedance measurements at different aging times.

Figure 49 shows increase in the ESR value for all the six capacitors under test over the period of time. Similarly, Figure 50 shows the decrease in the value of the capacitance as

the capacitor degrades over the aging period. From the plots in Figure 49 we observe that for the time for which the experiments were conducted the average ESR value increased by $54\% - 55\%$ while over the same period of time, the average capacitance decreased by more than 20% (threshold mark for a healthy capacitor). We used the collected data from the experiments to build dynamic degradation models of capacitors.

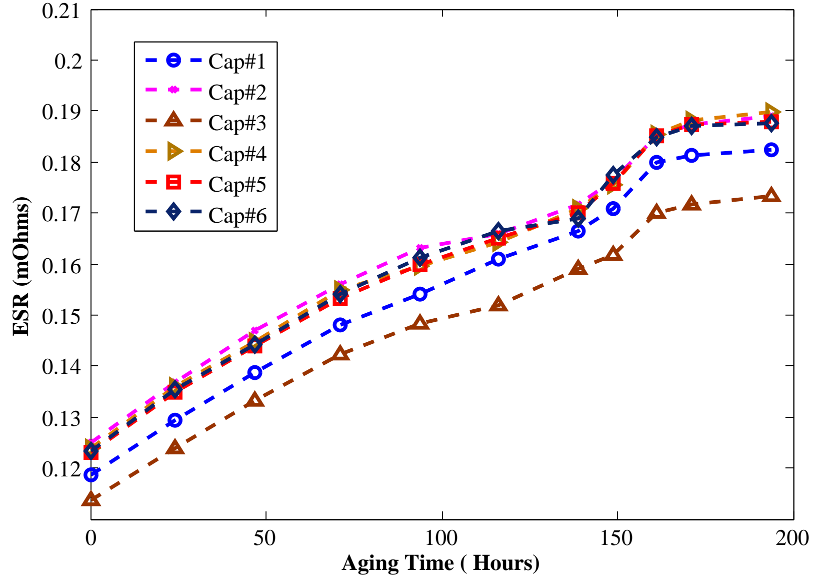

Figure 49: Degradation of capacitor performance, ESR increase as a function of aging time.

Prognostics Problem Formulation

In prognostics studies, it is important know when the performance of the device or system is going to lie outside an acceptable region of operation. When the capacitor parameters exceed specified thresholds, we consider the degrading device or system to have failed. For the device/system to be within the bounds of acceptable performance, we express a set of constraints, c_n, $\mathcal{C} = \{C_i\}_{i=1}^{c_n}$, where C_i is a function

$$C_i : \mathbb{R}^{n_x} \times \mathbb{R}^{n_\theta} \to \mathbb{B}$$

that maps a given point in the joint state-parameter space,$(x(t), \theta(t))$, to the Boolean domain $\mathbb{B} = [0, 1]$, where $C_i(x(t), \theta(t)) \triangleq 1$ indicates the constraint is satisfied or 0 (failed)

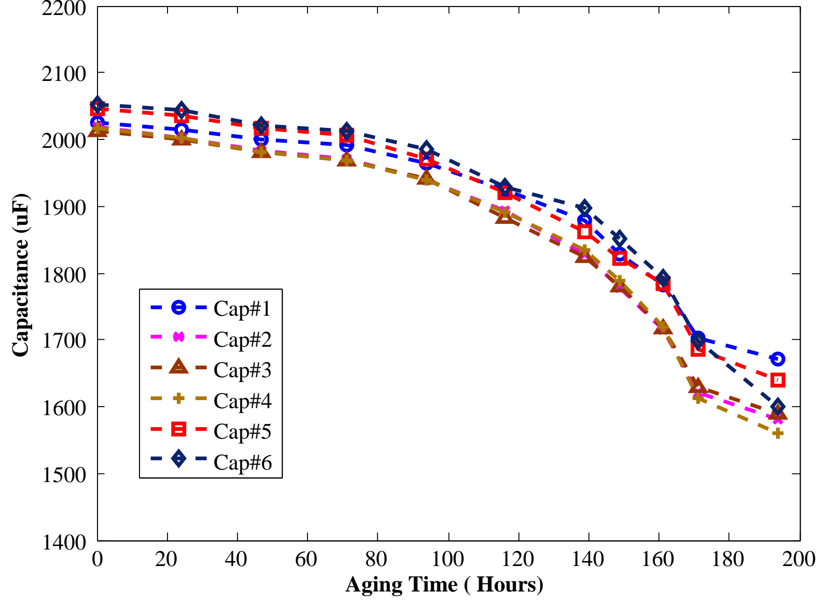

Figure 50: Degradation of capacitor performance, capacitance loss as a function of aging time.

if the constrained is not satisfied. Each individual constraint can be combined to form a single constraint output threshold function T_{EOL}, where

$$T_{EOL} : \mathbb{R}^{n_x} \times \mathbb{R}^{n_\theta} \rightarrow \mathbb{B}$$

which is defined as :

$$T_{EOL}(x(t), \theta(t)) = \begin{cases} 1, & 0 \in \{C_i(x(t), \theta(t))\}_{i=1}^{c} \\ 0, & \text{otherwise.} \end{cases} \tag{32}$$

Indicating the healthy state of a device/system T_{EOL} evaluates to 1, if any of the constraints are violated. At some instance in the aging cycle at time, t_p , the system is at $(x(t_P); \theta(t_P))$ and we are interested in predicting the time point t at which this state will evolve to $(x(t); \theta(t))$ such that $T_{EOL}(x(t), \theta(t)) = 1$. Using T_{EOL}, we formally define end of life (EOL) of a device/system as:

$$EOL_{t_p} \triangleq \inf \{t \in \mathbb{R} : t \geq t_p \wedge T_{EOL}(x(t), \theta(t)) = 1\}, \tag{33}$$

i.e., EOL is the earliest instance in the aging cycle at which at which T_{EOL} is valid for a healthy system. RUL is expressed using EOL as

$$RUL(t_p) \triangleq EOL(t_p) - t_p.$$

Empirical Model for Capacitance Degradation

This section discusses a procedure we have employed for deriving an empirical capacitor degradation model. The model is derived from the empirical data (Figure 50) collected from the experiments described above.

Degradation Model

The percentage loss in capacitance is used as a precursor of failure variable and it is used to build a model of the degradation process. This model relates aging time to the percentage loss in capacitance. Let C_l be the percentage loss of capacitance due to degradation as shown by Figure 50. The following equation represents an empirical *degradation model* $\mathcal{E}_1$ of the change in capacitor parameter over time. This empirical model represents an approximation of by model $\mathcal{M}_1$.

$$\mathcal{E}_1 : C_l(t) = e^{\alpha t} + \beta, \tag{34}$$

where α and β are degradation model parameters that will be estimated from the experimental data gathered from the accelerated aging experiments.

We employ the leave one out method to verify the derived model. Data from five of the six capacitors are used to estimate the model parameters, alpha and beta, and data from the sixth capacitor is used to validate the model. A nonlinear least-squares regression algorithm is used to estimate the model parameters. Table 7 presents definition of the test cases and the parameter estimation results. The mean estimate and 95% confidence interval was derived for parameters, α and β. In addition, the error variance is included as a way to assess the quality of model fit.

Validation test	Test capacitor	Training capacitor	α (95% CI)	β (95% CI)	σ_v^2
T_2	#2	#1, #3–#6	**0.0162** (0.0160, 0.0164)	**-0.8398** (-1.1373, -0.5423)	1.8778
T_3	#3	#1, #2, #4–#6	**0.0162** (0.0160, 0.0164)	**-0.8287** (-1.1211, -0.5363)	1.9654
T_4	#4	#1–#3, #5, #6	**0.0161** (0.0159, 0.0162)	**-0.8217** (-1.1125, -0.5308)	1.8860
T_5	#5	#1–#4, #6	**0.0162** (0.0161, 0.0164)	**-0.7847** (-1.1134, -0.4560)	2.1041
T_6	#6	#1–#5	**0.0169** (0.0167, 0.0170)	**-1.0049** (-1.2646, -0.7453)	2.9812

Table 7: Degradation model parameter estimation results.

Figure 51 plots the estimation results for test case T_6. The experimental data are presented together with results from the exponential fit function. It can be observed from the residuals that the estimation error increases with time. This is expected since the last data point measured for all the capacitors fall slightly off the exponential model. This seems to be the case that later in the aging cycle, additional degradation phenomena kick in, and a simple exponential (i.e., first-order) model may not be sufficient to represent the overall degradation process.

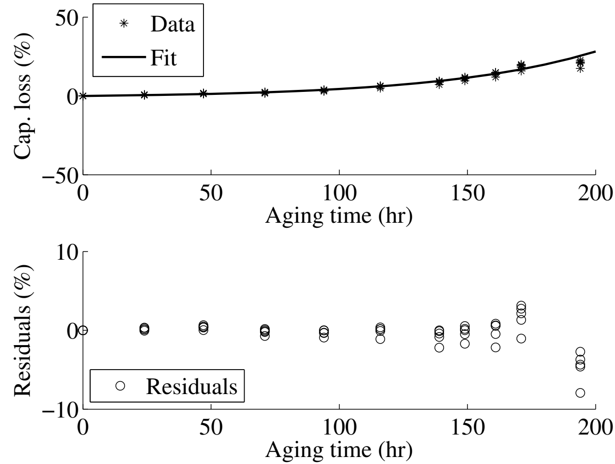

Figure 51: Estimation results for the empirical degradation model.

State-Space Model for Degradation Estimation

The estimated degradation model is used as part of a Bayesian tracking framework and implemented using a Kalman filter approach. This requires that the dynamic degradation model be represented as a discrete-time equation, with the state variable, $Capacitance(C)$, the degradation state at time t_k being represented as a function of the state at t_{k-1}. The exponential behavior described in the model is represented as a first order differential equation which can represent the time evolution of capacitance value, $C_l(t)$. Then, the model is discretized in time in order to obtain a discrete-time state-space model $\mathcal{E}_2$.

From equation (34) we have that $C_l(t) = e^{\alpha t} + \beta$ [1], taking the first derivative with respect to time and substituting $e^{\alpha t} = C_l(t) - \beta$ from Eq. (34) we have

$$\dot{C}_l = \frac{dC_l(t)}{dt} = \alpha C_l(t) - \alpha\beta. \tag{35}$$

Making the finite difference approximation for $\dot{C}_l$ with time interval Δt we have

$$\frac{C_l(t) - C_l(t-\Delta t)}{\Delta t} = \alpha C_l(t-\Delta t) - \alpha\beta, \text{ and}$$

$$C_l(t) = (1 + \alpha\Delta_t)C_l(t-\Delta t) - \alpha\beta\Delta_t.$$

Letting $t_k = t$ and $t_{k-1} = t - \Delta t$ we get the state-space model

$$\mathcal{E}_2 : C_l(t_k) = (1 + \alpha\Delta_k)C_l(t_{k-1}) - \alpha\beta\Delta_k. \tag{36}$$

This model can be used in a Bayesian tracking framework in order to continuously estimate the value of the loss in capacitance through time as measurement become available.

Prediction of Remaining Useful Life Results

State estimation and RUL prediction results are discussed for test case $T6$. Figure 52 shows the result of the filter tracking the complete degradation signal. The residuals show

[1] The α and β variables used in model $\mathcal{E}_2$ are not used further in other references

an increased error with aging. This is to be expected given the results observed from the model estimation process.

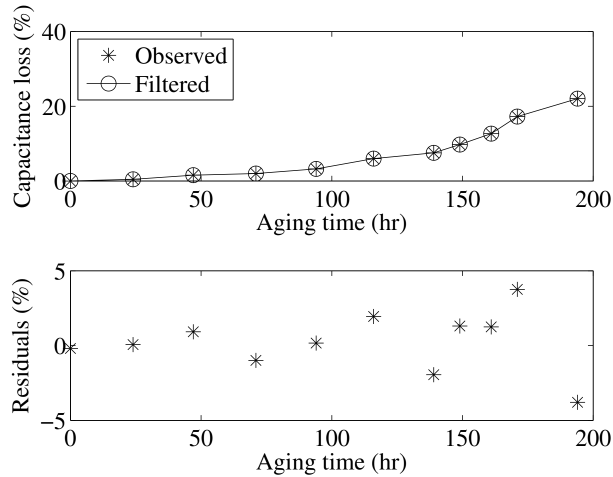

Figure 52: Tracking results for the Kalman filter implementation applied to test capacitor (capacitor #6).

Figure 53 presents the capacitance loss estimation and EOL prediction as the aging progresses. Predictions are made after each point in which measurements are available. It can be observed that the predictions become better as the prediction is made closer to the actual EOL. This is possible because the estimation process has more information to update the estimates as it nears EOL. Since EOL won't be known before hand, as some of the devices have not actually failed, CBM decisions are made based on the 20% capacitance decrease threshold. End of life (EOL) is defined as the time at which the forecasted percentage capacity loss trajectory crosses the EOL threshold. Therefore, RUL is EOL minus prediction hours.

Validation Tests

As discussed earlier we employ a leave one out method to verify the derived model. As summarized in Table 7, one capacitor is left out and parameter estimation is based on the data of remaining 5 capacitors. The derived model is then verified against the left out capacitor, this is carried out for all the remaining capacitors. An Alpha-Lambda(α-λ)[2] prognostics performance metric is presented in Figure 54 for validation test T_6. The blue line represents ground truth and the shaded region corresponds to a 30% ($\alpha = 0.3$) error bound in the

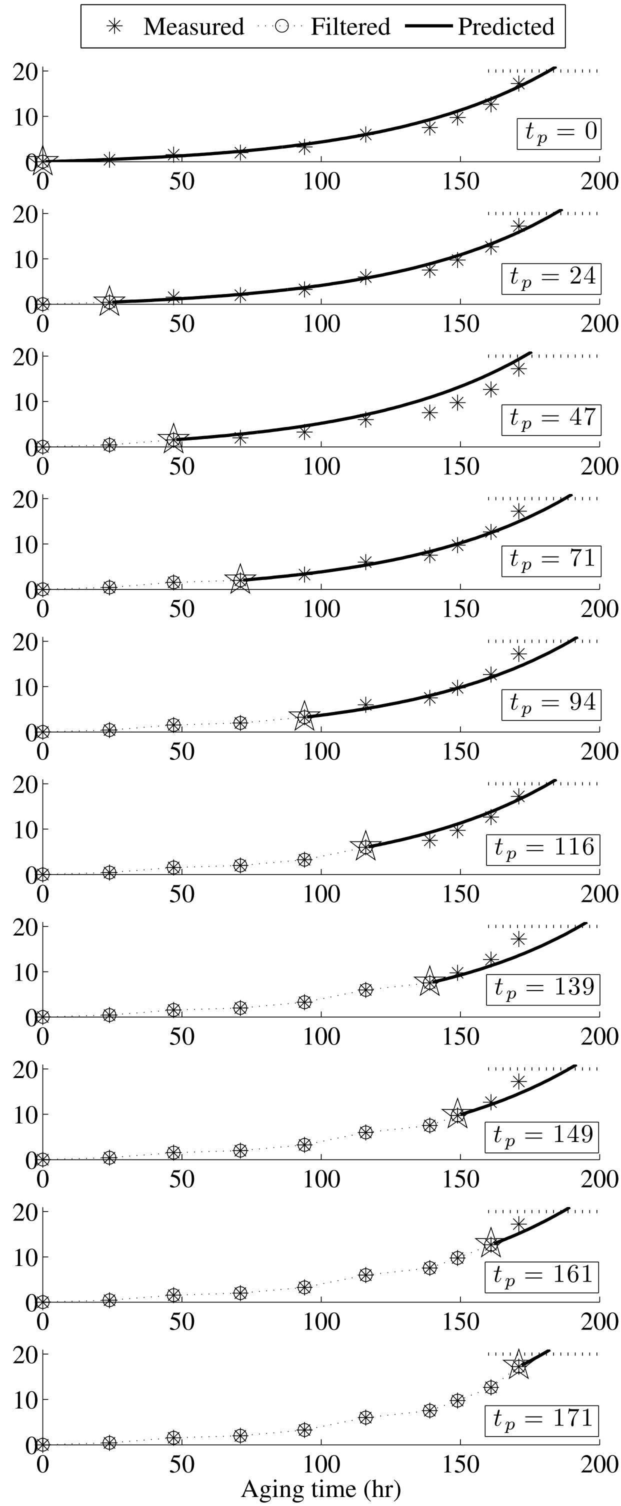

Figure 53: T_6: Health state estimation and forecasting of capacitance loss (%) at different times t_p during the aging time; $t_p = [0, 24, 47, 71, 94, 116, 139, 149, 161, 171]$.

RUL prediction. This metric specifies that the prediction is within the error bound halfway between first prediction and EOL ($\lambda = 0.5$).

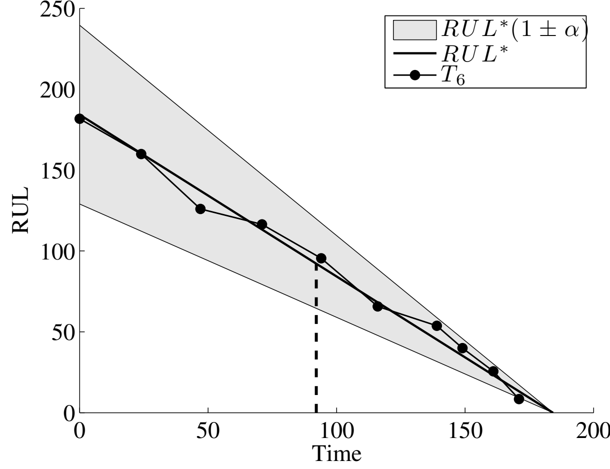

Figure 54: Performance based on Alpha-Lambda performance metric.

We use the relative accuracy measure, defined in Eqn (37) as a metric for validating the state space degradation model of the capacitance value.

$$RA = 100\left(1 - \frac{|RUL^* - RUL^{'}|}{RUL^*}\right) \tag{37}$$

The relative accuracy, computed as a percentage, represents a comparison against ground truth, as derived from the experimental results. RUL^* is the ground truth from the experimental data while $RUL^{'}$ is the predicted RUL. Table 8 lists the RA values for all capacitors at different time points of the aging process. The last column of the Table 8 represents the median RA of all the test cases for a particular prediction time.

It is observed that the RA values decrease considerably at aging time point $t_p = 171$ hours. This is consistent with previous observations indicating that the algorithm with a fixed-parameter model is not able to cope with the sudden drop in the capacitance value during that time interval on. This is a limitation that could be overcome by modeling additional phenomena that cause the enhanced degradation or more sophisticated online estimation degradation model.

[2]The α in the Alpha-Lambda performance metric is different from the α used in model $\mathcal{E}_2$

Table 8: Summary of validation results based on RA for model $\mathcal{E}_2$

Aging Time	C2	C3	C4	C5	C6	$\overline{RA}_a$
24	94.8	95.5	91.9	96.9	99.7	95.5
47	97.4	99.3	96.4	96.7	91.7	96.7
71	87.5	91.9	84.5	94.1	97.1	91.9
94	85.6	90	78.9	94.8	94.2	90
116	86	99.1	76.5	98	96.2	96.2
139	77.8	95.8	53.1	96.7	81.1	81.1
149	82.1	98.4	46.9	94.8	86.6	86.6
161	77.2	87.3	16.6	87.5	89.8	87.3
171	26.6	26.4	N/A	34.8	63.7	30.7
$\overline{RA}_b$	79.4	87.1	68.1	88.3	88.9	

$\overline{RA}_a$ is the mean relative accuracy of all capacitors at each prediction time (t_p)
$\overline{RA}_b$ is the mean relative accuracy of each capacitor at all prediction times

Physics Based Modeling Framework using Unscented Kalman Filter

A model-based prognostics methodology based on Unscented Kalman Filter is presented. The prognostic methodology implemented in this work consists two parts. The first part consists of a estimation step where the state based on the current conditions of the device and inputs. In second part the algorithm is able to predict remaining useful life of the capacitor till the health threshold of the device is crossed. In this section we will discuss the dynamic models for both capacitance and ESR degradation models. We first discuss the theory of UKF and then each of the degradation models with results will be summarized.

Unscented Kalman Filter

In model-based prognostics, degradation estimation reduces to joint state-parameter estimation i.e., computation of $p(x_t, \theta_t|y_{0:t})$. A simple solution to this is to implement a filter, where the unknown parameters augment the state vector [21]. Treating parameters as states in most cases makes the system nonlinear, even if it is a linear system. Most of the degradation models for prognostics are nonlinear since as discussed earlier degradation in a device is due to several underlying phenomenons which are present during the aging cycle. Since some of these are linear while some are non-linear in nature the overall degradation model becomes non-linear.

Estimation in nonlinear system is very important because many practical systems involve nonlinearities in their operation through one form or another. Estimation of the state accurately of such non-linear system is very important to diagnostics and implementing it further to prognostic applications is extremely difficult. The Extended Kalman Filter (EKF) which applies the KF to nonlinear system by linearizing all nonlinear models, has become a most widely used method for estimation of nonlinear system. Although the EKF maintains its computationally efficient recursive update form of the KF for non-linear systems, it suffers a number of serious limitations [134, 135].

1. It is only reliable if the error propagation to the future states can be approximated by a linear function.
2. Linearization can be applied only if the Jacobian matrix exists i.e, cannot be implemented if the system has discontinuities.
3. Calculating Jacobian matrices can be a very difficult and error-prone process.

The Unscented Kalman Filter (UKF) was proposed by [134,135] to overcome these problems in non-linear systems. The UKF, instead of approximating the nonlinearity, approximates the state distribution [134, 135]. This procedure maintains the nonlinear functions exactly, eliminating the need to calculate Jacobians, and thereby providing an easier implementation framework. In this section we will discuss the framework of UKF which has been implemented for prognostics in this work. A nonlinear system, described by the difference equation and the observation model with additive noise is given as :

$$\begin{aligned} \mathbf{x}_k &= \mathbf{F}[\mathbf{x}_{k-1}, u_{k-1}, k] + \mathbf{w}_{k-1} \\ \mathbf{z}_k &= \mathbf{H}[\mathbf{x}_k, k] + \mathbf{v}_k \end{aligned} \tag{38}$$

where $\mathbf{x}(k)$ is the n-dimensional state of the system at time step k, $u(k)$ is the input vector, $\mathbf{w}(k)$ is the process noise, Q, $\mathbf{z}(k)$ is the observation vector and $\mathbf{v}_k$ is the measurement noise, R.

The Unscented transform (UT), takes a random variable $\mathbf{x}$, with mean $\bar{\mathbf{x}}$ and covariance $\mathbf{P}_{xx}$, which is related to a second random variable $\mathbf{y}$ by a nonlinear function $\mathbf{y} = \mathbf{f}(\mathbf{x})$. A

small set of points (*sigma points*) with mean $\bar{\mathbf{y}}$ and covariance $\mathbf{P}_{xx}$ are selected [134], which are deterministically selected and weighted to exhibit properties to match the mean and covariance of the original distribution. A non-linear transformation is applied to each point to get the transformed points, statistics of the transformed points are then calculated to estimate the mean and covariance of the transformed points. The sigma point weights do not directly represent probabilities of the sigma points, and hence do not have to lie in the interval [0, 1]. The weights $\mathbf{w}_i$ can be positive or negative, but need to obey the following condition to provide an unbiased estimate.

$$\sum_i \mathbf{w}_i = 1 \tag{39}$$

Each sigma point is instantiated through the function (f) to obtain new set of sigma points $\mathcal{Y}$.

$$\mathcal{Y}_i = f(\mathcal{X}_i) \tag{40}$$

The mean of the transformed points is given by:

$$\bar{\mathbf{y}} = \sum_i w_i \mathcal{Y}_i \tag{41}$$

The covariance of the transformed points is given by:

$$\mathbf{P}_{yy} = \sum_i w_i (x_o - \mu_0)(x_0 - \mu_0)^T \tag{42}$$

The basic idea of the unscented transform is that it is easier to approximate a probability distribution x than it is to approximate an arbitrary nonlinear function f or transformation [135]. This basic principle is implemented in the unscented Kalman filter where the unscented transform is exploited for nonlinear state estimation [134, 135]. At each step, the unscented transform is applied to the state estimate and is used for a single step prediction. There are several methods which exists for selecting the sigma points out of which we implement the symmetric unscented transform for the prognosis problem [135, 136].

Symmetric Unscented Transform

In the symmetric unscented transform, $2n_x + 1$ sigma points are selected symmetrically about the mean as follows [135]:

$$
\begin{aligned}
\mathcal{X}_0 &= \bar{\mathbf{x}} \\
w_0 &= \frac{k}{n+k} \\
\mathcal{X}_i &= \bar{\mathbf{x}} + \left(\sqrt{(n+k)P_{xx}}\right)_i, i = 1, .., 2n_x \\
w_i &= \frac{k}{2(n+k)}, i = 1, ..2n_x \\
\mathcal{X}_{i+n} &= \bar{\mathbf{x}} - \left(\sqrt{(n+k)P_{xx}}\right)_i, i = n_x + 1, .., 2n_x \\
w_{i+n} &= \frac{k}{2(n+k)}, i = n_x + 1, .., 2n_x
\end{aligned}
\tag{43}
$$

where $\sqrt{((n+k)\mathbf{P}_{xx})_i}$ refers to the ith column of the matrix square root of $(n+k)\mathbf{P}_{xx}$, computed using the Cholesky decomposition since it is numerically efficient and stable. Parameter κ is used to tune the higher moments of distribution and suggested to have a smaller values as possible to bring the sigma points closer together. If x is assumed Gaussian, then selecting $k = 3 - n$ is recommended [134].

Update Step

The UKF assumes a generalized nonlinear form of the state and output equations, with additive Gaussian noise, and follows the same basic form as the Kalman and extended Kalman filters, modified to use the sigma points. First, n_s sigma points $\hat{\mathcal{X}}_{k-1|k-1}$ are derived from the current mean $\hat{\mathbf{x}}_{k-1|k-1}$ and covariance estimates $P_{k-1|k-1}$ using the sigma point selection algorithm of choice. The prediction step is:

$$\hat{\mathcal{X}}^i_{k|k-1} = f(\hat{\mathcal{X}}^i_{k-1|k-1}, u_{k-1}), i = 1, ..., n_s$$
$$\hat{\mathcal{Y}}^i_{k|k-1} = h(\hat{\mathcal{X}}^i_{k|k-1}), i = 1, ..., n_s$$
$$\hat{\mathbf{x}}_{k|k-1} = \sum_i^{n_s} w^i \mathcal{X}^i_{k|k-1} \tag{44}$$
$$\hat{\mathbf{y}}_{k|k-1} = \sum_i^{n_s} w^i \mathcal{Y}^i_{k|k-1},$$

$$P_{k|k-1} = Q + \sum_i^{n_s} w^i (\mathcal{X}^i_{k|k-1} - \hat{\mathbf{x}}_{k|k-1})(\mathcal{X}^i_{k|k-1} - \hat{\mathbf{x}}_{k|k-1})^T, \tag{45}$$

where Q is the process noise covariance matrix. The update step is :

$$\mathbf{P}_{yy} = R + \sum_i^{n_s} w^i (\mathcal{Y}^i_{k|k-1} - \hat{\mathbf{y}}_{k|k-1})(\mathcal{Y}^i_{k|k-1} - \hat{\mathbf{y}}_k|k-1)^T \tag{46}$$

$$\mathbf{P}_{xy} = \sum_i^{n_s} w^i (\mathcal{X}^i_{k|k-1} - \hat{\mathbf{x}}_{k|k-1})(\mathcal{Y}^i_{k|k-1} - \hat{\mathbf{y}}_{k|k-1})^{-1} \tag{47}$$

$$K_k = \mathbf{P}_{xy}\mathbf{P}^T_{yy}$$
$$\hat{\mathbf{x}}_{k|k} = \hat{\mathbf{x}}_{k|k-1} + K_k(\mathbf{y}_k - \hat{\mathbf{y}}_{k|k-1}) \tag{48}$$
$$\mathbf{P}_{k|k} = \mathbf{P}_{k|k-1} - K_k \mathbf{P}_{yy} K^T_k,$$

where R is the sensor noise covariance matrix.

Prediction Step

The RUL prediction is initiated at any given aging time t_p, using the current joint state-parameter estimate, $p(x_{tp}, \theta_{tp}|y_{0:t_p})$, which is the most updated information of the system at time t_p. The goal here is to compute $p(EOL_{tp}|y_{0:t_p})$ and $p(RUL_{tp}|y_{0:t_p})$. In contrast, to the UKF update step here, we apply the transform to the state parameter distribution at given single aging time point t_p , and use this for multi-step predictions to EOL. The

representation of $p(x_{tp}, \theta_{tp}|y_{0:t_p})$ distribution is represented by a finite set of weighted samples since we implement an UKF filter. An unscented transform is used to deterministically select a small number of samples to reduce the computations [137].

Given the finite set of N samples, $\left\{(x^i_{t_p}, \theta^i_{t_p})w^i_{t_p}\right\}_{i=1}^{N}$ each sample i is propagated out to EOL and use the original sample weight for the weight of that EOL prediction. Each sample is simulated forward to EOL to obtain the complete EOL distribution. The pseudocode for the prediction procedure is same as in [138] and given by Algorithm 1. Each sample, i from the distribution is propagated forward until $T_{EOL}(x_i^{t_p}, \theta_i^{t_p})$ evaluates to 1; at this time in the aging cycle the EOL of the device/system is considered to have reached. In this work we assume future inputs, $\hat{u_k}$ are known, since we have the collected experimental data.

Algorithm 1 EOL Prediction

INPUTS : $\left\{(x^i_{t_p}, \theta^i_{t_p})w^i_{t_p}\right\}_{i=1}^{N}$
OUTPUTS: $\left\{EOL^i_{t_p}, w^i_{t_p}\right\}_{i=1}^{N}$
for $i = 1 \rightarrow N$ **do**
  $t \leftarrow t_p$
  $x^i_t \leftarrow x^i_{t_p}$
  $\theta^i_t \leftarrow \theta^i_{t_p}$
  while $T_{EOL}(x^i_t, \theta^i_t) = 0$ **do**
    Predict $\hat{u}_t$
    $\theta^i_{t+1} \sim p(\theta_{t+1}|\theta^i_t)$
    $x^i_{t+1} \sim p(x_{t+1}|x^i_t, \theta^i_t, \hat{u}_t)$
    $t \leftarrow t + 1$
    $x^i_t \leftarrow x^i_{t+1}$
    $\theta^i_k \leftarrow \theta^i_{t+1}$
  $EOL^i_{tp} \leftarrow t$

Capacitance Degradation Dynamic Model

From Eqn.(25) and other derivations in Chapter V, we have the time dependent degradation models, $\mathcal{D}_1$ for capacitance (C) given by :

$$\mathcal{D}_1 : C(t) = \left(\frac{2\ \epsilon_R\ \epsilon_0\ c_b}{d_C}\right)\left(\frac{V_{e0} - V_e(t)}{j_{eo}\ t\ w_e}\right),$$

The degradation in capacitance is directly proportional to the damage variables V and c_b, respectively. As discussed earlier, increase in the core temperature evaporates the electrolyte thus decreasing the electrolyte volume leading to a gradual decrease in the capacitance. The resultant decrease in the capacitance can be computed using Eq. (25). In addition to the decrease in electrolyte volume, the oxide layer also degrades causing a breakdown in the oxide layer, which further leads to degradation in capacitance (C) and ESR.

The dynamic capacitor degradation model can be enhanced to include the effects of the oxide layer degradation, which is given by :

$$C_k = \left(\frac{2\epsilon_R \epsilon_0 c_b}{d_C}\right)\left(\frac{V_{e(k)}}{d_C}\right) \tag{49}$$

From the electrolyte evaporation discussion and Eq. (7), the first order discrete approximation for change in electrolyte volume can be expressed as:

$$\begin{aligned}
\frac{dV_e}{dt} &= -(w_e A_s j_{eo}),\\
V_{e(k+1)} &= V_{e(k)} + \frac{dV_e}{dt}\Delta t,\\
V_{e(k+1)} &= V_{e(k)} - (w_e A_s j_{eo})\Delta t.
\end{aligned} \tag{50}$$

From Eq. (49) we have,

$$\begin{aligned}
V_{e(k)} &= \frac{C_k}{2\epsilon_R \epsilon_0} d_C^2,\\
V_{e(k)} &= (C_k)\eta.
\end{aligned} \tag{51}$$

where:

$$\eta = \frac{d_C^2}{2\epsilon_R \epsilon_0 \ c_b}$$

We can express Eq. (51) as :

$$\begin{aligned}
C_{k+1}\eta &= C_k\eta + \frac{dV_e}{dt}\Delta t,\\
C_{k+1}\eta &= C_k\eta - (w_e A_s j_{eo})\Delta t, \text{ hence}\\
C_{k+1} &= C_k - \frac{(w_e A_s j_{eo})}{\eta}\Delta t.
\end{aligned} \tag{52}$$

In model, $\mathcal{D}_1$ the parameters which are temperature dependent are the rate of evaporation j_{eo} and oxide breakdown factor, c_b. Electrolyte evaporation and oxide breakdown under electrical stress is described by a thermal and oxide breakdown model in section V. Rate of evaporation, j_{eo} and resistance dependence oxide breakdown factor, c_b are the two parameters in the model which are estimated online based on the state variable value, C.

Though the applied stress conditions are similar, there may be variation in each capacitor and hence each capacitor may have slightly different evaporation rate. Hence the evaporation rate parameter, j_{eo} is estimated based on the first two reading in the experimental data for each capacitors when predictions are done. The exact formulation of the parameter is incorporated as modeling error/process noise in form of a stochastic process. Since there could be a variation in the temperature the corresponding evaporation rate value estimated had a mean and variance of the variation values.

While the capacitance dependence breakdown factor, c_b is a state parameter and estimated at each time step and the updated value is used in estimating the state. As discussed in Chapter V, this factor is related to the electrolyte evaporation and is expressed in the state space form as:

$$\begin{aligned} c_b &= -e^{\xi}, \\ &\text{where:} \\ \xi &= (V_{e0} - V_{e(t)}), \\ c_{b(k+1)} - c_{b(k)} &= -\xi e^{\xi}. \end{aligned} \tag{53}$$

The complete discrete time dynamic model for capacitance degradation can be summarized as:

$$\begin{aligned} \mathcal{D}_4 : C_{k+1} &= C_k - \frac{(2\epsilon_R \epsilon_0 w_e A_s j_{eo} c_b)}{d_C^2} \Delta t, \\ c_{b(k+1)} &= c_{b(k)} - \xi e^{\xi}. \end{aligned} \tag{54}$$

The model $\mathcal{D}_4$, is implemented in a Bayesian estimation framework. In this work, we implement the dynamic tracking function as an Unscented Kalman Filter (UKF) since the degradation in capacitance (state) due to decrease in electrolyte is considered to be a

dynamic non-linear model since evaporation rate (j_{eo}) and capacitance oxide breakdown factor (c_b) are estimated online based on the state values.

The following steps are implemented for model $\mathcal{D}_4$:

1. State Estimation: The current measured capacitance (C) is defined as the state variable to be estimated respectively for each of the model and the degradation model is expressed as a discrete time dynamic model in order to estimate current capacitance (C) due to decrease in electrolyte volume at the next available measurement. Direct measurements of the capacitance (C) is assumed for the filter.

2. Health state forecasting: It is necessary to forecast the state variable once there are no more measurements available at the end of step 1. This is done by evaluating the degradation model through time using the state estimate at time t_p as initial value.

3. Remaining useful life computation: RUL is computed as the time between time of prediction t_p and the time at which the forecasted state crosses a certain failure threshold value or EOL.

These steps are repeated for different aging time (t_p) through the life of the capacitor device under test.

There is an uncertainty both in the estimation step as well as in the prediction step. To include uncertainty, the effective way is to have probability distribution to be estimated since (i) the system state may not be directly measured and, (ii) addition to this is the sensor noise, (iii) the initial state of the system exactly exactly known, (iv) there could be uncertainty due to the derived system model, and (v) the process noise. In addition to this even if the system state is known, uncertainty is introduced in the prediction steps as, (i) the derived model may not be exactly depicting the degradation process, (ii) exact value of the process noise not known, and (iii) exact trajectory of the future inputs for the state space may not be known. Due to these additional sources of uncertainty inherent to the prognostics algorithm, the uncertainty in the predicted EOL/RUL will nominally be larger than the true variability in EOL/RUL [138]. In this work we only consider the model noise and the noise variance as discussed earlier. But for the prediction step we present the

means for all the EOL/RUL predictions in our results since the focus of this work is more on deriving the physics-based degradation, implementing it in a Bayesian framework and for prognostics predictions. Next we discuss the implementation of the Bayesian framework methodology for prognostics [108,136,139] .

UKF for Capacitance State Estimation

The state variable $\mathbf{x}_k$ (Capacitance) at time t_k is defined as the current measured capacitance C_k. Since the system measurements are capacitance (C) as well, the output equation is given by $\mathbf{y}_k = H_k\ \mathbf{x}_k$, where H is the identity matrix. The following system structure is implemented for filtering and prediction using a Unscented Kalman Filter.

$$\begin{aligned} \mathbf{x}_k &= A_k \mathbf{x}_{k-1} + B_k u + v, \\ \mathbf{y}_k &= H_k \mathbf{x}_k + \mathbf{w}. \end{aligned} \tag{55}$$

where,

$$\begin{aligned} A &= 1, \\ B &= -\frac{(2\epsilon_R \epsilon_0 w_e A_s j_{eo} c_b)}{d_C^2} \Delta t, \\ H &= 1, \\ u &= j_{eo}, c_b. \end{aligned} \tag{56}$$

In this work and application of UKF, the time increment between measurements Δt is not constant since measurements were taken at nonuniform time intervals i.e., the capacitors were characterized at different time intervals. This implies that some of the parameters of the model in Eqn. (72) will change as time progresses. Furthermore, v and w are normal random variables with zero mean and Q and R variance respectively. The model noise (process noise) variance Q was estimated from the model regression residuals and was used for the model noise in the Kalman filter implementation. The measurement noise variance R, was computed from the direct measurements of the capacitance with the EIS equipment,

the observed variance is 4.99×10^{-7}. A detailed description of the algorithm implemented in this work can be found in [140] , a description of how the algorithm is used for forecasting can be found in [141] and an example of its usage for prognostics can be found in [108,136].

ESR Degradation Dynamic Model

From Eqn. (26) the dynamic ESR degradation model can be represented as :

$$
\begin{aligned}
ESR_k &= \frac{1}{2}\left(\rho_E\ d_C\ P_E\ e_b\right)\left(\frac{d_C}{V_{e(k)}}\right), \\
V_{e(k)} &= \frac{1}{ESR_k}\left(\frac{1}{2}\right)\left(\rho_E\ {d_C}^2\ P_E\ e_b\right), \\
V_{e(k)} &= \frac{1}{ESR_k}(\gamma).
\end{aligned} \tag{57}
$$

where:

$$\gamma = \frac{1}{2}\left(\rho_E\ {d_C}^2\ P_E e_b\right)$$

From Eqn. (50) and Eqn. (57) we have :

$$
\begin{aligned}
\frac{\gamma}{ESR_{k+1}} &= \frac{\gamma}{ESR_k} + \frac{dV_e}{dt}\Delta t, \\
\frac{\gamma}{ESR_{k+1}} &= \frac{\gamma}{ESR_k} - (w_e A_s j_{eo})\Delta t, \text{ hence} \\
\frac{1}{ESR_{k+1}} &= \frac{1}{ESR_k} - \frac{(w_e A_s j_{eo})}{\gamma}\Delta t.
\end{aligned} \tag{58}
$$

The complete discrete time dynamic model for ESR degradation can be summarized as :

$$
\begin{aligned}
\mathcal{D}_5 : \frac{1}{ESR_{k+1}} &= \frac{1}{ESR_k} - \frac{2 w_e A_s j_{eo}}{\rho_E\ P_E\ d_C^2\ e_b}\Delta t, \\
e_{b(k+1)} &= e_{b(k)} - \xi.
\end{aligned} \tag{59}
$$

In model $\mathcal{D}_5$ the rate of evaporation j_{eo} and the correlation factor, P_E related to electrolyte spacer porosity and average liquid pathway are the two time-varying parameters. Electrolyte evaporation and oxide breakdown under electrical stress is described by a thermal and oxide breakdown model in Chapter V. Rate of evaporation, j_{eo} and resistance

dependence oxide breakdown factor, e_b are the two parameters in the model which are estimated online based on the state variable value, ESR.

The following steps are implemented for model $\mathcal{D}_5$:

1. State Estimation: The current measured ESR is defined as the state variable to be estimated respectively for each of the model and the degradation model is expressed as a discrete time dynamic model in order to estimate current ESR due to decrease in electrolyte volume at the next available measurement. Direct measurements of the ESR is assumed for the filter.

2. Health state forecasting: It is necessary to forecast the state variable once there are no more measurements available at the end of step 1. This is done by evaluating the degradation model through time using the state estimate at time t_p as initial value.

3. Remaining useful life computation: RUL is computed as the time between time of prediction t_p and the time at which the forecasted state crosses a certain failure threshold value or EOL.

The uncertainty conditions for the model are same as discussed for the capacitance degradation model.

UKF for ESR State Estimation

The state variable x_k (ESR) at time t_k is defined as the current measured capacitance ESR_k. Since the system measurements are ESR measured values as well, the output equation is given by $y_k = P_k\ x_k$, where P is the identity matrix. The following system structure is implemented for filtering and prediction using a Unscented Kalman Filter.

$$\begin{aligned} \mathbf{x}_k &= A_k \mathbf{x}_{k-1} + B_k u + \mathbf{v}, \\ \mathbf{y}_k &= P_k \mathbf{x}_k + \mathbf{w}. \end{aligned} \tag{60}$$

where,

$$
\begin{aligned}
A &= 1, \\
B &= -\frac{2 w_e A_s j_{eo}}{\rho_E \; P_E \; d_C^2 \; e_b} \Delta t, \\
P &= 1, \\
u &= j_{eo}, e_b.
\end{aligned} \tag{61}
$$

Table 9 summarizes the details the parameters that are used in the degradation models. Most of the parameters remain constant since similar type of capacitors are used. The initial value of evaporation rate, j_{eo} are referred from [125].

Table 9: Parameter values used for degradation models capacitance($\mathcal{D}_4$) and ESR($\mathcal{D}_5$) at 12V EOS

Parameter	Description	Value
ϵ_R	relative dielectric constant	10
ϵ_R	permitivity of free space	$8.8542 \times 10^{-9} F - cm^{-1}$
h_c	height of Capacitor Capsule	2 cm
d	diameter of capacitor capsule	0.7 cm
l_C	length of the spacer paper roll.	118 cm
T_{rated}	rated temperature	$85°C$
j_{eo}	evaporation rate	$0.1054 \times 10^{-3}\ mg/hr - cm^2$
d_c	thickness of oxide layer	2.22×10^{-5} cm
w_e	volume of ethyl glycol molecule.	$5.66 \times 10^{-9}\ cm^3$
ρ_E	electrolyte resistivity value	$8 \times 10^2\ \Omega - cm$
P_E	correlation factor of capacitor	$\approx 2 - 3.5$

Experiment II - 10V EOS Experiment

In Chapter V we discussed about deriving a generalized phyiscs-based degradation model and in the earlier section of this chapter we compared the results of a phyiscs-derived empirical model and derived phyiscs-based degradation model. In this section we implement the same models, the capacitance degradation model, $\mathcal{D}_4$ and ESR degradation model, $\mathcal{D}_5$. These we the same type of capacitors with similar ratings used in the experiment.

For this experiment eight capacitors of 2200μF capacitance, with a maximum rated voltage of $10V$, maximum current rating of $1A$ and maximum operating temperature of $85°C$

were used for the study. The ESR and capacitance values were estimated from the capacitor impedance frequency response measured using the EIS instrument. Using the lumped parameter model, $\mathcal{M}_1$ the ESR and capacitance (C) values given by Eqn. (25) and (26) at the beginning of the chapter, were estimated at each measurement. The average pristine condition ESR value was measured to be 0.155 Ω and average capacitance of 1958 μF for the set of capacitors under test. The ambient temperature for the experiment was controlled and kept at $25°C$. During each measurement the voltage source was shut down, the capacitors were discharged completely, and then the characterization procedure was carried out. Figure 47 shows the experimental setup for the 10V EOS experiment which the same setup as the earlier experiment. The boards were configured such that the amplifer output gave 10V with the rest of the system and experimental procedure remaining constant.

Figure 55 shows increase in the ESR value for all the six capacitors under test over the period of time. Similarly, Figure 56 shows the decrease in the value of the capacitance as the capacitor degrades over the aging period. From the plots in Figure 55 we observe that for the time for which the experiments were conducted the average ESR value increased on a average by $98\% - 115\%$ while over the same period of time, the average capacitance decreased by more than 15%. We used the collected data from the experiments to buid dynamic degradation models of capacitors.

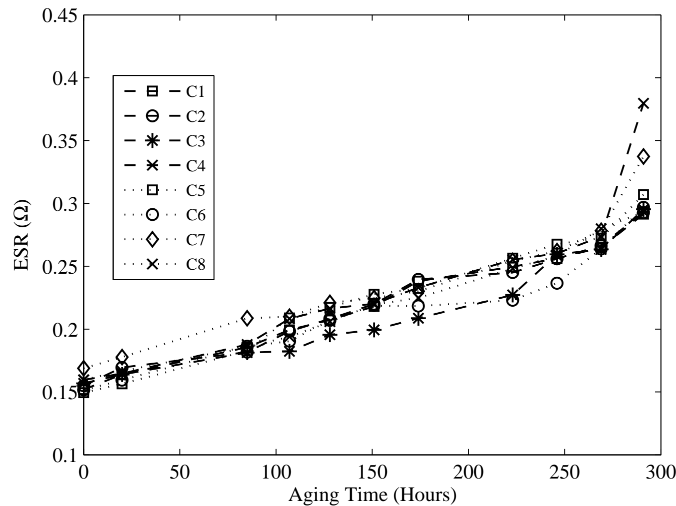

Figure 55: Degradation of capacitor performance, ESR increase as a function of aging time.

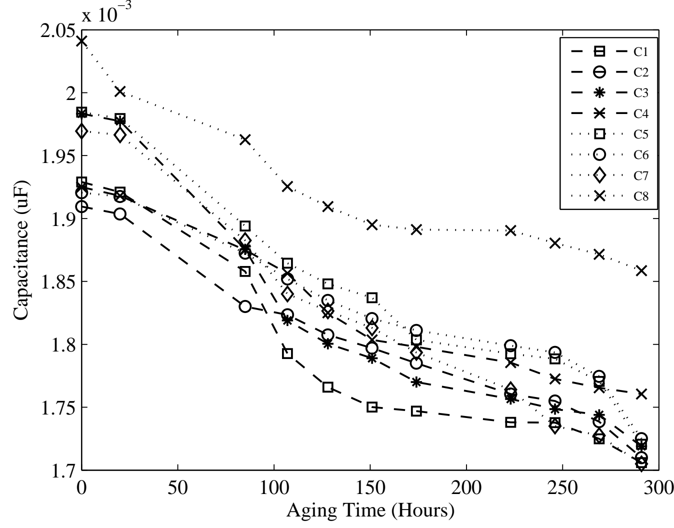

Figure 56: Degradation of capacitor performance, capacitance loss as a function of aging time.

The complete discrete time dynamic model for capacitance degradation as derived earlier is given as :

$$\mathcal{D}_4 : C_{k+1} = C_k - \frac{(2\epsilon_R \epsilon_0 w_e A_s j_{eo} c_b)}{d_C^2} \Delta t$$

And the discrete time dynamic model for ESR degradation as derived earlier is given as :

$$\mathcal{D}_5 : \frac{1}{ESR_{k+1}} = \frac{1}{ESR_k} - \frac{2 w_e A_s j_{eo}}{\rho_E \ P_E \ d_C^2 \ e_b} \Delta t$$

Similar steps are followed as the earlier approach. Table 10 summarizes the details the parameters that are used in degradation models. Most of the parameters remain constant since similar type of capacitors are used. The initial value of evaporation rate, j_{eo} are referred from [125].

Prediction of Remaining Useful Life Results and Validation Tests

This section discusses the remaining useful life predictions and validation results using the Alpha-Lambda prognostics metric for the derived degradation models $\mathcal{D}_4$, capacitance and $\mathcal{D}_5$, ESR respectively. These models were used for making RUL predictions for two different experimental data sets using similar type of capacitors. The discussions in the results and

Table 10: Parameter values used for degradation models capacitance($\mathcal{D}_4$) and ESR($\mathcal{D}_5$) at 10V EOS

Parameter	Description	Value
ϵ_R	relative dielectric constant	10
ϵ_R	permitivity of free space	$8.8542 \times 10^{-9} F - cm^{-1}$
h_c	height of capacitor capsule	2 cm
d	diameter of capacitor capsule	0.7 cm
l_C	length of the spacer paper roll.	118 cm
T_{rated}	rated temperature	$85°C$
j_{eo}	evaporation rate	$0.0491 \times 10^{-3}\ mg/hr - cm^2$
d_c	thickness of oxide layer	2.22×10^{-5} cm
w_e	volume of ethyl glycol molecule	$5.66 \times 10^{-9}\ cm^3$
ρ_E	electrolyte resistivity	$8 \times 10^2\ \Omega - cm$
P_E	correlation factor of capacitor	$\approx 2 - 3.5$

later complete one of our major goals to derive and validate generalized degradation models for electrolytic capacitors.

RUL can be estimated based on the derived physics-based degradation model till the EOL threshold of the device has reached. In the experiments conducted, all the capacitors under test did not reach EOL. The latest characterization reading for degradation in capacitance and ESR parameters was considered as the EOL for calculating the relative accuracy.

Results for Capacitor Degradation Model ($\mathcal{D}_4$) for Experiment I

In this section we discuss the RUL prediction and Validation tests for the capacitance degradation model in the 12V EOS experiment. State estimation and RUL prediction results are discussed for capacitor Cap # 2 out of a batch of 6 available capacitors under test.

Figure 57 shows the result of the filter tracking for completed degradation in capacitance computed upto 200 hours of aging time. The tolerance for the type of electrolytic capacitor under test is approx 15% and hence from the output errors it can be observed that the tracking of the model with respect to the data is acceptable.

Figure 58 shows the estimation plot for the capacitance degradation factor,c_b.

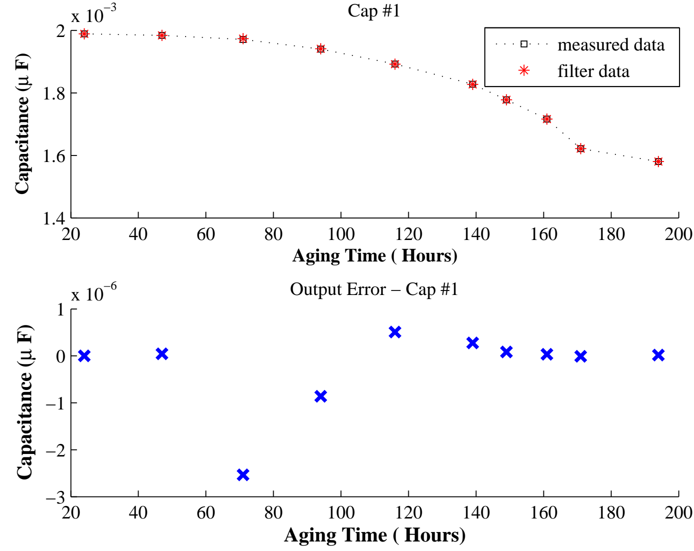

Figure 57: Tracking filter output against measurement data for Cap # 2

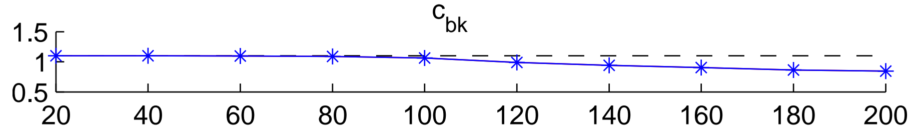

Figure 58: Estimation of capacitance dependance oxide layer breakdown factor (c_b)

RUL

Figure 59 presents results from the remaining useful life prediction algorithm at different aging times t_p = 24, 47, 94, 149, 171 (hrs), at which the capacitors are characterized and their ESR value is calculated. The experiments were run till almost 200 hours and hence the predictions are done till the end of experiments. End of life (EOL) is defined as the time at which the forecasted capacitance value trajectory crosses the EOL threshold. Therefore, RUL is EOL minus aging times calculated at $t_p = 24, 47, 47, 94, 149, 171$ (hrs).

Validation Tests

An Alpha - Lambda prognostics performance metric [22, 142] is presented in Figure 60 for test case of Cap #2. Performance metric identifies whether the algorithm performs within desired error margins (specified by the parameter α) of the actual RUL at any given time instant (specified by the parameter λ) [142]. The central dashed line represents ground truth and the shaded region corresponds to a 30% ($\alpha = 0.3$) error bound in the RUL

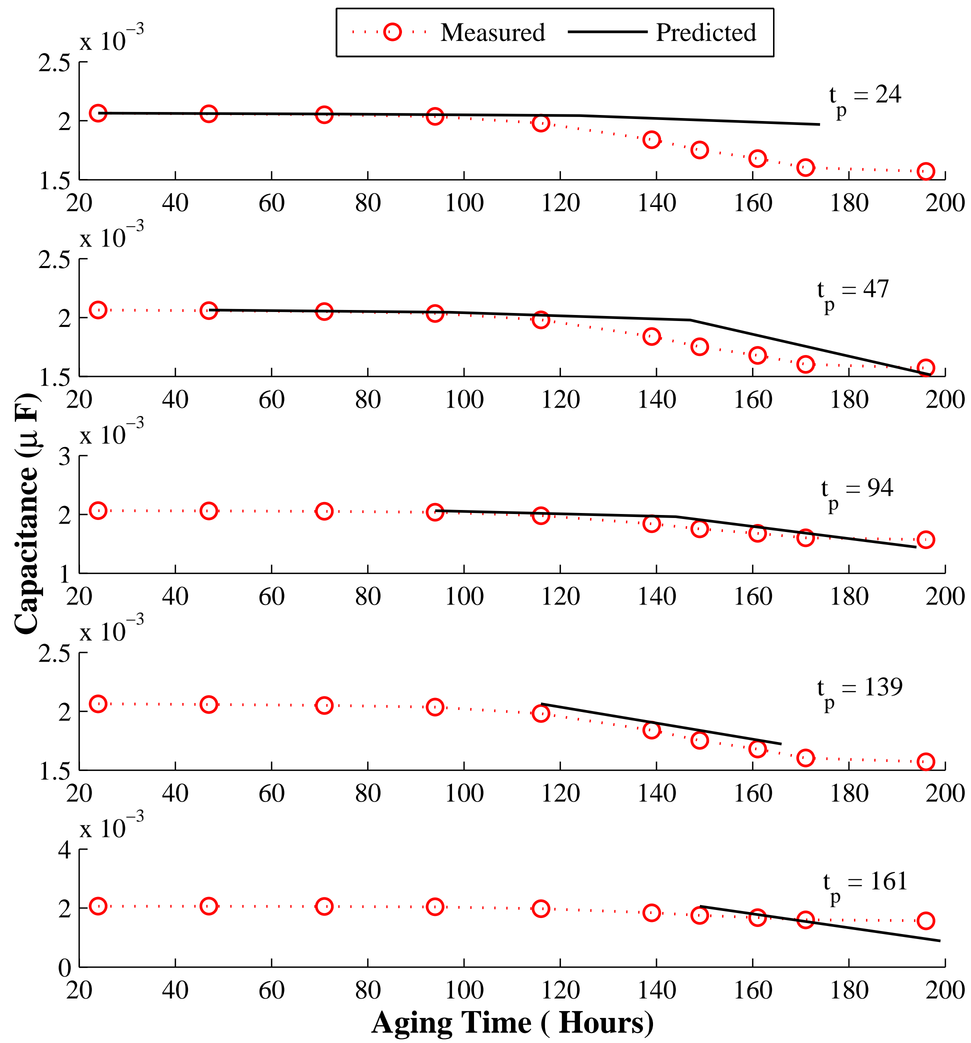

Figure 59: Capacitance decrease prediction at different Aging Time for Cap # 2

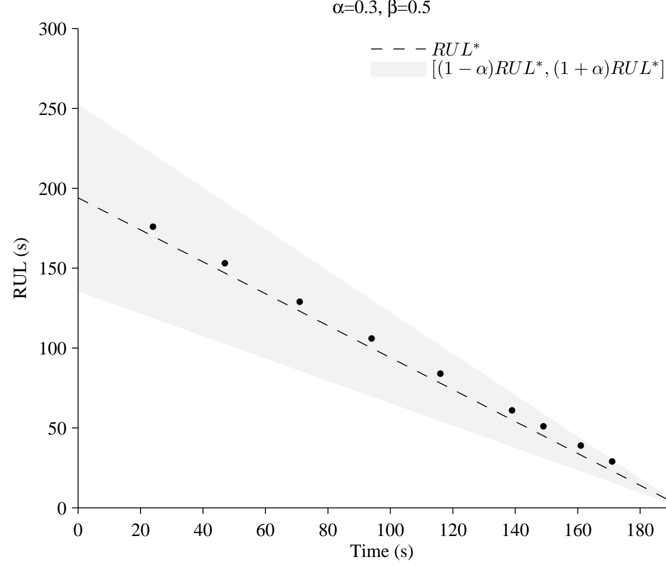

Figure 60: Performance based on Alpha-Lambda metric for Cap#2

prediction. From the metric plot in Figure 60 we note that the relative accuracy remains high till the end of the RUL prediction period. As mentioned earlier this can be attributed to the accuracy of the model, and the state-based tracking approach, where the state is updated as new data points become available.

Table 11: Summary of validation results based on RA for Capacitance degradation model $\mathcal{D}_4$ - 12V EOS Experiment

Aging Time	C1	C2	C3	C4	C5	C6	$\overline{RA}_a$
24	98.85	98.27	98.85	97.67	98.27	96.47	98.06
47	98.68	98.00	98.68	97.32	98.00	95.92	97.76
71	98.43	97.62	98.43	96.80	97.62	95.12	97.34
94	98.08	97.09	98.08	96.08	97.09	94.00	96.73
116	97.56	96.30	97.56	95.00	96.30	92.31	95.84
139	96.61	94.83	96.61	92.98	94.83	89.09	94.16
149	95.92	93.75	95.92	91.49	93.75	86.67	92.92
161	94.59	91.67	94.59	88.57	91.67	81.82	90.49
171	92.59	88.46	92.59	84.00	88.46	73.91	86.67
$\overline{RA}_b$	96.81	95.11	96.81	93.32	95.11	89.48	

$\overline{RA}_a$ is the mean relative accuracy of all capacitors at each prediction time (t_p)
$\overline{RA}_b$ is the mean relative accuracy of each capacitor at all prediction times

Discussion

When comparing the results generated by the empirical model in table 8, the physics-based degradation model in table 11, we note that the accuracy of the two models are comparable initially, but the empirical model results degrade toward the end of capacitor life. This is primarily because a simple linear first-order model with static parameter values is employed for tracking the capacitor degradation.

Physics-based model more accurately represents the actual degradation phenomena, and the use of the UKF allows for more accurate tracking, especially when the behaviors are nonlinear in the later stages of the aging cycle. The tuning and estimation of parameters in the empirical model using KF is relatively simpler and also computationally less expensive. On the other-hand, in UKF the parameters are tuned online as updated data is received and hence computationally expensive.

Overall both the models have their own pros and cons, the comparison of the two models and prediction results can help us decide which models to implement based on the requirements. If the model needs to be simpler and computationally less expensive then the empirical model can be implemented where the model prediction accuracy will be compromised while if accuracy is more important then a complex model and computationally expensive methodology can be implemented. We next discuss the physics-based ESR degradation model and the results for the same data set for the ESR measurements.

Results for Capacitor Degradation Model ($\mathcal{D}_4$) for Experiment II

In this section we discuss the RUL prediction and Validation tests for the capacitance degradation model in the 10V EOS experiment. State estimation and RUL prediction results are discussed for capacitor Cap # 5 out of a batch of 6 available capacitors under test. Figure 61 shows the result of the filter tracking for completed degradation in capacitance upto 200 hours of aging time and as can be observed from the residuals the tracking of the model with respect to the data is acceptable. The model tracks well since it includes the electrolyte evaporation (j_{eo}) parameter as well as the oxide layer breakdown parameter, (c_b).

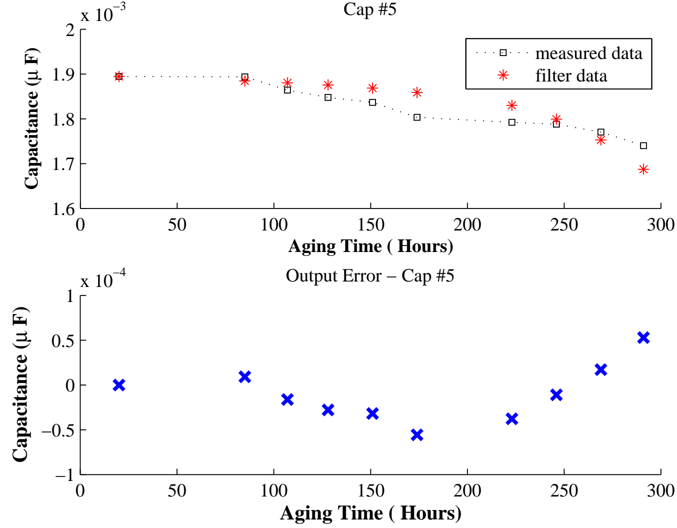

Figure 61: Tracking filter output against measurement data for Cap # 5

RUL

Figure 62 presents results from the remaining useful life prediction algorithm at different aging times t_p = 20, 85, 128, $174, 246$ (hrs), at which the capacitors are characterized and their capacitance value is calculated. The experiments were run till almost 300 hours and hence the predictions are done till the end of experiments. End of life (EOL) is defined as the time at which the forecasted capacitance value trajectory crosses the EOL threshold. Therefore, RUL is EOL minus aging times $t_p = 20, 85, 128, 94, 174, 246$ (hrs).

Validation Tests

An α-λ prognostics performance metric is presented in Figure 63 for test case of Cap #5. Performance metric identifies whether the algorithm performs within desired error margins (specified by the parameter α) of the actual RUL at any given time instant (specified by the parameter λ) [142]. The central dashed line represents ground truth and the shaded region is corresponding to a 30% ($\alpha = 0.3$) error bound in the RUL prediction. From the α-λ metric plot in Fig. 63 it can be observed that the relative accuracy is good till the end of the experiment time and the accuracy is good enough under acceptable limits. As mentioned earlier this is due to inclusion of the degradation parameters and estimating them as the capacitance changes with degradation.

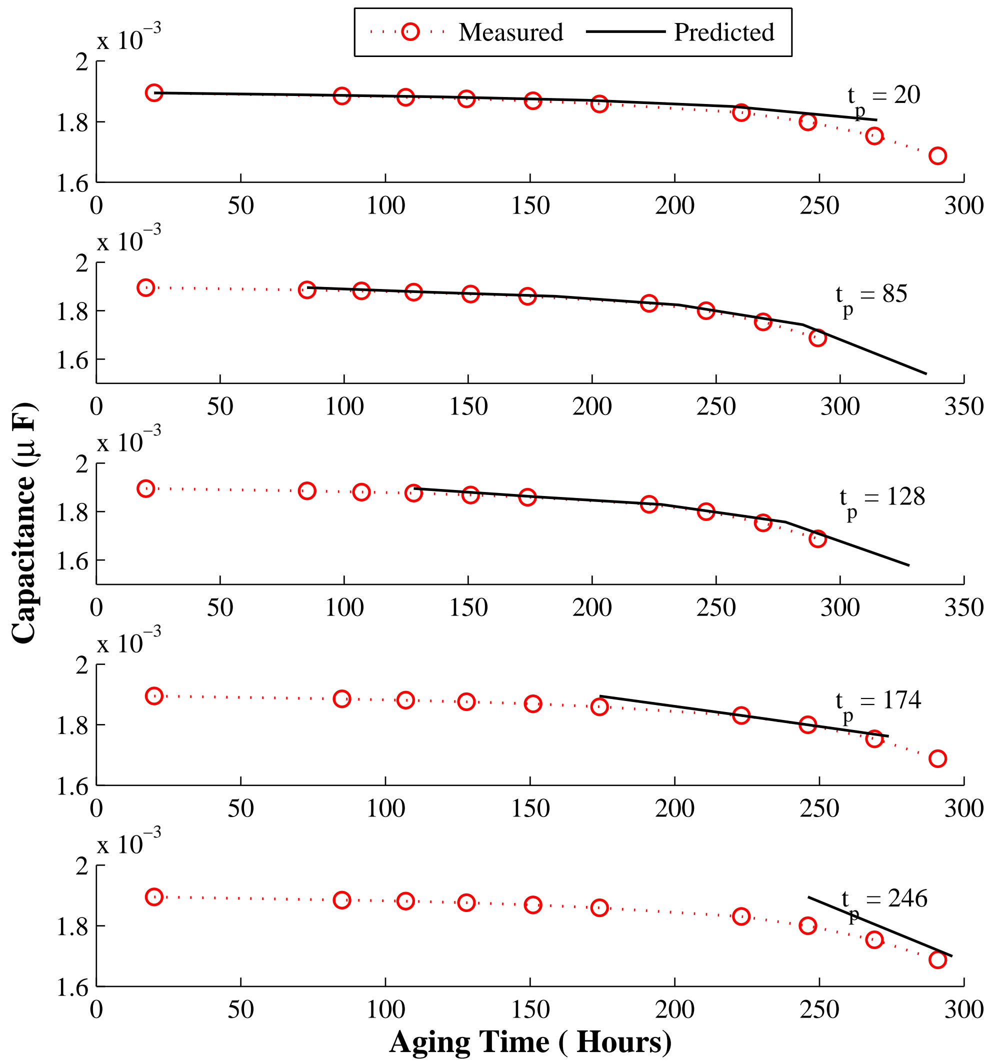

Figure 62: Capacitance decrease prediction at different Aging Time for Cap # 5

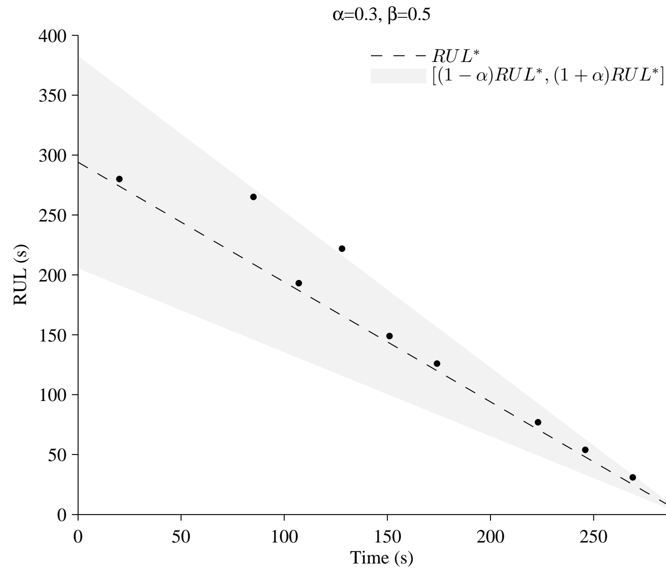

Figure 63: Performance based on Alpha-Lambda metric for Cap#5

Table 12: Summary of validation results based on RA for Capacitance degradation model $\mathcal{D}_4$ - 10V EOS Experiment

Aging Time	C1	C2	C3	C4	C5	C6	C7	C8	$\overline{RA}_a$
20	98.37	98.18	98.55	97.81	97.81	98.18	98.18	98.18	98.16
85	97.86	97.62	74.41	97.13	73.21	73.81	73.81	97.62	85.68
107	97.61	97.34	97.88	96.79	96.79	97.34	97.34	97.34	97.31
128	67.46	67.07	67.86	66.27	66.27	67.07	67.07	67.07	67.01
151	96.89	96.53	97.24	95.80	95.80	96.53	96.53	96.53	96.48
174	96.30	95.87	96.72	95.00	95.00	95.87	95.87	95.87	95.81
223	93.79	93.06	94.52	91.55	91.55	93.06	93.06	93.06	92.95
246	90.91	89.80	92.00	87.50	87.50	89.80	89.80	89.80	89.64
269	83.02	80.77	85.19	76.00	76.00	80.77	80.77	80.77	80.41
$\overline{RA}_b$	91.36	90.69	89.37	89.32	86.66	88.05	88.05	90.69	

$\overline{RA}_a$ is the mean relative accuracy of all capacitors at each prediction time
$\overline{RA}_b$ is the mean relative accuracy of each capacitor at all prediction times

Table 12 summarizes the results for all the capacitors and their percentage relative accuracy of capacitance degradation model $\mathcal{D}_4$ for all the capacitors under test. As mentioned earlier model $\mathcal{D}_4$ is used for making predictions for all the capacitors with same parameters, and though it is observed that in the later stages the model performance reduces by some margin the overall accuracy of the model is acceptable.

Results for ESR Degradation Model ($\mathcal{D}_5$) for Experiment I

State estimation and RUL prediction results are discussed for capacitor Cap #2. Figure 64 shows the result of the filter tracking for completed degradation in capacitance upto 200 hours of aging time. As can be observed from the residuals the tracking of the model with respect to the data in acceptable.

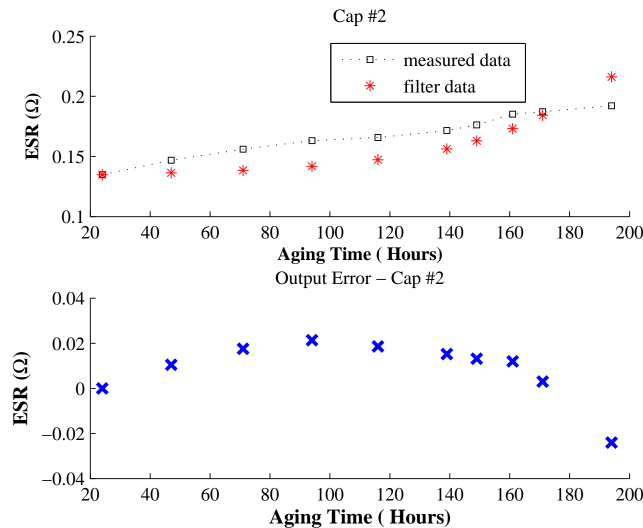

Figure 64: Tracking filter output against measurement data for Cap # 2

RUL

Figure 65 presents results from the remaining useful life prediction algorithm at different aging times $t_p = 24,\ 47,\ 94,\ 149, 171$ (hrs), at which the capacitors are characterized and their ESR value is calculated. Model $\mathcal{D}_5$ is implemented for predicting the increase in ESR while the measured values are the ESR measurements done at respective aging time intervals. The experiments were run till almost 200 hours and hence the predictions are done till the end of experiments. End of life (EOL) is defined as the time at which the forecasted

capacitance value trajectory crosses the EOL threshold at end of 200 hrs. Therefore, RUL is EOL minus aging times $t_p = 24, 47, 47, 94, 149, 171$ (hrs).

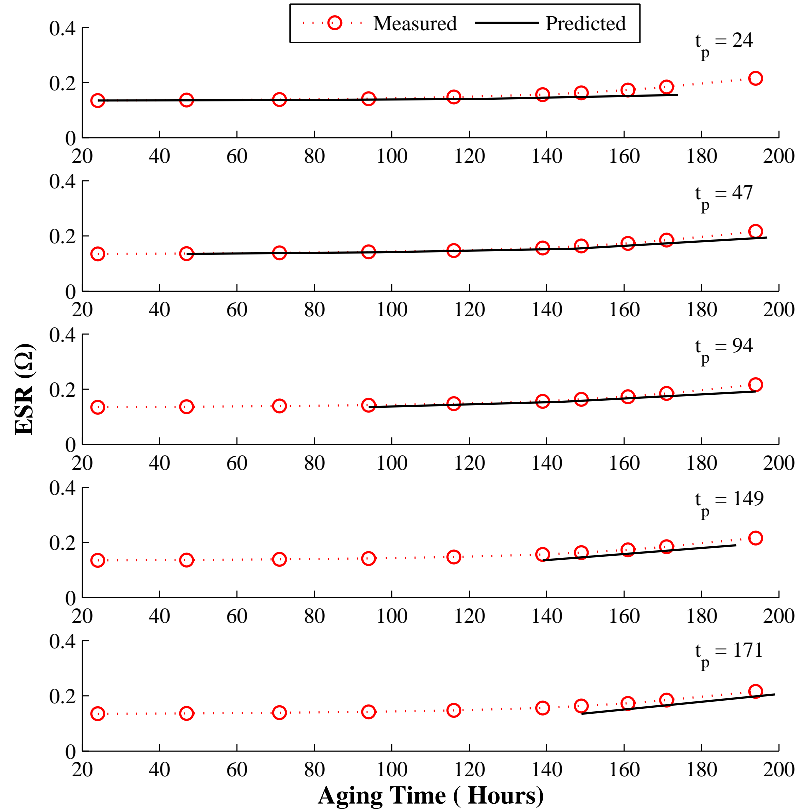

Figure 65: ESR prediction at different Aging Time for Cap # 2 by Model $\mathcal{D}_5$

Validation Tests

An Alpha-Lambda (α-λ) prognostics performance metric [22, 142] is presented in Figure 66 for test case of Cap #2. The central dashed line represents ground truth and the shaded region is corresponding to a 30% ($\alpha = 0.3$) error bound in the RUL prediction. From the α-λ metric plot in Figure 66 it can be observed that the relative accuracy is good till the end of the experiment time and the accuracy is good enough under acceptable limits. As mentioned earlier this is due to inclusion of the degradation parameters and estimating them as the ESR increases with degradation.

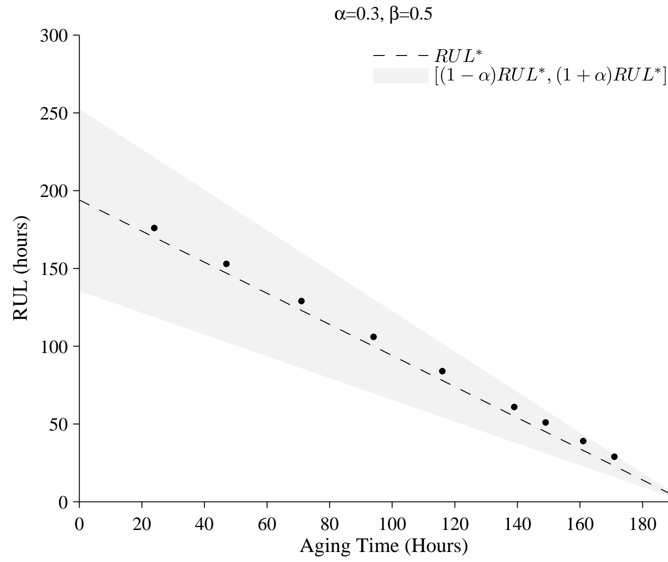

Figure 66: Performance based on Alpha-Lambda metric for Cap#2

Table 13: Summary of validation results based on RA for ESR degradation model $\mathcal{D}_5$ - 12V EOS Experiment

Aging Time	C1	C2	C3	C4	C5	C6	$\overline{RA}_a$
24	96.47	96.47	96.47	96.47	96.47	96.47	96.47
47	95.92	95.92	95.92	95.92	95.92	95.92	95.92
71	95.12	95.12	95.12	95.12	95.12	95.12	95.12
94	94.00	94.00	94.00	94.00	94.00	94.00	94.00
116	92.31	92.31	92.31	92.31	92.31	92.31	92.31
139	89.09	89.09	89.09	89.09	89.09	89.09	89.09
149	86.67	86.67	86.67	86.67	86.67	86.67	86.67
161	81.82	81.82	81.82	81.82	81.82	81.82	81.82
171	73.91	73.91	73.91	73.91	73.91	73.91	73.91
$\overline{RA}_b$	89.48	89.48	89.48	89.48	89.48	89.48	

$\overline{RA}_a$ is the mean relative accuracy of all capacitors at each prediction time (t_p)
$\overline{RA}_b$ is the mean relative accuracy of each capacitor at all prediction times

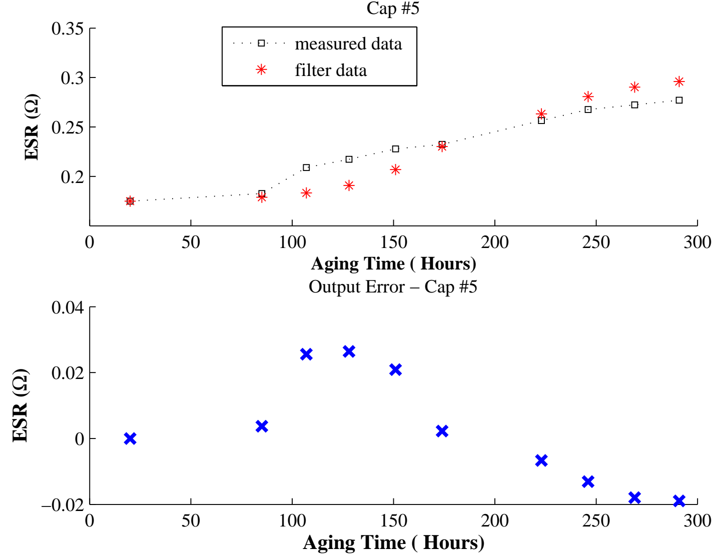

Figure 67: Tracking filter output against measurement data for Cap # 5

Results for ESR Degradation Model ($\mathcal{D}_5$) for Experiment II

State estimation and RUL prediction results are discussed for capacitor Cap #5. Figure 67 shows the result of the filter tracking for completed degradation in capacitance upto 200 hours of aging time. As can be observed from the residuals the tracking of the model with respect to the data in acceptable.

RUL

Figure 68 presents results from the remaining useful life prediction algorithm at different aging times $t_p = 20,\ 85,\ 128,\ 174, 246$ (hrs), at which the capacitors are characterized and their ESR value is calculated. Model $\mathcal{D}_5$ is implemented for predicting the increase in ESR while the measured values are the ESR measurements done at respective aging time intervals. The experiments were run till almost 300 hours and hence the predictions are done till the end of experiments. End of life (EOL) is defined as the time at which the forecasted capacitance value trajectory crosses the EOL threshold at end of 200 hrs. Therefore, RUL is EOL minus aging times $t_p = 20, 85, 128, 94, 174, 246$ (hrs).

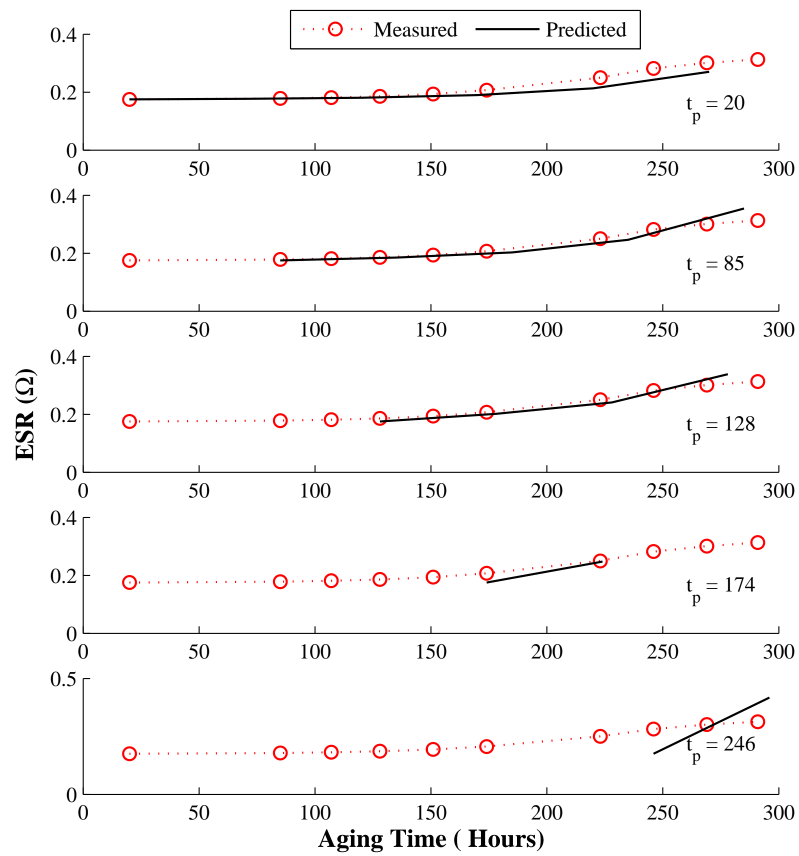

Figure 68: ESR prediction at different Aging Time for Cap # 5 by Model $\mathcal{D}_5$

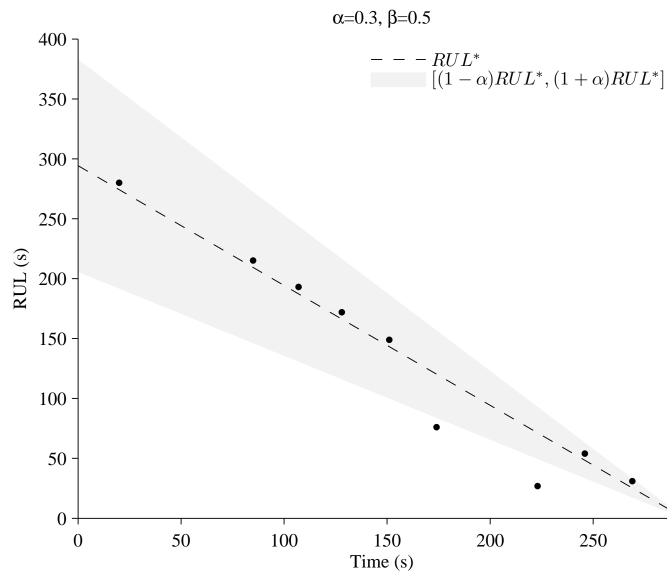

Figure 69: Performance based on Alpha-Lambda metric for Cap#5

Validation Tests

An α-λ prognostics performance metric is presented in Figure 69 for test case of Cap #5. The central dashed line represents ground truth and the shaded region is corresponding to a 30% ($\alpha = 0.3$) error bound in the RUL prediction. From the α-λ metric plot in Figure 69 it can be observed that the relative accuracy is good till the end of the experiment time and the accuracy is good enough under acceptable limits. As mentioned earlier this is due to inclusion of the degradation parameters and estimating them as the ESR increases with degradation.

Table 14: Summary of validation results based on RA for ESR degradation model $\mathcal{D}_5$ - 10V EOS Experiment

Aging Time	C1	C2	C3	C4	C5	C6	C7	C8	$\overline{RA}_a$
20	98.22	97.81	98.22	98.14	97.92	98.14	98.14	98.14	98.09
85	97.67	97.13	73.87	73.75	97.28	97.57	97.57	73.75	88.57
107	97.40	96.79	97.40	97.29	96.96	97.29	97.29	97.29	97.21
128	97.07	96.39	67.15	66.99	96.57	96.94	66.99	66.99	81.88
151	96.60	95.80	96.60	96.46	96.02	96.46	96.46	96.46	96.36
174	62.76	63.33	95.95	95.78	63.18	62.86	95.78	95.78	79.43
223	37.45	38.03	93.20	92.91	37.87	37.55	92.91	92.91	65.35
246	90.02	87.50	90.02	89.57	88.20	89.57	89.57	89.57	89.25
269	81.23	76.00	81.23	80.31	77.47	80.31	80.31	80.31	79.64
$\overline{RA}_a$	84.27	83.20	88.18	87.91	83.50	84.08	90.56	87.91	

$\overline{RA}_a$ is the mean relative accuracy of all capacitors at each prediction time
$\overline{RA}_b$ is the mean relative accuracy of each capacitor at all prediction times

Table 14 summarizes the results for all the capacitors and their percentage relative accuracy of ESR degradation model $\mathcal{D}_5$ for all the capacitors under test. As mentioned earlier model $\mathcal{D}_5$ is used for making predictions for all the capacitors with same parameters, and though it is observed that in the later stages the model performance reduces by some margin the overall accuracy of the model is with acceptable limits.

Discussion and Summary

An important goal achieved through the experiments I and II, was implementing same capacitance degradation model $\mathcal{D}_4$ and ESR degradation model $\mathcal{D}_5$ over a different set of

operating conditions and achieving results for both the models which are within acceptable limits. The only parameters which changed in the models for the experiment were the operating parameters while rest of the structural and geometrical parameters were kept constant for model validation. Early in the thesis work mentioned to implement a generalized physics-based degradation model based on underlying operating phenomenons which is shown through these experimental case studies.

Another interesting observation from the two data sets of the experimental cases were :

1. In Experiment-I under 12V electrical overstress operating at the end of 200 hours the overall degradation observed in the capacitance was more than 22% and ESR increase by over 54%.

2. In Experiment II under 10V electrical overstress operating at the end of 300 hours the overall degradation observed in the capacitance was more than 15% and ESR increase by over 105%.

Thus it was observed that under higher electrical stress the rate of capacitance degradation was higher as compared to ESR degradation while under relatively lower stress level ESR degradation was comparatively higher. This phenomenon could be hypothesized due to the variation in the internal core temperature under the two different operating conditions. At higher voltage more heat will be generated leading to increase in the core temperature and thus degrading the capacitance at a faster rate. While in the case of lower electrical stress, the heat generated internally is lower with lower evaporation rate causing the capacitance to degrade at a lower rate while the ESR increases predominantly.

The major contributions of the work presented in this chapter are:

1. Identification of the lumped-parameter model, $\mathcal{M}_1$ and $\mathcal{M}_4$, based on the equivalent electrical circuit of a real capacitor as a viable reduced-order model for prognostics-algorithm development;

2. Developing the electrical capacitance experiments based on the failure modes observed and collecting and analyzing data at regular intervals.

3. Identification of C and ESR as a failure precursor in the lumped parameter model, $\mathcal{M}_1$ as shown in Figure 70;
4. Implementing a empirical degradation model, $\mathcal{E}_2$ based on the 12V electrical overtress data and validating the model.
5. Development of the first principles based degradation models, $\mathcal{D}_4$ and $\mathcal{D}_5$ for capacitance and ESR degradation respectively, based on accelerated life test aging data as a function of time, evaporation rate and oxide breakdown;
6. Implementing the Unscented Kalman Filter framework for models $\mathcal{D}_4$ and $\mathcal{D}_5$ for predicting degradation.
7. Discussion of the validation results from physics-based empirical degradation model, $\mathcal{E}_2$ and degradation model, $\mathcal{D}_4$
8. The performance of degradation models, $\mathcal{D}_4$ and $\mathcal{D}_5$ implemented for predicting degradation in capacitance and ESR respectively under cases I and II, for similar type of capacitors operating under different operating conditions was within acceptable limits.

The derived degradation models can be updated and developed at a more finer granularity to be implemented for detailed prognostic implementation. The results presented here are based on electrical accelerated aging experimental data and on a accelerated life timescale.

CHAPTER VII

THERMAL OVERSTRESS

Introduction

In this chapter we discuss in detail the studies and related work of capacitor degradation under thermal overstress conditions. Exposure of the capacitors to temperatures that are greater than the rated operating temperatures (T_{rated}) for the capacitor results in accelerated aging of the devices [109, 123]. Higher ambient storage temperature accelerates the rate of electrolyte evaporation leading to degradation of the capacitance [128]. Refering to the fishbone diagram in Figure 35 thermal stress conditions have a prominent effect on degradation in capacitors.

In this chapter we discuss the degradation phenomenon under thermal overstress conditions. We then present the methodology for deriving the physics-based degradation models based on the discussion in Chapter V along with the thermal overstress experiment setup. As initial part of the research work, we derived a electrolyte degradation model which is discussed along with the development of the model and results. The next step was to derive a physics-based degradation model and since this was the first data set use for the model we first implemented a Kalman Filter approach keeping most of the parameters constant. We discuss the approach taken, steps involved in deriving the model and the results. The model was updated to estimate some the critical degradation parameters i.e., evaporation rate, j_{eo} and oxide breakdown factor, c_b to be estimated online based on the state. An Unscented KF was used for the updated model which gave better results. The prognostics results and the validation tests are discussed in the concluding sections.

Table 15 describes the datasets for the experiments that have been conducted to study and collect data for different type of capacitors subjected to simillar operating conditions. The first column describes the type of experiment conducted, the second column in the table gives details of the capacitors used for the experiment while the third column gives

the details of the experimental setup under which the capacitors were stressed. The last column indicates the number of capacitor devices used in each experiment.

Table 15: Thermal Overstress Degradation Experiments

Experiment	**Capacitors**	**Setup**	**Units**
Thermal Overstress	2200μF, 10V, 85°C	0V, 105°C	15
Thermal Overstress	10000μF, 10V, 85°C	0V, 105°C	15

Physics Based Modeling of Capacitor Degradation

In this section we present an approach for deriving physics-based degradation models for capacitors under thermal overstress conditions. Under thermal overstress conditions, since the device was subjected to only high temperature with no charge applied (i.e, the capacitors were in storage mode) the primary degradation phenomenon is electrolyte evaporation. The derived degradtion models are then validated using experimental data.

Equivalent Electrical Circuits

The structural details of the capacitor are discussed in Chapter V. Based on the earlier discussions, a simplified electrical lumped parameter model of impedance, $\mathcal{M}_1$, defined for a electrolytic capacitor is shown in Figure 70.

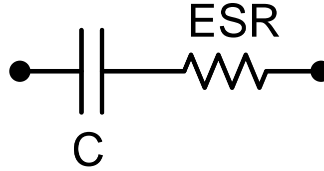

Figure 70: Lumped Parameter Model ($\mathcal{M}_1$)

Exposure of the capacitors to temperatures $T_{applied} > T_{rated}$ results in accelerated aging of the devices [123, 143, 144]. Higher ambient storage temperature accelerates the rate of electrolyte evaporation leading to degradation of the capacitance [128, 143]. The depletion in the volume as discussed in Chapter V earlier is given by:

$$V(t) = V_{e0} - (A_s \; j_{eo} \; w_e) \times t$$

From [121, 125, 128] and experiments conducted [144] under thermal overstress, it has been observed that the capacitance and ESR value depends of the electrolyte resistance R_E. A more detailed lumped parameter model derived for an electrolytic capacitor under thermal overstress condition, $\mathcal{M}_2$ can be modified from $\mathcal{M}_1$, as shown in Figure 71. R_1 is the combined series and parallel resistances in the model, R_E is the electrolyte resistance. The combined resistance of R_1 and R_E is the equivalent series resistance of the capacitor (ESR), while C is the total capacitance of the capacitor as discussed earlier.

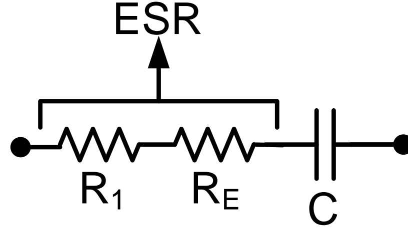

Figure 71: Lumped Parameter Model ($\mathcal{M}_2$)

Capacitance Degradation Model

The input impedance of the capacitor network is defined in terms of the total lumped series and parallel impedance of the simplified network. The total lumped capacitance of the structure is given by

$$C = (2\epsilon_R \epsilon_0 A_s)/d_C \tag{62}$$

From Eqn.(25) and other derivations in Chapter V, using the physics-based model of electrolyte evaporation, we have the time dependent degradation models, $\mathcal{D}_1$ for capacitance (C) given by :

$$\mathcal{D}_1 : C(t) = \left(\frac{2\epsilon_R \epsilon_0 c_b}{d_C} \right) \left(\frac{V_{e0} - V_e(t)}{j_{eo}\ t\ w_e} \right),$$

The degradation in capacitance is directly proportional to the damage variable, V_e, electrolyte evaporation. As discussed earlier, increase in the core temperature evaporates the electrolyte thus decreasing the electrolyte volume leading to degradation in capacitance. The resultant decrease in the capacitance can be computed using Eqn. (25).

Experimental Setup

We setup an experimental chamber where we emulated conditions of high temperature storage conditions. Capacitors were placed in a controlled chamber whose temperature was maintained above their rated specification [123]. Pristine capacitors rated at 2200 μF, 10V and maximum storage temperature of 85°C, from the same manufacturing lot were used for the experiment. The chamber temperature was gradually increased in steps of 25°C till the pre-determined temperature limit was reached. The capacitors were allowed to settle at a set temperature for 15 min and then the next step increase was applied and was continued till the required temperature was attained. The above procedure was followed to decrease any possibility of shocks due to sudden change in the temperature variations.

Figure 72: Capacitors in Thermal Chamber

For this experiment all the capacitors were subjected to a constant temperature of 105°C and the humidity factor is set at 3.4%. At the end of specific time interval the temperature was lowered in steps of 25°C till the required room temperature was reached. Before measurements were made on the capacitors were kept at room temperature for 30 min to stabilize the temperature of the capacitor capsule. The ESR value is the real impedance measured through the terminal software of the instrument. Similarly the capacitance value is computed from the imaginary impedance using Electrochemical Impedance Spectroscopy

(EIS). An SP-150 Biologic impedance measurement instrument was used making the measurements [145].

Experimental Data Analysis

Figure 73 shows the Nyquist plots for a capacitor characterized under different stages of degradation during accelerated thermal aging. As the capacitors degrade, we observe a considerable tilt away from the axis which indicates decrease in the capacitance. In contrast the point of origin has a smaller deflection away from the axis indicating that there is a considerably smaller change in the measured ESR value. Similarly the plots in Figure 74 shows the Bode plots for same capacitors when characterized at different time intervals in the aging cycle. From the magnitude plot we can observe the change in total impedance (Z) of the capacitor with the frequency sweep as the device degrades. As the capacitors degrade the magnitude plot shifts upwards indicating an increase in the total impedance of the capacitance, which in this case, is the increase in C and ESR values. From the phase plot, it is seen that as the device degrades there is shift in phase indicating change in capacitance, which can also be observed clearly from the Nyquist plot in Figure 73.

In the thermal overstress experiments, the capacitors were characterized periodically upto 3400 hours of operation. It was observed that the average capacitance value decreased by more than 15 - 18% while decrease in the ESR value was observed around 8 - 10%. Therefore, the capacitance value crossed the threshold limit ($\geq$ 10% degradation) whereas the ESR change observed was very low and hence not considered as a failure precursor. Since the capacitance degradation is clearly observed and is more significant, the C parameter was selected as a precursor to failure parameter to estimate the current health condition of the device.

Decrease in C is plotted as a function of aging time. The gradual decrease in the capacitance can be related to the physics of failure model derived earlier. As the temperature increases, the electrolyte soaked in the capacitors evaporates. From the thermal model discussed, decrease in the capacitance is directly linked to the decrease in the effective

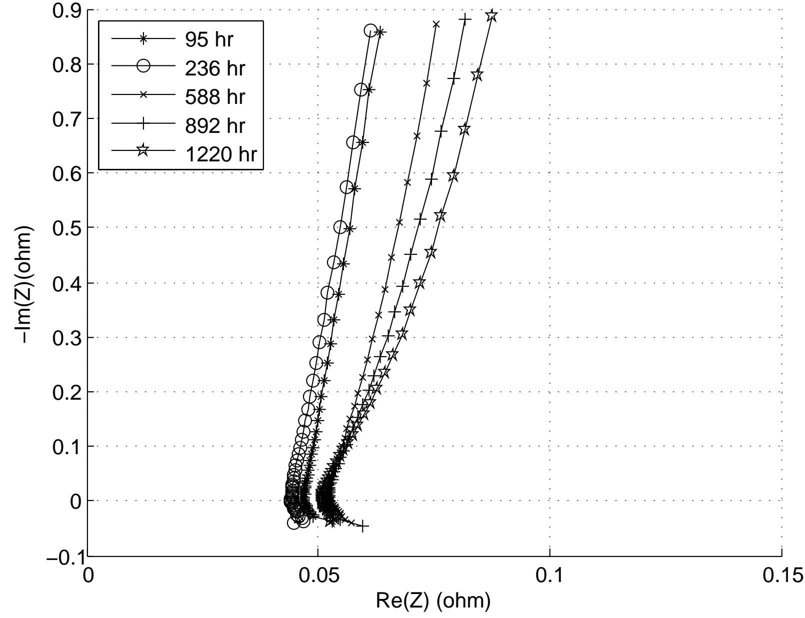

Figure 73: Nyquist Plot of a typical capacitor under Thermal Stress

oxide area (A_s) of the capacitor. This decrease in the oxide area is in turn directly related to the rate of evaporation [127] of the electrolyte given by Eqn. (8)

Figure 75 shows the plot for decrease in capacitance values for all the 15 capacitors (labeled capacitors #1 through #15) in the thermal overstress experiment. Till about 2400 hours of storage we observe a linear decrease in capacitance. This could be related to the electrolyte evaporation at a constant rate because the capacitor was stored at a fixed high temperature. As we continued the thermal aging cycle beyond this time period, from around 2450 hours onwards we observed a higher order effect that resulted in non-linear degradation. This non-linear phenomenon is related to degradation in the oxide layer of the capacitor. In the early stages of aging, the linear degradation phenomena linked to electrolyte evaporation dominates, where as the non-linear degradation phenomenon due to oxide layer becomes dominant in the later part of the aging cycle.

Electrolyte Volume Degradation Model

In this section we discuss our work where we have studied only the linear degradation due to electrolyte evaporation. The time dependent model, $\mathcal{D}_3$ derived for estimating the electrolyte volume, V_e implemented as a second order polynomial model for estimating the

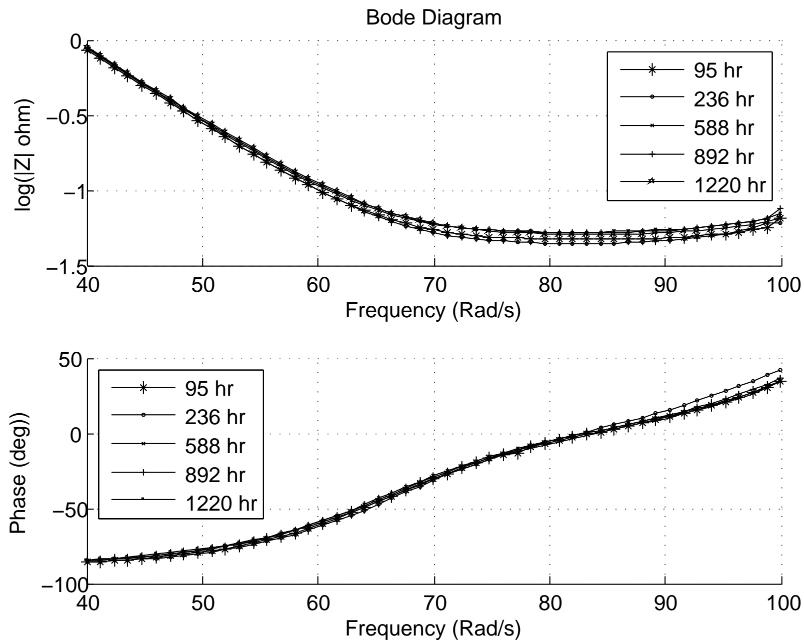

Figure 74: Bode Plot of a typical capacitor under Thermal Stress

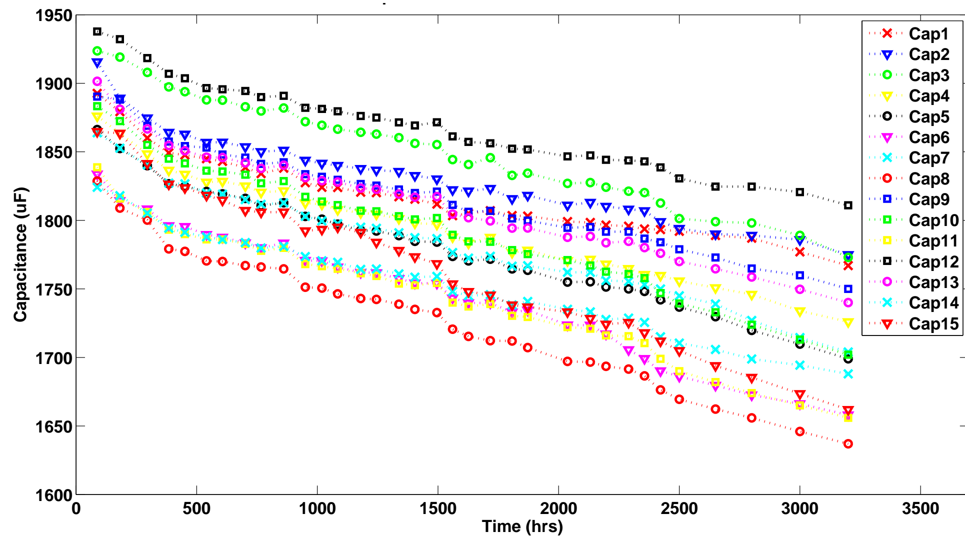

Figure 75: Thermal Overstress at 105° C - 2200uF

decrease in electrolyte volume over time. In this section we will discuss the parameter estimation for this model and study how well the developed degradation model, $\mathcal{D}_1$ behaves based on the estimated parameters.

The relationship between capacitance and electrolyte volume is given by model $\mathcal{D}_1$ in Eq. (25), can be rewritten to express the change in electrolyte volume, V_e over time given by :

$$\mathcal{D}_3 : V_e(t) = V_{e0} - C(t) \left(\frac{j_{eo}\ t\ w_e\ d_C}{2\epsilon_R \epsilon_0} \right) \tag{63}$$

Parameter Estimation Approach

Decrease in parameter, C is used as a precursor of failure, from the experimental data and literature studies [123, 125]. Based on the experiments, capacitance parameter values are computed by characterizing the capacitors at regular time intervals as shown in Figure 75. From the degradation model, $\mathcal{D}_1$ given a certain type of capacitor all the values in Eqn. (25) can be computed except the dispersion in electrolyte volume, V_e, which is computed based on the available data and used degradation model, $\mathcal{D}_3$. Initial electrolyte volume V_{e0} at pristine conditions is approximately computed from the structural details of the capacitor as discussed in Chapter V. From the experimental data the estimated volume computed decreases almost linearly through the initial phase of degradation. Hence for this work we propose a linear model, which relates aging time to the decrease in loss of electrolyte volume. The loss in electrolyte is linked to decrease in capacitance through Eqn. (25) and has the following form,

$$(V)_{e(k)} = \hat{\theta_1} - \hat{\theta_2}\ t_k + \hat{\theta_3}\ {t_k}^2 \tag{64}$$

where $\hat{\theta_1}$, $\hat{\theta_2}$ and $\hat{\theta_3}$ are model constants for decrease in electrolyte volume V_e, estimated from the experimental data of accelerated thermal aging experiments. In order to estimate the model parameters, 14 capacitors out of the 15 used for the experiment, are used for estimation, and the remaining capacitor is used to validate the model against experimental data. This Leave-one-out cross-validation, methodology is implemented for validating

the model against the computed capacitance degradation data. A nonlinear least-squares regression algorithm is used to estimate the model parameters.

Parameter Estimation Results

The goal of leave-one-out cross-validation is to estimate the expected level of fit of the derived physics-based model as discussed in Eqn. (25). The errors from the results of the predicted model and actual data are the summarized in Tables (16) and (17), and compared using the mean ($\bar{X}$), median absolute deviation ($\tilde{X}$), root mean squared error (RMSE), root mean squared percentage error (RMSPE), standard deviation (SD), and confidence interval (CI) to study the overall predicted model behavior.

To demonstrate the approach we selected capacitors #4 and #5 from the set of 15 capacitors to show the detailed plots for volume and capacitance estimation. In Figure 76 based on the measurement data from capacitors #1 - #3 and #5 through #15, volume parameters, $\hat{\theta}_1$, $\hat{\theta}_2$ and $\hat{\theta}_3$ were estimated. Degradation model, $\mathcal{D}_3$ was validated against the computed change in volume of capacitor #4, and model, $\mathcal{D}_1$ was validated for decrease in capacitance. Similarly for capacitor #5 parameters were estimated based on data from capacitors #1 - #4 and #6 through #15. The estimated and computed values degradation in volume and capacitance respectively for capacitor #5 are shown in plots of Figure 77.

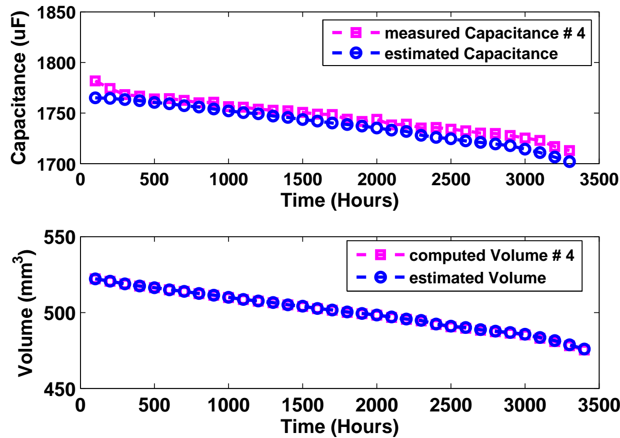

Figure 76: Volume and Capacitance Estimation (Cap # 4)

It can be observed from the residuals of Figure 79 that the estimation error increases with time. This is to be expected since capacitance decrease is mostly linear till 2500 hrs,

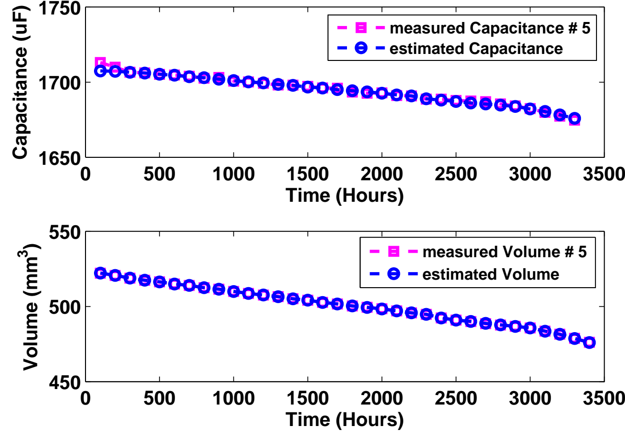

Figure 77: Volume and Capacitance Estimation (Cap # 5)

and then becomes non-linear, causing the residuals to increase. This indicates that there is a secondary phenomenon occurring in addition to the linear decrease due to loss in electrolyte volume, V_e. This is the oxide layer breakdown phenomenon which simultaneously degrades the capacitor and is non-linear in nature. The phenomenon kicks-in prominently in the later stages of aging as seen from the data.

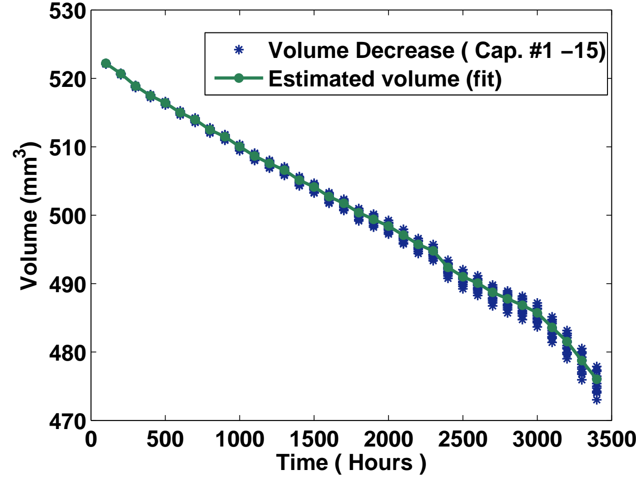

Figure 78: Estimation results for the degradation model

Table (16) summarizes the estimated parameters results for degradation in electrolyte volume in all the 15 capacitors under test. Root mean squared error (RMSE) is calculated for the difference between the computed electrolyte volume, V_e and predicted electrolyte volume, $\hat{V_e}$ by degradation model, $\mathcal{D}_3$ while root mean square percentage error, RMSPE is computed from the average percentage error at different aging times for each capacitor.

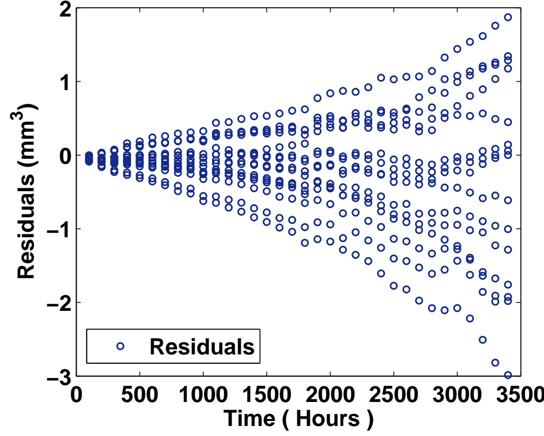

Figure 79: Electrolyte volume (V_e) estimation residuals

The overall model parameters for the set of capacitors is summarized in Table (17). $\bar{X}$ and $\tilde{X}$ give the mean and median values for $\hat{\theta}_1$, $\hat{\theta}_2$ and $\hat{\theta}_3$ respectively along with RMSE and RMSPE error parameters for each capacitor. Standard deviation and confidence interval for the overall model are also summarized in the table.

Table 16: Parameter Estimation for Degradation Model, $\mathcal{D}_3$

Case	$\hat{\theta_1}(mm^3)$	$\hat{\theta_2}(mm^2/t)$	$\hat{\theta_3}(mm/t^2)$	RMSE	RMSPE
1	523.6123	0.01613	3.7100×10^{-7}	26.1851	0.8577
2	523.6122	0.01613	3.7099×10^{-7}	26.1741	0.8573
3	523.6159	0.01614	3.9403×10^{-7}	26.1602	0.8568
4	523.6109	0.01609	3.8072×10^{-7}	26.2178	0.8587
5	523.6128	0.01614	3.8428×10^{-7}	26.2370	0.8594
6	523.6100	0.01613	3.7867×10^{-7}	26.2795	0.8608
7	523.6081	0.01614	3.7269×10^{-7}	26.2317	0.8592
8	523.6089	0.01613	3.7988×10^{-7}	26.3005	0.8614
9	523.6111	0.01616	3.7447×10^{-7}	26.1931	0.8579
10	523.6122	0.01613	3.8470×10^{-7}	26.2277	0.8591
11	523.6076	0.01611	3.7350×10^{-7}	26.2786	0.8607
12	523.6065	0.01614	3.7313×10^{-7}	26.1356	0.8560
13	523.6147	0.01609	3.8906×10^{-7}	26.2006	0.8592
14	523.6120	0.01612	3.8276×10^{-7}	26.2608	0.8601
15	523.6113	0.01616	3.8317×10^{-7}	26.2658	0.8603

The parameters in Table (17) were used in degradation model, $\mathcal{D}_1$ to estimate the (C) values. Figure 80 summarizes the plot showing residuals for difference between measured capacitance, (C) and estimated capacitance, ($\hat{C}$) from the model, $\mathcal{D}_1$ for all the 15 capacitors. From the residuals it is observed that initially the residuals are high, as the capacitance

Table 17: Error Summary for Degradation Model, $\mathcal{D}_3$

Parameter	$\bar{X}$	$\tilde{X}$	S.D	C.I
$\hat{\theta}_1(mm^3)$	523.6112	523.6113	0.0026	[523.6098, 523.6127]
$\hat{\theta}_2(mm^2/t)$	0.0161	0.0161	1.8748×10^{-5}	[0.01614, 0.01611]
$\hat{\theta}_3(mm/t^2)$	3.8077×10^{-7}	3.8072×10^{-7}	6.9373×10^{-9}	[0.3769×10^{-6}, 0.3846×10^{-6}]
RMSE	26.2232	26.2277	0.0483	[26.1965, 26.2500]
RMSPE	0.8589	0.8591	0.0016	[0.8580, 0.8598]

calculated from the initial average estimated electrolyte volume value is higher. In the later stages of the aging cycle we observe increase in residual error due to the phenomenon of oxide breakdown discussed earlier in the section.

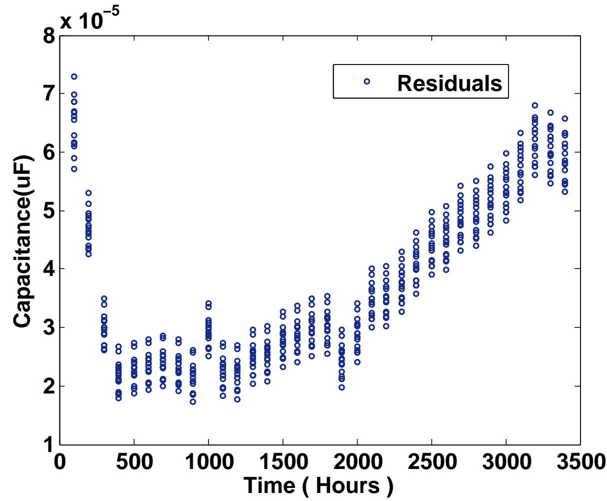

Figure 80: Capacitance (C) measured and estimation residuals

Physics-Based Degradation Models using Kalman Filter

In this section we present extension of our previous work [109,146] . A model-based prognostics algorithm based on Kalman filter and a physics inspired empirical degradation model is presented. The prognostic methodology implemented in this work consists of two parts. The first part consists of a estimation framework where the algorithm estimates the state based on the current conditions of the device and inputs. In second part the algorithm predicts RUL which is defined as the time until health threshold crossed.

In this work we implement a Kalman Filter (KF) since the degradation in capacitance (state) due to decrease in electrolyte is considered to be a dynamic linear model due to the assumption of constant evaporation rate (j_{eo}) under constant thermal stress conditions and the model does not include the capacitance dependence breakdown factor (c_b).

Dynamic Models

From Chapter V and the structure of capacitor we have the electrolyte volume(V_e) expressed in the form of oxide surface area (A_s) as :

$$\begin{aligned} V_e &= A_s.d_C, \\ A_s &= \frac{V_e}{d_C}. \end{aligned} \tag{65}$$

substituting from the Eq. (65) the capacitance for foil type capacitor as discussed earlier is given as:

$$C = \frac{2\epsilon_R \epsilon_0 A_s}{d_C}$$

where:

ϵ_R : relative dielectric constant,

ϵ_O : permitivity of free space,

d_C : oxide layer thickness,

A_s : effective oxide surface area.

From Eq. (20) and Eq. (65), dynamic capacitor degradation model can be updated as :

$$C_k = \left(\frac{2\epsilon_R \epsilon_0}{d_C}\right)\left(\frac{V_{e(k)}}{d_C}\right) \tag{66}$$

From Eq. (20) the first order discrete approximation for change in electrolyte volume can be expressed as:

$$\begin{aligned}\frac{dV_e}{dt} &= -(w_e A_s j_{eo}),\\ V_{e(k+1)} &= V_{e(k)} + \frac{dV_e}{dt}\Delta t,\\ V_{e(k+1)} &= V_{e(k)} - (w_e A_s j_{eo})\Delta t.\end{aligned} \tag{67}$$

From Eq. (66) we have,

$$\begin{aligned}V_{e(k)} &= \frac{C_k}{2\epsilon_R\epsilon_0}d_C^2,\\ V_{e(k)} &= (C_k)\nu.\end{aligned} \tag{68}$$

where:

$$\nu = \frac{d_C^2}{2\epsilon_R\epsilon_0}$$

From Eq. (68) we can express Eq. (67) as :

$$\begin{aligned}C_{k+1}\nu &= C_k\nu + \frac{dC}{dt}\Delta t,\\ C_{k+1}\nu &= C_k\nu - (w_e A_s j_{eo})\Delta t, \text{ hence}\\ C_{k+1} &= C_k - \frac{(w_e A_s j_{eo})}{\nu}\Delta t.\end{aligned} \tag{69}$$

The complete discrete time dynamic model for capacitance degradation can be summarized as :

$$\mathcal{D}_6 : C_{k+1} = C_k - \frac{(2\epsilon_R\epsilon_0 w_e A_s j_{eo})}{d_C^2}\Delta t \tag{70}$$

The model $\mathcal{D}_6$, is implemented in a Bayesian estimation framework. Next we discuss the implementation of the Bayesian framework methodology for prognostics [108,136,139] .

The following steps are implemented in this approach:

1. State estimation: The current measured capacitance (C) is defined as the state variable to be estimated and the degradation model is expressed as a discrete time dynamic model in order to estimate current C, due to decrease in electrolyte volume at the next available measurement. Direct measurements of the C are assumed for the filter.

2. Health state forecasting: It is necessary to forecast the state variable once there are no more measurements available at the end of step 1. This is done by simulating the degradation model through time using the state estimate at time t as initial value.

3. Remaining useful life computation: RUL is computed as the time between time of prediction t and the time at which the forecasted state crosses the failure threshold value.

These steps are repeated for different aging time (t_p) through the life of the capacitor device under test. Thee conditions for uncertainty both in the estimation step as well as in the prediction step are as discussed in Chapter VI for electrical overstress degradation model implementation.

Kalman Filter for Sate Estimation

A state-space dynamic model is needed for filtering. The state variable x_k is the Capacitance and y_k is measured capacitance C_k. Since the system measurements are capacitance (C) as well, the output equation is given by $y_k = H_k\ x_k$, where the value of H is equal to one. The following system structure is implemented for filtering and prediction using a Kalman Filter.

$$\begin{aligned} \mathbf{x}_k &= A_k \mathbf{x}_{k-1} + B_k u + \mathbf{v}, \\ \mathbf{y}_k &= H_k\ \mathbf{x}_k + \mathbf{w}. \end{aligned} \tag{71}$$

where,

$$\begin{aligned} A &= 1, \\ B &= -\frac{(2\epsilon_R \epsilon_0 w_e A_s j_{eo})}{d_C^2} \Delta t, \\ H &= 1, \\ u &= j_{eo}. \end{aligned} \tag{72}$$

In this work and application of KF, the time increment between measurements Δt is not constant since measurements were taken at nonuniform time intervals i.e., the capacitors

were characterized at different time intervals. This implies that some of the parameters of the model in Eqn. (71) will change through time. Furthermore, $\mathbf{v}$ and $\mathbf{w}$ are normal random variables with zero mean and Q and R variance respectively. In order to avoid arbitrary tuning of the covariance matrices, we characterized the model noise (process noise) variance Q based on the estimated value from the model regression residuals and was used for the model noise in the Kalman filter implementation. The measurement noise variance R, was computed from the direct measurements of the capacitance with the EIS equipment, the observed variance is 4.99×10^{-7}. A detailed description of the KF algorithm implemented in this work can be found in [140] , a description of how the algorithm is used for forecasting can be found in [141].

Prognostics Thresholds

In prognostic implementation, it is important know when the performance of the device or system is going to lie outside an unacceptable region of operation. In this region we consider the degraded device or system to have failed. For the device/system to be within the bounds of acceptable performance, we express a set of constraints,c_n, $\mathcal{C} = \{C_i\}_{i=1}^{c_n}$, where C_i is a function

$$C_i : \mathbb{R}^{n_x} \times \mathbb{R}^{n_\theta} \rightarrow \mathbb{B}$$

that maps a given point in the joint state-parameter space,$(x(t), \theta(t)$, to the Boolean domain $\mathbb{R} = [0, 1]$, where $C_i(x(t), \theta(t)) \triangleq 1$ indicates the constrained is satisfied or 0 (failed) if the constrained is not satisfied. Each individual constraint can be combined to form a single constraint output threshold function T_{EOL}, where

$$T_{EOL} : \mathbb{R}^{n_x} \times \mathbb{R}^{n_\theta} \rightarrow \mathbb{B}$$

which is defined as :

$$T_{EOL}(x(t), \theta(t)) = \begin{cases} 1, & 0 \in \{C_i(x(t), \theta(t))\}_{i=1}^{c} \\ 0, & \text{otherwise.} \end{cases} \tag{73}$$

Indicating the for a healthy state of a device/systemT_{EOL} evaluates to 1 and 0 if any of the constraints are violated. At some instance in the aging cyclye at time, t_p , the system is at $(x(t_P);\theta(t_P))$ and we are interested in predicting the time point t at which this state will evolve to $(x(t);\theta(t))$ such that $T_{EOL}(x(t);\theta(t)) = 1$. Using T_{EOL}, we formally define end of life (EOL) of a device/system as:

$$EOL_{t_p} \triangleq \inf\left\{t \in \mathbb{R} : t \geq t_p \wedge T_{EOS}(x(t), \theta(t)) = 1\right\}, \tag{74}$$

i.e., EOL is the earliest instance in the aging cycle at which at which T_{EOL} is valied for a healthy system. RUL is expressed using EOL as

$$RUL(t_p) \triangleq EOL(t_p) - t_p.$$

Prediction Step

Prediction is initiated at a given aging time t_p. Using the current joint state-parameter estimate, $p(x_{tp}, \theta_{tp}|y_{0:t_p})$, which is the current updated information of the system at time t_p , the goal is to compute $p(EOL_{tp}|y_{0:t_p})$ and $p(RUL_{tp}|y_{0:t_p})$.

In case of an Kalman Filter the distribution representation $p(x_{tp}, \theta_{tp}|y_{0:t_p})$ is specified by mean and covariance matrix. Given the finite set of N samples, $\left\{(x_i^{t_p}, \theta_i^{t_p})w_i^{t_p}\right\}_{i=1}^{N}$ each sample i is propagated out to EOL. Each sample is simulated forward to EOL to obtain the complete EOL distribution. The pseudocode for the prediction procedure is given as Algorithm 1 [147, 148]. Each sample, i from the distribution is propagated forward until $T_{EOL}(x_i^{t_p}, \theta_i^{t_p})$ evaluates to 1; at this time in the aging cycle the EOL of the device/system is considered to have reached. In this work we assume future inputs, $\hat{u_k}$ are known, since we have the collected experimental data.

RUL and Validation Results

State estimation and RUL prediction results are discussed for capacitor Cap # 5. Figure 84 out of a batch of 15 available capacitors under test, shows the result of the filter tracking for completed degradation in capacitance upto 3200 hours of aging time. The residuals show an

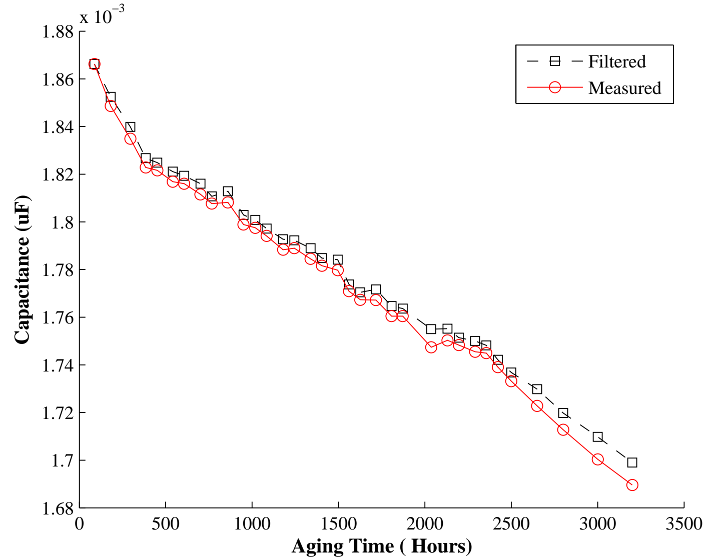

Figure 81: Tracking filter outuput against measurement data for Cap # 5

increased error with aging time, since we have implemented degradation due to a constant evaporation rate under thermal overstress condition and the breakdown in the oxide layer due to stress is not considered for this model which starts to dominate in the later stages of aging of the device. This breakdown is exponential in nature and as we can observe a dip in the capacitance values from the linear path in the later stages.

Figure 85 presents results from the remaining useful life prediction algorithm at different aging times t_p = 87.5, 607, 1495, $2131, 2800$ (hrs), at which the capacitors are characterized and their capacitance (C) value is calculated. The failure threshold is considered to be 10% decrease in capacitance value, which in this case is at 3200 hours of aging time. End of life (EOL) is defined as the time at which the forecasted capacitance value trajectory crosses the EOL threshold. Therefore, RUL is EOL minus aging times $t_p = 87.5, 607, 1495, 2131, 2800$ (hrs).

An α-λ prognostics performance metric $[22, 142]$ is presented in figure 86 for test case of Cap #5. Performance metric identifies whether the algorithm performs within desired error margins (specified by the parameter α) of the actual RUL at any given time instant (specified by the parameter λ) [142]. The central dashed line represents ground truth and the shaded region is corresponding to a 10% ($\alpha = 0.1$) error bound in the RUL prediction.

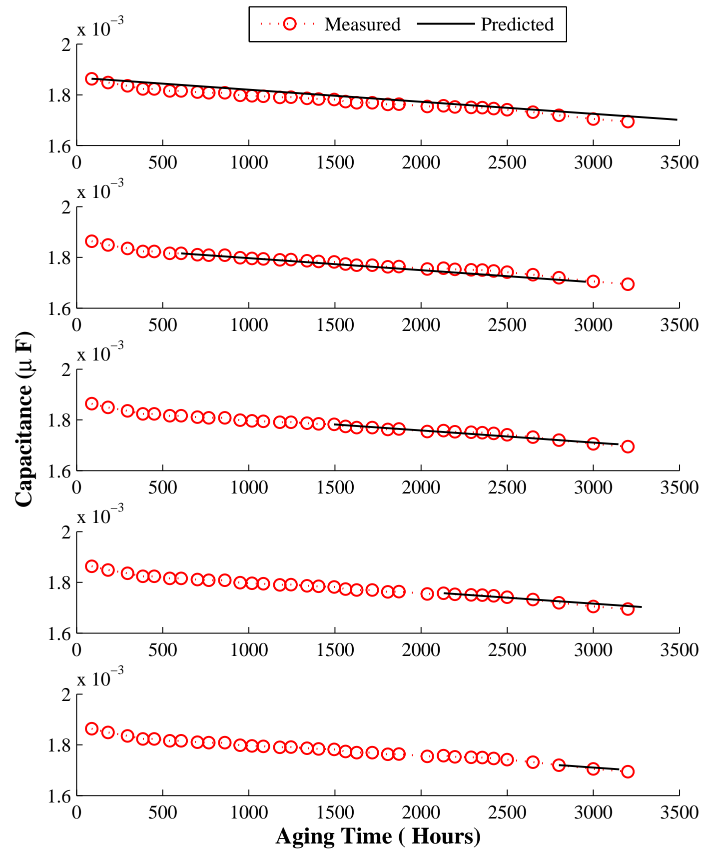

Figure 82: Capacitance decrease prediction at different Aging Time for Cap # 5

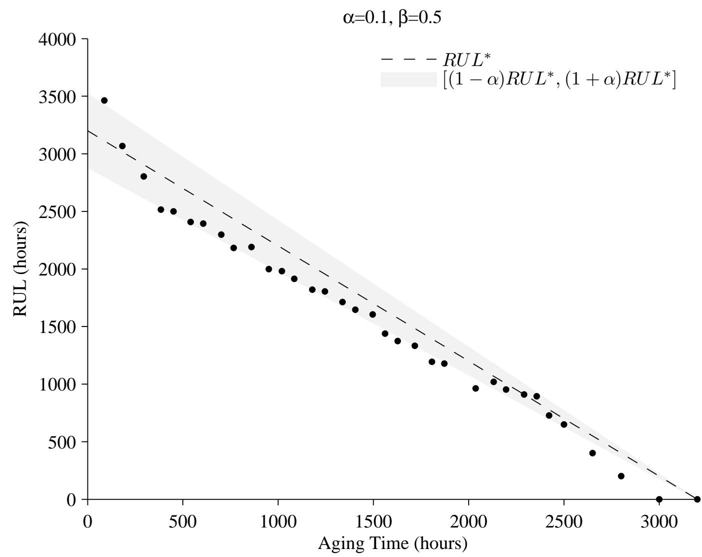

Figure 83: Performance based on Alpha-Lambda metric for Cap#5

From the α-λ metric plot in Fig. 86 it can be observed that the relative accuracy is not as good at the end. But since the type of capacitor we are using have a tolerance of 15-18% the model accuracy is good enough under acceptable limits. For the most part the algorithm is conservative, i.e., RUL predictions are earlier than in reality. Hence the results for this model are not accurate and it is always better to underestimate if the model is not making accurate predictions than than overstimating the RUL. This is due to the non-linearity observed in the data at the end of the aging time. It can be seen that most of the points satisfy the performance metrics and the noise observed in the central part is mainly due to the correction action taken. Other wise we would have observed a biased straight line in case no correction action was applied to the state estimate.

Physics-Based Modeling Framework using Unscented Kalman Filter

In this section we present extension of our previous work [109, 146] . A model-based prognostics algorithm based on UKF and derived physics-based degradation model is presented. The prognostic methodology implemented is similar to the one explained for the KF implementation discussed in the earlier section.

In this work we implement an UKF since the degradation in capacitance (state) due to decrease in electrolyte is considered to be a dynamic linear model. Though the applied stress conditions are similar, there may be variation in each capacitor and hence each device may have a varying evaporation rate. Hence as explained in Chapter VI, evaporation rate (j_{eo}) under constant thermal stress conditions is incorporated as a modeling error in form of a stochastic process and estimated at each step. The model does not include the capacitance dependence breakdown factor (c_b), implementation of which will be discussed in the next section.

From Eqn (21) and derivations for dynamic models discussed in Chapter VI, the derived model, $\mathcal{D}_4$, is given by :

$$\mathcal{D}_4 : C_{k+1} = C_k - \frac{(2\epsilon_R \epsilon_0 w_e A_s j_{eo} c_b)}{d_C^2} \Delta t,$$

Table 18 summarizes the details the parameters that are used in degradation model $\mathcal{D}_4$. Most of the parameters remain constant since similar type of capacitors are used. The initial value of evaporation rate, j_{eo} are referred from [125].

Table 18: Parameter values used for model $\mathcal{D}_4$ - 2200 μF at 105°C

Parameter	Description	Value
ϵ_R	relative dielectric constant	10
ϵ_R	permitivity of free space	$8.8542 \times 10^{-9} F - cm^{-1}$
h_c	height of capacitor capsule	2 cm
d	diameter of capacitor capsule	0.7 cm
l_C	length of the spacer paper roll.	118 cm
T_{rated}	rated temperature	$85°C$
j_{eo}	evaporation rate	$\approx 0.2079 \times 10^{-3}\ mg/hr - cm^2$
d_c	thickness of oxide layer	2.22×10^{-5} cm
w_e	volume of ethyl glycol molecule	$5.66 \times 10^{-9}\ cm^3$
ρ_E	electrolyte resistivity	$8 \times 10^2\ \Omega - cm$
P_E	correlation factor of capacitor	$\approx 2 - 3.5$

Model $\mathcal{D}_4$, is implemented in a Bayesian tracking framework. In this work we are implementing a unscented Kalman filter (UKF). As seen in previous section, results with KF not so good, and hypothesis is that, a constant j_{eo} was used as input for all the capacitors. Though each capacitor is manufactured from the same batch and subjected to same conditions due to variations each capacitors degrades in slightly different manner. Hence to improve the model it is essential to estimate the evaporation rate parameter online in addition to the state (instead of having it as an input). Next we discuss the implementation of the Bayesian framework methodology for prognostics [21, 108, 136].

The steps followed for UKF filter implementation as same as discussed for model $\mathcal{D}_4$ in Chapter VI along with the conditions specified for uncertainty, conditions for prognostics thresholds and prediction steps.

Prediction of RUL and Validation Tests

State estimation and RUL estimation results are discussed for capacitor Cap # 5 out of a batch of 15 available capacitors under test. Figure 84 shows the result of filter tracking for degradation in capacitance upto 3200 hours of aging time. The capacitance tolerance is around 15% and the output errors are in the range of $10 - 20\mu F$ indicating the estimates for model tracking are within acceptable limits.

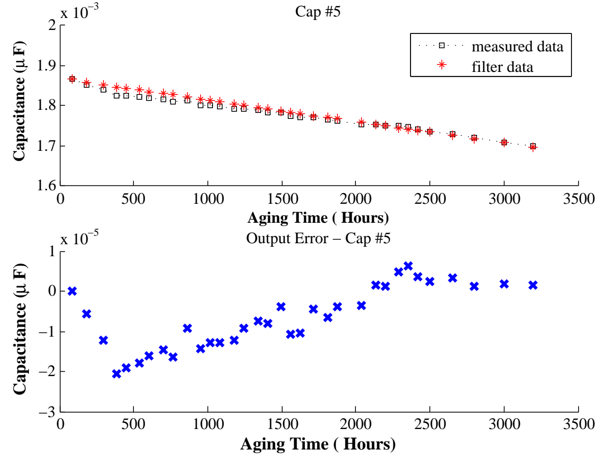

Figure 84: Tracking filter output against measurement data for Cap # 5

RUL

Figure 85 presents results from the remaining useful life prediction algorithm at different aging times $t_p = 87$, 607, 1495, $2131, 2800$ (hrs), at which the capacitors are characterized and their capacitance (C) value is calculated. The failure threshold is considered to be 10% decrease in capacitance value, which in this case is at 3200 hours of aging time. End of life (EOL) is defined as the time at which the forecasted capacitance value trajectory crosses the EOL threshold. Therefore, RUL is EOL minus aging times $t_p = 87.5, 607, 1495, 2131, 2800$ (hrs).

Validation Test

An Alpha-Lambda(α-λ) prognostics performance metric [22, 142] is presented in Figure 86 for test case of Cap #5. The central dashed line represents ground truth and the shaded

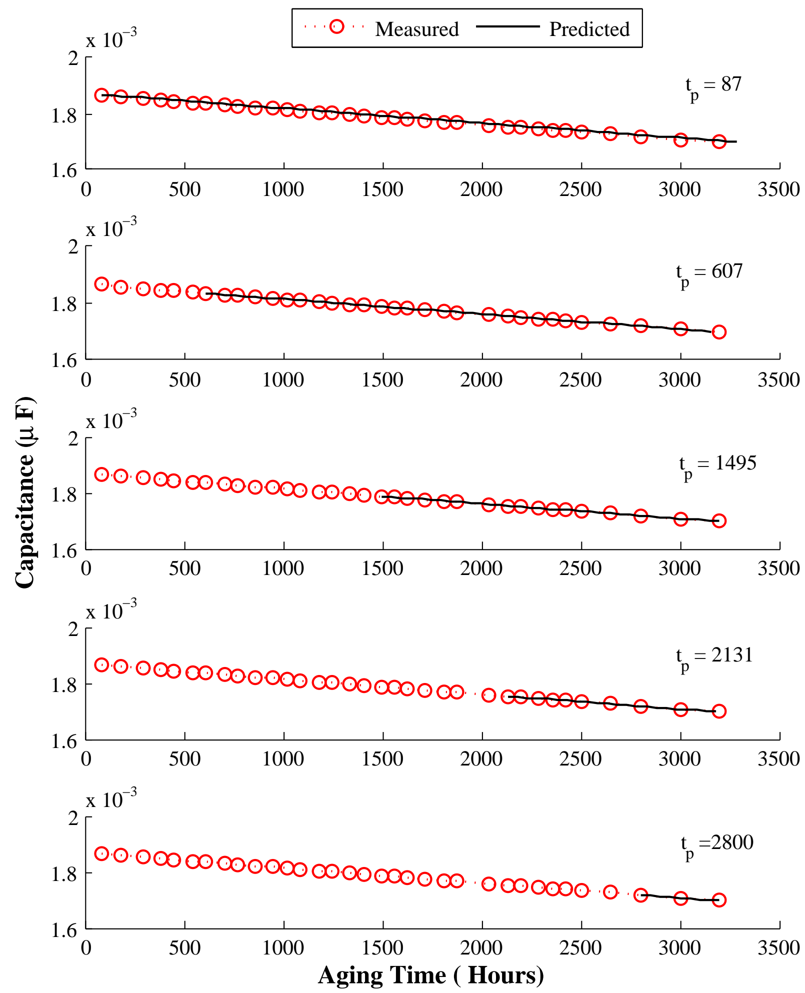

Figure 85: Capacitance decrease prediction at different Aging Time for Cap # 5

region is corresponding to a 30% ($\alpha = 0.3$) error bound in the RUL prediction. Performance metric identifies whether the algorithm performs within desired error margins (specified by the parameter α) of the actual RUL at any given time instant (specified by the parameter λ) [142] and is based on relative accuracy (RA) metric in Eqn. (75). With the α-λ metric, we check at each prediction point whether β of the distribution lies within α of the true RUL. In the figure, the accuracy bound defined by $\alpha = 30\%$ is shown as a gray cone, and we select $\beta = 50\%$.

$$RA = 100\left(1 - \frac{|RUL^{*} - RUL^{'}|}{RUL^{*}}\right) \tag{75}$$

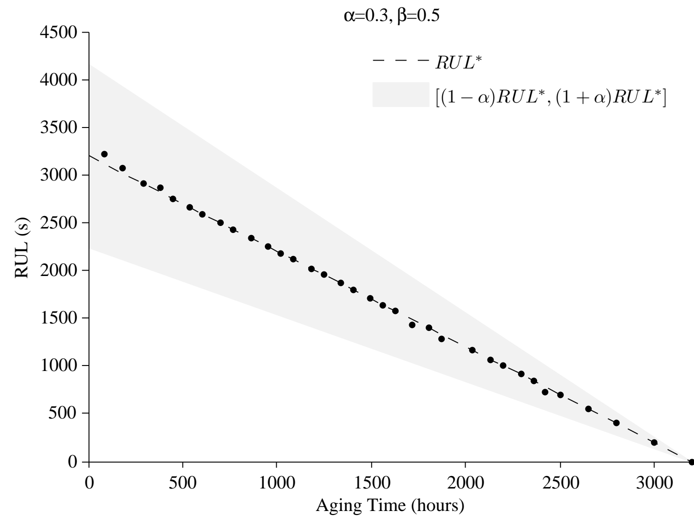

Figure 86: Performance based on Alpha-Lambda metric for Cap#5

Table 19 shows the performance summary based on the RA of all the capacitors under thermal stress performance. RUL^{*} is the ground truth from the experimental data while $RUL^{'}$ is the predicted RUL. These metrics allows for an assessment of the percentage accuracy relative to the ground-truth value. RA values of 100 represent perfect accuracy. The RA is presented for all the test cases for different prediction times. The last column of Table 19 represents the median RA of all the test cases for a particular prediction time. It must be noted that if the prediction error magnitude grows beyond 100% RA gives a negative value. We do not consider such cases since these cases would not have qualify the tests for calculating RA [142], these are indicated by NA in Table 19.

From the α-λ metric plot in Figure 86 it can be observed that the relative accuracy is not as good at the end but the accuracy is good enough under acceptable limits. This is due to the non-linearity observed in the data at the end of the aging time and the limitation of the model due to not including the oxide layer breakdown. The residuals show an increased error with aging time, since the breakdown in the oxide layer observed due to stress is not considered for this model which starts to dominate in the later stages of aging of the device. This breakdown is exponential in nature and as we can observe a dip in the capacitance values from the linear path in the later stages.

Table 19: Summary of RUL forecasting results with j_{eo} estimation - 2200μF

Aging Time	C1	C2	C3	C4	C5	C6	C7	C8	C9	C10	C11	C12	C13	C14	C15	$\overline{RA}_a$
181.67	98.34	95.03	100.00	98.34	98.34	98.34	98.34	93.37	98.34	96.69	91.72	91.72	98.34	98.34	96.69	96.80
295.38	98.28	94.84	98.28	100.00	100.00	98.28	98.28	93.11	98.28	96.56	93.11	91.39	98.28	100.00	96.56	97.02
384.47	98.22	94.67	100.00	100.00	98.22	98.22	98.22	92.90	98.22	96.45	91.12	91.12	98.22	98.22	96.45	96.69
450.93	98.18	94.54	98.18	100.00	100.00	100.00	98.18	92.72	98.18	96.36	92.72	90.91	98.18	100.00	98.18	97.09
540.77	98.12	94.36	100.00	100.00	100.00	98.12	98.12	92.48	98.12	96.24	92.48	90.60	98.12	100.00	96.24	96.87
607.07	98.07	94.22	98.07	100.00	100.00	100.00	98.07	92.29	98.07	96.14	92.29	90.36	98.07	100.00	98.07	96.91
701.62	98.00	94.00	98.00	100.00	100.00	100.00	98.00	91.99	98.00	96.00	91.99	89.99	98.00	100.00	98.00	96.80
766.83	97.95	91.78	97.95	100.00	100.00	100.00	100.00	93.84	97.95	93.84	91.78	89.73	97.95	100.00	97.95	96.71
860.43	97.86	93.59	97.86	100.00	100.00	100.00	97.86	93.59	97.86	95.73	91.45	89.31	97.86	100.00	97.86	96.72
950.07	97.78	93.33	97.78	100.00	100.00	100.00	97.78	93.33	97.78	95.56	91.11	88.89	97.78	100.00	97.78	96.59
1019	100.00	90.83	97.71	100.00	100.00	100.00	100.00	93.12	97.71	93.12	93.12	88.54	95.41	100.00	97.71	96.48
1084.47	97.64	92.91	100.00	100.00	100.00	100.00	97.64	92.91	97.64	95.27	90.55	90.55	97.64	100.00	97.64	96.69
1179.5	97.53	92.58	100.00	100.00	100.00	100.00	97.53	92.58	97.53	95.05	90.10	90.10	97.53	100.00	97.53	96.54
1244.82	97.44	92.33	100.00	100.00	100.00	100.00	97.44	92.33	97.44	94.89	92.33	89.77	97.44	100.00	97.44	96.59
1338.18	97.31	91.94	100.00	100.00	100.00	100.00	97.31	94.63	97.31	94.63	91.94	89.26	97.31	100.00	97.31	96.60
1404.48	97.22	91.65	100.00	100.00	100.00	97.22	100.00	94.43	97.22	94.43	91.65	88.86	97.22	100.00	97.22	96.47
1495.4	97.07	91.20	100.00	100.00	100.00	97.07	97.07	94.13	97.07	94.13	91.20	88.27	97.07	100.00	97.07	96.09
1560.48	96.95	90.85	100.00	100.00	100.00	96.95	100.00	96.95	96.95	90.85	93.90	87.80	96.95	96.95	100.00	96.34
1626.53	96.82	93.64	96.82	100.00	100.00	96.82	96.82	96.82	100.00	93.64	90.47	90.47	96.82	100.00	96.82	96.40
1716.57	96.63	89.89	100.00	100.00	96.63	93.26	100.00	100.00	96.63	89.89	93.26	86.52	96.63	96.63	100.00	95.73
1807.02	96.41	89.23	96.41	100.00	100.00	92.82	100.00	100.00	96.41	92.82	96.41	89.23	96.41	96.41	100.00	96.17
1871.62	96.24	88.71	96.24	100.00	96.24	92.47	100.00	96.24	96.24	88.71	96.24	88.71	96.24	96.24	96.24	94.98
2036.88	91.40	91.40	91.40	100.00	100.00	91.40	95.70	95.70	100.00	91.40	95.70	91.40	100.00	95.70	100.00	95.41
2131.35	90.64	95.32	90.64	95.32	100.00	90.64	95.32	95.32	95.32	90.64	95.32	90.64	100.00	95.32	95.32	94.39
2196.1	90.04	95.02	90.04	100.00	100.00	90.04	95.02	90.04	95.02	90.04	100.00	95.02	100.00	95.02	95.02	94.69
2290.12	83.51	94.50	83.51	94.50	100.00	89.01	94.50	83.51	94.50	89.01	100.00	94.50	100.00	94.50	94.50	92.67
2355.97	82.23	94.08	82.23	94.08	100.00	82.23	94.08	82.23	94.08	88.15	100.00	100.00	100.00	94.08	88.15	91.71
2421.92	80.72	100.00	80.72	100.00	93.57	74.30	100.00	74.30	93.57	87.15	93.57	100.00	100.00	87.15	87.15	90.15
2500	71.43	100.00	71.43	92.86	100.00	71.43	92.86	64.29	85.71	85.71	92.86	92.86	92.86	85.71	85.71	85.71
2650	54.55	90.91	54.55	90.91	100.00	63.64	90.91	54.55	72.73	90.91	81.82	81.82	90.91	81.82	72.73	78.18
2800	37.50	75.00	37.50	75.00	100.00	37.50	87.50	25.00	62.50	87.50	75.00	62.50	75.00	75.00	62.50	65.00
3000	NA	25.00	NA	50.00	100.00	0.00	75.00	NA	0.00	75.00	25.00	NA	50.00	50.00	25.00	43.18
$\overline{RA}_b$	87.13	90.78	87.99	96.60	99.39	89.29	94.45	85.73	92.14	92.50	90.32	87.15	95.49	94.97	92.38	

Physics Based Modeling Framework using UKF for 2200 μF capacitors

In this section we present extension of the work to the earlier section where we estimated the evaporation rate parameter j_{eo}. In this section we discuss the degradation model where we update the model to estimate oxide breakdown factor,(c_b) in addition with evaporation rate, j_{eo}. The details of the derived model are explained in section VII. The degradation data for this set is as shown in Figure 75.

From Eqn.25 and other derivations in Chapter V, we have the time dependent degradation models, $\mathcal{D}_1$ for capacitance (C) given by :

$$\mathcal{D}_1 : C(t) = \left(\frac{2\ \epsilon_R\ \epsilon_0\ c_b}{d_C}\right)\left(\frac{V_{e0} - V_e(t)}{j_{eo}\ t\ w_e}\right),$$

The complete discrete time dynamic model for capacitance degradation as derived in section VII is :

$$\begin{aligned}\mathcal{D}_4 : C_{k+1} &= C_k - \frac{(2\epsilon_R\epsilon_0 w_e A_s j_{eo} c_b)}{d_C^2}\Delta t,\\ c_{b(k+1)} &= c_{b(k)} - \xi e^{\xi}.\end{aligned}$$

The model $\mathcal{D}_4$, in Eqn. (VIII) is implemented in a Bayesian tracking framework. An Unscented Kalman Filter (K.F) framework is implemented since the degradation in capacitance (state) due to decrease in electrolyte is considered to be a dynamic non-linear model since evaporation rate (j_{eo}) and oxide layer breakdown factor (c_b) are estimated online based on the state values. The steps followed for UKF filter implementation as same as discussed for model $\mathcal{D}_4$ in Chapter VI along with the conditions specified for uncertainty, conditions for prognostics thresholds and prediction steps.

Table 20 summarizes the details the parameters that are used in degradation models $\mathcal{D}_4$. Most of the parameters remain constant since similar type of capacitors are used. The initial value of evaporation rate, j_{eo} are referred from [125].

Table 20: Parameter values used for models $\mathcal{D}_4$ - 2200 μF at 105°C

Parameter	Description	Value
ϵ_R	relative dielectric constant	10
ϵ_R	permitivity of free space	$8.8542 \times 10^{-9} F - cm^{-1}$
h_c	height of capacitor capsule	2 cm
d	diameter of capacitor capsule	0.7 cm
l_C	length of the spacer paper roll.	118 cm
T_{rated}	rated temperature	$85°C$
j_{eo}	evaporation rate	$0.2079 \times 10^{-3}\ mg/hr - cm^2$
d_c	thickness of oxide layer	2.22×10^{-5} cm
w_e	volume of ethyl glycol molecule	$5.66 \times 10^{-9}\ cm^3$
ρ_E	electrolyte resistivity	$8 \times 10^2\ \Omega - cm$
P_E	correlation factor of capacitor	$\approx 2 - 3.5$

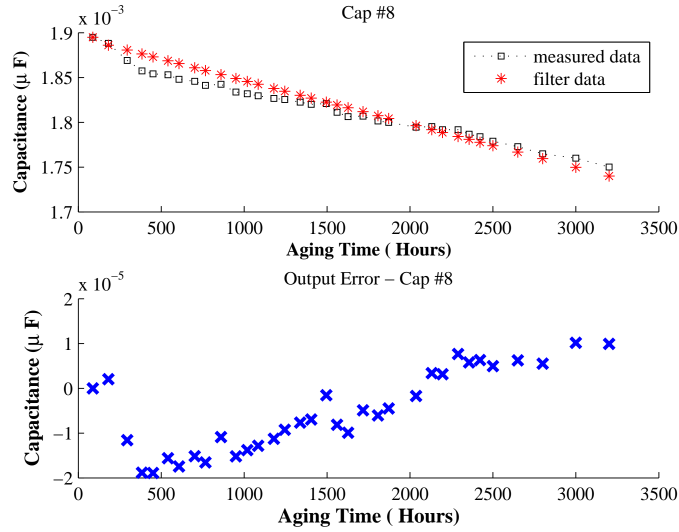

Figure 87: Tracking filter output against measurement data for Cap # 8

Prediction of RUL and Validation Tests

State estimation and RUL prediction results are discussed for capacitor Cap # 8. Figure 87 out of a batch of 15 available capacitors under test, shows the result of the filter tracking for completed degradation in capacitance upto 3200 hours of aging time. As can be observed from the residuals the tracking of the model with respect to the data in acceptable. The model tracks well since it incorporates the electrolyte evaporation (j_{eo}) parameter as well as the oxide layer breakdown factor, (c_b).

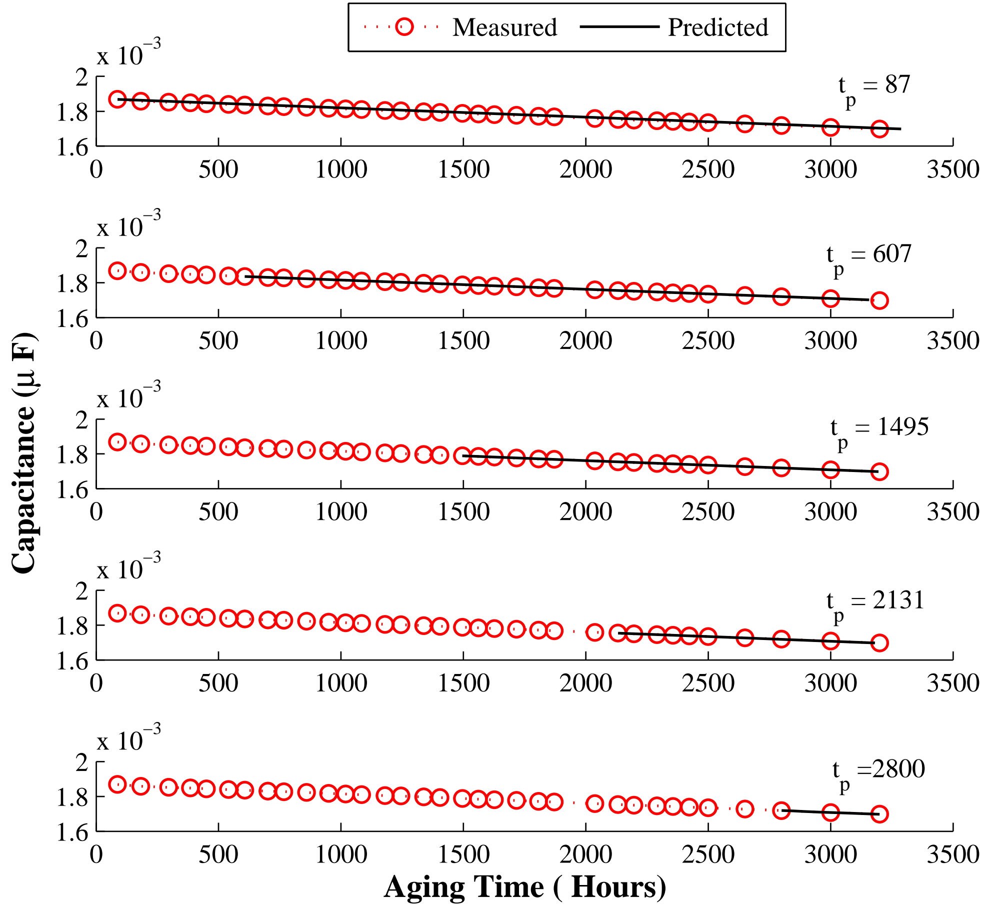

Figure 88: Capacitance decrease prediction at different Aging Time for Cap # 8

RUL

Figure 88 presents results from the remaining useful life prediction algorithm at different aging times $t_p = 87.5, 607, 1495, 2131, 2800$ (hrs), at which the capacitors are characterized and their capacitance (C) value is calculated. The failure threshold is considered to be 10% decrease in capacitance value, which in this case is at 3200 hours of aging time. End of life (EOL) is defined as the time at which the forecasted capacitance value trajectory crosses the EOL threshold. Therefore, RUL is EOL minus aging times $t_p = 87.5, 607, 1495, 2131, 2800$ (hrs).

Validation Tests

An α-λ prognostics performance metric [22, 142] is presented in Figure 89 for test case of Cap #8. The central dashed line represents ground truth and the shaded region is

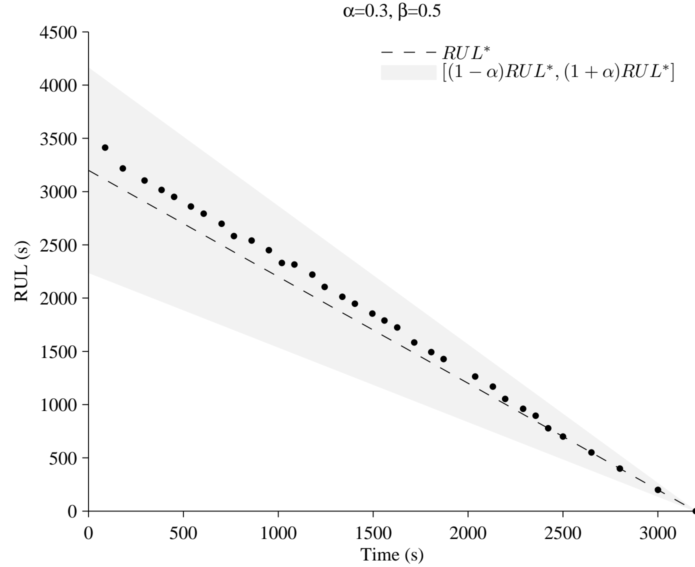

Figure 89: Performance based on Alpha-Lambda metric for Cap#8

corresponding to a 30% ($\alpha = 0.3$) error bound in the RUL prediction. From the α-λ metric plot in Figure. 89 it can be observed that the relative accuracy is good till the end of the experiment time and the accuracy is good enough under acceptable limits. As mentioned earlier this is due to inclusion of the degradation parameters and estimating them as the capacitance changes with degradation.

Table 21 presents the capacitance loss estimation and EOL prediction at different points during the aging time. Predictions are made after each point in which measurements are available. It can be observed that the predictions become better as the prediction is made closer to the actual EOL. This is possible because the estimation process has more information to update the estimates as it nears EOL.

Table 21: Summary of RUL forecasting results with j_{eo} and c_b estimation - 2200μF

Aging Time	C1	C2	C3	C4	C5	C6	C7	C8	C9	C10	C11	C12	C13	C14	C15	$\overline{RA}_a$
181.67	90.36	90.36	90.36	90.36	90.36	90.36	90.36	90.36	90.36	90.36	90.36	90.36	90.36	90.36	90.36	90.36
295.38	93.37	93.37	93.37	93.37	93.37	93.37	93.37	93.37	93.37	93.37	93.37	93.37	93.37	93.37	93.37	93.37
384.47	93.11	93.11	93.11	93.11	93.11	93.11	93.11	93.11	93.11	93.11	93.11	93.11	93.11	93.11	93.11	93.11
450.93	92.90	92.90	92.90	92.90	92.90	92.90	92.90	92.90	92.90	92.90	92.90	92.90	92.90	92.90	92.90	92.90
540.77	92.72	92.72	92.72	92.72	92.72	92.72	92.72	92.72	92.72	92.72	92.72	92.72	92.72	92.72	92.72	92.72
607.07	92.48	92.48	92.48	92.48	92.48	92.48	92.48	92.48	92.48	92.48	92.48	92.48	92.48	92.48	92.48	92.48
701.62	94.22	94.22	94.22	94.22	94.22	92.29	94.22	92.29	94.22	94.22	92.29	94.22	94.22	92.29	92.29	93.57
766.83	94.00	94.00	94.00	94.00	94.00	91.99	94.00	91.99	94.00	94.00	91.99	94.00	94.00	91.99	91.99	93.33
860.43	93.84	93.84	93.84	93.84	93.84	93.84	93.84	93.84	93.84	93.84	93.84	93.84	93.84	93.84	93.84	93.84
950.07	93.59	93.59	93.59	93.59	93.59	91.45	93.59	91.45	93.59	93.59	91.45	93.59	93.59	91.45	91.45	92.88
1019	93.33	93.33	93.33	93.33	93.33	91.11	93.33	91.11	93.33	93.33	91.11	93.33	93.33	91.11	91.11	92.59
1084.47	93.12	93.12	93.12	93.12	93.12	93.12	93.12	93.12	93.12	93.12	93.12	93.12	93.12	93.12	93.12	93.12
1179.5	90.55	90.55	90.55	92.91	92.91	90.55	92.91	90.55	90.55	92.91	90.55	90.55	90.55	90.55	90.55	91.18
1244.82	90.10	90.10	90.10	92.58	92.58	90.10	92.58	90.10	90.10	92.58	90.10	90.10	90.10	90.10	90.10	90.76
1338.18	92.33	92.33	92.33	92.33	92.33	92.33	92.33	92.33	92.33	92.33	92.33	92.33	92.33	92.33	89.77	92.16
1404.48	91.94	91.94	91.94	91.94	91.94	91.94	91.94	91.94	91.94	91.94	91.94	91.94	91.94	91.94	89.26	91.76
1495.4	91.65	91.65	91.65	91.65	91.65	91.65	91.65	91.65	91.65	91.65	91.65	91.65	91.65	91.65	91.65	91.65
1560.48	91.20	91.20	91.20	91.20	91.20	91.20	91.20	91.20	91.20	91.20	91.20	91.20	91.20	91.20	91.20	91.20
1626.53	93.90	93.90	93.90	93.90	93.90	90.85	93.90	90.85	93.90	93.90	90.85	93.90	93.90	90.85	90.85	92.88
1716.57	90.47	90.47	90.47	90.47	90.47	90.47	90.47	90.47	90.47	90.47	90.47	90.47	90.47	90.47	90.47	90.47
1807.02	93.26	93.26	93.26	93.26	93.26	93.26	93.26	93.26	93.26	93.26	93.26	93.26	93.26	93.26	93.26	93.26
1871.62	92.82	92.82	92.82	92.82	92.82	92.82	92.82	92.82	92.82	92.82	92.82	92.82	92.82	92.82	92.82	92.82
2036.88	96.24	96.24	92.47	96.24	96.24	92.47	96.24	92.47	96.24	96.24	92.47	92.47	96.24	92.47	92.47	94.48
2131.35	91.40	91.40	91.40	91.40	91.40	91.40	91.40	91.40	91.40	91.40	91.40	91.40	91.40	91.40	91.40	91.40
2196.1	90.64	90.64	90.64	90.64	95.32	90.64	90.64	90.64	90.64	90.64	90.64	90.64	90.64	90.64	90.64	90.95
2290.12	95.02	90.04	90.04	95.02	95.02	90.04	95.02	95.02	95.02	95.02	90.04	90.04	95.02	90.04	90.04	92.70
2355.97	94.50	94.50	89.01	94.50	94.50	94.50	94.50	94.50	94.50	94.50	94.50	89.01	94.50	89.01	89.01	93.04
2421.92	94.08	94.08	94.08	94.08	100.00	94.08	100.00	94.08	94.08	94.08	94.08	88.15	94.08	94.08	94.08	94.47
2500	100.00	93.57	93.57	100.00	100.00	100.00	100.00	100.00	100.00	100.00	100.00	93.57	100.00	93.57	93.57	97.86
2650	92.86	92.86	92.86	100.00	100.00	92.86	100.00	100.00	92.86	100.00	92.86	85.71	92.86	92.86	92.86	94.76
2800	90.91	90.91	90.91	100.00	100.00	100.00	100.00	100.00	90.91	100.00	100.00	81.82	100.00	90.91	90.91	95.15
3000	87.50	87.50	87.50	100.00	100.00	100.00	100.00	100.00	87.50	100.00	100.00	75.00	100.00	100.00	100.00	95.00
3200	75.00	75.00	75.00	100.00	100.00	100.00	100.00	100.00	75.00	100.00	100.00	50.00	100.00	100.00	100.00	90.00
$\overline{RA}_b$	92.22	91.88	91.60	94.00	94.32	93.03	94.18	93.39	92.22	94.00	93.03	89.79	93.64	92.39	92.23	

Physics Based Modeling Framework using UKF for 10000 μF capacitors

In this section we present our work where we use the same physics degradation model to validate against a different set of capacitors. In this experiment we subjected set of capacitors rated at at 10000 μF, 10V and maximum storage temperature of 85°C, from the same manufacturing lot were used for the experiment. Similar to the earlier thermal overstress setup the chamber temperature was gradually increased in steps of 25°C till the pre-determined temperature limit was reached. The capacitors were allowed to settle at a set temperature for 15 min and then the next step increase was applied and was continued till the required temperature was attained. The degradation data for this set is as shown in Figure 75.

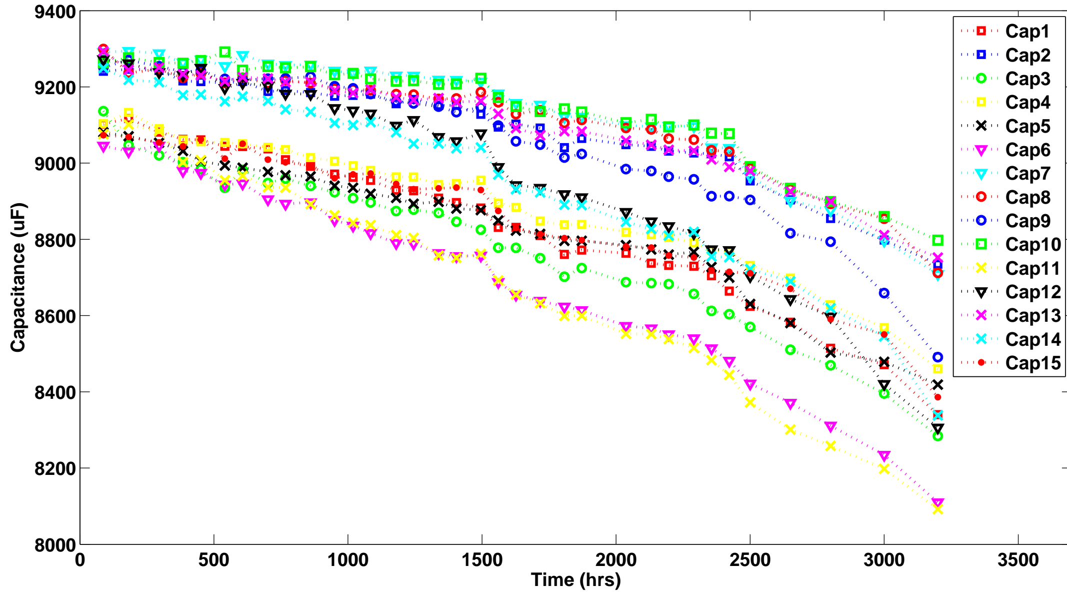

Figure 90: Thermal Overstress at 105° C - 10000uF

Similar to the earlier section we estimate the oxide layer breakdown factor,(c_b) in addition with evaporation rate, j_{eo} for a different set of data with same derived physics degradation models. The only parameters which were updated in this model were the structural parameters of height(h_c), paper length, (l_c) to estimate the initial electrolyte volume. The details of the derived model are explained in section VII.

From Eqn.25 and other derivations in Chapter V, we have the time dependent degradation models, $\mathcal{D}_1$ for capacitance (C) given by :

$$\mathcal{D}_1 : C(t) = \left(\frac{2\ \epsilon_R\ \epsilon_0\ c_b}{d_C}\right)\left(\frac{V_{e0} - V_e(t)}{j_{eo}\ t\ w_e}\right),$$

And the complete discrete time dynamic model for capacitance degradation as derived in section VII is :

$$\mathcal{D}_4 : C_{k+1} = C_k - \frac{(2\epsilon_R\epsilon_0 w_e A_s j_{eo} c_b)}{d_C^2}\Delta t,$$
$$c_{b(k+1)} = c_{b(k)} - \xi e^{\xi}.$$

The model $\mathcal{D}_4$, in Eqn. (VIII) is implemented in a Bayesian tracking framework. An Unscented Kalman Filter (K.F) framework is implemented since the degradation in capacitance (state) due to decrease in electrolyte is considered to be a dynamic non-linear model since evaporation rate (j_{eo}) and oxide breakdown factor (c_b) are estimated online based on the state values. Table 22 summarizes the details the parameters that are used in degradation models $\mathcal{D}_4$. Most of the parameters remain constant since similar type of capacitors are used. The initial value of evaporation rate, j_{eo} are referred from [125].

Table 22: Parameter values used for models $\mathcal{D}_4$ - 10000 μF at 105°C

Parameter	Description	Value
ϵ_R	relative dielectric constant	10
ϵ_R	permitivity of free space	$8.8542 \times 10^{-9} F - cm^{-1}$
h_c	height of capacitor capsule	3.5 cm
d	diameter of capacitor capsule	1.0 cm
l_C	length of the spacer paper roll.	118 cm
T_{rated}	rated temperature	$85°C$
j_{eo}	evaporation rate	$0.2079 \times 10^{-3}\ mg/hr - cm^2$
d_c	thickness of oxide layer	2.22×10^{-5} cm
w_e	volume of ethyl glycol molecule	$5.66 \times 10^{-9}\ cm^3$
ρ_E	electrolyte resistivity	$8 \times 10^2\ \Omega - cm$
P_E	correlation factor of capacitor	$\approx 2 - 3.5$

Prediction of RUL and Validation Tests

Plots of State estimation and RUL prediction results are discussed for capacitor Cap #7. Figure 91 out of a batch of 15 available capacitors under test, shows the result of the filter tracking for completed degradation in capacitance upto 3200 hours of aging time. As can be

observed from the residuals the tracking of the model with respect to the data in acceptable. The model tracks well since it incorporates the electrolyte evaporation (j_{eo}) parameter as well as the oxide layer breakdown factor, (c_b).

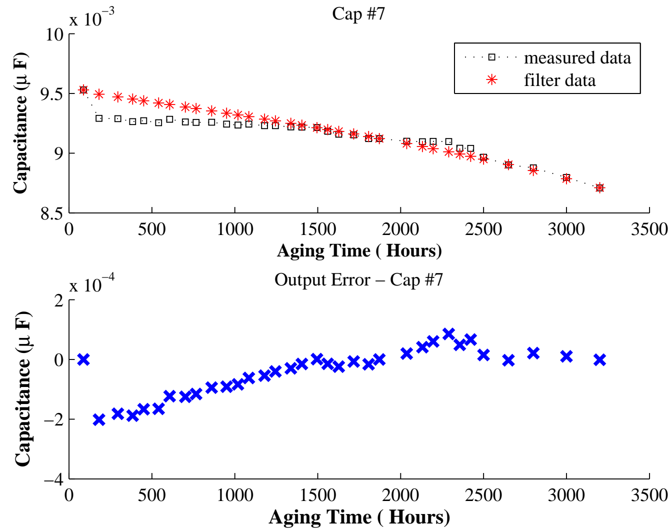

Figure 91: Tracking filter output against measurement data for Cap # 7

RUL

Figure 92 presents results from the remaining useful life prediction algorithm at different aging times $t_p = 87.5$, 607, 1495, $2131, 2800$ (hrs), at which the capacitors are characterized and their capacitance (C) value is calculated. The failure threshold is considered to be 10% decrease in capacitance value, which in this case is at 3200 hours of aging time. End of life (EOL) is defined as the time at which the forecasted capacitance value trajectory crosses the EOL threshold. Therefore, RUL is EOL minus aging times $t_p = 87.5, 607, 1495, 2131, 2800$ (hrs).

Validation Tests

An Alpha-Lambda (α-λ) prognostics performance metric for 10000μF is presented in figure 93 for test case of Cap #7. Performance metric identifies whether the algorithm performs within desired error margins (specified by the parameter α) of the actual RUL at any given time instant (specified by the parameter λ) [142]. The α-λ metric also allows us to visual-

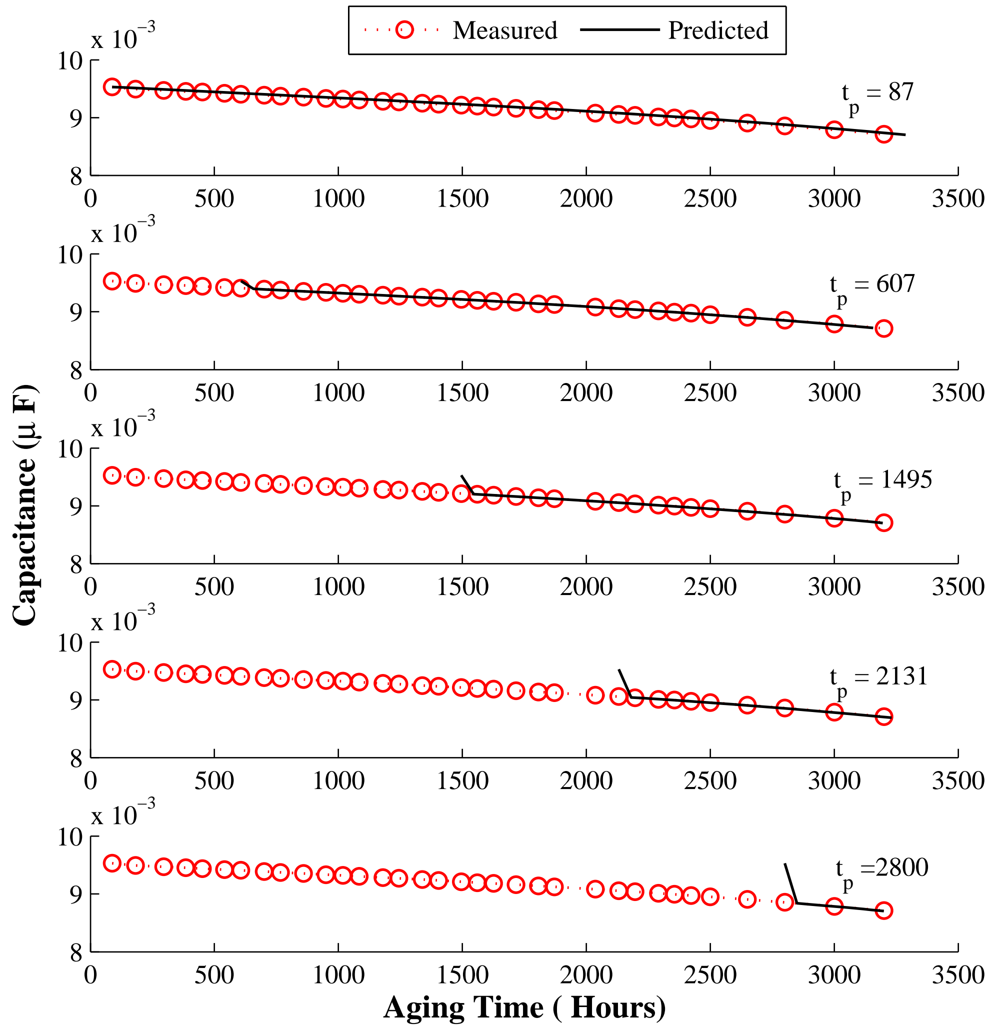

Figure 92: Capacitance decrease prediction at different Aging Time for Cap # 7

ize how the RUL prediction performance changes as data closer to EOL becomes available. The central dashed line represents ground truth and the shaded region is corresponding to a 30% ($\alpha = 0.3$) error bound in the RUL prediction. From the α-λ metric plot in Fig. 93 it can be observed that the relative accuracy is good till the end of the experiment time and the accuracy is good enough under acceptable limits. As mentioned earlier this is due to inclusion of the degradation parameters and estimating them as the capacitance changes with degradation.

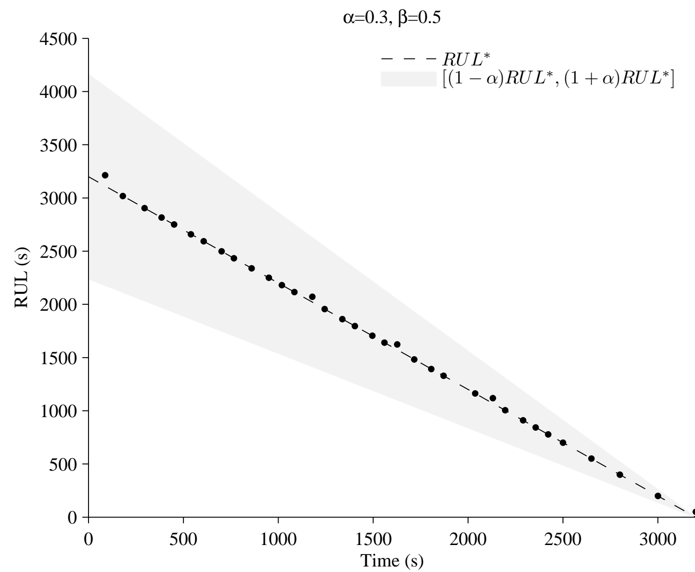

Figure 93: Performance based on Alpha-Lambda metric for Cap#7

Table 23 presents the capacitance loss estimation and EOL prediction at different points during the aging time. Predictions are made after each point in which measurements are available. It can be observed that the predictions become better as the prediction is made closer to the actual EOL. This is possible because the estimation process has more information to update the estimates as it nears EOL.

Table 23: Summary of RUL forecasting results with j_{eo} and c_b estimation - 10000μF

Aging Time	C1	C2	C3	C4	C5	C6	C7	C8	C9	C10	C11	C12	C13	C14	C15	$\overline{RA}_a$
87.75	98.39	98.39	96.79	96.79	96.79	96.79	96.79	96.79	95.18	98.39	96.79	96.79	100.00	98.39	96.79	97.32
181.67	98.34	96.69	100.00	100.00	100.00	100.00	100.00	100.00	98.34	98.34	100.00	100.00	98.34	100.00	100.00	99.34
295.38	98.28	94.84	100.00	100.00	100.00	100.00	100.00	100.00	98.28	98.28	100.00	100.00	98.28	98.28	100.00	99.08
384.47	98.22	96.45	100.00	100.00	100.00	100.00	100.00	100.00	98.22	98.22	100.00	100.00	98.22	98.22	100.00	99.17
450.93	98.18	94.54	100.00	100.00	100.00	100.00	100.00	100.00	98.18	98.18	100.00	100.00	96.36	98.18	100.00	98.91
540.77	98.12	96.24	100.00	100.00	100.00	100.00	100.00	100.00	98.12	98.12	100.00	100.00	98.12	98.12	100.00	99.12
607.07	98.07	94.22	100.00	100.00	100.00	100.00	100.00	100.00	100.00	98.07	100.00	100.00	96.14	98.07	100.00	98.97
701.62	98.00	94.00	100.00	100.00	100.00	100.00	100.00	100.00	98.00	98.00	100.00	100.00	96.00	98.00	100.00	98.80
766.83	97.95	93.84	97.95	97.95	100.00	97.95	100.00	100.00	100.00	97.95	97.95	97.95	95.89	97.95	97.95	98.08
860.43	97.86	93.59	97.86	100.00	100.00	97.86	100.00	100.00	100.00	97.86	100.00	100.00	95.73	97.86	100.00	98.58
950.07	97.78	93.33	100.00	100.00	100.00	100.00	100.00	100.00	97.78	97.78	100.00	100.00	95.56	97.78	100.00	98.67
1019	97.71	93.12	97.71	97.71	100.00	97.71	100.00	100.00	100.00	97.71	97.71	97.71	95.41	97.71	97.71	97.86
1084.47	97.64	95.27	100.00	100.00	100.00	100.00	100.00	100.00	97.64	97.64	100.00	100.00	97.64	97.64	100.00	98.90
1179.5	100.00	95.05	100.00	100.00	100.00	100.00	97.53	100.00	97.53	97.53	100.00	100.00	97.53	100.00	100.00	99.01
1244.82	97.44	92.33	100.00	100.00	100.00	100.00	100.00	100.00	97.44	97.44	100.00	100.00	97.44	97.44	100.00	98.64
1338.18	97.31	94.63	100.00	100.00	100.00	100.00	100.00	100.00	97.31	97.31	100.00	100.00	97.31	97.31	100.00	98.75
1404.48	97.22	91.65	100.00	100.00	100.00	100.00	100.00	100.00	97.22	97.22	100.00	100.00	94.43	97.22	100.00	98.33
1495.4	97.07	91.20	100.00	100.00	100.00	100.00	100.00	100.00	97.07	97.07	100.00	100.00	97.07	97.07	100.00	98.44
1560.48	96.95	90.85	96.95	100.00	100.00	96.95	100.00	100.00	100.00	96.95	100.00	100.00	93.90	96.95	100.00	97.97
1626.53	100.00	93.64	100.00	100.00	100.00	100.00	96.82	100.00	96.82	96.82	100.00	100.00	96.82	100.00	100.00	98.73
1716.57	96.63	89.89	96.63	96.63	100.00	96.63	100.00	100.00	100.00	96.63	96.63	100.00	93.26	96.63	96.63	97.08
1807.02	96.41	89.23	100.00	100.00	100.00	100.00	100.00	100.00	96.41	96.41	100.00	100.00	92.82	96.41	100.00	97.85
1871.62	96.24	88.71	96.24	96.24	100.00	96.24	100.00	100.00	100.00	96.24	96.24	96.24	92.47	96.24	96.24	96.49
2036.88	95.70	91.40	100.00	100.00	100.00	100.00	100.00	100.00	95.70	95.70	100.00	100.00	95.70	100.00	100.00	98.28
2131.35	100.00	90.64	100.00	100.00	100.00	100.00	95.32	100.00	95.32	95.32	100.00	100.00	95.32	100.00	100.00	98.13
2196.1	95.02	85.06	100.00	100.00	100.00	100.00	100.00	100.00	95.02	95.02	100.00	100.00	95.02	95.02	100.00	97.34
2290.12	94.50	89.01	100.00	100.00	100.00	100.00	100.00	100.00	94.50	94.50	100.00	100.00	94.50	94.50	100.00	97.44
2355.97	94.08	82.23	100.00	100.00	100.00	100.00	100.00	100.00	94.08	94.08	100.00	100.00	88.15	94.08	100.00	96.45
2421.92	93.57	80.72	93.57	93.57	100.00	93.57	100.00	100.00	100.00	93.57	93.57	100.00	87.15	93.57	93.57	94.43
2500	92.86	78.57	100.00	100.00	100.00	100.00	100.00	100.00	92.86	92.86	100.00	100.00	85.71	92.86	100.00	95.71
2650	90.91	72.73	100.00	100.00	100.00	100.00	100.00	100.00	90.91	90.91	100.00	100.00	81.82	90.91	100.00	94.55
2800	87.50	62.50	100.00	100.00	100.00	100.00	100.00	100.00	87.50	87.50	100.00	100.00	75.00	100.00	100.00	93.33
3000	100.00	25.00	100.00	100.00	100.00	100.00	100.00	100.00	75.00	75.00	100.00	100.00	50.00	100.00	100.00	88.33
$\overline{RA}_b$	96.79	88.17	99.20	99.36	99.90	99.20	99.59	99.90	96.38	95.72	99.36	99.66	92.82	97.35	99.36	

Discussion and Summary

This chapter presents a first principles based degradation electrolytic capacitor model and a parameter estimation algorithm to validate the derived model, based on the thermal overstress experimental data. The major contributions of the work presented in this chapter are:

1. Identification of the lumped-parameter model, $\mathcal{M}_2$ and $\mathcal{M}_3$, based on the equivalent electrical circuit of a real capacitor as a viable reduced-order model for prognostics-algorithm development;
2. Developing the thermal capacitance experiments based on the failure modes observed and collecting and analyzing data at regular intervals.
3. Identification of C as a failure precursor in the lumped parameter model, $\mathcal{M}_2$ as shown in Figure 70;
4. Estimating the electrolyte volume from structural model of the capacitor to be implemented in the first principles degradation model, $\mathcal{D}_3$;
5. Implementation of parameter estimation algorithm to cross validate the derived first principles degradation model, $\mathcal{D}_1$.
6. Development of the first principles degradation model based on accelerated life test aging data which includes decrease in capacitance as a function of time and evaporation rate linked to temperature conditions;
7. We discussed the results and prediction implementing the Kalman Filter and Unscented Kalman Filters.

The physics-based capacitance degradation model, $\mathcal{D}_1$ gives an indication of how a specific device degrades based on its geometric structure and operating conditions. The derived model can be updated and developed at a more finer granularlarity to be implemented for detailed prognostic implementation. The results presented here are based on accelerated

aging experimental data and on the accelerated life timescale. This extends our previous work where we derived empirical degradation models from accelerated aging data.

The performance of the derived physics-based capacitance degradation model, $\mathcal{D}_4$ was successfully achieved based on the RUL results for the experimental data and cross validation performance for the two separate data sets.

CHAPTER VIII

NOMINAL DEGRADATION

Introduction

Nominal degradation is the damage observed in the capacitor when it is operated for long periods under normal operating conditions. We study continuous operation of these capacitors in DC-DC power converters. Continuous operation under rated or below rated applied voltage also results in a slow but steady accumulation of damage. The damage accumulation or performance degradation for these capacitors is monotonic during most of the aging period and it accelerates exponentially during the end of life stage. A study of the literature [126, 149–151] indicates that the degradation in electrolytic capacitors under EOS can be primarily attributed to three phenomena

1. The operation of the capacitors under nominal rating will result in slow electrolyte evaporation.
2. Electrolyte evaporation results in a decrease in C and an increase in ESR.
3. This evaporation process is slow, and visible degradation effects may take years to manifest.
4. Aging of oxide material leading to breakdown. Again, this may take a long time to manifest, but once the phenomena occurs, the degradation process accelerates.

The heat generated internally when current passes through the capacitor during its nominal operation cycle is transmitted from the core to the surface of the capacitor, leads to evaporation of the electrolyte [116]. Though as mentioned earlier this is a slower process since relatively less heat is generated during nominal operation. In addition to this, as the capacitor continues to degrade over time, eventually another phenomenon manifests in the form of oxide layer breakdown, which leads to further deterioration in the capacitor causing the capacitance to decrease significantly. The physics-based degradation models associated

with electrolyte evaporation and oxide layer breakdown were discussed in Chapter V. Their relevance and application to accelerated degradation situations were described in Chapter VI and Chapter VII. In this chapter, we first discuss the electrical equivalent model and the setup for the nominal degradation experiments. We then implement an empirical model for ESR and further study each of the derived degradation model in detail along with the RUL prediction results and discussion.

Equivalent Electrical Circuits

A simplified electrical lumped parameter model of impedance, $\mathcal{M}_1$, also used for our electrical and thermal overstress models is shown in Fig.94.

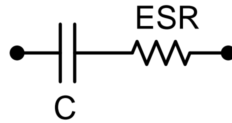

Figure 94: Lumped Parameter Model ($\mathcal{M}_1$)

Nominal Degradation Experiment

Under nominal operation, the DC-DC converters we use(Figure 95) has a rated input voltage of 22V-28V DC, sourced through a power supply operating at room temperature . This source is likely to be 28V DC in case of avionics systems. This converter, purchased off the shelf, met all the specifications for the experiment. Configuration for the converter hardware is similar to the schematic of the DC-DC converter presented earlier in Chapter IV. The main hardware components include the MOSFET's, isolating transformers, pulse width modulation (PWM) controller chip and an electrolytic capacitor functioning as a filter at the output. The capacitor is subjected to stresses due to long periods of operations at a constant voltage output. The capacitor leads are made available so that measurements can be made easily without any added measurement noise and without disturbing the rest of the system setup.

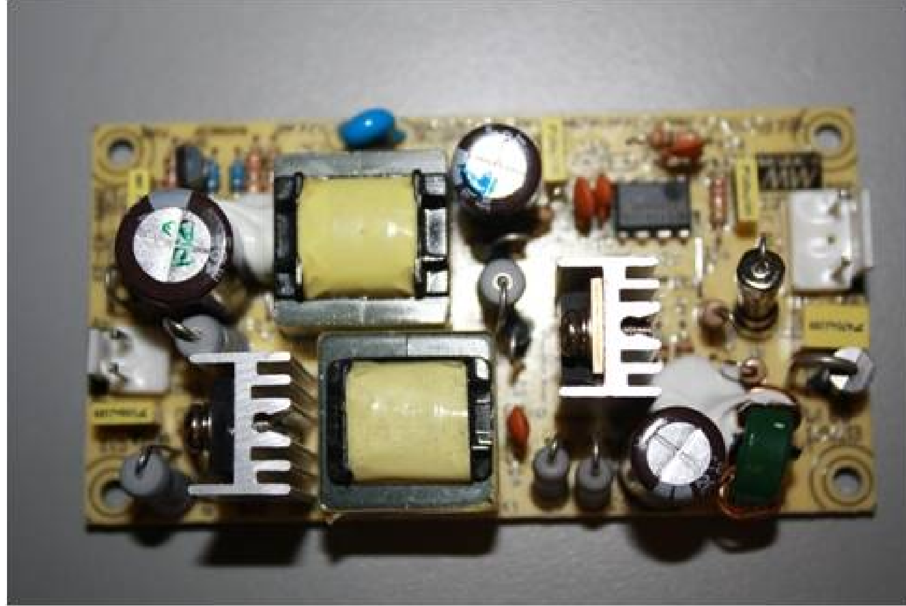

Figure 95: DC-DC converter Hardware

Three sets of DC-DC converter hardware units were considered for the experiment as seen in Fig. 96. Electrolytic capacitors of 2200μF capacitance value, with a maximum rated voltage of 10V, maximum current rating of 1A and maximum operating temperature of 85°C were used for the study suggested by the manufacturers of the converters. The capacitors used for the experiments were picked from the same manufacturing lot, and all the capacitors in the lot had similar specifications. The electrolytic capacitors under test were characterized using an the Biologic SP-150 [145], which measures the impedance parameters.

The average initial ESR value was measured to be around 0.049Ω and the average capacitance of 2068μF for the three electrolytic capacitors under test. An input DC voltage of 22V is supplied from a steady voltage source to the DC-DC power supply converter. At the output, a constant value of 5V with ripples within the accepted noise tolerance of 1% was observed. All the three converters were subjected to testing test under similar opeating conditions, measurements for all the three capacitors on these converters were taken at the same time interval.

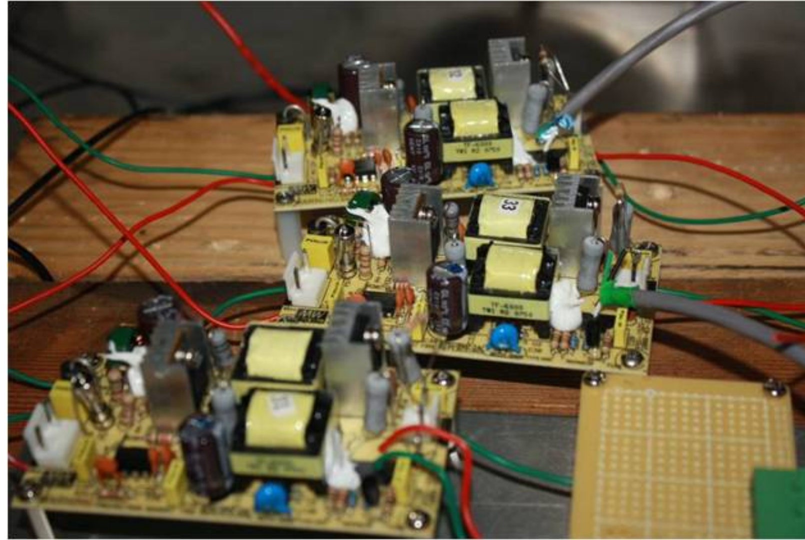

Figure 96: Experimental Setup for 3 DC-DC converter Units

The ESR measurements were made approximately every 150 - 200 hours during the aging process. The ambient temperature for the experiment was controlled and kept at 25°C. During each measurement the voltage source was shut down, all the capacitors were allowed to discharge completely before they were characterized using the impedance measurement instrument. The EIS measurements and steps are the same that are followed in Chapter VI. Keeping all the conditions intact the experiment was started again till the next measurement. This procedure was repeated for all the subsequent measurements in the experiment.

Plots in Figure 98 show the decrease in capacitance value while plots if Figure 97 show ESR increase for all the three capacitor devices under test operating under normal conditions . The three capacitors and the converter units were subjected to similar conditions of temperature, input voltage and loading. As observed from Figure 97 upto 3200 hours of operation we observed almost a linear increase in the ESR value, and a change in the slope was observed in the ESR value after about 3200 hours of operation indicating inception of the breakdown phenomenon in the degradation process. At the end of 3600 hours of operation the average capacitor ESR value increased by approximately 110% of the initial value.

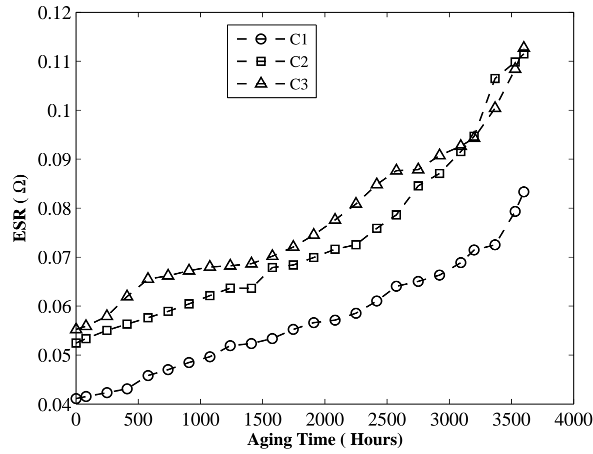

Figure 97: ESR degradation under Nominal Operating Conditions

Similarly in Figure 98 an initial decrease in the capacitance value was observed which then stabilized after a few hundred hours and decreased at a linear rate towards the middle aging period. When the aging time reached 2800 hrs, a non-linear change in the capacitance was observed. As discussed earlier in the EOS and TOS experiments this could be attributed to increase in dominance of the oxide breakdown phenomenon. It was observed that at the end of 3600 hours the capacitance decreased by and average of 12% from its initial value.

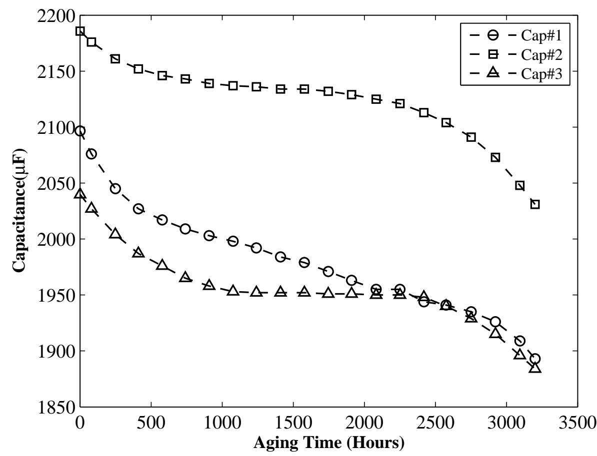

Figure 98: Capacitance Degradation under Nominal Operating Conditions

Empirical Model

In the initial stages of the research work we analyzed the data and implemented an empirical model to study degradation in ESR. The data analyzed from the experiments was compared

with empirical model based on the Arrhenius Law [149]. A linear inverse model has been derived as an extension of Arrhenius Law to define the change in ESR value over time for a capacitor subjected to a constant high temperature. This model was first discussed in [24,41]. The linear inverse model for computing ESR value at time t for a given operating temperature T is given by:

$$\frac{1}{ESR_t} = \frac{1}{ESR_0}\left[1 - k.t.exp\left(\frac{-4700}{T+273}\right)\right] \tag{76}$$

where :

- ESR_t : ESR value at time t,

- T : operating temperature,

- t : aging time,

- ESR_0 : initial ESR value at pristine condition.

- k : constant factor which depends on the design and the construction of the capacitor.

The factor k depends on the parameters, such as the size of the capacitor. The value of k is typically determined empirically for a particular class of capacitors and derived in [24]. We simulated the model under similar conditions of the nominal degradation experiment and compared the results against each capacitor. The plots in Figures 99, 100 and 101 compare the results from the empirical model against the actuals ESR measurements from experimental data.

As can be observed from the plots, the empirical model tracks the degradation well in the initial stages of aging cycle. Though all the three capacitors are from the same manufacturing lots and type, each capacitor degrades differently and the model could not predict these variations. Furthermore, for two capacitors specifically #1 and #3 the capacitors degrade at a different rate than predicted by the model.

These models are specifically used in reliability studies to make generalized failure estimations for a set of manufactured components. While in case of physics-derived models, since the underlying degradation phenomenon due to operation is considered while deriving

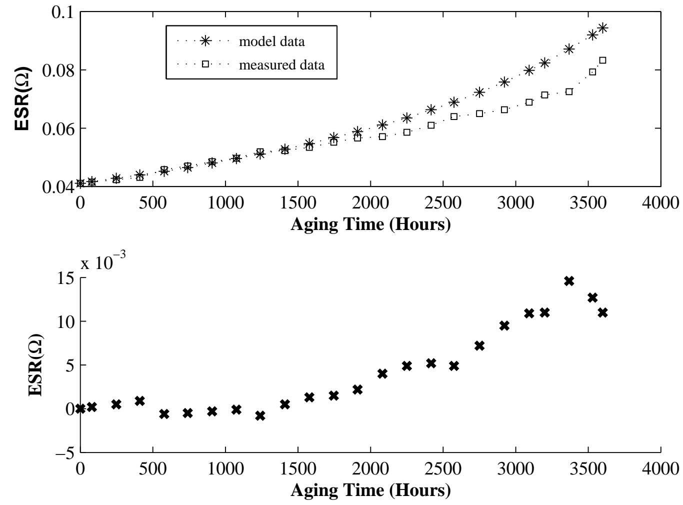

Figure 99: Arrhenius model data against measurement data for Cap# 1

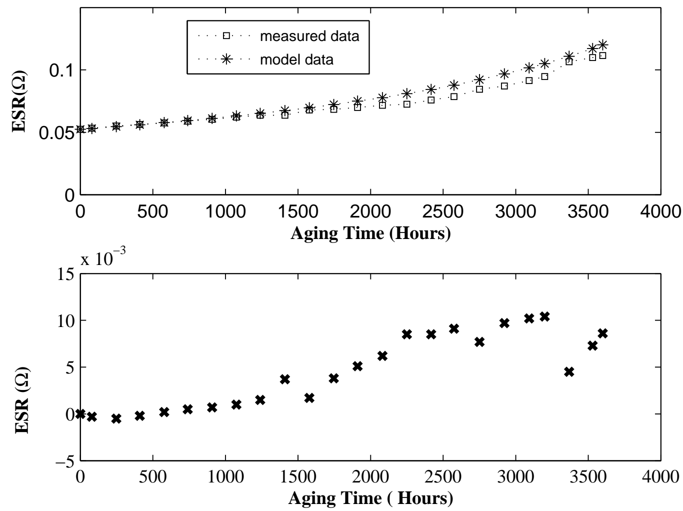

Figure 100: Arrhenius model data against measurement data for Cap# 2

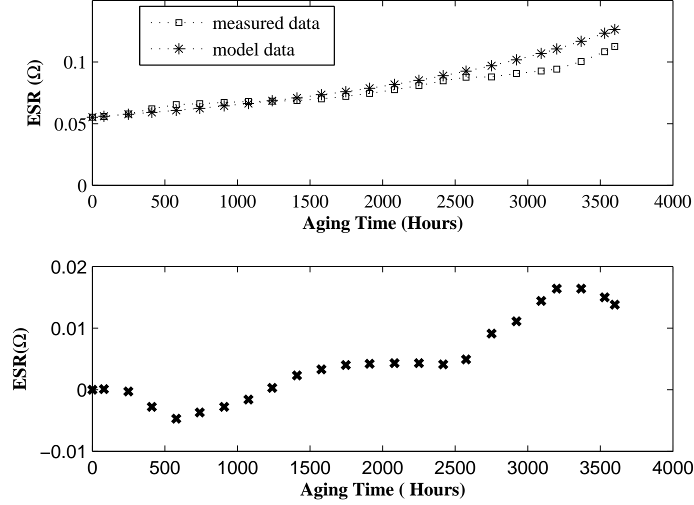

Figure 101: Arrhenius model data against measurement data for Cap# 3

the models we are able to track the degradation changes and make more perfect estimates than an empirical model. In the next section we discuss the physics-based degradation model and results for nominal degradation experiment data.

Degradation Dynamic Models

We used the same degradation model which we derived in Chapter V. From Eqn.(25) and other derivations in Chapter V, we have the time dependent degradation models, $\mathcal{D}_1$ for capacitance (C) given by :

$$\mathcal{D}_1 : C(t) = \left(\frac{2\ \epsilon_R\ \epsilon_0\ c_b}{d_C} \right) \left(\frac{V_{e0} - V_e(t)}{j_{eo}\ t\ w_e} \right),$$

The degradation in capacitance is directly proportional to the variable V_e, which represents the electrolyte volume, capacitance degradation factor, c_b respectively. It also depends on the evaporation rate, j_{eo} which is directly proportional to the operating temperature. Under nominal operating conditions, the oxide layer breakdown has a less prominent effect in the early stages of the aging cycle, the breakdown phenomenon will start to dominate very late in the aging cycle. As discussed earlier, increase in the core temperature evaporates the electrolyte thus decreasing the electrolyte volume leading to degradation in capacitance. Since under nominal condition the amount of heat generated is relatively low we observe

a lower degradation rate as compared to high stress conditions, where the core temperature is high. The resultant decrease in the capacitance can be computed using Eq. (25). The complete discrete time dynamic model for capacitance degradation as derived earlier is given as :

$$\mathcal{D}_4 : C_{k+1} = C_k - \frac{(2\epsilon_R \epsilon_0 w_e A_s j_{eo} c_b)}{d_C^2} \Delta t,$$

$$c_{b(k+1)} = c_{b(k)} - \xi e^{\xi}.$$

Similarly from Eqn. (26), the dynamic ESR degradation model can be expressed as :

$$ESR_k = \frac{1}{2} (\rho_E \; d_C \; P_E \; e_b) \left(\frac{j_{eo} \; t \; w_e}{V_{e(k)}} \right),$$

The complete discrete time dynamic model for ESR degradation derived earlier is given by :

$$\mathcal{D}_5 : \frac{1}{ESR_{k+1}} = \frac{1}{ESR_k} - \frac{2 w_e A_s j_{eo}}{\rho_E \; P_E \; d_C^2 \; e_b} \Delta t,$$

$$e_{b(k+1)} = e_{b(k)} - \xi.$$

The models $\mathcal{D}_4$, and $\mathcal{D}_5$ using a Unscented Kalman Filter (UKF) since in model $\mathcal{D}_4$ the degradation in capacitance (state) due to decrease in electrolyte is considered to be a dynamic non-linear model since evaporation rate (j_{eo}) and capacitance oxide breakdown factor (c_b) are estimated online based on the state values. While in model $\mathcal{D}_5$ the degradation in ESR (state) due to decrease in electrolyte is considered to be a dynamic non-linear model since evaporation rate (j_{eo}) and resistive breakdown factor (c_b) are estimated online based on the state values

Similar steps are followed as in the electrical overstress approach. Table 24 summarizes details of the parameters that are used for degradation models $\mathcal{D}_4$ and $\mathcal{D}_5$. Most of the parameters remain constant since similar type of capacitors are used. The initial value of evaporation rate, j_{eo} for nominal operation is obtained and computed from [125].

Table 24: Parameter values used for degradation models $\mathcal{D}_4$ and $\mathcal{D}_5$ - Nominal

Parameter	Description	Value
ϵ_R	relative dielectric constant	10
ϵ_R	permitivity of free space	$8.8542 \times 10^{-9} F - cm^{-1}$
h_c	height of capacitor capsule	2 cm
d	diameter of capacitor capsule	0.7 cm
l_C	length of the spacer paper roll.	118 cm
T_{rated}	rated temperature	$85°C$
j_{eo}	evaporation rate	$0.0075 \times 10^{-3}\ mg/hr - cm^2$
d_c	thickness of oxide layer	2.22×10^{-5} cm
w_e	volume of ethyl glycol molecule	$5.66 \times 10^{-9}\ cm^3$
ρ_E	electrolyte resistivity	$8 \times 10^2\ \Omega - cm$
P_E	correlation factor of capacitor	$\approx 2 - 3.5$

Prediction of RUL and Validation Tests for Capacitance Degradation Model, $\mathcal{D}_4$

State estimation and RUL prediction results are discussed for all the three capacitors under test. Figures 102, 103 and 104 shows the result of the filter tracking for degradation in capacitance upto 3600 hours of aging time. For all the three capacitors we observed a non-linear decrease in the capacitance very early in the aging cycle, since the model considers an initial linear decrease in the capacitance value we see that the model does not track well in this early aging cycle. This initial decrease stabilizes in the later periods of aging and the model is able to track the degradation in capacitance well. Though we observe higher residuals between the model and the measured data, they are acceptable and still within acceptable limits. In the later stages of the aging cycle when the breakdown phenomenon starts dominating, the model tracks the capacitance data more accurately since it includes the electrolyte evaporation (j_{eo}) parameters as well as the oxide layer breakdown factor, (c_b).

RUL

Plots in Figures 105, 106 and 107, presents results from the remaining useful life prediction algorithm at different aging times $t_p = 80,\ 740,\ 1578,\ 2418, 3200$ (hrs), respectively, at which the three capacitors are characterized and their capacitance value is calculated. The experiments were run till almost 3600 hours and hence the predictions are done till the end of

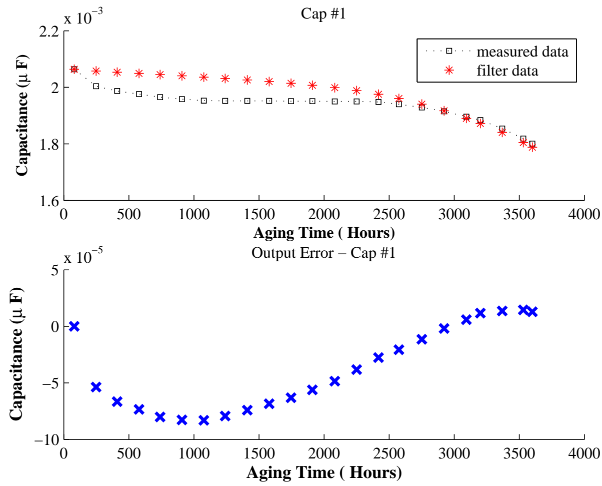

Figure 102: Tracking filter output against measurement data for Cap # 1

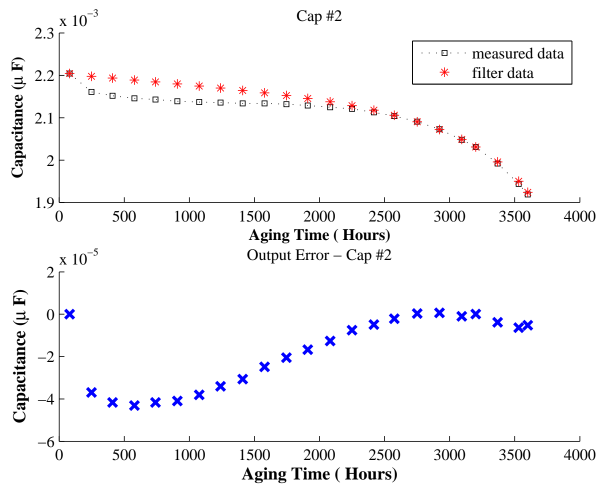

Figure 103: Tracking filter output against measurement data for Cap # 2

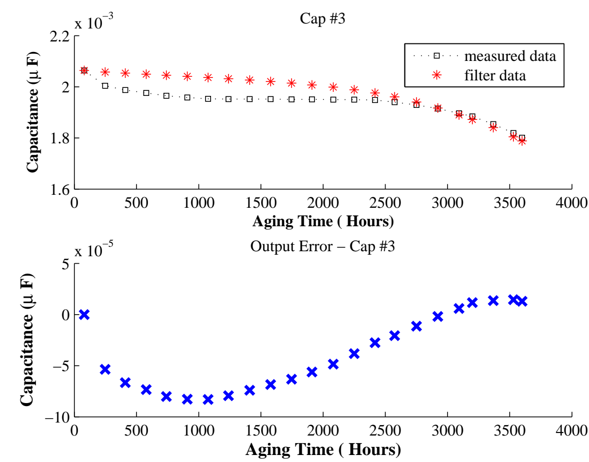

Figure 104: Tracking filter output against measurement data for Cap # 3

experiments. End of life (EOL) is defined as the time at which the forecasted capacitance value trajectory crosses the EOL threshold. Therefore, RUL is EOL minus aging times $t_p = 80, 740, 1578, 2418, 3200$ (hrs).

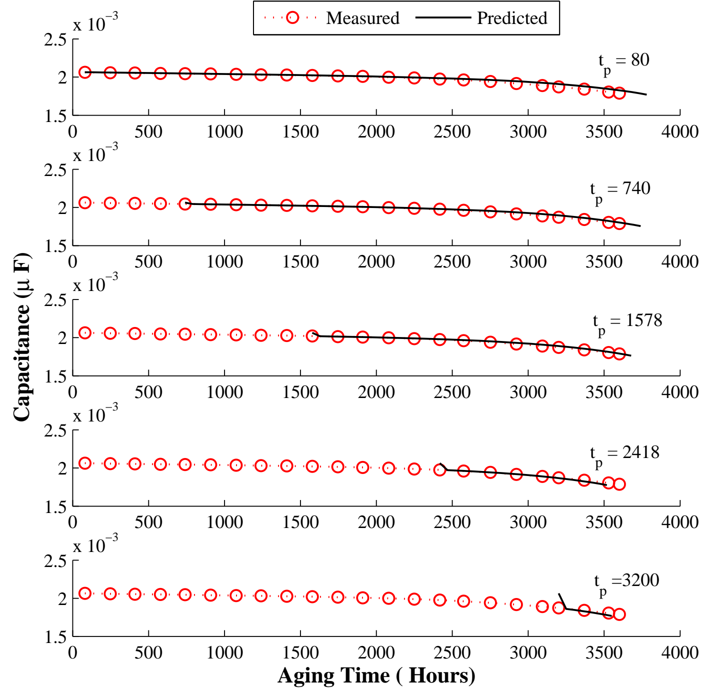

Figure 105: Capacitance decrease prediction at different Aging Time for Cap # 1

Validation Tests

An Alpha-Lambda (α-λ) prognostics performance metric for each of the three capacitors is presented in Figures 108, 109 and 110, respectively. Performance metric identifies whether the algorithm performs within desired error margins (specified by the parameter α) of the actual RUL at any given time instant (specified by the parameter λ) [142]. The central dashed line represents ground truth and the shaded region is corresponding to a 30% ($\alpha = 0.3$) error bound in the RUL prediction. From the α-λ metric plot for all the three figures it can be observed that the relative accuracy is good till the end of the experiment time and the accuracy is good enough under acceptable limits. As mentioned earlier this is due to inclusion of the degradation parameters and estimating them as the capacitance changes with degradation.

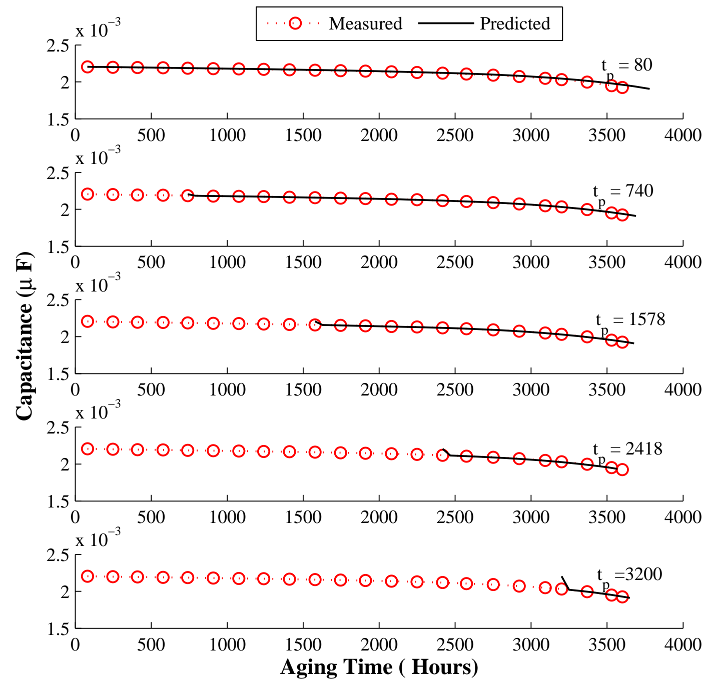

Figure 106: Capacitance decrease prediction at different Aging Time for Cap # 2

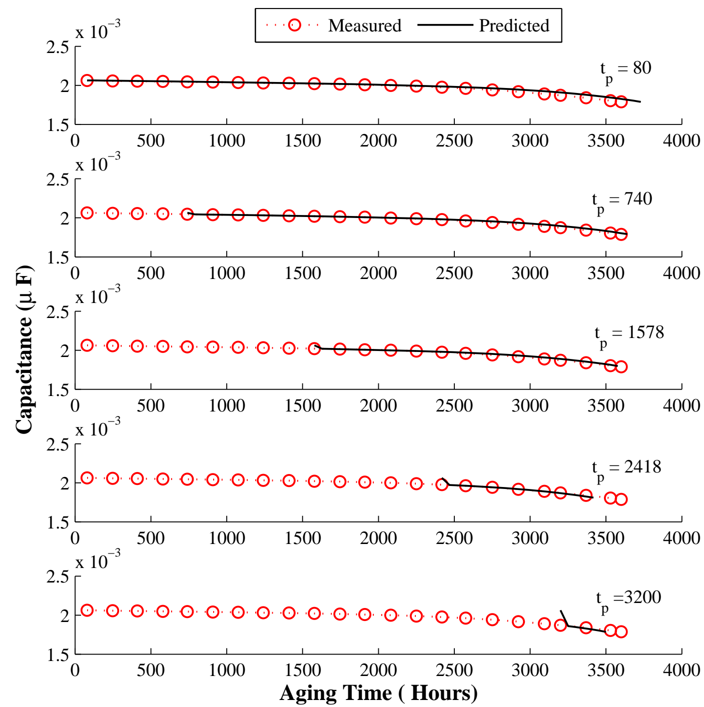

Figure 107: Capacitance decrease prediction at different Aging Time for Cap # 3

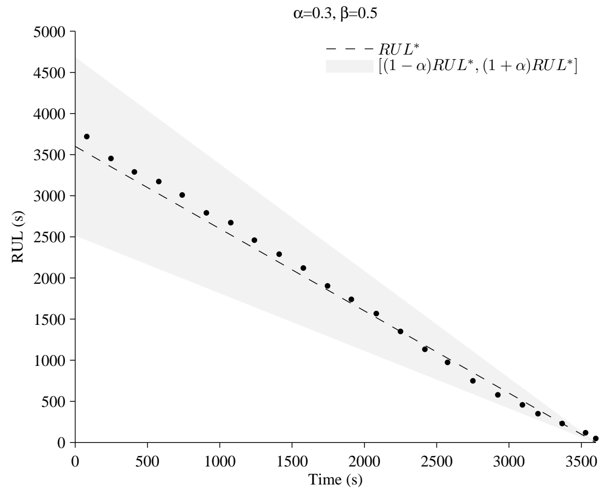

Figure 108: Performance based on Alpha-Lambda metric for Cap#1

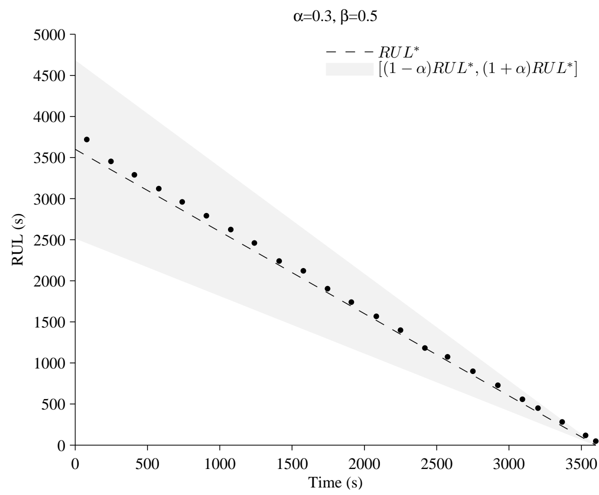

Figure 109: Performance based on Alpha-Lambda metric for Cap#2

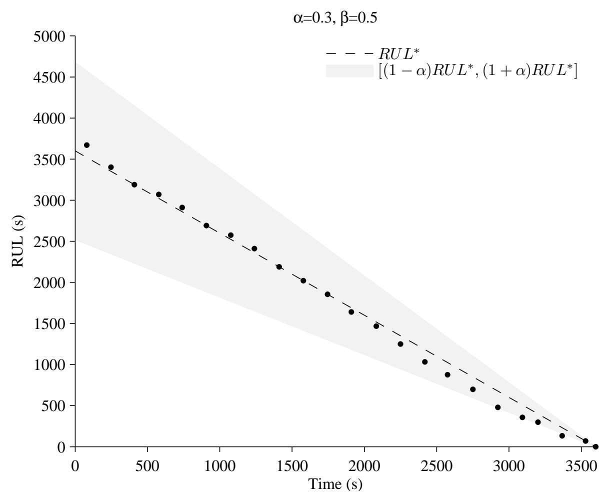

Figure 110: Performance based on Alpha-Lambda metric for Cap#3

Table 25 summarizes the results for all the capacitors and their percentage relative accuracy of capacitance degradation model $\mathcal{D}_4$ for all the capacitors under test. As mentioned earlier model $\mathcal{D}_4$ is used for making predictions for all the capacitors with same parameters, and though it is observed that in the later stages the model performance reduces by some margin the overall accuracy of the model is acceptable.

Table 25: Summary of validation results based on RA for Capacitance degradation model $\mathcal{D}_4$ - Nominal

Aging Time	C1	C2	C3	$\overline{RA}_a$
80	94.32	94.32	95.74	94.79
248	97.02	97.02	98.51	97.51
410	96.87	96.87	100.00	97.91
578	95.04	96.69	98.35	96.69
740	94.76	96.50	98.25	96.50
908	96.29	96.29	100.00	97.52
1076	94.06	96.04	98.02	96.04
1240	95.76	95.76	97.88	96.47
1410	95.43	97.72	100.00	97.72
1578	95.05	95.05	100.00	96.70
1746	97.30	97.30	100.00	98.20
1910	97.04	97.04	97.04	97.04
2082	96.71	96.71	96.71	96.71
2250	100.00	96.30	92.59	96.30
2418	95.77	100.00	87.31	94.36
2575	95.12	95.12	85.37	91.87
2751	88.22	94.11	82.33	88.22
2922	85.25	92.63	70.50	82.79
3093	90.14	90.14	70.41	83.56
3200	87.50	87.50	75.00	83.33
3368	100.00	78.45	56.90	78.45
3530	28.57	28.57	100.00	52.38
$\overline{RA}_b$	91.65	91.64	90.95	

$\overline{RA}_a$ is the mean relative accuracy of all capacitors at each prediction time
$\overline{RA}_b$ is the mean relative accuracy of each capacitor at all prediction times

Prediction of RUL and Validation Tests for ESR Degradation Model, $\mathcal{D}_5$

State estimation and RUL prediction results are discussed for all three capacitors. Figures 111,112, and 113, show the results of the filter tracking degradation in capacitance upto 3600 hours of aging time. As can be observed from the residuals the tracking of the model with respect to the data in acceptable.

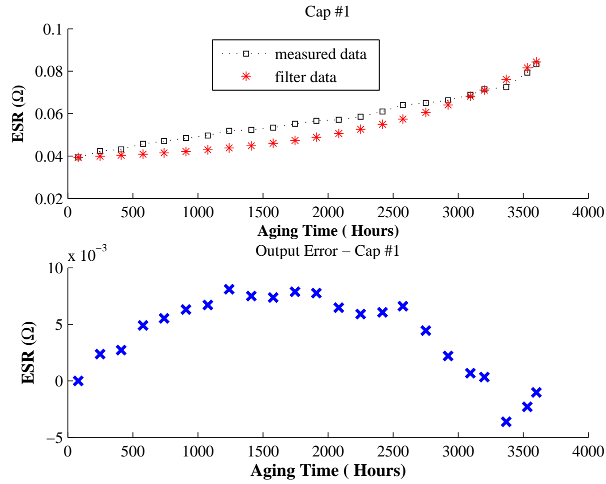

Figure 111: Tracking filter output against measurement data for Cap # 1

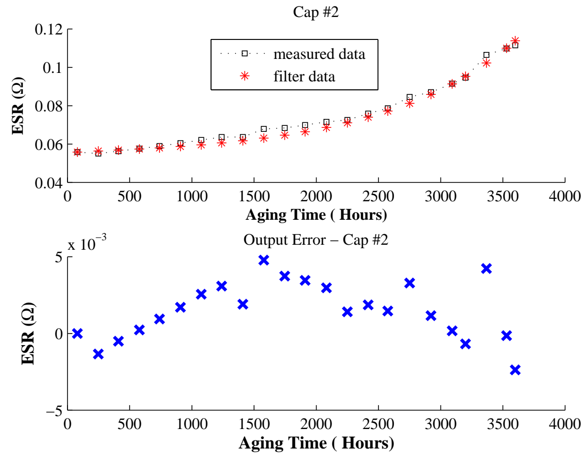

Figure 112: Tracking filter output against measurement data for Cap # 2

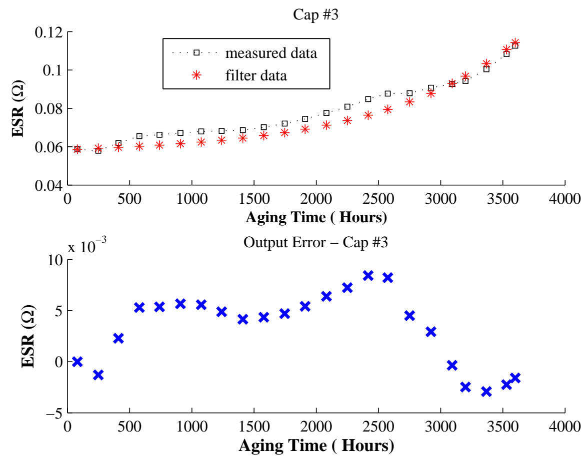

Figure 113: Tracking filter output against measurement data for Cap # 3

RUL

Figures 114, 115 and 116 presents results from the remaining useful life prediction algorithm at different aging times t_p = 80, 740, 1578, 2418, 3200 (hrs), at which the capacitors are characterized and their ESR value is calculated. Model $\mathcal{D}_5$ is implemented for predicting the increase in ESR while the measured values are the ESR measurements done at respective aging time intervals. The experiments were run till almost 3600 hours and hence the predictions are done till the end of experiments. End of life (EOL) is defined as the time at which the forecasted capacitance value trajectory crosses the EOL threshold at end of 200 hrs. Therefore, RUL is EOL minus aging times $t_p = 80, 740, 1578, 2418, 3200$ (hrs).

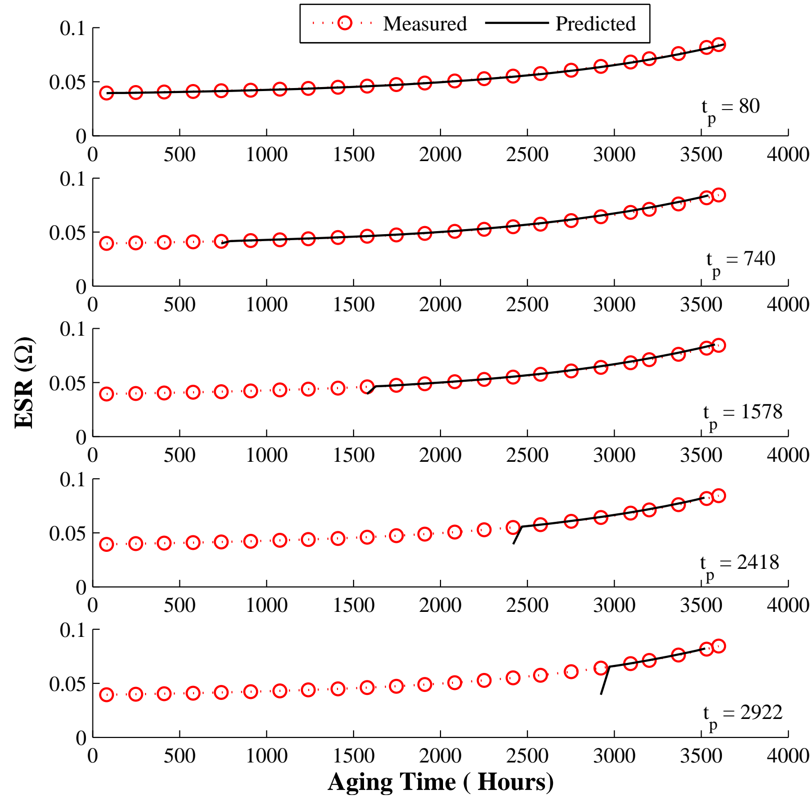

Figure 114: ESR prediction at different Aging Time for Cap # 1 by Model $\mathcal{D}_5$

Validation Tests

An Alpha-Lambda (α-λ) prognostics performance metric is presented in Figure 117, 118 and 119 for all the three capacitors under test respectively. The central dashed line represents ground truth and the shaded region is corresponding to a 30% ($\alpha = 0.3$) error bound in

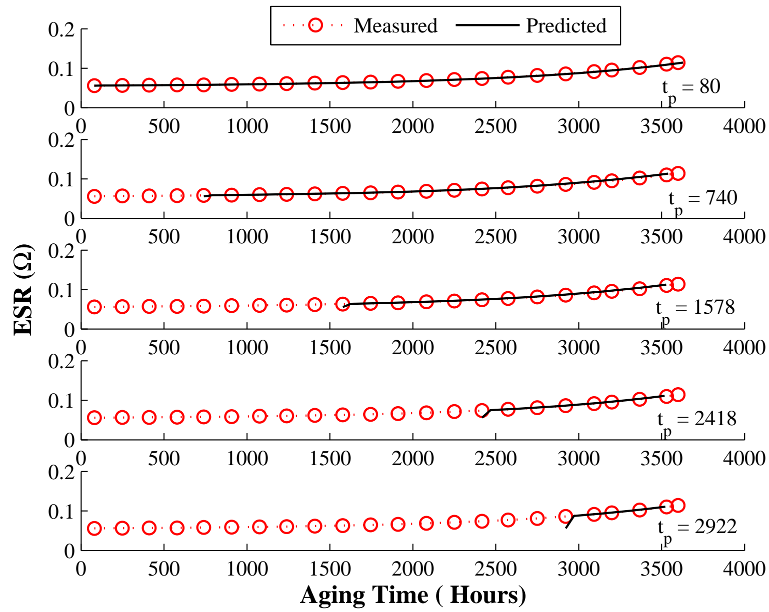

Figure 115: ESR prediction at different Aging Time for Cap # 2 by Model $\mathcal{D}_5$

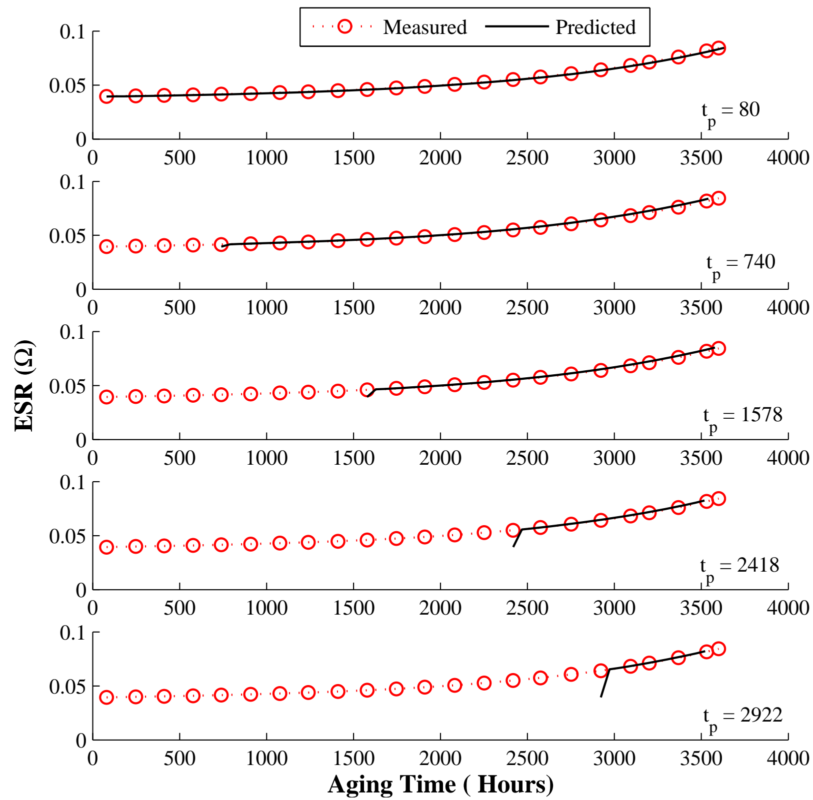

Figure 116: ESR prediction at different Aging Time for Cap # 3 by Model $\mathcal{D}_5$

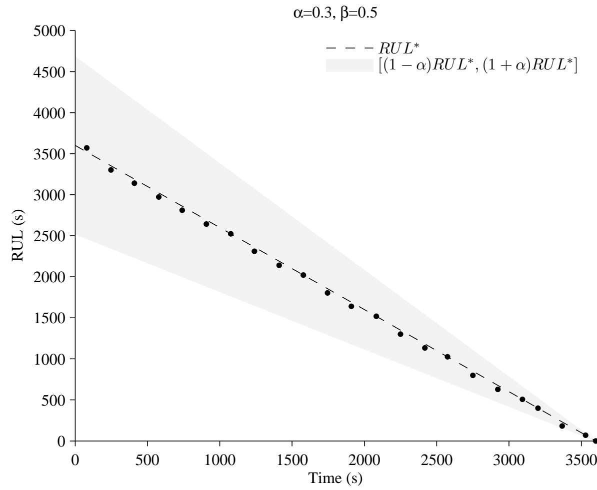

Figure 117: Performance based on Alpha-Lambda metric for Cap#1

the RUL prediction. From the α-λ metric plot in the figures it can be observed that the relative accuracy is good till the end of the experiment time and the accuracy is good enough under acceptable limits. As mentioned earlier this is due to inclusion of the degradation parameters and estimating them as the ESR increases with degradation.

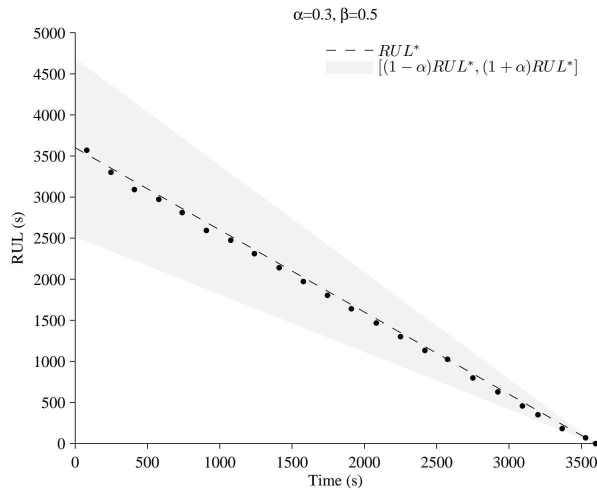

Figure 118: Performance based on Alpha-Lambda metric for Cap#2

Table 26 summarizes the results for all the capacitors and their percentage relative accuracy of ESR degradation model $\mathcal{D}_5$ for all the capacitors under test. As mentioned earlier model $\mathcal{D}_5$ is used for making predictions for all the capacitors with same parameters, and it is observed from the results that overall the model performs better for estimating the increase in ESR parameter value.

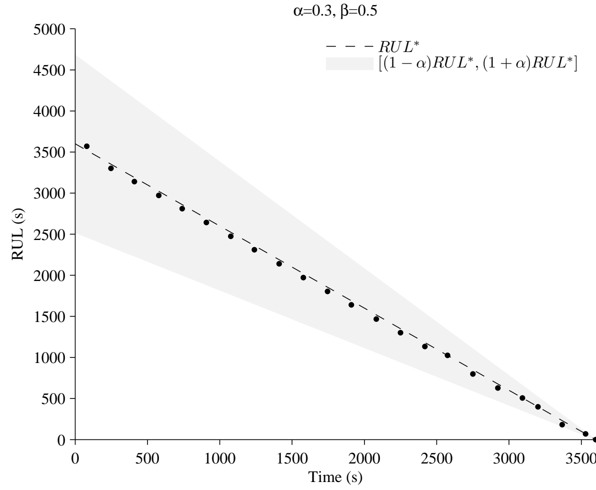

Figure 119: Performance based on Alpha-Lambda metric for Cap#3

Table 26: Summary of validation results based on RA for Capacitance degradation model $\mathcal{D}_5$ - Nominal

Aging Time	C1	C2	C3	$\overline{RA}_a$
80	98.58	98.58	98.58	98.58
248	98.51	98.51	98.51	98.51
410	98.43	96.87	98.43	97.91
578	98.35	98.35	98.35	98.35
740	98.25	98.25	98.25	98.25
908	98.14	96.29	98.14	97.52
1076	100.00	98.02	98.02	98.68
1240	97.88	97.88	97.88	97.88
1410	97.72	97.72	97.72	97.72
1578	100.00	97.53	97.53	98.35
1746	97.30	97.30	97.30	97.30
1910	97.04	97.04	97.04	97.04
2082	100.00	96.71	96.71	97.80
2250	96.30	96.30	96.30	96.30
2418	95.77	95.77	95.77	95.77
2575	100.00	100.00	100.00	100.00
2751	94.11	94.11	94.11	94.11
2922	92.63	92.63	92.63	92.63
3093	100.00	90.14	100.00	96.71
3200	100.00	87.50	100.00	95.83
3368	78.45	78.45	78.45	78.45
3530	100.00	100.00	100.00	100.00
$\overline{RA}_b$	97.16	95.63	96.80	

$\overline{RA}_a$ is the mean relative accuracy of all capacitors at each prediction time
$\overline{RA}_b$ is the mean relative accuracy of each capacitor at all prediction times

Discussion and Summary

An important goal achieved through the nominal experiment case, shows that the same degradation models $\mathcal{D}_4$, for capacitance, and $\mathcal{D}_5$ for ESR degradation applies to both the nominal and overstress conditions. The only parameters which changed in the models for the experiment were ones related to the operating experimental conditions while rest of the structural and geometrical parameters were kept constant for model validation. This confirms that we have been successful in developing a generalized physics-based degradation model based on underlying operating phenomenons and demonstrated its effectiveness through these experimental case studies.

Another interesting observation from the two data sets of the experimental cases were :

1. In Case I under 12V electrical overstress operating at the end of 200 hours the overall degradation observed in the capacitance was more than 22% and ESR increase by over 54%.

2. In Case II under 10V electrical overstress operating at the end of 300 hours the overall degradation observed in the capacitance was more than 15% and ESR increase by over 105%.

3. In the nominal operating experiments at the end of 3600 hours of operation the overall degradation observed in the capacitance was more than 12% and ESR increase by over 110%.

Thus it was observed that under higher electrical stress the rate of capacitance degradation was higher as compared to ESR degradation while under relatively lower stress level ESR degradation was comparatively higher. This phenomenon could be hypothesized due to the variation in the internal core temperature variations due to change operating conditions. At higher voltage more heat will be generated leading to increase in the core temperature and thus degrading the capacitance at a faster rate. While in the case of lower electrical stress, the heat generated internally is lower with lower evaporation rate causing the capacitance to degrade at a lower rate while the ESR increases predominantly.

The major contributions of the work presented in this chapter are:

1. Developing the nominal operation experiments based on the failure modes observed and collecting and analyzing data at regular intervals.

2. Identification of C and ESR as a failure precursor in the lumped parameter model, $\mathcal{M}_1$ as shown in Figure 94;

3. Implementing a empirical ESR change model , based on the nominal degradation data.

4. Implementing the Unscented Kalman Filter framework to the derived models $\mathcal{D}_4$ and $\mathcal{D}_5$ for predicting degradation.

5. Discussion of the validation results from ESR empirical model and degradation model, $\mathcal{D}_5$. It is observed that the physics based model is more accurate and tracking the ESR degradation of each capacitor and also predicting the RUL.

6. The performance of degradation models, $\mathcal{D}_4$ and $\mathcal{D}_5$ implemented for predicting degradation in capacitance and ESR respectively under nominal degradation, was within acceptable limits.

As can be observed from the capacitance data, an initial non-linearity was observed which was not considered in $\mathcal{D}_5$. The derived degradation model can be updated and developed at a more finer granularity to be implemented for detailed prognostic computations.

CHAPTER IX

CONCLUSIONS

This thesis has extended previous data-driven approaches to prognostics of electrolytic capacitors by deriving physics-based models to model the degradation phenomena in capacitors, and then employing experimental data to estimate model parameters and also validate the model for RUL predictions. A secondary contribution of this work are the design of experimental frameworks, and the the collection of data to support the model building and model validation efforts.

Summary of Contributions

Our contributions have focused on enhancements to implementing physics-based degradation modeling methodologies to prognostics and health management in electronic components and systems and experimental validation of our approach.

1. **Fault detection and isolation at System level :** The work presented in Chapter III demonstrated implementation of a model based methodology using fault signature techniques that can be applied to online diagnosis of faults in critical avionics electronic systems. The task was especially challenging because the system was embedded, and combination of a significant number of software (computational) as well as hardware components. Therefore, our fault modeling, detection, and isolation schemes was applied to heterogeneous subsystems. Techniques were also designed to handle the interactions between these subsystems. We developed a fault signature framework, where the fault signatures were derived by systematic analysis of combined physical system and computational models. In all of these cases, the challenge was to build these models at the right level of abstraction, so as not to be overwhelmed by computational complexity, at the same time, include sufficient detail to model capture the fault effects. The overall contributions to this section of the research can be summarized as :

(a) Development of an Integrated Avionics Simulator that included the power supply, the GPS, and INAV system..

(b) Identification of ten critical hardware and software faults. Developed mechanism for simulating these faults within the avionics simulator.

(c) Developed fault detectors and reasoner to demonstrate the ability to isolate a number of single faults across the three subsystems.

(d) Incorporated the physics-based capacitor degradation models into the power supply system model, and demonstrated how that could be used to simulate performance degradation using Monte Carlo methods.

2. **Physics-based degradation models :** In Chapter V, we discussed the structure of an electrolytic capacitor and its equivalent electrical lumped circuit models. As summarized in the fishbone diagram (Figure 35) the most common stressors leading to degradation in capacitors are electrical and thermal overstress conditions respectively. A thorough literature survey of the two degradation phenomena led to the derivation of physics-based models that modeled the effects of electrolyte evaporation and oxide layer breakdown on equivalent series resistance (ESR) and capacitance parameters as a function of capacitor aging.

   The internal structure of the capacitor was then combined with the physics-based phenomena to derive accurate dynamic models of capacitor aging when they were subjected to different stressor conditions. To support the physics-based modeling tasks, we developed appropriate experimental setups, and conducted laboratory experiments for simulating collecting degradation data on the capacitors under different operating conditions. Under these conditions the capacitors were regularly characterized and data was collected for all the capacitors to study the underlying degradation phenomenon. The data from these experiments was then used to test and validate each of the derived models.

3. **Electrical Overstress Case Study** : The goal achieved in this work, was implementation of the capacitance degradation model $\mathcal{D}_4$ and ESR degradation model $\mathcal{D}_5$ over

a different data sets of electrical operating conditions and achieving results for both the models which are within acceptable limits. The only parameters which changed in the models for the experiment were the operating parameters as per experimental conditions while rest of the structural and geometrical parameters were kept constant for model validation. Early in the thesis work we mentioned to implement a generalized physics-based degradation model based on underlying operating phenomenons which is shown through these experimental case studies.

The major accomplishments in this chapter were can be summarized as :

(a) Identification of the lumped-parameter model, $\mathcal{M}_1$ and $\mathcal{M}_4$, based on the equivalent electrical circuit of a real capacitor as a viable reduced-order model for prognostics-algorithm development;

(b) Developing the electrical capacitance experiments based on the failure modes observed and collecting and analyzing data at regular intervals.

(c) Identification of C and ESR as a failure precursor in the lumped parameter model, $\mathcal{M}_1$ as shown in Figure 70;

(d) Implementing a physics-based empirical degradation model, $\mathcal{E}_2$ based on the 12V electrical overtress data and validating the model.

(e) Development of the first principles based degradation models, $\mathcal{D}_4$ and $\mathcal{D}_5$ for capacitance and ESR degradation respectively, based on accelerated life test aging data as a function of time, evaporation rate and oxide breakdown;

(f) Implementing the Unscented Kalman Filter framework for models $\mathcal{D}_4$ and $\mathcal{D}_5$ for predicting degradation.

(g) Discussion of the validation results from physics-based empirical degradation model, $\mathcal{E}_2$ and degradation model, $\mathcal{D}_4$

(h) The performance of degradation models, $\mathcal{D}_4$ and $\mathcal{D}_5$, implemented for predicting degradation in capacitance and ESR respectively under different case, for similar type of capacitors operating under different operating conditions was analysed and found to be withing acceptable limits.

The derived degradation models can be updated and developed at a more finer granularity to be implemented for detailed prognostic implementation. The results presented here are based on electrical accelerated aging experimental data and on a accelerated life timescale.

4. **Thermal Overstress Case Study :** Chapter VII, presented a physics-based degradation model and a parameter estimation algorithm to validate the derived physics-based degradation models under thermal overstress experimental data. The major contributions of the work can be summarized as:

   (a) Identification of the lumped-parameter model, $\mathcal{M}_2$ and $\mathcal{M}_3$, based on the equivalent electrical circuit of a real capacitor as a viable reduced-order model for prognostics-algorithm development;

   (b) Developing the thermal capacitance experiments based on the failure modes observed and collecting and analyzing data at regular intervals.

   (c) Identification of C as a failure precursor in the lumped parameter model, $\mathcal{M}_2$ as shown in Figure 70;

   (d) Estimating the electrolyte volume from structural model of the capacitor to be implemented in the first principles degradation model, $\mathcal{D}_3$;

   (e) Implementation of parameter estimation algorithm to cross validate the derived first principles degradation model, $\mathcal{D}_1$.

   (f) Development of the first principles degradation model based on accelerated life test aging data which includes decrease in capacitance as a function of time and evaporation rate linked to temperature conditions;

   (g) We discussed the results and prediction implementing the Kalman Filter and Unscented Kalman Filters.

   The performance of the derived physics-based capacitance degradation model, $\mathcal{D}_1$ was successful based on the quality of the model fit to the experimental data and cross validation performance based on the parameter estimations done. A derived second order parameterized volume degradation model provided good results.

5. **Nominal Degradation Case Study :** In Chapter VIII, we implemented models $\mathcal{D}_4$ and $\mathcal{D}_5$ for the nominal experiment case. The only parameters which changed in the models for the experiment were ones related to the operating experimental conditions while rest of the structural and geometrical parameters were kept constant for model validation. Early in the thesis work mentioned to implement a generalized physics-based degradation model based on underlying operating phenomenons which is shown through these experimental case studies.

   Thus it was observed that under higher electrical stress the rate of capacitance degradation was higher as compared to ESR degradation while under relatively lower stress level ESR degradation was comparatively higher. This phenomenon could be hypothesized due to the variation in the internal core temperature variations due to change operating conditions. At higher voltage more heat will be generated leading to increase in the core temperature and thus degrading the capacitance at a faster rate. While in the case of lower electrical stress, the heat generated internally is lower with lower evaporation rate causing the capacitance to degrade at a lower rate while the ESR increases predominantly.

   The major contributions of the work presented in this chapter are:

   (a) Developing the nominal operation experiments based on the failure modes observed and collecting and analyzing data at regular intervals.

   (b) Identification of C and ESR as a failure precursor in the lumped parameter model, $\mathcal{M}_1$ as shown in Figure 94;

   (c) Implementing a empirical ESR change model , based on the nominal degradation data.

   (d) Implementing the Unscented Kalman Filter framework to the derived models $\mathcal{D}_4$ and $\mathcal{D}_5$ for predicting degradation.

   (e) Discussion of the validation results from ESR empirical model and degradation model, $\mathcal{D}_5$. It is observed that the physics based model is more accurate and tracking the ESR degradation of each capacitor and also predicting the RUL.

(f) The performance of degradation models, $\mathcal{D}_4$ and $\mathcal{D}_5$ implemented for predicting degradation in capacitance and ESR respectively under nominal degradation, was within acceptable limits.

As can be observed from the capacitance data, an initial non-linearity was observed in the data which was not considered in the derived model $\mathcal{D}_5$. The derived degradation model can be updated and developed at a more finer level of granularity to be implemented for nominal degradation operation of the capacitors.

Future Directions

We consider a number of extensions to our current work on model-based diagnostics and a combination of model-based and data-driven prognostics. In the area of diagnostics, our work could be extended beyond the qualitative fault signature approach to quantitative approaches than can combine diagnostics and prognostics to support performance-driven analysis of subsystems and systems.

System Level Prognostics

As discussed and presented in Chapter III, extending our prognostics approach from the component level to the sub-system level will be an important future step to take is work to the next level. A majority of the discussion and results presented in this research work are focused at the component level, some of the work in diagnostics was at the subsystem and systems level, and some preliminary studies were conducted in combining component-level prognostics with subsystem level diagnostics. As future work, we can extend our methods by combining physics-based models of different components e.g., electrolytic capacitors and MOSFET at the subsystem and system levels to make predictions of system behavior and performance.

Since more and more electronic components are being used on systems in power drives, power supplies for avionics electronic which require a system and sub-system level prognostics capability. The research work presented is an important and first step towards moving at the next level. Knowing the prediction degradation models of the different components

in a system will improve in making RUL predicitions for a system and thus help in making logistic decessions of replacing or repairing the degradaded system.

Granularity of the Models

In this work the granularity of the models was to the level where we could estimate the parameters based on the experimental measurements. With the current granularity of the derived degradation models we are able to make fairly accurate predictions as can be seen from the validation results. As discussed in ChapterVIII, in the capacitance degradation data we observed some non-linearity in the initial stages of aging cycle which the degradation model $\mathcal{D}_5$ was not able to capture well.

Analyzing the data from both the accelerated aging and nominal aging tests, as mentioned in the summary of the fishbone diagram some of the degradation phenomenons are similar but with different operating conditions other phenomenons also come into play. Thus the basic degradation models remains same but with change in the operational conditions some dormant parameters need to be updated in the model for more better prediction accuracy.

In the current work we had three devices under test for the nominal degradation experiment. The degradation model can be improved with conducting more experiments and tracking the data to help understand the other underlying degradation phenomenons. This will be helpful in deriving more accurate degradation models which will be able to track the degradation phenomenon more precisely.

More systematic methods need to be developed to extend the results of accelerated aging to more nominal modes of operations, and to make the degradation models more sensitive to the environmental conditions. This will enable better dynamic tracking of systems, and also the ability to track degradation under varying environmental conditions. More experiments and data will help us develop more precise and accurate models of the different degradation phenomena, and also to determine ways in which multiple models of degradation phenomena may be combined to define an overall degradation model.

Handling Uncertainty

In Chapters VI, VII, and VIII, we discussed implementation of Bayesian frameworks that combined with the physics-based degradation phenomena were employed to track the degradation states of the capacitor under nominal or stressed conditions. The models used in these methodologies are mathematical abstractions of the time evolution of the degradation process and used for the estimation of remaining useful life. The Bayesian tracking framework allows for estimation of state of health parameters in prognostics making use of available measurements from the system under consideration. In this framework, health parameters are regarded as random variables for which, in the case of Kalman and Extended Kalman filters, their distribution are regarded as Normal and the estimation process focuses on computing estimates of the expected value and variance parameters as they relate to the mean and variance of the parameterized Gaussian distributions. In addition to the health estimation process, forecasting of the health parameters in future time points provides the framework for computing the RUL of the component.

In this research work we did not include all the uncertainty measures associated with the entire methodology models. Some of the uncertainties that relate to this work are [152]include

1. Structural Uncertainties: these uncertainties arise from inherent variability modeling dynamic processes. These certainties were considered in our experiments by taking taking multiple measurements for a single reading and computing the measurement error. Examples of such uncertainties include manufacturing variations and difference in material properties depending on the manufacturing lot that the devices come from, and also variations created by different manufacturers. These uncertainties can be mitigated to some extent by using multiple experimental runs, and also running experiments with components from different manufacturing batches.

2. Systematic Uncertainties: these uncertainties arise due to unknown details in the experimental set up and experimental measurements that cannot easily be identified and eliminated. These uncertainties are often modeled as drift and bias terms in the component and system models. Additional uncertainties arise because of modeling errors

and noisy measurements. These are often modeled as additive stochastic phenomena added to appropriate parts of the component and system models. With improved methods and deeper investigations these uncertainties may be reduced but are rarely eliminated. Modeling uncertainties fall under this category and include modeling errors due to unmodeled phenomena in both system model and the fault propagation model.

3. Prejudicial Uncertainties: these uncertainties arise due to the way a process is set up, and it is expected to change if the process is redesigned. Conceptually these can be considered a type of epistemic uncertainty, except it is possible to control these by redesigning the experimental and measurement set up. Examples for these uncertainties include, sensor coverage, information loss due to data processing, various approximations and simplifications, and numerical errors.

The Bayesian tracking framework, especially the Kalman filter framework, allows for modeling of modeling uncertainties and measurement noise as Gaussian processes. For example, measurement noise is considered to be additive, and is modeled as a Gaussian distribution with zero mean and a predefined covariance. This allows for the aggregation of different sources of uncertainty o track and estimate the health state of a component or system. Its implications on the uncertainty estimation for remaining useful life (RUL) omputations have been dealt with in a simplistic way in this thesis research. However, these methods can be extended using sequential Monte Carlo and a variety of particle filtering schemes [138, 152]. Recent work by [138, 152] have discussed representing uncertainty in model-based prognostics in electronic systems, and this is very relevant to future extension of this research.

When employing the KF and UKF approaches, better methods have to be developed for estimating the parameters of the modeling uncertainty and measurement noise uncertainty distributions. If considered as tuning parameters, then the generated uncertainty in probability density function will not be representative of the real process. A proper propagation of uncertainty through the RUL prediction step as well as its correct interpretation are key to developing decision-making methodologies that make use of the remaining useful life pre-

diction estimates and their corresponding uncertainties in order to make actionable choices that will optimize reliability, operations or safety in view of the prognostics information.

APPENDIX A

PUBLICATIONS

Submitted

J1 **Kulkarni C.S.**, J Celaya, G. Biswas, and K Goebel, *"Physics Based Degradation Models for Capacitor Prognostics under Thermal Overtress Conditions"*, International Journal of Prognostics and Health Management. ISSN 2153-2648.

2012

J2 J Celaya, **Kulkarni C.S.**, G. Biswas, and K Goebel, *"Prognostic Studies and Physics of failure modeling under High Electrical Stress for Electrolytic Capacitors"*, International Journal of Prognostics and Health Management. ISSN 2153-2648 (accepted for publication)

C1 **Kulkarni C.S.**, J Celaya, K Goebel, and G. Biswas, *"Bayesian Framework Approach for Prognostic Studies in Electrolytic Capacitor under Thermal Overstress Conditions "*, Annual Conference of the Prognostics and Health Management Society(PHM 2012), September 23-27, 2012, Minneapolis, MN. ISBN: 978-1-936263-05-9. (**Best Paper Award**)

C2 **Kulkarni C.S.**, J Celaya, G. Biswas, and K Goebel, *"Accelerated Aging Experiments for Capacitor Health Monitoring and Prognostics"*, IEEE AUTOTESTCON, September 10 - 13, 2012, Anaheim, CA

C3 **Kulkarni C.S.**, J Celaya, G. Biswas, and K Goebel, *"Prognostics of Power Electronics, methods and validation experiments"*, IEEE AUTOTESTCON, September 10 - 13, 2012, Anaheim, CA

C4 **Kulkarni C.S.**, J Celaya, G. Biswas, and K Goebel , *"Prognostics Health Management and Physics based failure Models for Electrolytic Capacitors"*, American Institute

of Aeronautics and Astronautics, AIAA Infotech@Aerospace Conference, 19 - 21 June, 2012, Garden Grove, CA AIAA 2012-2602. (**Best Student Paper Award**)

C5 **Kulkarni C.S.**, J Celaya, K Goebel, and G. Biswas, *"Physics Based Electrolytic Capacitor Degradation Models for Prognostic Studies under Thermal Overstress"*, First European Conference of the Prognostics and Health Management Society, July 3-5, 2012, Dresden, Germany. ISBN: 978-1-936263-04-2 (**Honorable Mention for Best Paper Award**).

C6 J. Celaya, **Kulkarni C.S.**, S. Saha, G. Biswas, and K. Goebel, *"Accelerated Aging in Electrolytic Capacitors for Prognostics"*, IEEE - The Annual Reliability and Maintainability Symposium , January 23-26, 2012, Reno, Nevada

C7 J. Celaya, A. Saxena, **Kulkarni C.S.**, S. Saha, and K. Goebel, *"Prognostics Approach for Power MOSFET under Thermal-Stress Aging "*, IEEE - The Annual Reliability and Maintainability Symposium , January 23-26, 2012, Reno, Nevada

<u>2011</u>

C8 J. Celaya, **Kulkarni C.S.**, G. Biswas, S. Saha and K. Goebel, *"A Model-based Prognostics Methodology for Electrolytic Capacitors Based on Electrical Overstress Accelerated Aging"*, Proceedings of Annual Conference of the Prognostics and Health Management Society(PHM 2011), September 25-29, 2011, Montreal, Canada. ISBN: 978-1-936263-03-5.(**Best Paper Award**).

C9 **Kulkarni C.S.**, J. Celaya, G. Biswas, and K. Goebel , *"Prognostic Modeling and Experimental Techniques for Electrolytic Capacitor Health Monitoring"*, The 8th International Workshop on Structural Health Monitoring 2011, Vol 1, pp 1225 - 1232, September 13-15, 2011, Stanford University, Stanford, CA

C10 J. Celaya, **Kulkarni C.S.**, G. Biswas, and K. Goebel *"Towards Prognostic of Electrolytic Capacitors"*, American Institute of Aeronautics and Astronautics, AIAA Infotech @Aerospace 2011, March 2011, St. Louis, Missouri. AIAA-2011-1519

C11 **Kulkarni C.S.**, J. Celaya , G. Biswas and K. Goebel , *"Prognostic Techniques for Capacitor Degradation and Health Monitoring"*, The Maintenance & Reliability Conference, MARCON 2011, February 2011, Knoxville, TN

2010

C12 **Kulkarni C.S.**, G. Biswas, X. Koutsoukos, K. Goebel and J. Celaya, *"Experimental studies of aging in electrolytic capacitors"*, Proceedings of Annual Conference of the Prognostics and Health Management Society, October 2010, Portland, OR. ISBN: 978-1-936263-01-1

C13 **Kulkarni C.S.**, G. Biswas, X. Koutsoukos, K. Goebel and J. Celaya, *"Diagnostic/Prognostic Experiments for Capacitor Degradation and Health Monitoring in DC-DC converters"*, ASME 2010 Conference on Smart Materials, Adaptive Structures and Intelligent Systems, pp. 775-781, October 2010, Philadelphia, PA. SMASIS2010-3862

C14 **Kulkarni C.S.**, G. Biswas, X. Koutsoukos, K. Goebel and J. Celaya, *"Integrated Diagnostic/Prognostic Experimental Setup for Capacitor Degradation and Health Monitoring"*, IEEE AUTOTESTCON 2010, pp 1-7, September 2010, Orlando, FL. (**Best Student Paper Award**)

C15 Raj Bharadwaj, K. Kim, **Kulkarni C.S.**, G. Biswas, *"Model-Based Avionics Systems Fault Simulation and Detection "*, American Institute of Aeronautics and Astronautics, Infotech@Aerospace 2010, April 2010, Atlanta, GA. AIAA-2010-3328

C16 **Kulkarni C.S.**, G. Biswas, R. Bharadwaj and K. Kim *" Effects of Degradation in DC-DC Converters on Avionics Systems: A Model Based Approach"*, Machinery Failure Prevention Technology Conference, Page 8-13, MFPT 2010, April 2010, Huntsville, AL

C17 **Kulkarni C.S.**, G. Biswas, X. Koutsoukos, K. Goebel and J. Celaya, *"Physics of Failure Models for Capacitor Degradation in DC-DC Converters"*, The Maintenance & Reliability Conference, MARCON 2010, February 2010, Knoxville, TN

2009

C18 **Kulkarni C.S.**, G. Biswas, and X. Koutsoukos, *"A prognosis case study for electrolytic capacitor degradation in DC-DC converters"*, Proceedings of Annual Conference of the Prognostics and Health Management Society, October 2009, San Diego, CA. ISBN: 978-1-936263-00-4 (Poster)

Workshops

W1 **Kulkarni C.S.**, G. Biswas, J Celaya and K Goebel , *"Prognostics Health Management and Failure Analysis Modeling techniques for Accelerated Life testing in Electrolytic Capacitors"*, IEEE 2011 Workshop on Accelerated Stress Testing & Reliability, September 28-30, 2011, San Francisco, CA

W2 **Kulkarni C.S.**, G. Biswas and X. Koutsoukos *"Experiment and Prognostic Studies of Aging in Electrolytic Capacitors"*, Doctoral Consortium, Proceedings the Annual Conference of the Prognostics and Health Management Society, October 2010, Portland, OR (**Doctoral Consortium Fellowship Award**)

APPENDIX B

ELECTRICAL OVERSTRESS - PRINTED CIRCUIT BOARD

This section shows the PCB layout designs for the boards developed for the Electrical Overtress Experiments. These boards are the second version of the experiment.

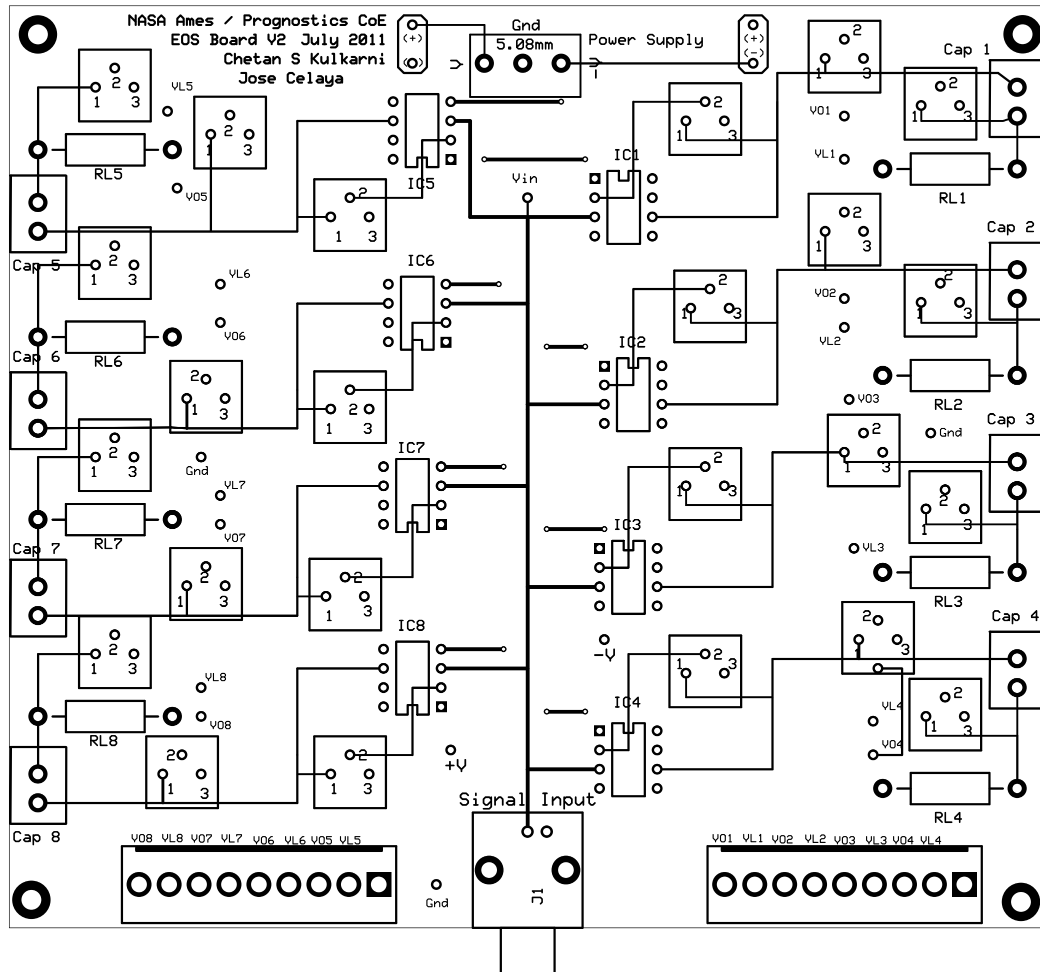

Figure 120: Top Layout of the EOS Board

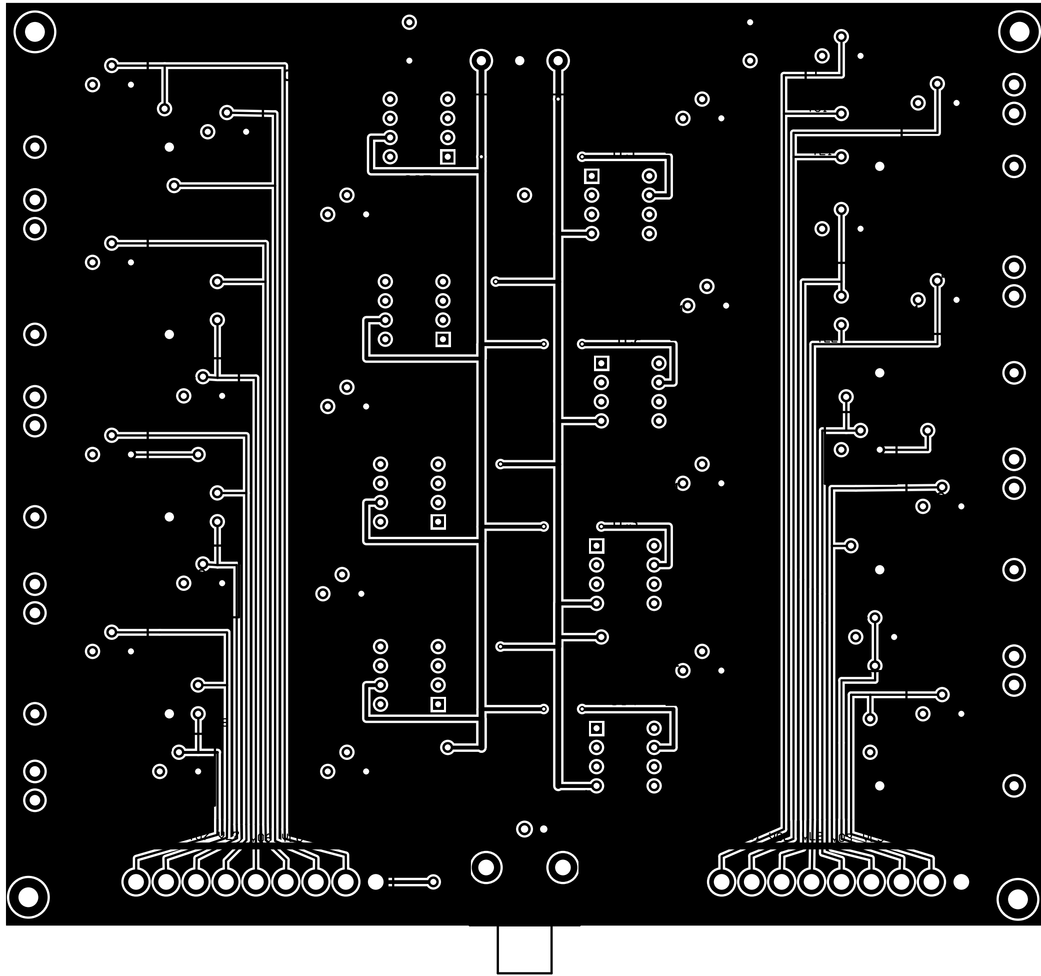

Figure 121: Bottom Layout of the EOS Board

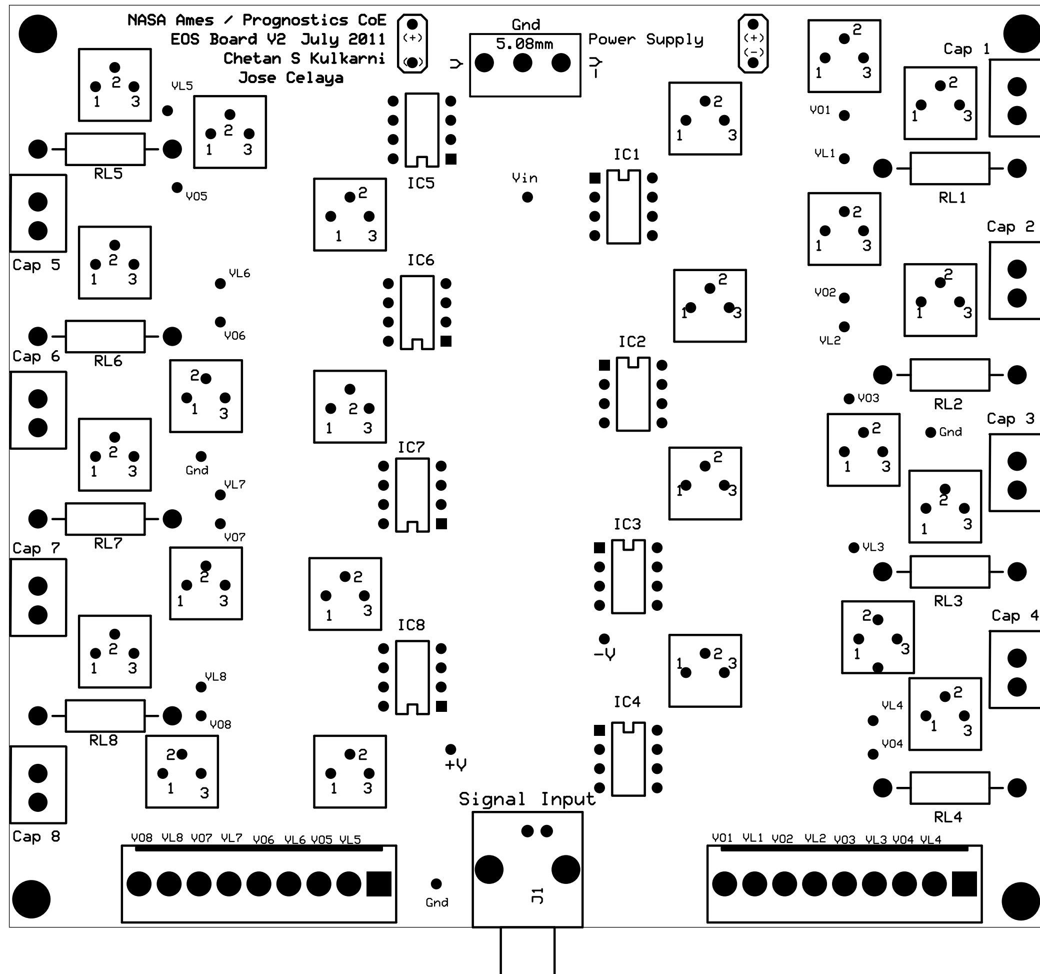

Figure 122: Component Layout of the EOS Board

BIBLIOGRAPHY

[1] N. Vichare and M. Pecht, "Prognostics and health management of electronics," *IEEE Transactions on Components and Packaging Technologies*, vol. Vol 29, pp. 222 – 229, 2006.

[2] C. Leonard and M. G. Pecht, "Improved techniques for cost effective electronics," *Proceedings of Reliability Maintainability Symposium*, pp. 174 – 182, 1991.

[3] M. Karyagina, "Designing for fault-tolerance in the commercial environment," *Proc. Reliability Maintainability Symp*, pp. 258 – 262, 1996.

[4] A. A. Shapiro, S. X. Ling, S. Ganesan, R. S. Cozy, D. J. Hunter, D. V., Schatzel, M. M. Mojarradi, and E. A. Kolawa, "Electronic packaging for extended mars surface missions," *Proc. IEEE Aerospace Conf*, vol. Vol 4, pp. 2515 – 2527, 2004.

[5] J. Celaya, A. Saxena, P. Wysocki, S. Saha, and K. Goebel, "Towards prognostics of power mosfets: Accelerated aging and precursors of failure," *Proceedings of Annual Conference of the PHM Society, October 10-16, Portland, OR*, 2010.

[6] E. Balaban, A. Saxena, S. Narasimhan, I. Roychoudhury, K. Goebel, and M. Koopmans, "Airborne electro-mechanical actuator test stand for development of prognostic health management systems," *Proceedings of Annual Conference of the PHM Society 2010, October 10-16, Portland, OR*, 2010.

[7] DoD, "Mil-hdbk 217 military handbook for reliability prediction of electronic epuipment version a washington dc," *U.S. Department of Defense*, 1965.

[8] TelcordiaTechnologies, "Special report sr-332 - reliability prediction procedure for electronic equipment," *Telcordia Customer Service, Piscataway, NJ*, vol. 1, 2001.

[9] W. Denson, "A tutorial: Prism," *RAC Journal*, pp. 1 – 6, 1999.

[10] FIDESGroup, "Reliability methodology for electronic systems," *FIDES Guide issue A*, 2004.

[11] K. L. Wong, "What is wrong with the existing reliability prediction methods?" *Quality and Reliability Engineering International*, vol. Vol. 6, pp. 251 – 258, 1990.

[12] M. J. Cushing, D. Mortin, T. Stadterman, and A. Malhotra, "Comparison of electronics-reliability assessment approaches," *IEEE Transactions on Reliability*, vol. Vol. 42, NO. 4, pp. 542 – 546, 1993.

[13] M. Talmor and S. Arueti, "Reliability prediction: The turn-over point," *Proceedings of the Annual Reliability and Maintainability Symposium*, pp. 254 – 262, 1997.

[14] C. Leonard, "Mil-hdbk-217 - it's time to rethink it," *Electronic Design*, pp. 79 – 82, 1991.

[15] S. F. Morris, "Use and application of mil - hdbk-217." *Solid State Technology*, pp. 65 – 69, 1990.

[16] M. Pecht, M. Dube, M. Natishan, and I. Knowles, "An evaluation of built-in test," *IEEE Transactions on Aerospace and Electronic Systems*, vol. 37, pp. 266 – 272, 2001.

[17] D. Johnson, "Review of fault management techniques used in safety critical avionic systems," *Progress in Aerospace Science*, vol. 31, pp. 415 – 431, October 1996.

[18] M. Pecht, *Prognostics and Health Management of Electronics.* WILEY, 2008.

[19] J. Celaya and K. Goebel, "Isothermal accelerated aging system for power semiconductor prognostics," *Proceedings of Autotestcon 2010*, 2010.

[20] B. Saha, K. Goebel, and J. Christophersen., "Comparison of prognostic algorithms for estimating remaining useful life of batteries," *Transactions of the Institute of Measurement & Control, No. 3-4*, vol. 31, pp. 293 – 308, 2009.

[21] M. Daigle and K. Goebel, "Multiple damage progression paths in model-based prognostics," *Proceedings of the 2011 IEEE Aerospace Conference*, 2011.

[22] A. Saxena, J. Celaya, E. Balaban, K. Goebel, B. Saha, S. Saha, and M. Schwabacher, "Metrics for evaluating performance of prognostic techniques," in *International Conference on Prognostics and Health Management 2008*, 2008.

[23] U. Bhatti and O. W, "Failure modes and models for integrated gps/ins systems," *The Journal of Navigation*, vol. 60, 2007.

[24] C. Kulkarni, G. Biswas, X. Koutsoukos, K. Goebel, and J. Celaya, "Physics of failure models for capacitor degradation in dc-dc converters," *The Maintenance and Reliability Conference, MARCON , Knoxville, TN*, February 2010.

[25] N. B. Taylor, *Stedmans Medical Dictionary, 18th ed.* Baltimore: Williams & Wilkins, 1953.

[26] G. J. Kacprzynski, M. J. Roemer, G. Modgil, and A. Palladino, "Enhancement of physics of failure prognostic models with system level features," *Proc. IEEE Aerospace Conf*, vol. 6, pp. 2919 – 2925, 2002.

[27] M. Pecht, B. Tuchband, N. Vichare, and Q. J. Ying, "Prognostics and health monitoring of electronics," *International Conference on Thermal, Mechanical and Multi-Physics Simulation Experiments in Microelectronics and Micro-Systems*, pp. 1 – 8, April 2007.

[28] J. Xie and M. Pecht, "Application of in-situ health monitoring and prognostic sensors," *Proceedings of 9th Pan Pacific Microelectronics Symposium Exhibits Conference*, 2004.

[29] M. Krok and K. Goebel, "Prognostics for advanced compressor health monitoring," *Proc. SPIE*, vol. 5107, pp. 1 – 12, 2003.

[30] I. Tumer and A. Bajwa, "A survey of aircraft engine health monitoring systems," *Proceedings of AIAA*, pp. 1 – 6, 1999.

[31] N. Vichare, P. Rodgers, V. Eveloy, and M. G. Pecht, "Monitoring environment and usage of electronic products for health assessment and product design," *Proceedings of IEEEWorkshop Accelerated Stress Testing Reliability (ASTR)*, 2005.

[32] C. Kulkarni, G. Biswas, and X. Koutsoukos, "A prognosis case study for electrolytic capacitor degradation in dc-dc converters," *Proceedings of Annual Conference of the PHM Society, San Diego, CA*, 2009.

[33] L. Nasser and M. Curtin, "Electronics reliability prognosis through material modeling and simulation," *Proceedings of IEEE Aerospace Conference*, March 2006.

[34] A. Ramakrishnan and M. Pecht, "Life consumption monitoring methodology for electronic systems," *IEEE Transactions on Components and Packaging technologies*, vol. 26, pp. 625 – 634, September 2003.

[35] J. Gu and M. Pecht, "Prognostics and health management using physics-of-failure," *54th Annual Reliability and Maintainability Symposium (RAMS)*, 2008.

[36] G. Vachtsevanos, *Intelligent Fault Diagnosis and Prognosis for Engineering Systems*. Wiley, 2006.

[37] P. Kalgren and et'al, "Application of prognostic health management in digital electronic system," *Aerospace Conference, 2007 IEEE*, pp. 1 – 9, March 2007.

[38] D. W. Brown, P. W. Kalgren, C. S. Byington, and R. F. Orsagh, "Electronic prognostics - a case study using global positioning system (gps)," *IEEE Autotestcon*, 2005.

[39] R. Orsagh and et'al, "Prognostic health management for avionics system power supplies," *Aerospace Conference, 2006 IEEE*, pp. 1 – 7, March 2006.

[40] B. L. Ferrell, "JSF prognostics and health management," *IEEE Aerospace Conference*, 1999.

[41] C. Kulkarni, G. Biswas, R. Bharadwaj, and K. Kim, "Effects of degradation in dc-dc converters on avionics systems: A model based approach," *Proceedings of the Machinery Failure Prevention Technology Conference (MFPT)*, pp. 8 – 13, April 2010.

[42] J. Judkins, D. Goodman, and S. Vonhout, "Practical considerations for power electronics system and actuator prognostics implementations," *Autotestcon IEEE*, pp. 553 – 560, 2007.

[43] R. G. Inc, "Electronic prognostics for dc to dc converters," *Electronic Prognostic Workshop, Integrated Diagnostics Committee, National Defense Industrial Association*, 2004.

[44] J. B. Judkins, J. Hofmeister, and S. Vohnout, "A prognostic sensor for voltage regulated switch-mode power supplies," *IEEE Aerospace Conference*, vol. 1, pp. 1 – 8, 2007.

[45] C. Byington, M. Watson, and D. Edwards, "A model-based approach to prognostics and health management for flight control actuators," *Proceeding of IEEE Aerospace Conference*, 2004.

[46] G. J. Kacprzynski, A. Sarlashkar, M. Roemer, A. Hess, and W. Hardman, "Predicting remaining life by fusing the physics of failure modeling with diagnostics," *JOM: Journal of the Minerals, Metals and Materials Society*, vol. 56, 2004.

[47] J. Luo, M. Namburu, K. Pattipati, and et'al, "Model-based prognostic techniques," *AUTOTESTCON 2003. IEEE Systems Readiness Technology Conference. Proceedings*, pp. 330 – 340, Sep 2003.

[48] Y. B. Shalom, X.-R. Li, and T. Kirubarajan, "Estimation with applications to tracking and navigation," *John Wiley and Sons, INC*, 2001.

[49] D. E. Adams, "Nonlinear damage models for diagnosis and prognosis in structural dynamic systems," *SPIE Conference Proceedings*, vol. 4733, pp. 180 – 191, 2002.

[50] D. Chelidze, "Multimode damage tracking and failure prognosis in eletromechanical system," *SPIE Conference Proceedings*, vol. 4733, pp. 1 – 12, 2002.

[51] D. Chelidze, J.P.Cusumano, and A. Chatterjee, "Dynamical systems approach to damage evolution tracking, part i: The experimental method," *Journal of Vibration and Acoustics*, vol. 124, pp. 250 – 257, 2002.

[52] C. S. Byington, M. Watson, D. Edwards, and P. Stoelting, "A model-based approach to prognostics and health management for flight control actuators," *IEEE Aerospace Conference Proceedings*, vol. 6, pp. 3551 – 3562, 2004.

[53] S. Wegerich and R. Pipke, "Residual signal alert generation for condition monitoring using approximated sprt distribution," *Patent*, vol. 1, no. 6975962, December 2005.

[54] L. Lopez, "Advanced electronic prognostics through system telemetry and pattern recognition methods," *ScienceDirect Microelectronics Reliability*, vol. 47, pp. 1865 – 1873, 2007.

[55] M. Roemer, G. Kacprzynski, E. Nwadiogbu, and G. Bloor, "Development of diagnostic and prognostic technologies for aerospace health management applications," *IEEE Aerospace Conference Proceedings*, vol. 6, pp. 139 – 147, 2001.

[56] D. F. Specht, "Probabilistic neural networks," *Neural Networks*, vol. 3, pp. 109 – 118, 1990.

[57] P. Wang and G. Vachtsevanos, "Fault prognostics using dynamic wavelet neural networks," *Artificial Intelligence for Engineering Design, Analysis and Manufacturing*, vol. 15, pp. 349 – 365, 2001.

[58] H. Konrad and R. Isermann, "Diagnosis of different faults in milling using drive signals and process models," *Proceedings of the 13th World Congress International Federation of Automatic Control*, vol. B, pp. 91 – 96, 1996.

[59] D. Mylaraswamy and V. Venkatasubramanian, "A hybrid framework for large scale process fault diagnosis," *Computers & Chemical Engineering*, vol. 21, pp. 935 – 940, 1997.

[60] C. Bunks, D. McCarthy, and T. Ani, "Condition-based maintenance of machines using hidden markov models," *Mechanical Systems and Signal Processing*, vol. Vol 14, pp. 597 – 612, 2000.

[61] M. Schwabacher, "A survey of data-driven prognostics (aiaa)," *Infotech at Aerospace*, Sep 2005.

[62] S. Mishra, S. Ganesan, M. Pecht, and J. Xie, "Life consumption monitoring for electronics prognostics," *Proceedings of the IEEE Aerospace Conference*, vol. 5, pp. 3455 – 3467, 2004.

[63] K. Vaidyanathan and K. C. Gross, "Monte carlo simulation of telemetric signals for enhanced proactive fault monitoring of computer servers," *Simulation Multi-Conference, Philadelphia, PA*, 2005.

[64] K. C. Gross and K. Mishra, "Improved methods for early fault detection in enterprise computing servers using sas tools," *SAS Users Group International (SUGI 29)*, 2004.

[65] K. Mishra and K. C. Gross, "Dynamic stimulation tool for improved performance modeling and resource provisioning of enterprise servers," *Proceedings of 14th IEEE International Symposium on Software Reliability Ena ISSRE031*, 2003.

[66] H. Chestnut, *Systems Engineering Tools*. Wiley, New York, 1965.

[67] F. L. Lewis, *Optimal Estimation: With an Introduction to Stochastic Control Theory*. Wiley, New York, 1986.

[68] ——, *Applied Optimal Control and Estimation*. Englewood Cliffs, NJ: Prentice-Hall, 1992.

[69] P. G. Groer, "Analysis of time-to-failure with a weibull model," *Proceedings of the Maintenance and Reliability Conference, MARCON 2000, Knoxville, TN*, 2000.

[70] A. Schomig and O. Rose, "On the suitability of the weibull distribution for the approximation of machine failures," *Proceedings of the 2003 Industrial Engineering Research Conference, Portland, OR*, 2003.

[71] K. Gross and W. Lu, "Early detection of signal and process anomalies in enterprise computing systems," *IEEE international conference on machine learning and applications*, 2002.

[72] K. Gross, "Proactive fault monitoring in enterprise servers," *IEEE international multiconference in computer science and computer engineering*, 2005.

[73] ——, "Electronic prognostics through continuous system telemetry," *60th meeting of the society for machinery failure prevention technology (MFPT06)*, 2006.

[74] P. Hansen and P. McCluskey, "Failure models in power device interconnects," *European Conference on Power Electronics and Applications*, pp. 1 – 9, 2007.

[75] M. Pecht and A. Dasgupta, "Physics-of-failure: An approach to reliable product development," *Journal of the Institute of Environmental Sciences*, vol. 38, pp. 30 – 34, 1995.

[76] J. Snook, J. Marshall, and R. M. Newman, "Physics of failure - as an integrated part of design for reliability," *Annual Reliability and Maintainability Symposium*, pp. 46 – 54, 2003.

[77] R. Friedman and H. L. Eidenoff, "A two-stage fatigue life prediction method," *Grumman Advanced Development Report, Bethpage, NY*, 1990.

[78] J. C. Newman, "Fastran-ii: A fatigue crack growth structural analysis program," *NASA Technical Memorandum, 1992 Langley Research Center, Hampton, VA.*, 1992.

[79] K. N. Meyyappan, P. Hansen, and P. McCluskey, "Wire fatigue models for power electronic modules," *ASME Congress 2003, Washington DC*, 2003.

[80] P. Hansen, P. D. Jensens, K. Meyyappan, and P. McCluskey, "Wire flexure fatigue model for asymmetric bond height," *Proceedings of IPACK 03: International Electronic Packaging Technical Conference and Exhibition, July 6-11, 2003, Maui, Hawaii, USA*, 2003.

[81] K. Upadhyayula and A. Dasgupta, "Guidelines for physics-of-failure based accelerated stress testing," *Annual Reliability and Maintainability Symposium*, pp. 345 – 357, 1998.

[82] G. F. Watson, "Mil reliabiliy: A new approach," *IEEE Spectrum*, vol. August 1992, pp. 46 – 49, 1992.

[83] P. Hansen, F. Blaabjergand, K. Madsen, J. Pedersen, and E. Ritchie, "An accurate method for power loss measurements in energy optimized apparatus and systems," *8th European Conference on Power Electronics and Applications*, 1999.

[84] M. Delgadoa and H. Sira-Ramrez, "A bond graph approach to the modeling and simulation of switch regulated dc-to-dc power supplies," *Simulation Practice and Theory*, pp. 631 – 646, November 1998.

[85] V. Vorperian., "Simplified analysis of pwm converters using model of pwm switch continuous conduction mode." *IEEE Transactions on Aerospace and Electronic Systems*, pp. 490 – 496, May 1990.

[86] D. Goodman, "Practical application of phm/prognostics to cots power converters," *Aerospace Conference, 2005 IEEE*, pp. 3573 – 3578, March 2005.

[87] G. Biswas and E. Manders, "Integrated systems health management to achieve autonomy in complex systems," *2006 American Control Conference, Minneapolis, MN, June*, 2006.

[88] G. Biswas and G. Bloor, "A model based approach to constructing performance degradation monitoring systems," *Paper no. 1269, IEEE Aerospace Conference, Big Sky, Montana, March 2006*, 2006.

[89] I. Roychoudhury, M. Daigle, G. Biswas, and X. Koutsoukos, "An efficient method for simulating complex systems with switching behaviors using hybrid bond graphs," *Simulation News Europe, December 2008*, vol. 18, pp. 5 – 13, 2008.

[90] E. Manders, S. Narasimhan, G. Biswas, and P. Mosterman, "A combined qualitative/quantitative approach for fault isolation in continuous dynamic systems," *Proc. IFAC Safeprocess 2000, Budapest, Hungary*, vol. 1, pp. 1074 – 1079, 2000.

[91] R. Bharadwaj, C. Kulkarni, G. Biswas, and K. Kim, "Model-based avionics systems fault simulation and detection," *American Institute of Aeronautics and Astronautics, AIAA Infotech@Aerospace 2010, AIAA-2010-3328*, April 2010.

[92] A. T. S. Bureau, "In-flight upset event 240 km north-west of perth, wa, boeing company 777-200, 9m-mrg, 1 august 2005," *Aviation Occurrence Report 200503722 March 13*, 2007.

[93] ——, "In-flight upset 154 km west of learmonth, wa, 7 october 2008, vh-qpa, airbus a330-303 (interim factual)," *Aviation Occurrence Investigation AO-2008-070, March 6*, 2009.

[94] K. Borre, "The easy suite - matlab code for the gps newcomer," *http://www.ngs.noaa.gov/gps-toolbox/Borre2.htm.*, 1999.

[95] Borre and Kai, "The easy suite - matlab code for the gps newcomer," *GPS Solutions*, vol. Number 1, pp. 47 – 51, 2003.

[96] NAVCEN, "Gps standard positioning service signal specification," *http://www.navcen.uscg.gov/pubs/gps/sigspec/gpssps1.pdf*, June 1995.

[97] H. Cobb and et. al, "Observed gps signal continuity interruptions," *ION-GPS-95, Palm Springs, CA*, pp. 793 – 795, 1995.

[98] W. Lewandowski, G. Petit, and C. Thomas, "The need for gps standardization," *23rd annual Precise Time and Time Interval (PTTI) applications and planning meeting. Pasadena, CA*, pp. 1 – 14, 1991.

[99] M. E. Orejas, V. L., and S. M, "Multiple sensor integration for autonomous vehicle navigation," *MOSATT*, 2009.

[100] M. R. Rogers, "Applied mathematics in integrated navigation systems 2nd ed," *AIAA Education series*, 2003.

[101] Garcia-Gomez, S. Rimaux, and M. Delgado, "Bond graphs in the design of adaptive passivity-based controllers for dc/dc power converters," *IEEE International Conference on Industrial Technology, 2006. ICIT 2006.*, pp. 132 – 137, Dec 2006.

[102] D. Karnopp and R. Rosenberg, *Introduction to Physical System Dynamics.* Mcgraw-Hill College, New York, NY, 1983.

[103] D. Antic, B. Vidojkovic, and M. Mladenovic, "An introduction to bond graph modelling of dynamic systems," *TELSIKS*, 1999.

[104] S. Narasimhan and G. Biswas, "Model-based diagnosis of hybrid systems," *IEEE Transaction on Systems, Man and Cybernetics, Part A: Systems and Humans No.3*, vol. 37, 2007.

[105] D. Antic, B. Vidojkovic, and M. Mladenovic, "An introduction to bond graph modelling of dynamic systems," *TELSIKS'99*, Oct 1999.

[106] P. J. Mosterman and G. Biswas, "Diagnosis of continuous valued systems in transient operating," *IEEE Transactions on Systems, Man, and Cybernetics - PART A: Systems and Humans*, vol. 29, November 1999.

[107] A. M. Imam, T. Habetler, R. Harley, and D. Divan, "Condition monitoring of electrolytic capacitor in power electronic circuits using adaptive filter modeling," *IEEE 36th Power Electronics Specialists Conference, 2005. PESC '05.*, pp. 601 – 607, June 2005.

[108] B. Saha and K. Goebel, "Modeling li-ion battery capacity depletion in a particle filtering framework," *Conference of the Prognostics and Health Management Society 2009*, 2009.

[109] J. Celaya, C. Kulkarni, G. Biswas, and K. Goebel, "A model-based prognostics methodology for electrolytic capacitors based on electrical overstress accelerated aging," *Proceedings of Annual Conference of the PHM Society, September 25-29, Montreal, Canada*, 2011.

[110] C. Kulkarni, J. Celaya, K. Goebel, and G. Biswas, "Physics based electrolytic capacitor degradation models for prognostic studies under thermal overstress," *Proceedings of First European Conference of the Prognostics and Health Management Society*, July 2012.

[111] M. L. Gasperi, "Life prediction model for aluminum electrolytic capacitors," *31st Annual Meeting of the IEEE-IAS*, vol. 4, no. 1, pp. 1347 – 1351, October 1996.

[112] J. Fife, "Wet electrolytic capacitors," AVX Corporation, Myrtle Beach, SC, Patent No: 7,099 1, August 2006.

[113] Chen, *Ripple Current Confusion*, KEME Electronic Corporation, 2004.

[114] R. S. Alwitt and S. G. Parler, "Heat generation during pulse operation of prototype aluminum electrolytic capacitors," *Journal of Applied Electrochemistry*, vol. Volume 25, Number 6, pp. 533 – 542, 1995.

[115] J. Brettle and N. F. Jackson, "Failure mechanisms in solid electrolytic capacitors," *Electrocomponent Science and Technology*, vol. 3, pp. 233 – 246, 1977.

[116] R. P. Tye, *Thermal Conductivity.* Burlington, MA: Academic Press Inc, 1968.

[117] J. M. Albella, C. Gomez-Aleixandre, and J. M. Martinez-Duart, "Dielectric characteristics of miniature aluminium electrolytic capacitors under stressed voltage conditions," *Journal of Applied Electrochemistry*, vol. Volume 14, Number 1, pp. 9 – 14, 1984.

[118] H. D. Wit and C. Crevecoeur, "The dielectric breakdown of anodic aluminum oxide," *Physics Letters A*, vol. Volume 50, Issue 5, pp. 365 – 366, 1974.

[119] S. Ikonopisov, "Theory of electrical breakdown during formation of barrier anodic films," *Electrochimica Acta*, vol. ,Volume 22, Issue 10, pp. 1077 – 1082, 1977.

[120] C. Gomez-Aleixandre, J. M. Albella, and J. M. Martinez-Duart, "Gas evolution in aluminum electrolytic capacitors," *Journal of Electrochem. Society*, vol. Volume 131, Issue 3, pp. 612 – 614, 1984.

[121] V. Roederstein, "Aluminum capacitors - general information," *Document - 25001 January 2007*, 2007.

[122] MIL-C-62F, "General specification for capacitors," *Fixed Electrolytic*, 2008.

[123] IEC-60068-1, "Environmental testing, part 1: General and guidance," *IEC Standards*, 1988.

[124] A. R. Morley and D. S. Campbell, "Electrolytic capacitors: Their fabrication and the interpretation of their operational behaviour," in *The Radio and Electronic Engineers*, vol. 43, no. 7, July 1973, pp. 421 – 429.

[125] M. Rusdi, Y. Moroi, H. Nakahara, and O. Shibata, "Evaporation from water ethylene glycol liquid mixture," *Langmuir - American Chemical Society*, vol. 21 (16), pp. 7308 – 7310, 2005.

[126] IEC-60384-4-1, "Fixed capacitors for use in electronic equipment," *IEC Standards*, 2007.

[127] S. C. Rodner, P. Wedin, and L. Bergstram, "Effect of electrolyte and evaporation rate on the structural features of dried silica monolayer films," *Langmuir*, vol. 18, no. 24, pp. 9327 – 9333, 2002.

[128] A. Bengt, "Electrolytic capacitors theory and applications," *RIFA Electrolytic Capacitors*, 1995.

[129] V. Kadary and N. Klein, "Electrical breakdown: I . during the anodic growth of tantalum pentoxide," *The Journal of the Electrochemical Society*, vol. 127, pp. 139 – 151, 1980.

[130] N. Klein, V. Moskovici, and V. Kadary, "Electrical breakdown - ii during the anodic growth of aluminum oxide," *Journal of the Electrochemical Society*, vol. 127, pp. 152 – 155, 1980.

[131] N. Klein, "Electrical breakdown in thin dielectric films," *The Journal of the Electrochemical Society*, vol. 116, pp. 963 – 972, 1969.

[132] C. Gomez-Aleixandre, J. M. Albella, and J. M. Martnez-duart, "Pressure build-up in aluminum electrolytic capacitors under stressed voltage conditions," *Journal of Applied Electrochemistry*, vol. Volume 16, Number 1, pp. 109 – 115, 1986.

[133] D. M. Tasca, "Pulse power response and damage characterization of capacitors," *Electrical Overstress-Electrostatic Discharge Symposium Proceedings, EOS/ESD Association*, vol. 3, 1981.

[134] S. J. Julier and J. K. Uhlmann, "A new extension of the kalman filter to nonlinear systems," *Proceedings of the 11th International Symposium on Aerospace/Defense Sensing, Simulation and Controls*, pp. 182 – 193, 1997.

[135] S. J. Julier, "Unscented filtering and nonlinear estimation," *Proceedings of the IEEE*, vol. 92, no. 3, pp. 401 – 422, 2004.

[136] M. Daigle, B. Saha, and K. Goebel, "A comparison of filter-based approaches for model-based prognostics," in *Proceedings of the 2012 IEEE Aerospace Conference*, March 2012.

[137] M. Daigle and K. Goebel, "Improving computational efficiency of prediction in model-based prognostics using the unscented transform," in *Annual Conference of the Prognostics and Health Management Society 2010*, October 2010.

[138] M. Daigle, A. Saxena, and K. Goebel, "An efficient deterministic approach to model-based prediction uncertainty estimation," in *Annual Conference of the Prognostics and Health Management Society 2012*, September 2012, pp. 326 – 335.

[139] M. E. Orchard, "A particle filtering-based framework for on-line fault diagnosis and failure prognosis," Ph.D. dissertation, Georgia Institute of Technology, 2007.

[140] R. Stengel, *Optimal Control and Estimation.* Dover Books on Advanced Mathematics, 1994.

[141] C. Chatfield, *The Analysis of Time Series: An Introduction.* Chapman & Hall/CRC, 2003.

[142] A. Saxena, J. Celaya, B. Saha, S. Saha, and K. Goebel, "On applying the prognostic performance metrics," in *Annual Conference of the Prognostics and Health Management Society*, September 2009.

[143] C. Kulkarni, J. Celaya, G. Biswas, and K. Goebel, "Prognostic modeling and experimental techniques for electrolytic capacitor health monitoring," *The 8th International Workshop on Structural Health Monitoring 2011 (IWSHM) , September 13-15, Stanford University, Stanford, CA*, 2011.

[144] C. Kulkarni, G. Biswas, J. Celaya, and K. Goebel, "A case study for capacitor prognostics under accelerated degradation," *IEEE 2011 Workshop on Accelerated Stress Testing & Reliability (ASTR), September 28-30, San Francisco, CA*, 2011.

[145] Biologic, *Application note 14-Zfit and equivalent electrical circuits*, BioLogic Science Instruments, 2010.

[146] J. Celaya, C. Kulkarni, G. Biswas, and K. Goebel, "Towards prognostic of electrolytic capacitors," *American Institute of Aeronautics and Astronautics, AIAA Infotech@Aerospace 2011, March 2011, St. Louis, Missouri*, 2011.

[147] M. Daigle and K. Goebel, "Model-based prognostics under limited sensing," in *Proceedings of the 2010 IEEE Aerospace Conference*, March 2010.

[148] A. Doucet, S. Godsill, and C. Andrieu, "On sequential monte carlo sampling methods for bayesian filtering," *Statistics and Computing*, vol. 10, pp. 197 – 208, 2000.

[149] P. Venet, H. Darnand, and G. Grellet, "Detection of faults of filter capacitors in a converter. application to predictive maintenance," *INTELEC Proc*, vol. 2, pp. 229 – 234, 1993.

[150] EIA-815, "Miniature aluminum electrolytic capacitor (leaded) qualification specification," *EIA*.

[151] EIA-395, "Polarized aluminum electrolytic capacitors for long life (type 1) and for general purpose application (type 2)," *EIA*.

[152] J. Celaya, A. Saxena, and K. Goebel, "Uncertainty representation and interpretation in model-based prognostics algorithms based on kalman filter estimation," *Proceedings of the Annual Conference of the PHM Society 2012, September 23- 27*, 2012.